

# **From diatomic to polyatomic quantum-state-resolved molecule-surface scattering**

Dissertation

zur Erlangung des mathematisch-naturwissenschaftlichen Doktorgrades

„Doctor rerum naturalium“

der Georg-August-Universität Göttingen

im Promotionsprogramm Chemie

der Georg-August University School of Science (GAUSS)

vorgelegt von

**Bastian Christopher Krüger**

aus Wilhelmshaven

Göttingen, 2017

### **Betreuungsausschuss**

Prof. Dr. Alec M. Wodtke  
Institut für Physikalische Chemie, Georg-August-Universität Göttingen

Prof. Dr. Dirk Schwarzer  
Max-Planck-Institut für biophysikalische Chemie, Göttingen

### **Mitglieder der Prüfungskommission**

Referent: Prof. Dr. Alec M. Wodtke  
Institut für Physikalische Chemie, Georg-August-Universität Göttingen

Korreferent: Prof. Dr. Dirk Schwarzer  
Max-Planck-Institut für biophysikalische Chemie, Göttingen

### **Weitere Mitglieder der Prüfungskommission**

Prof. Dr. Theofanis N. Kitsopoulos  
Institut für Physikalische Chemie, Georg-August-Universität Göttingen

Dr. Sebastian Kruss  
Institut für Physikalische Chemie, Georg-August-Universität Göttingen

Prof. Dr. Ricardo Mata  
Institut für Physikalische Chemie, Georg-August-Universität Göttingen

Prof. Dr. Jörg Schroeder  
Institut für Physikalische Chemie, Georg-August-Universität Göttingen

Tag der mündlichen Prüfung: 4. Oktober 2017

The work described in this thesis was carried out under the supervision of Prof. Dr. Alec M. Wodtke at the Institute for Physical Chemistry of the University of Göttingen between January 2014 and August 2017.

Parts of this thesis have been published in reviewed print journals as indicated below:

N. Bartels, B. C. Krüger, D. J. Auerbach, A. M. Wodtke, T. Schäfer, Controlling an electron-transfer reaction at a metal surface by manipulating reactant motion and orientation, *Angew. Chem. Int. Ed.* **2014**, *53*(50), 13690-13694.

B. C. Krüger, N. Bartels, C. Bartels, A. Kandratsenka, J. C. Tully, A. M. Wodtke, T. Schäfer, NO Vibrational Energy Transfer on a Metal Surface: Still a Challenge to First-Principles Theory, *J. Phys. Chem. C* **2015**, *119*(6), 3268-3272.

B. C. Krüger, N. Bartels, J. Altschäffel, A. M. Wodtke, T. Schäfer, Controlling collisions of highly vibrationally excited NO with a Au(111) surface, *Bunsenmagazin* **2015**, *5*, 185.

G. B. Park, B. C. Krüger, S. Meyer, A. M. Wodtke, T. Schäfer, A 1+1' resonance-enhanced multiphoton ionization scheme for rotationally state-selective detection of formaldehyde via the  $\tilde{A}^1A_2 \leftarrow \tilde{X}^1A_1$  transition, *Phys. Chem. Chem. Phys.* **2016**, *18*, 22355-22363.

G. B. Park, B. C. Krüger, S. Meyer, D. Schwarzer, T. Schäfer, The  $\nu_6$  fundamental frequency of the  $\tilde{A}$  state of formaldehyde and Coriolis perturbations in the  $3\nu_4$  level, *J. Chem. Phys.* **2016**, *144*(19), 194308.

B. C. Krüger, N. Bartels, A. M. Wodtke, T. Schäfer, Final rotational state distributions from NO( $\nu_1 = 11$ ) in collisions with Au(111): the magnitude of vibrational energy transfer depends on orientation in molecule-surface collisions, *Phys. Chem. Chem. Phys.* **2016**, *18*, 14976-14979.

B. C. Krüger, S. Meyer, A. Kandratsenka, A. M. Wodtke, T. Schäfer, Vibrational Inelasticity of Highly Vibrationally Excited NO on Ag(111), *J. Phys. Chem. Lett.* **2016**, *7*(3), 441-446.

B. C. Krüger, G. B. Park, S. Meyer, R. J. V. Wagner, A. M. Wodtke, T. Schäfer, Trapping-desorption and direct-scattering of formaldehyde at Au(111), *Phys. Chem. Chem. Phys.* **2017**, *19*, 19896-19903.

G. B. Park, B. C. Krüger, S. Meyer, A. Kandratsenka, A. M. Wodtke, T. Schäfer, An axis-specific rotational rainbow in the direct scatter of formaldehyde from Au(111) and its influence on trapping probability, *Phys. Chem. Chem. Phys.* **2017**, *19*, 19904-19915.



# Abstract

In this work, molecule-surface scattering is studied for the diatomic molecule nitric oxide (NO) and the polyatomic molecule formaldehyde. Following the approach of “molecular surface science”, elementary steps in the interaction of molecules with surfaces are revealed using a molecular beam surface scattering apparatus which permits the examination of the collision process under well-defined conditions. This requires that the initial molecular degrees of freedom are well controlled and that the final distribution over the molecular degrees of freedom can be obtained resolving single quantum states.

For nitric oxide (NO) surface scattering a number of powerful optical methods exists for the manipulation of the initial vibrational and rotational state as well as the initial orientation. These methods are used in this work to investigate the scattering of NO in the initial vibrational state  $v_i = 11$  with a vibrational energy of 2.5 eV from the single crystal surfaces Au(111), Ag(111), and Ge(111). The NO/Au(111) surface system has already been extensively studied and is a showcase system for nonadiabatic behavior. Many experimentally observed processes such as multi-quantum vibrational excitation and relaxation can only be described by theories going beyond the Born-Oppenheimer approximation. In particular the relaxation process of highly vibrationally excited NO molecules has been shown to be a strong manifestation of nonadiabatic effects involving the direct transfer of vibrational energy to electronic excitation. Up to now, however, a systematic study on the coupling of different molecular degrees of freedom during the scattering process of initially highly vibrationally excited NO molecules was missing. In this work, the exact coupling between vibrational energy loss, final rotational energy, and final translational energy is revealed by state-resolved time-of-flight experiments on laser-prepared NO molecules that have been scattered from surfaces. The results do not only allow the exact determination of the energy transferred to the surface but also contribute to the multidimensional dataset that is available for the NO/Au(111) system and thus support the development of accurate theories of nonadiabatic surface dynamics. In addition, the influence of surface properties on multi-quantum vibrational relaxation is investigated in scattering experiments of NO( $v_i = 11$ ) from Ag(111) and Ge(111). The vibrational

energy loss observed at Ag(111) is dramatically increased with respect to the energy loss at Au(111). This observation can be qualitatively understood in the framework of the existing mechanistic picture in which the vibrational energy is transferred to electronic excitation in the metal mediated by the transient formation of the nitric oxide anion. Due to the lower work function of Ag(111) the anion is more stable at the Ag(111) than at the Au(111) surface which leads to more efficient relaxation at Ag(111). Though the best available *ab initio* theory predicts an increased vibrational relaxation probability at Ag(111) the probability and magnitude of vibrational relaxation observed in the experiment is underestimated.

For formaldehyde the first molecular beam surface scattering experiments are presented. As a part of this work, a new 1+1' resonance-enhanced multiphoton ionization (REMPI) scheme via the  $\tilde{A}$  state has been developed providing an efficient and rotational-state-resolved detection method for scattered formaldehyde. This technique is applied together with time-of-flight methods employing 2+1 REMPI detection via the  $3 p_x$  Rydberg state to investigate formaldehyde/Au(111) surface scattering. The scattering of ground vibrational state formaldehyde is characterized as a competition between two mechanisms: trapping-desorption dominates at low incidence translational energies and direct-scattering dominates at high incidence translational energies. The trapping probabilities are found to be higher than expected by a simple hard cube model. The comparatively high amount of rotational excitation observed in the direct-scattering channel suggests that rotational excitation promotes the trapping process via efficient energy transfer of initial translational energy to rotational excitation and subsequent thermalization. An analysis of the rotational state distributions of directly scattered formaldehyde supports this hypothesis. The characterization of the vibrationally elastic ground vibrational state scattering process together with a required increase in the absolute densities of formaldehyde in the molecular beam would open up the opportunity for a number of interesting experiments on vibrationally excited formaldehyde. In this work, it is demonstrated that formaldehyde in the vibrational states  $2_14_1$  and  $2_16_1$  can efficiently be prepared in a molecular beam using a narrow-bandwidth IR laser source and can be detected in the incoming beam using the new 1+1' REMPI scheme. In a future experiment, the vibrational relaxation process in direct-scattering of formaldehyde initially prepared in  $2_14_1$  could be studied by monitoring the population of the scattered formaldehyde in the  $2_1$  and the  $4_1$  state. This will potentially reveal mode-specific vibrational relaxation induced by nonadiabatic effects in the interactions between formaldehyde and the Au(111) surface.

# Contents

<b>1. Introduction</b>	<b>1</b>
<b>2. Scientific context</b>	<b>5</b>
2.1. Spectroscopy of nitric oxide . . . . .	5
2.1.1. The $X^2\Pi_{\Omega}$ ground electronic state . . . . .	6
2.1.2. The first excited state: $A^2\Sigma^+$ . . . . .	7
2.1.3. 1+1 A-X REMPI of NO: Selection rules, branches, and detection efficiencies . . . . .	7
2.2. Spectroscopy of formaldehyde . . . . .	8
2.2.1. The asymmetric top Hamiltonian . . . . .	10
2.2.2. The $\tilde{A}^1A_2 \leftarrow \tilde{X}^1A_1 (4_0^1)$ transition and its rotational branches . . . . .	12
2.2.3. Calculation of line strength . . . . .	14
2.3. Nonadiabatic transitions . . . . .	15
2.3.1. Born-Oppenheimer separation . . . . .	15
2.3.2. Adiabatic and diabatic representations . . . . .	17
2.3.3. Landau-Zener-Stueckelberg approximation . . . . .	19
2.4. The structure of gold, silver and germanium . . . . .	19
2.5. Nonreactive dynamics at surfaces . . . . .	21
2.5.1. Trapping-desorption and direct-scattering . . . . .	21
2.5.2. Rotational rainbows in molecule-surface scattering . . . . .	25
2.5.3. Nonadiabatic dynamics at surfaces . . . . .	26
2.5.4. Polyatomic molecule-surface scattering . . . . .	31
<b>3. Experimental setup</b>	<b>35</b>
3.1. Surface scattering apparatus . . . . .	35
3.1.1. A heatable nozzle . . . . .	36
3.1.2. Using the MCP detector . . . . .	38

3.2.	Lasers . . . . .	40
3.2.1.	Dye lasers . . . . .	40
3.2.2.	Sunlite Ex OPO with FX 1 UV frequency extension . . . . .	40
3.2.3.	Homebuilt optical parametric oscillators . . . . .	40
3.2.4.	Fluorine laser . . . . .	41
3.2.5.	Narrow-bandwidth IR-laser . . . . .	42
<b>4.</b>	<b>Experimental procedures</b>	<b>45</b>
4.1.	Experiments on nitric oxide scattering . . . . .	45
4.1.1.	Preparation of NO $X^2\Pi_{1/2}(v = 11)$ . . . . .	45
4.1.2.	1+1 REMPI via the A state as a detection for surface scattered ground electronic state NO . . . . .	45
4.1.3.	Time-of-flight experiments on NO $X^2\Pi_{1/2}(v = 11)$ . . . . .	46
4.2.	Experiments on formaldehyde scattering . . . . .	47
4.2.1.	1+1' REMPI of formaldehyde via the $\tilde{A}$ state . . . . .	49
4.2.2.	2+1 REMPI of formaldehyde via the $3 p_x$ Rydberg state . . . . .	49
4.2.3.	Preparation of formaldehyde in vibrationally excited states . . . . .	50
4.3.	Temperature programmed desorption . . . . .	50
<b>5.</b>	<b>Analysis</b>	<b>51</b>
5.1.	Spectral analysis . . . . .	51
5.1.1.	Nitric oxide . . . . .	51
5.1.2.	Formaldehyde . . . . .	53
5.2.	Time-of-flight analysis . . . . .	54
5.2.1.	Nitric oxide . . . . .	55
5.2.2.	Formaldehyde . . . . .	57
<b>6.</b>	<b>Scattering of highly vibrationally excited NO – results and discussion</b>	<b>59</b>
6.1.	Scattering from Au(111) . . . . .	59
6.1.1.	Rotational state distributions as fingerprints of dynamical effects in NO( $v_i = 11$ )/Au(111) scattering . . . . .	59
6.1.2.	Translational inelasticity accompanying multi-quantum vibrational relaxation at Au(111) . . . . .	66
6.1.3.	Artifact resulting from collisions with a detector part . . . . .	74
6.1.4.	Effect of the surface temperature on multi-quantum vibrational relaxation . . . . .	76



6.2.	Scattering from Ag(111) . . . . .	78
6.2.1.	Multi-quantum vibrational relaxation at Ag(111): The vibrational state distribution . . . . .	78
6.2.2.	Multi-quantum vibrational relaxation at Ag(111): The rotational state distributions . . . . .	85
6.2.3.	Multi-quantum vibrational relaxation at Ag(111): Translational inelasticity . . . . .	87
6.3.	Scattering of highly vibrationally excited NO( $v_i = 11$ ) from Ge(111) . . .	89
<b>7.</b>	<b>Formaldehyde at Au(111) – results and discussion</b>	<b>97</b>
7.1.	Temperature programmed desorption . . . . .	97
7.2.	1+1' REMPI of formaldehyde via the $\tilde{A}$ state . . . . .	98
7.2.1.	Laser fluence dependence . . . . .	100
7.2.2.	1+1' REMPI spectra of formaldehyde in a cold molecular beam .	102
7.2.3.	Applying the REMPI scheme to surface scattering . . . . .	106
7.3.	Scattering of formaldehyde from Au(111) . . . . .	108
7.3.1.	Characterization of the incoming beam . . . . .	108
7.3.2.	Manipulation of the incoming beam - preparation of vibrationally excited formaldehyde . . . . .	110
7.3.3.	Translational inelasticity in the scattering of formaldehyde from Au(111) . . . . .	115
7.3.4.	Rotational state distributions . . . . .	126
7.3.5.	Comparison of experimentally derived rotational state distributions to predictions of classical trajectory calculations . . . . .	136
<b>8.</b>	<b>Conclusions and outlook</b>	<b>143</b>
<b>A.</b>	<b>Appendix</b>	<b>149</b>
A.1.	MATLAB code for simulating 1+1' REMPI spectra . . . . .	149
A.2.	Best fit parameters for rotationally resolved 1+1' REMPI spectra of directly scattered formaldehyde from Au(111) . . . . .	176
A.3.	MATHEMATICA program for classical trajectory calculations . . . . .	176
<b>B.</b>	<b>List of abbreviations</b>	<b>195</b>
<b>C.</b>	<b>References</b>	<b>197</b>



# 1. Introduction

Many important basic large-scale chemical processes, such as the synthesis of sulfuric acid or ammonia, are based on heterogeneous catalysis.<sup>[1]</sup> In these processes, gas phase molecules interact with solid surfaces. The elementary steps of these processes can be studied in detail for idealized systems which is known as the “molecular surface science” approach.<sup>[2]</sup> For the ammonia synthesis it has been demonstrated that a more detailed theoretical understanding of the elementary processes<sup>[3]</sup> can lead to an improvement of the industrial process.<sup>[2]</sup> The relevance of this research becomes obvious considering the high energy consumption of industrial ammonia synthesis as well as the impact of ammonia on agriculture as a base chemical for fertilizer production.<sup>[4]</sup>

However, today’s understanding of collision processes at surfaces is for many systems still far from satisfying and lags behind the understanding of pure gas phase processes. This becomes clear from a comparison of the accuracy of the best available *ab initio* theory for two scattering processes for which detailed experimental data exist —nitric oxide(NO)/rare gas atom scattering<sup>[5]</sup> and the scattering of highly vibrationally excited NO from a Au(111) surface.<sup>[6]</sup> Figure 1.1a) shows a comparison between an experimental observation of the angular distribution in NO-rare gas cross beam experiments detecting the scattered NO via velocity map imaging and an unbiased prediction of the angular distribution based on a high level quantum mechanical close coupling prediction of the differential cross sections. The convincing agreement between experiment and theory shows that these collision events in the gas phase are well understood. On contrary, the experimental observations and theoretical predictions disagree for highly vibrationally excited NO/Au(111) surface scattering.<sup>[7]</sup> Figure 1.1b) shows the final vibrational state distribution observed in the experiment<sup>[6]</sup> (black) and the theoretical prediction based on the IESH theory<sup>[8]</sup> (red). The severe underestimation of the amount of vibrational relaxation observed in the experiment reflects the difficulties and challenges related with the theory on molecule-surface collisions.

In general, the increasing system size and increasing dimensionality that arises from the replacement of a gas phase projectile with a surface limits the feasible theoretical

## 1. Introduction

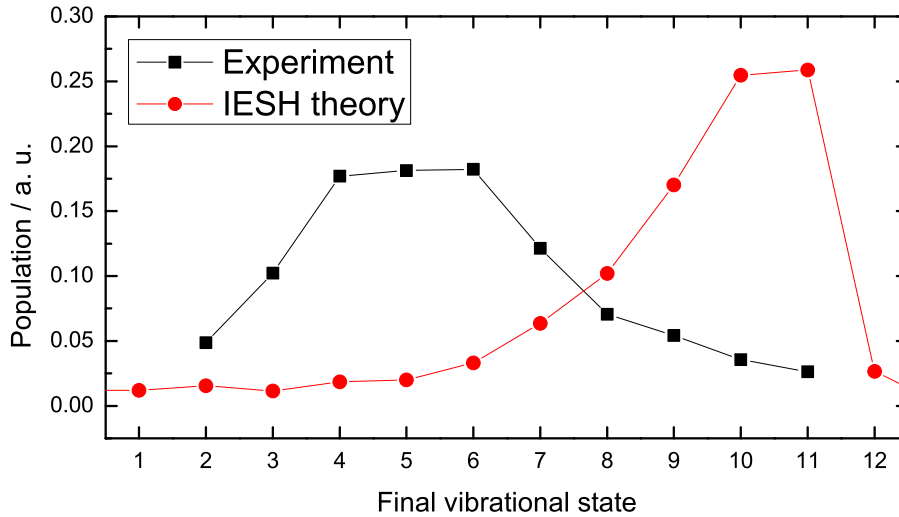
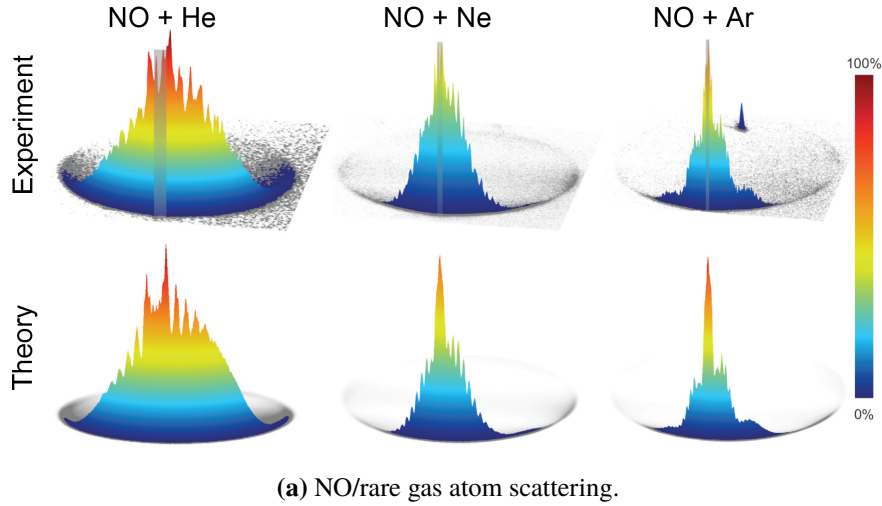


**Figure 1.1.:** a) Three-dimensional representation of the angular distribution of nitric oxide (NO) in NO/rare gas atom ( $Rg = \text{He, Ne, Ar}$ ) scattering for the process  $\text{NO}(J = 0.5, f) + Rg \rightarrow \text{NO}(J = 1.5, e) + Rg$ .  $J$  denotes the rotational quantum number, and  $e$  and  $f$  denote the symmetry. The radius in the plot corresponds to the speed of the molecules and the height corresponds to the scattered intensity at a certain angle in the center of mass frame. The upper panel shows the experimental data obtained by velocity map imaging. The lower panel shows a prediction based on the theoretical calculation of the state-to-state differential cross sections. The figure is adapted with permission from Macmillan Publishers Ltd: reference [5]. b) Vibrational state distribution in highly vibrationally excited NO/Au(111) surface scattering. The initial vibrational state is  $v_i = 11$  and the incidence translational energy is 0.51 eV. The vibrational state distribution obtained in an experiment is shown in black. Theoretical predictions based on the independent electron surface hopping (IESH) theory are shown in red. Data taken from reference [7].

approaches in almost every case to rather inaccurate density functional theory (DFT) and excludes pure wavefunction methods.<sup>[9]</sup> In addition, the properties of the NO/Au surface system (i.e., the high electron affinity of the molecule and the metallic nature of gold) give rise to so called nonadiabatic couplings between nuclear and electronic motion reflecting the breakdown of the Born-Oppenheimer approximation<sup>[10]</sup>. The importance of the non-adiabatic couplings in the scattering process has been demonstrated by a comparison of the scattering of highly vibrationally excited NO at a metal and an insulator surface. The extremely efficient multi-quantum vibrational relaxation of NO observed at Au(111) is absent in the scattering at LiF.<sup>[11]</sup> A large contribution of phonon-coupling can be excluded based on a comparison of the available low energy phonon modes and the large vibrational spacing of the molecule. The authors in reference [11] concluded that the mechanism for vibrational energy loss involves excitation of electrons via the transient formation of the nitric oxide anion. In the following years, the NO/metal surface system has been extensively studied experimentally. In addition to the multi-quantum vibrational relaxation process, strong vibrational excitation<sup>[12]</sup> and electron emission<sup>[13]</sup> have been identified as manifestations of nonadiabatic dynamics.<sup>[14]</sup> In this way, the NO/metal surface system became a showcase model for nonadiabatic behavior providing experimental data for testing theories that go beyond the Born-Oppenheimer approximation. Two different theoretical approaches describing the nonadiabatic dynamics via electronic friction<sup>[15]</sup> or an independent electron surface hopping (IESH) algorithm<sup>[8]</sup> seemed to reproduce the vibrational state distributions observed in the relaxation experiment successfully. However, a detailed investigation of vibrational excitation<sup>[12]</sup> as well as the incidence parameter dependence<sup>[6]</sup> and the translational inelasticity in vibrational relaxation showed the failure of both theories.<sup>[7,16]</sup> This demonstrates the value of a detailed multidimensional experimental dataset for testing theories.

In this work, this dataset will be extended following three basic questions. First, how are the different molecular degrees of freedom coupled in the multi-quantum vibrational relaxation of initially highly vibrationally excited NO at Au(111)? In order to answer this question, state-resolved time-of-flight techniques<sup>[17]</sup> are adapted to study the scattering of highly vibrationally excited NO. The coupling between translational, rotational, and vibrational motion is revealed allowing the determination of the energy conversion to surface degrees of freedom as well as conclusions on the mechanism behind the coupling between the degrees of freedom. Second, how do surface properties alter the efficiency of multi-quantum vibrational relaxation? Apart from an early study on vibrational excitation of NO at Ag(111)<sup>[18]</sup> little is known on vibrationally inelastic scattering of NO at metal

## 1. Introduction

surfaces other than Au(111). In this work, experimental data on the scattering of highly vibrationally excited NO from Ag(111) and Ge(111) is presented for the first time. It will be shown that the results for Ag(111) can be qualitatively understood based on the existing mechanistic picture, which involves the transient formation of the nitric oxide anion as a mediator for electronic excitation. The experiments presented here motivated an additional study of the vibrational relaxation process of NO at ultrathin Ag films deposited with controllable thickness on a Au(111) surface which is presented elsewhere<sup>[19]</sup>. Third, are the nonadiabatic vibrationally inelastic processes observed for the NO/metal surface systems more general thus also observable for other molecules? This question can already be answered with yes. However, only a limited amount of data for the diatomic molecules HCl<sup>[20]</sup> and CO<sup>[21]</sup> is available and data for polyatomic molecules is desirable. In this work, surface scattering of the polyatomic molecule formaldehyde is presented for the first time. Formaldehyde is chosen as an ideal candidate for studies on nonadiabatic surface dynamics as its electron affinity of  $-0.65$  eV<sup>[22]</sup> is well below the electron affinity of CO<sup>[23]</sup> and comparable to that of HCl<sup>[24]</sup>. Experimental methods for the investigation of the scattering process are presented and basic questions concerning the scattering mechanism for vibrational ground state formaldehyde are addressed. Experiments on vibrationally inelastic scattering that might reveal nonadiabatic effects are left to future investigations. In detail, a new REMPI detection scheme for formaldehyde is developed enabling efficient rotationally resolved detection of scattered formaldehyde. Together with time-of-flight methods based on detection via a 2+1 REMPI scheme<sup>[25]</sup> this enables the characterization of trapping-desorption and direct-scattering in the scattering of formaldehyde from Au(111) for incidence translational energies between 0.1 eV and 1.3 eV. The translational inelasticity in formaldehyde/Au(111) surface scattering is revealed. For the first time a rotational-state resolved surface scattering experiment on an asymmetric top molecule is presented revealing an axis specific rotational rainbow. In addition, a method for producing vibrationally excited formaldehyde is successfully tested for the first time.

## 2. Scientific context

In the sections 2.1 and 2.2 an overview of the electronic spectroscopy of nitric oxide and formaldehyde is provided. The sections are focused on the description of electronic states and transitions relevant for the spectroscopy employed in this work. The second part of this chapter is devoted to the scientific context relevant to the scattering experiments. This includes an introduction to nonadiabatic effects (see Section 2.3) which are central themes of investigation in this work and a brief description of the structure of the surfaces Au(111), Ag(111) and Ge(111) investigated in the scattering experiment (see Section 2.4). In the last Section 2.5 important contributions to the investigation of surface scattering are presented. A general introduction to basic mechanisms in surface scattering is followed by an overview of more recent contributions to quantum-state-resolved molecule-surface scattering with the focus on the two central issues of this work: nonadiabatic effects in molecule-surface scattering and polyatomic molecule-surface scattering.

### 2.1. Spectroscopy of nitric oxide

Nitric oxide is probably the most thoroughly studied molecule in spectroscopy. A high number of electronic states have been observed.<sup>[26]</sup> In particular, the  $X^2\Pi_{\Omega}$  ground electronic state  $\Omega = \frac{1}{2}, \frac{3}{2}$  and the lowest excited state  $A^2\Sigma^+$  are of interest for this work. NO in its ground electronic state can easily be quantum-state specifically detected via allowed spectroscopic transitions belonging to the  $\gamma$ -band system ( $A^2\Sigma^+ \leftarrow X^2\Pi_{\Omega}$ ). A well understood and sensitive 1+1 REMPI scheme using these transitions is available.<sup>[27]</sup> In the next two sections the two relevant electronic states are described following the remarks in reference [28], [29] and [30]. In the subsequent section, the transition frequencies and selection rules are explained.

## 2. Scientific context

### 2.1.1. The X $^2\Pi_\Omega$ ground electronic state

In this section, a sufficiently accurate description of the X $^2\Pi_\Omega$  state in order to assign and simulate 1+1 REMPI spectra of NO via the A state is given. An effective Hamiltonian for diatomic molecules is given in reference [31]. It is most conveniently divided into two parts. See Equation 2.1.

$$H = H_0 + V \quad (2.1)$$

$H_0$  contains all information on the vibrational structure, whereas  $V = H_{SO} + H_{Rot} + H_{SR}$  describes fine structure arising due to the interaction of electronic angular momentum with spin ( $H_{SO}$ ), due to molecular rotation ( $H_{Rot}$ ), and due to the interaction between spin and rotation  $H_{SR}$ . The matrix element for the Hamiltonian can be written in the Hund's case (a) basis. Then the wave functions are:

$$|JM\Omega\epsilon\rangle = \frac{1}{\sqrt{2}}(|JM + \Omega\rangle + \epsilon |JM - \Omega\rangle). \quad (2.2)$$

Here,  $J$ ,  $M$ , and  $\Omega$  are the quantum numbers for total angular momentum, projection of the angular momentum on a lab frame axis, and the projection of orbital angular momentum and spin onto the internuclear axis, respectively.  $\epsilon$  can be +1 or -1, which is denoted as e or f. The e/f-notation is for this electronic state related to the total parity (+/-) via  $(-1)^{J-\frac{\epsilon}{2}}$ . The Hamiltonian  $H$  can then be written in the form of two 2x2-matrices, one for each parity:

$$H_\epsilon = \begin{pmatrix} H_{11,\epsilon,(\Omega=3/2)} & H_{12,\epsilon} \\ H_{12,\epsilon} & H_{22,\epsilon,(\Omega=1/2)} \end{pmatrix}. \quad (2.3)$$

The matrix elements can be related to spectroscopic constants in  $\text{cm}^{-1}$  units as shown in the following equations:

$$H_{11,e} = H_{11,f} = hc(T_0 + W + 0.5A + 0.5A_D \cdot z + B \cdot z - D \cdot z(z+1) + H \cdot z(z+1)(z+2)) \quad (2.4)$$

$$\begin{aligned} H_{22,\epsilon} = & hc(T_0 + W - 0.5A - 0.5A_D \cdot (z+2) \\ & + B \cdot (z+2) - D \cdot (z+1)(z+4) + H \cdot (z+1)(z^2 + 8z + 8) \\ & - 0.5\epsilon \cdot p_\Lambda \cdot (J+0.5) - \epsilon \cdot q_\Lambda \cdot (J+0.5)) \end{aligned} \quad (2.5)$$

$$\begin{aligned} H_{12,\epsilon} = & hc(-B \cdot z^{0.5} + 2D \cdot z^{0.5}(z+1) - H \cdot z^{0.5}(z+1)(3z+4) \\ & + 0.5\epsilon \cdot q_\Lambda \cdot z^{0.5}(J+0.5)). \end{aligned} \quad (2.6)$$



Here,  $J$  is the quantum number for the total angular momentum and  $z$  is defined as  $z = (J - 0.5)(J + 0.5)$ .  $T_0$  is the electronic term energy and  $W$  is the vibrational term energy.  $B$ ,  $D$  and  $H$  are rotational constants.  $A$  and  $A_D$  describe the spin-orbit splitting. The  $q_\Lambda$  and  $p_\Lambda$  parameters describe  $\Lambda$ -doubling due to interactions of the ground state with excited electronic states. It is commonly accepted that the main contribution to  $\Lambda$ -doubling arises from perturbations with  $^2\Sigma^-$  states. The splitting effect is stronger for the lower  $\Omega = 1/2$  state.

All spectroscopic parameters besides  $T_0$  depend on the vibrational quantum number. For calculation of term energies the eigenvalues of matrix 2.3 are calculated with  $q_\Lambda$  and  $p_\Lambda$  parameters taken from reference [32]. All other parameters are taken from reference [30]. Hund's case (a) is appropriate for low rotational energy up to  $J \approx 35.5$ .

### 2.1.2. The first excited state: $A^2\Sigma^+$

Since the A state is a  $\Sigma$  state, Hund's case (b) is a good description for the term energies. In order to simplify calculations of transition frequencies between A and X state (Hund's case (a)), the term energies are calculated using  $J$  instead of the quantum number  $N$  for pure nuclear rotational motion, which is usually used to describe the A state. The term energies can be calculated using Equation 2.7 and 2.8.

$$H_e = hc(T_A + W_A + B_A \cdot (J - 0.5)(J + 0.5) - D_A(J - 0.5)^2(J + 0.5)^2 + 0.5\gamma_A(J - 0.5)) \quad (2.7)$$

$$H_f = hc(T_A + W_A + B_A \cdot (J - 0.5)(J + 0.5) - D_A(J - 0.5)^2(J + 0.5)^2 - 0.5\gamma_A(J + 1.5)) \quad (2.8)$$

Here,  $T_A$  and  $W_A$  are the electronic and vibrational term energies.  $B_A$  and  $D_A$  are the rotational constants. Their values depend on the vibrational quantum number in the A state  $v_A$ .  $\gamma_A$  is the spin splitting constant and describes the spin-rotation interaction.

### 2.1.3. 1+1 A-X REMPI of NO: Selection rules, branches, and detection efficiencies

A vibrational band belonging to the  $\gamma$ -band system consists of 12 rotational branches. The selection rules are given below:

## 2. Scientific context

$$\Delta J = 0, \pm 1 \quad (2.9)$$

$$\Delta S = 0 \quad (2.10)$$

$$\Delta \Lambda = 0, \pm 1 \quad (2.11)$$

$$+ \leftrightarrow -, + \leftrightarrow +, - \leftrightarrow - \quad (2.12)$$

Equation 2.9 and 2.12 are important in order to explain the occurrence of the variety of different branches. The  $\Delta J = -1, 0, +1$  transitions give rise to P, Q, and R branches. According to selection rule 2.12 only transitions between levels with opposite parity are allowed. Hence, twelve rotational branches result. See Figure 2.1. They are labeled as  $\Delta J_{F''F'}$  using the spin labels F1 and F2. As a consequence of spin-orbit coupling in the X state rovibronic states with F1 belong to the  $\Omega = 0.5$  state whereas those with F2 belong to the  $\Omega = 1.5$  state. On the contrary, in the A state F1 and F2 components are only separated by a small splitting resulting from spin-rotation interaction as can be seen in Equation 2.7 and 2.8.

The dependence of the observed REMPI intensities on the ground electronic state population is exactly known for the 1+1 A-X REMPI scheme. Following a method described in reference [27], ground electronic state population factors can be obtained correcting for Hönl-London-factors and intermediate state alignment.

## 2.2. Spectroscopy of formaldehyde

Formaldehyde is one of the spectroscopically most extensively studied polyatomic molecules.<sup>[34]</sup> The following sections are meant to present the most important information in order to understand electronic spectra of the  $\tilde{A}^1A_2 \leftarrow \tilde{X}^1A_1$  transition. The symmetry of formaldehyde in its ground electronic state can be described by the point group  $C_{2v}$ . Important symmetry properties are given in Table 2.1. The symmetry properties of operators such as vibrational coordinates are important to understand selection rules and branch structure of the rovibronic spectroscopy of formaldehyde presented in the following sections. Section 2.2.1 provides the description of the rotational states of the formaldehyde molecule following the remarks in reference [36]. In Section 2.2.2 the vibrational structure is introduced and consequences for the electronic spectra of the  $\tilde{A}^1A_2 \leftarrow \tilde{X}^1A_1$  transition are given based on reference [37]. In Section 2.2.3 a method for calculating relative line strength is presented following the remarks in reference [35].

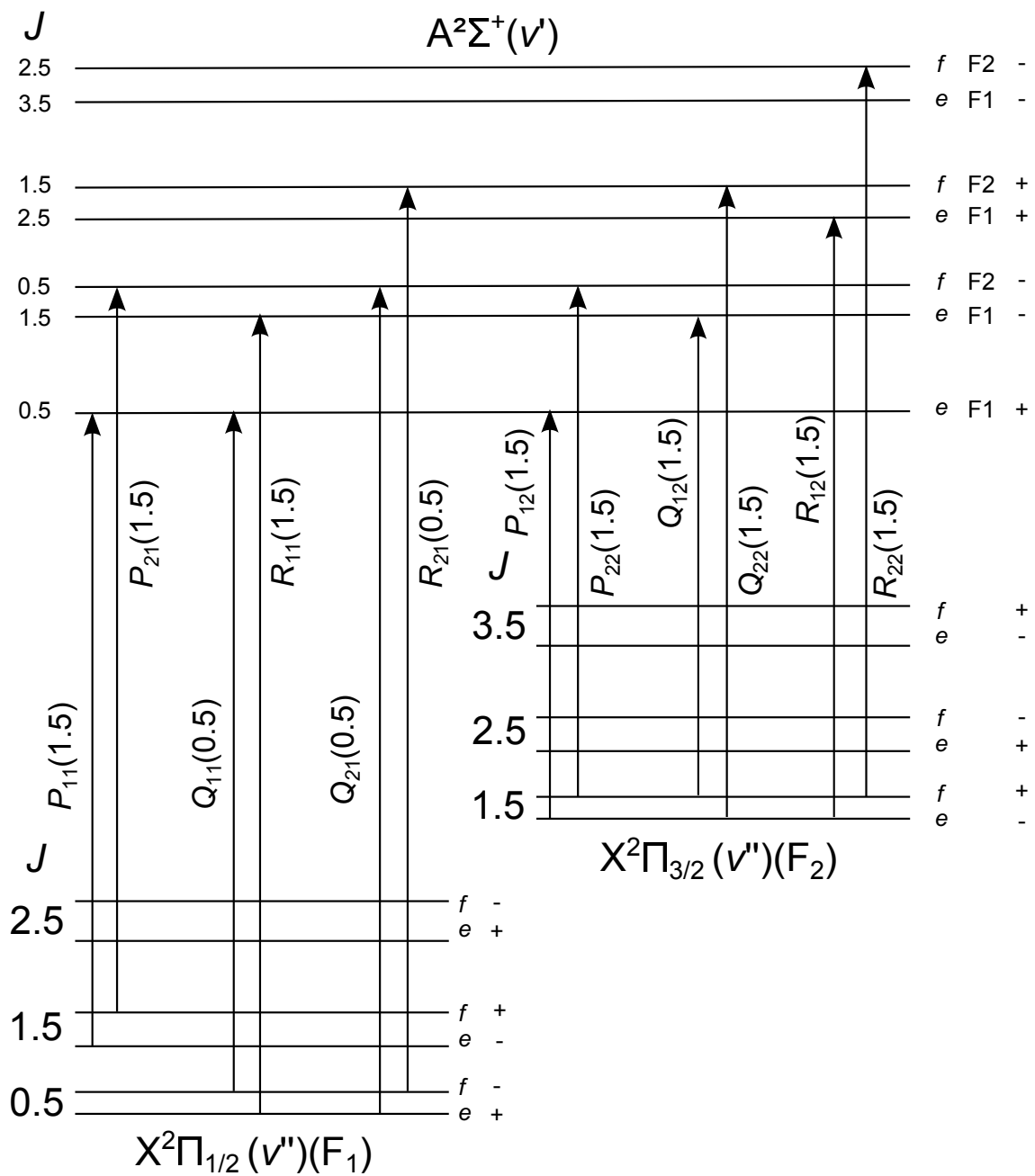


**Figure 2.1.:** Rotational branches for a vibrational band belonging to the  $\gamma$ -band system. Adapted from reference [33] and modified.

## 2. Scientific context

**Table 2.1.:** Character table of the point group  $C_{2v}$  and important symmetry properties of objects belonging to the formaldehyde molecule. The symmetry properties given in the table are derived from the information given in reference [35].

$C_{2v}$	E E $R^0$	$C_{2a}$ (12) $R_a^\pi$	$\sigma_{ab}$ $E^*$ $R_c^\pi$	$\sigma_{ac}$ (12)* $R_b^\pi$	vectors	rotational wavefunctions $K_a, K_c$	vibrational modes	nuclear wavefunctions
$A_1$	1	1	1	1	$T_a$	ee	$\nu_1, \nu_2, \nu_3$	ortho
$A_2$	1	1	-1	-1	$J_a$	eo		
$B_1$	1	-1	-1	1	$T_c, J_b$	oo	$\nu_4$	
$B_2$	1	-1	1	-1	$T_b, J_c$	oe	$\nu_5, \nu_6$	para

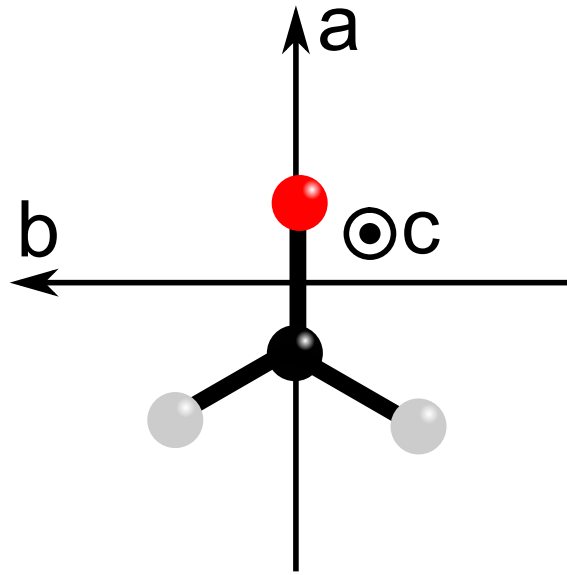


**Figure 2.2.:** Conventional choice of the coordinate system for formaldehyde. Adapted from reference [34].

### 2.2.1. The asymmetric top Hamiltonian

Since formaldehyde exhibits three different moments of inertia about the axes  $a$ ,  $b$ , and  $c$  it has to be described as an asymmetric top. The coordinate system is chosen such that the C-O bond points along the  $a$ -axis as shown in Figure 2.2. An elegant, compact form of the Hamiltonian appropriate for formaldehyde is the reduction of the Watson Hamiltonian through quartic centrifugal distortion terms shown below.<sup>[38]</sup>

$$\begin{aligned}
 H = & A\mathbf{J}_z^2 + 0.5(B + C)(\mathbf{J}^2 - \mathbf{J}_z^2) + 0.25(B - C)(\mathbf{J}_+^2 - \mathbf{J}_-^2) \\
 & - \Delta_J \mathbf{J}^4 - \Delta_{JK} \mathbf{J}^2 \mathbf{J}_z^2 - \Delta_K \mathbf{J}_z^4 \\
 & - 0.5((\delta_J \mathbf{J}^2 + \delta_K \mathbf{J}_z^2)(\mathbf{J}_+^2 + \mathbf{J}_-^2) + (\mathbf{J}_+^2 + \mathbf{J}_-^2)(\delta_J \mathbf{J}^2 + \delta_K \mathbf{J}_z^2))
 \end{aligned} \tag{2.13}$$

The Hamiltonian in Equation 2.13 is expressed in form of the rotational constants  $A$ ,  $B$  and  $C$  and various constants arising from centrifugal distortion labeled as  $\Delta$  or  $\delta$ . The operators for the total angular momentum  $\mathbf{J}$  and for its projection onto the  $a$ -axis  $\mathbf{J}_z$  act on the symmetric top wave functions  $|J, K\rangle$  used as a basis set as shown in Equations 2.14 and 2.15.

$$\mathbf{J} |J, K\rangle = J(J + 1) |J, K\rangle \quad (2.14)$$

$$\mathbf{J}_z |J, K\rangle = K |J, K\rangle \quad (2.15)$$

Here the quantum number  $K$  can have the values  $K = -J, \dots, J$ . Thus, the operators  $\mathbf{J}$  and  $\mathbf{J}_z$  leave the wave functions unchanged. However, the ladder operators  $\mathbf{J}_+$  and  $\mathbf{J}_-$  give rise to off-diagonal elements as shown in Equations 2.16 and 2.17.

$$\mathbf{J}_+ |J, K\rangle = (J(J + 1) - K(K - 1))^{0.5} |J, K - 1\rangle \quad (2.16)$$

$$\mathbf{J}_- |J, K\rangle = (J(J + 1) - K(K + 1))^{0.5} |J, K + 1\rangle \quad (2.17)$$

Here the Condon-Shortley phase convention is used (See reference [39] for an explanation of the convention). The energy levels for the asymmetric top can only be obtained by diagonalization of the Hamiltonian matrix. In practice, it is useful to apply the Wang transformation in order to reduce numerical errors in the calculation. The new basis set is then defined as  $|JK\pm\rangle = (|JK\rangle \pm |J - K\rangle)$ .<sup>[37]</sup> Neglecting centrifugal distortion (only considering the first line in Equation 2.13) shows that even in the rigid rotor approximation the 2-fold  $K$ -degeneracy of the symmetric top is lifted due to the expression  $+0.25(B - C)(\mathbf{J}_+^2 - \mathbf{J}_-^2)$ . Furthermore, the Hamiltonian exhibits only quadratic ladder operators. Hence, the only nonzero off diagonal elements fulfill the condition  $\Delta K = \pm 2$  as long as Coriolis interactions can be neglected. A certain rotational state is labeled according to  $J_{K_a, K_c}$ . Here,  $J$  is the quantum number for the total angular momentum and  $K_a$  is the quantum number for the projection of the total angular momentum on the  $a$ -axis.  $K_c$  is only formally the quantum number of the projection along the  $c$ -axis. It rather is a parity descriptor. Since formaldehyde is a near prolate top ( $A \gg B \approx C$ )  $K_a$  governs the rotational energy expression, and the splitting due to the term  $+0.25(B - C)(\mathbf{J}_+^2 - \mathbf{J}_-^2)$  is small. The spectroscopic constants for the first excited state  $\tilde{A}^1A_2$  and the ground electronic state  $\tilde{X}^1A_1$  are taken from reference [34] and reference [40], respectively.

## 2. Scientific context

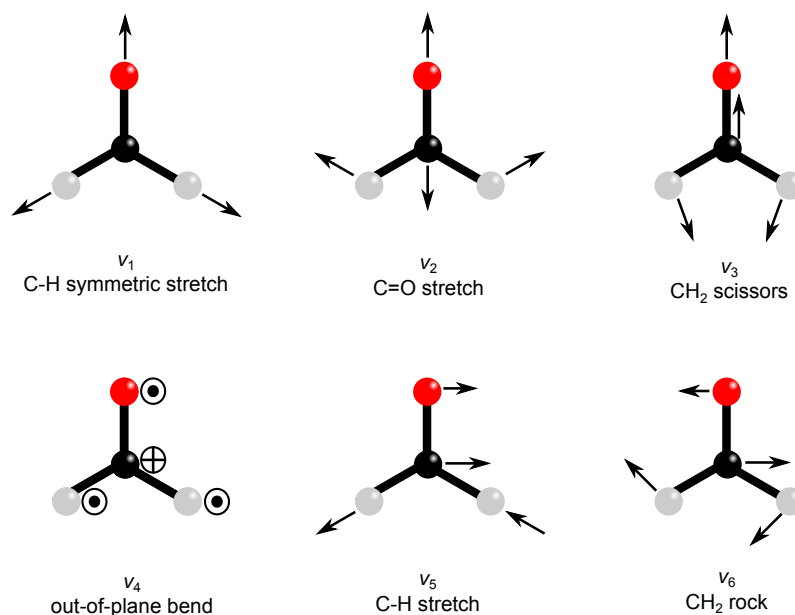


**Figure 2.3.:** Vibrational modes of formaldehyde. Adapted from reference [37].

### 2.2.2. The $\tilde{A}^1A_2 \leftarrow \tilde{X}^1A_1 (4_0^1)$ transition and its rotational branches

The vibrational modes of formaldehyde are shown in Figure 2.3. Table 2.2 provides an overview of the fundamental wavenumbers of the modes in the  $\tilde{X}^1A_1$  and the  $\tilde{A}^1A_2$  state.

**Table 2.2.:** Fundamental wavenumbers of the six modes in the  $\tilde{A}^1A_2$  and the  $\tilde{X}^1A_1$  state, taken from reference [37].

	$\tilde{\nu}_1/\text{cm}^{-1}$	$\tilde{\nu}_2/\text{cm}^{-1}$	$\tilde{\nu}_3/\text{cm}^{-1}$	$\tilde{\nu}_4/\text{cm}^{-1}$	$\tilde{\nu}_5/\text{cm}^{-1}$	$\tilde{\nu}_6/\text{cm}^{-1}$
$\tilde{A}^1A_2$	2816	1183	1293.1	124.5	2968.3	904
$\tilde{X}^1A_1$	2782.5	1746.0	1500.2	1167.3	2842.2	1249.1

Mode 4 exhibits the lowest energy fundamental transition in the  $\tilde{X}$  state. However, in the  $\tilde{A}$  state its fundamental transition is even lower by an order of magnitude. This curious behavior arises from a slightly non planar equilibrium geometry of the  $\tilde{A}$  state.<sup>[41]</sup> A barrier to inversion results in a double minimum potential in the coordinate of the  $\nu_4$  mode. This results in a tunneling splitting which explains the low energy difference between zero and one quanta of excitation. Hence, the  $\tilde{A} \leftarrow \tilde{X} (4_0^1)$  band is observed close to the origin (0-0 transition). The notation  $n_{\nu_n}^{\nu_n'}$  is used here to describe the change of vibrational quanta in a particular mode  $n$  during the electronic transition. However, in general the  $\tilde{A} \leftarrow \tilde{X}$  band system is electronic dipole forbidden which becomes clear when comparing the irreducible representations of the ground and excited electronic states as well as the possible irreducible representations for components of the electronic dipole moment in

the character table (Table 2.1). Note that the components of the dipole moment transform like the corresponding polar vectors  $T$ . Due to intensity borrowing via vibronic coupling some of the bands involving a change of vibrational symmetry such as  $4_0^1$  are nevertheless “pretty visible”. On the contrary, the intensity of the 0-0 transition is low because it is only allowed due to a magnetic dipole transition moment.<sup>[42]</sup> Thus, spectroscopy of the  $4_0^1$  transition is the method of choice in order to derive the population of rotational states in ground state formaldehyde, because it offers acceptable transition strength together with the benefit that the final states lie in the least complex region of the  $\tilde{A}$  state.

Group theory allows the component of the transition dipole moment that induces the  $\tilde{A} \leftarrow \tilde{X} (4_0^1)$  to be characterized and the selection rules with respect to the rotational quantum numbers to be derived. The vibronic symmetry of one quantum of excitation in  $\nu_4$  ( $B_1$ ) in the  $\tilde{A}^1A_2$  state is  $B_2$ . Thus, by evaluating the character table (Table 2.1) it can be concluded that only the  $b$ -component of the electric dipole moment can induce the electronic  $\tilde{A} \leftarrow \tilde{X} (4_0^1)$  transition. Based on this finding the band is called  $b$ -type. The selection rules for a  $b$ -type band are

$$\Delta K_a = \text{odd} \quad (2.18)$$

$$\Delta K_c = \text{odd}. \quad (2.19)$$

In the following, a plausible explanation for the selection rules 2.18 and 2.19 is given based on the remarks in reference [35]. The lab-frame projection of the dipole moment  $\mu_A$  (the projection of the dipole moment onto the polarization axis of the electric field) for the vibronic transition is calculated from the components of the dipole moment operator in the molecule fixed axes system ( $\mu_a, \mu_b, \mu_c$ ) and the direction cosines  $\lambda$  that relate the molecule fixed coordinate system with the spaced fixed axes. See Equation 2.20 below.

$$\mu_A = \lambda_{aA}\mu_a + \lambda_{bA}\mu_b + \lambda_{cA}\mu_c \quad (2.20)$$

The line strength of an electronic dipole transition will be proportional to the square of the matrix element given in Equation 2.21.

$$\langle \Phi' | \mu_A | \Phi'' \rangle = \left\langle \Phi'_{\text{nspin}} \left| \Phi''_{\text{nspin}} \right. \right\rangle \sum_{\alpha=a,b,c} \langle \Phi'_{\text{vib}} | \mu_\alpha | \Phi''_{\text{vib}} \rangle \times \left\langle N'_{K'_a, K'_c} \left| \lambda_{\alpha, A} \right| N''_{K''_a, K''_c} \right\rangle \quad (2.21)$$

In this equation,  $\Phi_{\text{nspin}}$  are the nuclear spin wave functions,  $\Phi_{\text{vib}}$  are the vibronic wave functions and  $N_{K_a, K_c}$  are the rotational wave functions for the upper and lower state indicated by ' and '', respectively. The direction cosines  $\lambda_{\alpha, A}$  have the same irreducible

## 2. Scientific context

representation in the point group  $C_{2v}$  as the corresponding axial vectors  $J_\alpha$ . See Table 2.1. For a  $b$ -type band only the term with  $\alpha = b$  has to be considered since all other integrals for the vibronic part are zero by symmetry. Now, the rotational part is only nonzero if condition 2.22 holds.

$$\Gamma_{N'} \otimes \Gamma_{\lambda_{bA}} \otimes \Gamma_{N''} = A_1 \quad (2.22)$$

$\lambda_{bA}$  has the irreducible representation  $B_1$ . If the two rotational quantum numbers  $K_a''$  and  $K_c''$  in the lower electronic state are even, then the irreducible representation of the rotational wave function is  $A_1$ . The only way that the integral  $\langle N'_{K'_a, K'_c} | \lambda_{\alpha, A} | N''_{K''_a, K''_c} \rangle$  does not vanish is that  $N'_{K'_a, K'_c}$  belongs to the irreducible representation  $B_1$ . This means that  $K'_a$  and  $K'_c$  have to be odd. Thus, the quantum numbers have to change by an odd number during the electronic transition. This can analogously be derived for the case when one of the rotational quantum numbers is odd and the other one is even. By actually evaluating the matrix element in Equation 2.22 one finds that  $\Delta K_a = \pm 1$  and  $\Delta K_c = \pm 1(\pm 3)$  transitions will dominate the band. As long as the asymmetry splitting due to  $K_c$  is not resolved, it is sufficient to use the labeling  $\Delta K_a \Delta J_{K''_a}$ . Here, changes of these quantum numbers by  $+1/0/-1$  correspond to the labels R/Q/P. If the symmetry splitting is resolved the notation  $\Delta K_a, \Delta K_c \Delta J_{K''_a, K''_c}(J'')$  can be used to label individual lines.

### 2.2.3. Calculation of line strength

The line strength may be calculated from Equation 2.21. However, it is more straightforward to use the available analytical expressions for the matrix elements in the symmetric top basis. The asymmetric top wave functions  $N(J, K_a, K_c)$  in a singlet state can be expressed as a linear combination of the symmetric top basis functions  $|J, K, m\rangle$  with  $m$  as the quantum number for the projection of the total angular momentum onto a preference axis in the laboratory frame as can be seen in Equation 2.23.

$$N(J, K_a, K_c) = \sum_{K=-J}^{K=J} c_K^{(J)} |J, K, m\rangle \quad (2.23)$$

The coefficients  $c_K^{(J)}$  can be obtained from the eigenvectors of the Hamiltonian of the asymmetric top given in Equation 2.13. In the case of a one-photon transition the relevant matrix element describing the strength of an electronic transition is then given using the



analytical expression derived in reference [43] and shown in Equation 2.24.

$$\begin{aligned}
 \langle \Phi' | \mu_s^{(1,\sigma)} | \Phi'' \rangle &= \langle \Phi'_{\text{nspin}} | \Phi''_{\text{nspin}} \rangle (-1)^{m'} ((2J'' + 1)(2J' + 1))^{0.5} \\
 &\times \begin{pmatrix} J'' & 1 & J' \\ m'' & \sigma & -m' \end{pmatrix} \sum_{K'=-J'}^{J'} \sum_{K''=-J''}^{J''} (-1)^{K'} c_{K'}^{(J')} c_{K''}^{(J'')} \\
 &\times \sum_{\sigma'=-1}^1 \langle \Phi'_{\text{vib}} | \mu_m^{(1,\sigma')} | \Phi''_{\text{vib}} \rangle \begin{pmatrix} J'' & 1 & J' \\ K'' & \sigma' & -K' \end{pmatrix}
 \end{aligned} \tag{2.24}$$

Note that the matrix element above contains two Wigner 3-j symbols. A nice introduction to these symbols can be found in reference [44] where the relation to Clebsch-Gordan coefficients is explained as well. Furthermore, quantities and quantum numbers for the upper and lower state are marked by ' and ''.  $\mu_s^{(1,\sigma)}$  is the dipole moment in the laboratory frame. It is connected to the components along the Cartesian coordinates  $X$ ,  $Y$ ,  $Z$  via Equations 2.25 and 2.26.

$$\mu_s^{(1,\pm 1)} = (\mp \mu_X + i \mu_Y)(2)^{-0.5} \tag{2.25}$$

$$\mu_s^{(1,0)} = \mu_Z \tag{2.26}$$

Analogously, the dipole moment in the molecular frame is defined as

$$\mu_m^{(1,\pm 1)} = (\mp \mu_b + i \mu_c)(2)^{-0.5} \tag{2.27}$$

$$\mu_m^{(1,0)} = \mu_a. \tag{2.28}$$

## 2.3. Nonadiabatic transitions

In the following sections, a basic introduction to the theoretical treatment of nonadiabatic transitions is given following the remarks in reference [45] and [10]. First, the Born-Oppenheimer separation is introduced and limits of the Born-Oppenheimer approximation<sup>[46]</sup> are discussed. Then the difference between the adiabatic and the diabatic representation is explained. Finally, the transition probability in the Landau-Zener-Stueckelberg approximation is given.

### 2.3.1. Born-Oppenheimer separation

The description of molecular structure and dynamics is given by the Schrödinger equation containing the Hamiltonian operator  $H$ , the wave function  $\Psi$  and the eigenvalues  $E$ .

## 2. Scientific context

$$(H - E)\Psi(r, R) = 0 \quad (2.29)$$

$R$  and  $r$  denote the nuclear and electronic coordinates, respectively. The Hamiltonian operator can be separated into two parts:

$$H = T_R + H_0 \quad (2.30)$$

with

$$T_R = \sum_{\alpha}^N \frac{\hbar^2}{2M_{\alpha}} \nabla_M^2. \quad (2.31)$$

Here, the operator  $T_R$  describes the kinetic energy of the nuclei and  $M_{\alpha}$  is the mass of the nucleus  $\alpha$ .  $H_0$  is the electronic Hamiltonian describing the kinetic energy of the electron, the electron-electron, electron-nuclei, and nuclei-nuclei interactions for fixed nuclear positions. The basis set of electronic wave functions  $\phi_k(r; R)$  is chosen such that the wave functions depend only parametrically on the nuclear coordinates. The complete system can be described by the overall wave function  $\Psi(r, R)$  given in Equation 2.32.

$$\Psi(r, R) = \sum_k \phi_k(r; R) \chi_k(R) \quad (2.32)$$

In this equation,  $\chi_k(R)$  is a nuclear wave function that is defined for a particular electronic state  $k$ . Substituting Equation 2.30 and 2.32 into 2.29 yields a set of coupled equations.

$$(T_R + T''_{kk} + U_{kk} - E)\chi_k(R) = \sum_{k' \neq k} (T'_{kk'} + T''_{kk'} + U_{kk'})\chi_{k'}(R) \quad (2.33)$$

Here,  $T$  denotes matrix elements arising from the nuclear kinetic energy operator acting on the electronic wave functions, whereas  $U$  specifies elements arising from the electronic Hamiltonian operator. The index  $kk$  labels a diagonal element, whereas  $kk'$  indicates that two electronic states are coupled via these matrix elements. Note that there are diagonal elements  $T''_{kk}$  arising from the nuclear kinetic energy operator acting on electronic wave functions, which can be thought of as nonadiabatic corrections to the potential energy surface. However, these are usually small enough to be neglected. The off-diagonal elements  $T'_{kk'}$  and  $T''_{kk'}$  are given here explicitly because these elements are neglected in the Born-Oppenheimer approximation and give rise to so-called nonadiabatic transitions between adiabatic potential energy surfaces.

$$T'_{kk'} = \sum_{\alpha}^N \frac{\hbar^2}{2M_{\alpha}} d_{kk'}^{(M)} \nabla_M \quad (2.34)$$

$$d_{kk'}^{(M)} = \langle \phi_k | \nabla_M \phi_k' \rangle \quad (2.35)$$

$$T''_{kk'} = \sum_{\alpha}^N \frac{\hbar^2}{2M_{\alpha}} D_{kk'}^{(M)} \quad (2.36)$$

$$D_{kk'}^{(M)} = \langle \phi_k | \nabla_M^2 \phi_k' \rangle \quad (2.37)$$

Here, the contribution of  $T'_{kk'}$  is in general larger than the one of  $T''_{kk'}$ . Since the nonadiabatic coupling  $T'_{kk'}$  includes  $\nabla_M$ , the operator for the translational energy of the nuclei, Equation 2.34 already shows that the nonadiabatic coupling will be velocity dependent. Often, the Massey criterion<sup>[47]</sup> can be used as a rough guide to decide whether a process can be described in the framework of the Born-Oppenheimer approximation:

$$\frac{\hbar v d_{kk'}}{E_k - E_{k'}} \ll 1. \quad (2.38)$$

In this equation,  $v$  is the classical velocity along the coordinate of interest and  $E_k - E_{k'}$  is the energetic separation between two electronic states  $k$  and  $k'$ . If Criterion 2.38 holds, the Born-Oppenheimer approximation is expected to be a good description.

### 2.3.2. Adiabatic and diabatic representations

Equation 2.33 shows that for an arbitrary selection of an electronic basis there are non-zero off-diagonal elements for the electronic Hamiltonian operator. However, if the electronic wave functions are chosen as the eigenfunctions of  $H_0$ , then all off-diagonal elements  $U_{kk'}$  become zero. This representation is called the adiabatic basis. If, in addition,  $T'_{kk'}$  and  $T''_{kk'}$  are neglected, the right hand side of Equation 2.33 becomes zero.

$$(T_R + U_{kk} - E)\chi_k(R) = 0 \quad (2.39)$$

Hence, following the Born-Oppenheimer approximation and using an adiabatic basis, the nuclear motion is described by the Schrödinger Equation 2.39. This description is only valid as long as the motion along the nuclear coordinates is slow and the electronic character does not change rapidly with  $R$ . If this is not the case, the nonadiabatic couplings  $T'_{kk'}$  and  $T''_{kk'}$  have to be taken into account and nonadiabatic transitions between the adiabatic potential energy surfaces occur. Most often this is the case in a region where two adiabatic

## 2. Scientific context

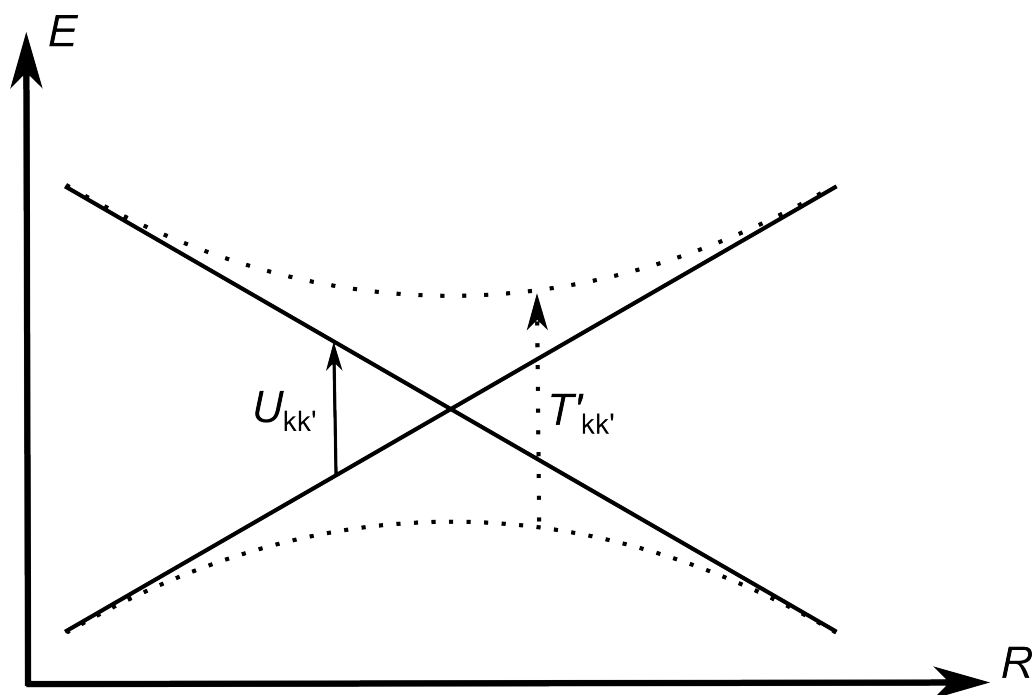


**Figure 2.4.:** An avoided crossing in the diabatic and adiabatic picture. The diabatic potential energy curves are shown as solid lines. A transition between these curves is most likely induced by an off-diagonal element of the electronic Hamiltonian  $U_{kk'}$ . The adiabatic curves are shown as dashed lines. A so called nonadiabatic transition takes place between two adiabatic states and is mediated by an off-diagonal element  $T_{kk'}$  arising from the nuclear kinetic energy operator acting on electronic wave functions.

curves approach each other closely, for example when the electronic character changes from neutral to anionic along the nuclear coordinate. In the case of very fast motion through this region an alternative diabatic representation can be useful for the description of the process. In the diabatic representation, the electronic basis functions can be chosen as the approximate functions for the respective electronic configuration, for instance neutral and ionic states. However, there is no general definition of the diabatic representation. The functions are often chosen such that  $T'_{kk'}$  and  $T''_{kk'}$  are minimized. Now, transitions between the diabats are caused by the nonzero off-diagonal elements of the electronic Hamiltonian  $U_{kk'}$ . Figure 2.4 depicts an avoided crossing and gives an overview of the terminology used in the two different representations. As shown in the figure, diabats cross each other whereas a so called avoided crossing occurs in the adiabatic picture. Note that a nonadiabatic transition describing the jump between two different adiabatic potential energy surfaces corresponds to the evolution of the system on a single diabatic surface.

### 2.3.3. Landau-Zener-Stueckelberg approximation

The Landau-Zener-Stueckelberg approximation has been derived independently by Landau<sup>[48]</sup>, Zener<sup>[49]</sup>, and Stueckelberg<sup>[50]</sup>. It describes the transition probability between two crossing diabatic states in the strong coupling regime. It is assumed that there is only one external coordinate  $R$  and that the velocity along the external coordinate is constant in the coupling region. The electronic basis functions are chosen such that the nonadiabatic coupling elements are zero and the electronic coupling of the two diabatic states is  $A_{LZS}$ . Note that  $A_{LZS}$  is related to the separation  $\Delta E$  of the adiabatic curves at the crossing of the diabats by  $A_{LZS} = 0.5\Delta E$ . Furthermore, the two diabatic curves are assumed to be linear in the coupling region with the difference in slopes  $B_{LZS}$ . If these requirements are met, the nonadiabatic transition probability between the adiabatic states is given by the following equation.

$$P_{LZS} = \exp\left(\frac{-2\pi A_{LZS}}{B_{LZS} \dot{R} \hbar}\right) \quad (2.40)$$

From this equation we can see that the nonadiabatic transition probability increases with the velocity  $\dot{R}$  and the parameter  $B_{LZS}$  whereas it decreases with increasing energy separation between the two adiabatic states. Thus, the higher the velocity and the “steeper” the curve crossing the more likely the dynamics continue on the initial diabat.

## 2.4. The structure of gold, silver and germanium

In the following, basic information on the atomic and electronic structure of gold, silver and germanium crystals and their (111) surfaces is given. The fundamental difference between the two noble metals and the semiconductor germanium becomes obvious by inspection of the crystal structure. Whereas the two metal crystals are face-centered cubic, the crystal structure of germanium is diamond cubic. For the Ag crystal, a cut along the (111) face results in the fcc(111) surface shown in Figure 2.5. The structure of the gold surface is more complicated, since it reconstructs to a structure with a large unit cell often referred to as herringbone reconstruction.<sup>[51]</sup> Nevertheless, the small range structure can be described approximately as the simple fcc(111) surface, as is often done in theoretical approaches<sup>[52]</sup> to surface scattering at the Au(111) surface. Cutting a germanium crystal along the (111) face results in dangling bonds, which give rise to the observed c(2x8) reconstruction after the surface is annealed.<sup>[53]</sup> Figure 2.6 shows the structure that results from the addition of adatoms, which is energetically favorable since dangling bonds are

## 2. Scientific context

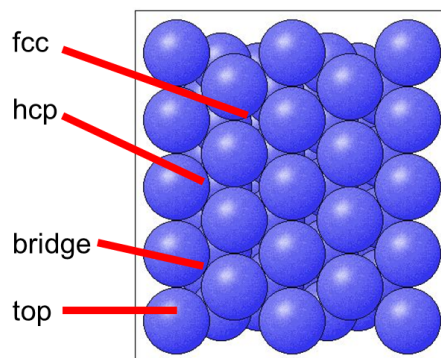


**Figure 2.5.:** The structure of a fcc(111) surface. The different surface sites are labeled. The labels “hcp” and “fcc” indicate the two different hollow sites that exist on the surface. An hcp-hollow site is characterized by an atom in the layer below the hollow site whereas there is no atom directly below a fcc-hollow site. The surface plot was generated using the SURFACE EXPLORER<sup>[55]</sup> based on the BALSAC program.

saturated. However, if the surface is heated above 573 K, as is the case in the scattering experiment, a phase transition to a more disordered “1x1” structure occurs.<sup>[54]</sup>

An important electronic characteristic of a surface is the work function  $\Phi$  describing the energy needed in order to transfer an electron from the bulk to the vacuum. The values for the surfaces relevant to this thesis are:  $\Phi_{\text{Au}(111)} = 5.31 \text{ eV}$ <sup>[56]</sup>,  $\Phi_{\text{Ag}(111)} = 4.74 \text{ eV}$ <sup>[56]</sup>, and  $\Phi_{\text{Ge}(111)} = 4.8 \text{ eV}$ <sup>[57]</sup>. A powerful method for probing the populated electronic states of a solid is photoelectron spectroscopy. Figure 2.7 shows the spectra for the two noble metals. It shows that there is a high number of populated states up to the Fermi energy. However, the d-bands, which are characterized by a structured region of high intensity in the photoelectron spectra and thus high density of states of both gold and silver, are located several eV below the Fermi energy. Note that this technique does not allow the characterization of the continuum of empty states above the Fermi energy. Furthermore, the spectra show a surface state, labeled as SF, that is located very close to the Fermi energy for silver and somewhat lower for gold. Recent measurements yield the relative position of the surface states with respect to the Fermi energy as  $-63 \text{ meV}$  for Ag(111) and  $-484 \text{ meV}$  for Au(111).<sup>[58]</sup> The electronic structure of germanium is fundamentally different from that of the metals, since it has a band gap between the valence and the conduction band, as can be seen in Figure 2.8. The direct band gap of germanium at the 673 K surface temperature used in the scattering experiment is 0.6 eV.<sup>[59]</sup> Note that the gap is filled by surface states. Nevertheless, the density of states of the semiconductor is drastically reduced with respect to the density of states of a metal close to the Fermi

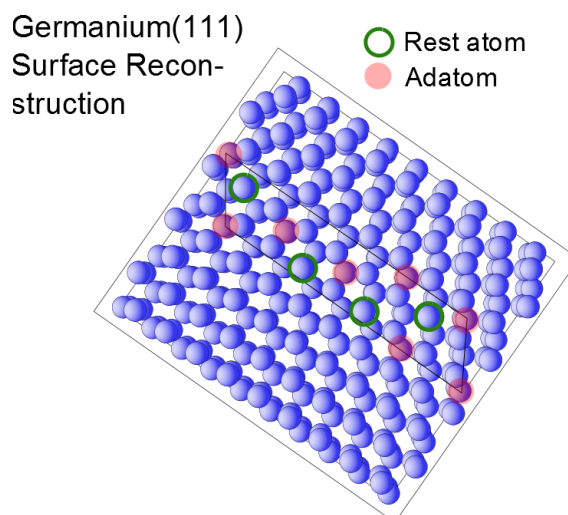


**Figure 2.6.:** The structure of the reconstructed germanium (111) c(2x8) surface. The adatoms and rest atoms are labeled in red and green, respectively. The surface plot was generated using the SURFACE EXPLORER<sup>[55]</sup> based on the BALSAC program.

energy.

## 2.5. Nonreactive dynamics at surfaces

In the following sections, a brief overview of experimental and theoretical work concerning nonreactive dynamic processes at surfaces is given with the focus on molecular beam-surface scattering experiments. The first section provides an introduction to basic mechanisms in molecule-surface scattering. The subsequent sections focus on scattering phenomena that are of particular relevance for this work.

### 2.5.1. Trapping-desorption and direct-scattering

Under particular conditions (for instance 0.14 eV incidence energy, grazing incidence angle, and a surface temperature of 185 K) a bimodal velocity distribution is observed in the scattering of Xe from Pt(111).<sup>[62]</sup> The peak at earlier arrival times (faster scattered velocity) occurs at the specular angle. This early component exhibits a narrow angular distribution. In contrast, the late component exhibits a broad angular distribution, which can be described as a  $\cos(\theta)$ -function peaking at the surface normal. These observations are interpreted in terms of two competing mechanisms: the early component of the velocity distribution is attributed to direct-scattering and the late component to trapping-

2. Scientific context

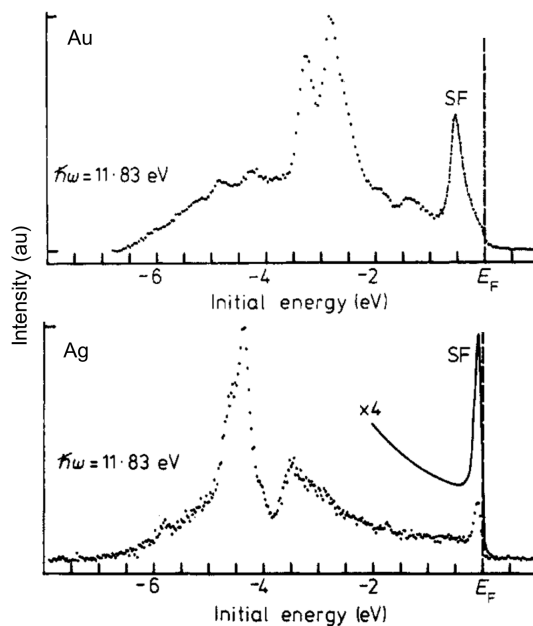


**Figure 2.7.:** The photoelectron spectra are shown for Au and Ag. Energies are given relative to the Fermi energy  $E_F$ . Figure reproduced with permission from reference [60]. © IOP Publishing. All rights reserved.

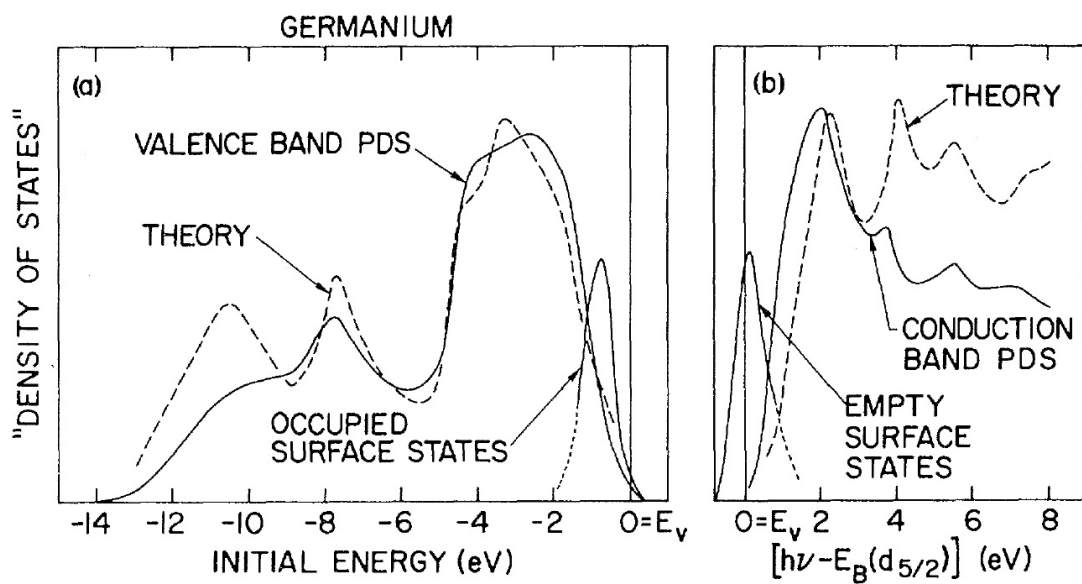


**Figure 2.8.:** The density of states in the valence band and conduction band of germanium. Reprinted figure with permission from reference [61]. Copyright (1975) by the American Physical Society.



desorption. These two mechanisms have been found to be appropriate for the description of the scattering process in many projectile-surface systems. Both channels could be identified in atom-surface scattering as in the example discussed above, molecule-surface scattering for example in CO and NO<sup>[63,64]</sup> scattering from Au(111), and even in the scattering of large water clusters<sup>[65]</sup> from a graphite surface.

Trapping-desorption is thought to proceed as follows: The projectile approaches the surface and during the collision enough translational energy is transferred to surface degrees of freedom or to internal degrees of freedom of the projectile, such that it stays “trapped” long enough to be equilibrated with the surface. A rough estimate of the residence time is given by  $(10^{13} \text{ s}^{-1} \exp(-E_b/k_B T))^{-1}$ .<sup>[64]</sup> For a weakly bound molecule with the binding energy  $E_b = 0.3 \text{ eV}$  at a 300 K surface, this yields a residence time of 10 ns. After this timespan, the projectile desorbs and its translational energy as well as the internal state distribution is determined by the surface temperature. This does not necessarily mean that for example the velocity distribution of the molecule can be described by a Maxwell-Boltzmann distribution at the surface temperature. The effective desorption temperature can be affected by the desorption well depth, which can be understood as a consequence of detailed balance.<sup>[66]</sup> Moreover, in certain cases it can be shown that the residence time of the molecule at the surface is not long enough to equilibrate all the molecular degrees of freedom. This is the case for the high energy vibration of HCl( $v = 2$ ), which has been shown to trap and desorb with a thermal velocity distribution while the vibrational quantum number is conserved.<sup>[67]</sup>

Nevertheless, the classification trapping-desorption is helpful to differentiate against direct-scattering. In this process, the interaction time of the projectile with the surface is short and typically on the order of femto- to picoseconds.<sup>[63]</sup> Direct-scattering is characterized by strong departures in the scattered energy distributions from thermal expectation as well as a “memory effect”, meaning that the scattered projectile’s distribution of the excitation of different degrees of freedom can be directly influenced by incidence parameters. Both characteristics can be identified in the direct-scattering of nitric oxide from Ag(111).<sup>[68]</sup> For this system, it has been shown that the rotational state distributions do not follow a Boltzmann distribution. Instead, the distributions are characterized by strong rotational rainbow features (as discussed in detail in Section 2.5.2), which depart strongly from the thermal expectation. In addition, both the final translational and rotational energy of the molecule scale with the incidence translational energy of the molecule, which is a classic example for the “memory effect” in direct-scattering.

A simple model that describes the trapping probability and thus also the branching ratio

## 2. Scientific context

between direct-scattering and trapping-desorption is known as the hard cube model.<sup>[69]</sup> In this model the collision is treated as a collision of two hard cubes with the surface atom mass  $m$  and the mass of the projectile  $M$ . It is assumed that the projectile is accelerated by a structureless potential well with the depth  $\epsilon$  before a purely impulsive collision occurs. The surface atom motion can be described by a 1D-Maxwell-Boltzmann distribution at the surface temperature  $T$ . In this case, the trapping probability  $P$  can be described by Equations 2.41-2.44.<sup>[70]</sup>

$$a = \sqrt{\frac{m}{2k_{\text{B}}T}} \quad (2.41)$$

$$u = \sqrt{\frac{2(E_i + \epsilon)}{M}} \quad (2.42)$$

$$v_c = 0.5 \left( \left(1 + \frac{M}{m}\right) \sqrt{\frac{2\epsilon}{M}} + 1 \left(1 - \frac{M}{m}\right) u \right) \quad (2.43)$$

$$P(E_i, \epsilon, M, m, T) = 0.5 + 0.5\text{erf}(av_c) + \frac{e^{(-a^2v_c^2)}}{2\pi^2ua} \quad (2.44)$$

Here,  $E_i$  denotes the normal incidence translational energy of the projectile. This model predicts a trapping probability of 50 % at a critical incidence translational energy of  $E_i = \left(\left(\frac{m+M}{m-M}\right)^2 - 1\right) \epsilon$ . Moreover, an increase of the surface temperature reduces the slope of the decline of the trapping probability from unity at low incidence translational energies to zero at high incidence translational energies. The hard cube model has been used to describe the trapping probability for many different systems. See for instance references [70, 71]. However, by a comparison between different projectile-surface systems Rettner *et al.* found that a molecular projectile with more internal degrees of freedom is more easily trapped than an atom with comparable mass and binding energy.<sup>[72]</sup> The more internal degrees of freedom are available in the projectile the larger is the underestimation of the trapping probability by the hard cube model. This can be taken as a strong indication that this simple model fails for molecular projectiles, and excitation of internal degrees of freedom in the collision might have a strong impact on the probability for trapping. For some diatomic molecule-surface systems rotational excitation has been shown to promote trapping.<sup>[73,74]</sup> The trapping probability in NO/Ag(111) surface scattering is enhanced if the incoming molecule points with the O-atom towards the surface, though this configuration is energetically less favorable than the opposite orientation. This observation is explained in terms of a more efficient translational energy transfer to rotational excitation for orientations in which the O-atom points towards the surface.

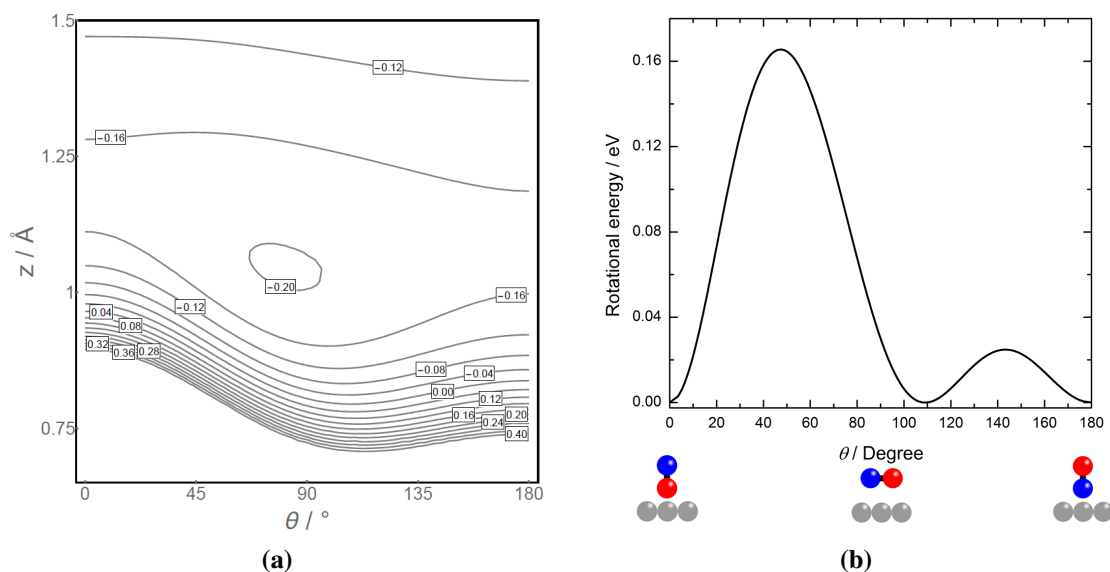


**Figure 2.9.:** a) Potential energy surface for the NO/Ag(111) surface interaction<sup>[77]</sup> as a function of the molecule-surface distance  $z$  and the orientation angle  $\theta$ . For each contour the potential energy is given in eV. b) Correlation between rotational excitation in the collision and the orientation angle  $\theta$  based on classical trajectory calculations. Adapted from reference [77].

## 2.5.2. Rotational rainbows in molecule-surface scattering

As mentioned earlier, the rotational state distribution in direct-scattering will in general depart from thermal expectations and be affected by the incidence translational energy of the molecule. Moreover, the rotational excitation in the collision will be strongly related to the orientation of the molecule, since rotational excitation is driven by the gradients of the potential energy surface along the angles describing the orientation and the rotation of the molecule. If one considers a diatomic molecule interacting with a flat and structureless surface, then the rotational excitation experienced during the collision will only depend on the incidence parameters and the potential energy surface with respect to one orientation angle  $\theta$  and the molecule-surface distance  $z$ . As an example, the NO/Ag(111) system will be introduced to explain the occurrence of rotational rainbows. Experimentally, it has been found that rotational state distributions for this system deviate strongly from Boltzmann distributions which underestimate the population of high  $J$  states.<sup>[68,75]</sup> Furthermore, using oriented molecular beams of NO, the high- $J$  part of the rotational state distribution could be attributed to collisions with initial orientations in which the O-atom points towards the surface.<sup>[76]</sup> Theoretically, the rotational state distributions are understood as consisting of

## 2. Scientific context

two rotational rainbows.<sup>[78]</sup> The origin of these rainbows is due to extrema in the angular momentum  $J$  as a function of the orientation angle  $\theta$ . The results of classical trajectory calculations facilitate an interpretation of the relevant dynamics. Figure 2.9a) shows one of the most recent model potentials for NO/Ag(111) as a function of  $\theta$  and  $z$ .  $\theta$  is defined as the angle between the NO bond and the surface normal, where  $\theta = 0$  means that the molecule points with the O-atom towards the surface. Dynamical calculations based on this potential reproduce the rotational state distributions observed in the experiment quite nicely. The bimodal rotational state distribution with a maximum at low- and high- $J$  can only be explained by considering both an anisotropic repulsion as well as an anisotropic attraction. The potential is more repulsive for the O-atom than for the N-atom and exhibits a global minimum for a side-on geometry. As a consequence, the absolute gradient at the position of the repulsive wall along  $\theta$  is steeper at  $\theta = 45^\circ$  than at  $\theta = 135^\circ$ . Thus, the achievable amount of rotational excitation is higher for O-atom first collisions than for N-atom first collisions as can be seen in Figure 2.9b). This plot also illustrates that if there is a maximum in the rotational excitation as a function of the incident orientation, then many different orientations lead to similar rotational energies. This effect leads to a singularity in the rotational energy distribution in a classical calculation, which is called a rotational rainbow. In a quantum calculation the singularity is replaced by a maximum located at about a value of  $J$  corresponding approximately to the rotational energy where the singularity is observed in the classical calculation.<sup>[79]</sup>

The observation of rotational rainbows is not limited to the NO/Ag(111) system. On the contrary, the rotational rainbow phenomenon has been proven to be a quite general observation in direct-scattering of diatomic molecules, for example in a system with a high binding energy such as NO from Pt(111)<sup>[80]</sup>, as well as for different molecules such as CO at Ni(111).<sup>[74]</sup> In addition, the extremely large population of the low energy rotational states in the direct-scattering of NH<sub>3</sub> from Au(111) has been interpreted as a rotational rainbow.<sup>[81][82]</sup>

### 2.5.3. Nonadiabatic dynamics at surfaces

Experiments and theoretical approaches to nonadiabatic dynamics at surfaces have recently been reviewed.<sup>[9,14]</sup> The importance of nonadiabatic effects has been demonstrated for a variety of different systems. Especially, for dynamics at metal surfaces, it is obvious that the Born-Oppenheimer approximation might not lead to an accurate description. This is because there is a continuum of electronic states and thus the Massey criterion 2.38 that gives the condition under which a process can be described precisely in the adiabatic

picture is not fulfilled. In reference [9], the authors showed in general that the parameter  $\Phi - E_a$  is a good descriptor for the nonadiabaticity of a surface process. Here,  $\Phi$  is the work function of the material and  $E_a$  is the electron affinity of a projectile. The smaller  $\Phi - E_a$ , the more likely nonadiabatic effects are to play an important role. A nice example of the Born-Oppenheimer breakdown is given by experiments on H-atom scattering from the Au(111) surface. The breakdown of the Born-Oppenheimer approximation becomes clear by a comparison to the analogous experiment at the insulating Xe-surface.<sup>[83]</sup> Figure 2.10 shows the results of time-of-flight experiments on the scattered H-atoms for both surfaces and the derived translational energy loss distributions. Obviously, the translational energy loss is much larger at the Au(111) surface than at the Xe-surface. In a simple impulsive collision picture the energy loss is expected to be small since the H-atom mass is much lighter than the surface atom mass such that considering energy and momentum conservation nearly the complete collision energy is retained in the atom. This is the case for scattering from Xe. At the metallic Au(111) surface, however, the energy loss is very large and can only be described by taking nonadiabatic effects into account. In reference [83] the authors showed that this process can be understood treating the nonadiabatic interactions as a kind of friction experienced by the H-atom in an electron bath. This approach is known as molecular dynamics with electronic friction. In this method the dynamics can still be described by a single effective potential energy surface and nonadiabatic effects are treated implicitly as frictional and fluctuating forces.

In the following, the remarks will be focused on molecule/metal surface scattering that, in contrast to the H-atom scattering experiment, presumably cannot be understood in an electronic friction picture. In the scattering of highly vibrationally excited NO with an initial vibrational quantum number of  $v_i = 15$  from Au(111) the average vibrational energy loss is very large (1.4 eV) compared to similar experiments at the insulating LiF surface where almost no vibrational relaxation is observed.<sup>[11]</sup> The Debye frequency of Au is  $115 \text{ cm}^{-1}$ <sup>[84]</sup> and  $448 \text{ cm}^{-1}$ <sup>[85]</sup> for LiF. The fundamental frequency of NO is  $1876 \text{ cm}^{-1}$ . Based on these values and simple mechanic arguments the vibrational energy transfer should be less efficient at the Au surface than at the LiF surface. The efficient vibrational relaxation of the NO molecule can only be explained by taking the coupling between vibrational motion and electronic excitation into account. In addition to relaxation, the vibrational excitation has also been investigated on Ag(111)<sup>[86]</sup> and Au (111)<sup>[12]</sup>. Figure 2.11 shows the dependence of the vibrational excitation on surface temperature and incidence translational energy. The Arrhenius-like surface temperature dependence with the slope close to the vibrational spacing of the NO molecule (see Figure 2.11a)) as well

## 2. Scientific context

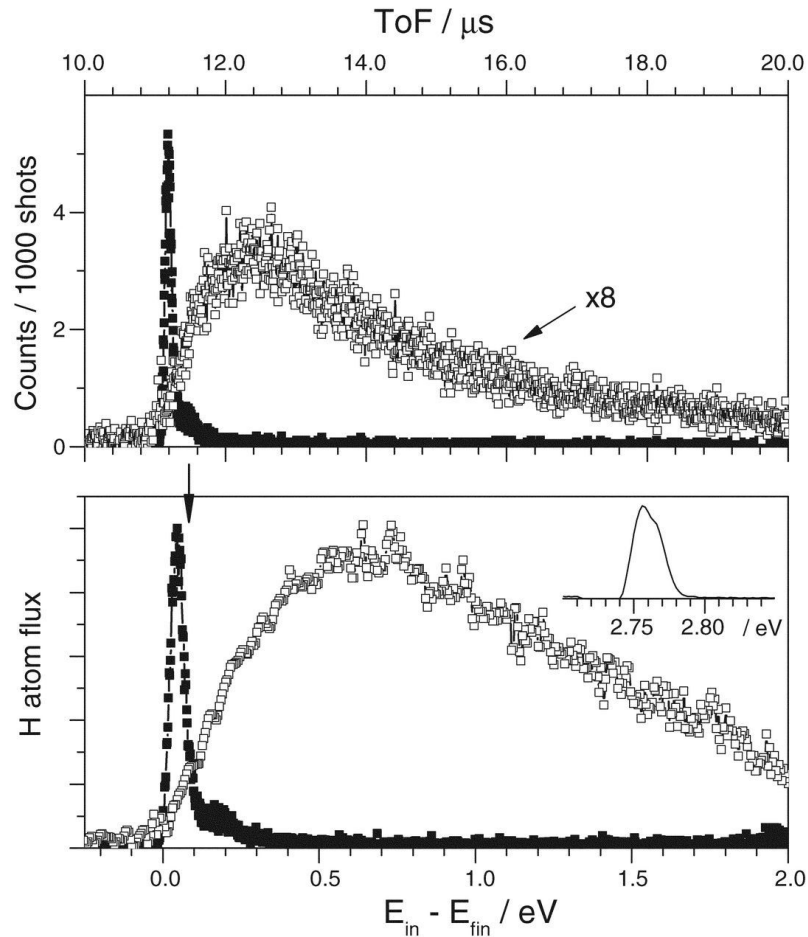


**Figure 2.10.:** Upper panel: Arrival time distribution of H-atom at the detector for scattering from a Xe surface (filled squares) and a Au(111) surface (open circles). The incidence parameters are  $E_i = 2.76$  eV and  $45^\circ$  incidence angle. Scattered H-atoms are detected at the specular angle. Lower panel: Derived translational energy loss in the collision of H-atom at the Xe-surface (filled squares) and at the Au(111) surface (open circles). Figure taken from reference [83]. Reprinted with permission from AAAS.

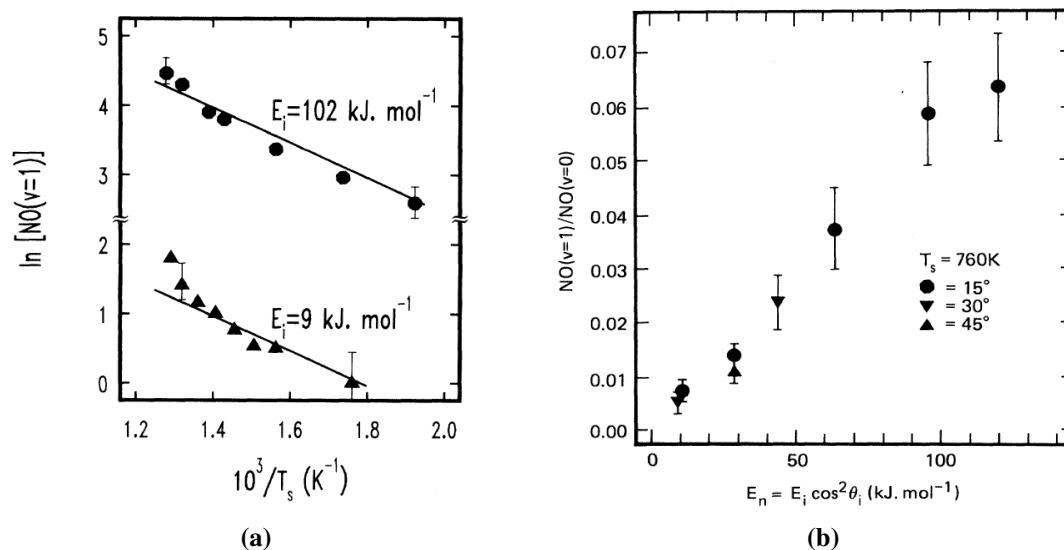


**Figure 2.11.:** a) Vibrational excitation probability of NO at Ag(111) as a function of the inverse surface temperature. b) Branching ratio between NO( $v = 1$ ) and NO( $v = 0$ ) as a function of the incidence translational energy. Figures taken from reference [86]. Reprinted with permission. Copyright (1985) by the American Physical Society.

as the zero incidence translational energy threshold (see Figure 2.11b)) have been interpreted in terms of electron-hole pairs providing the energy for vibrational excitation.<sup>[24]</sup> Furthermore, electron emission has been observed for scattering experiments with highly vibrationally excited NO at low work function caesiated surfaces.<sup>[13]</sup> Interestingly, the electron emission increases approximately linearly with incidence vibrational energy of the NO molecule starting at a threshold corresponding to the work function of the caesiated surface. This observation was interpreted such that during certain scattering events the complete vibrational energy of the molecule can be transferred to a single electron.

There have been several theoretical approaches for understanding vibrational energy transfer in the NO/Au(111) surface system, which employ Monte Carlo wave packet dynamics<sup>[87]</sup>, molecular dynamics with electronic friction<sup>[15]</sup> on model potentials, or independent electron surface hopping (IESH) on a DFT-derived potential.<sup>[8]</sup> Little attention has been paid to the Monte Carlo wave packet study. Those three approaches were used to calculate the final vibrational state distribution after vibrational relaxation at the surface. Thus, the predictions can be directly compared to the outcome of the experiment. All three studies almost quantitatively reproduced the final vibrational state distribution for NO( $v_i = 15$ ) scattered from Au(111) at a low incidence translational energy. Furthermore, the predictions of molecular dynamics with electronic friction theory as well as the

## 2. Scientific context

IESH program were directly compared to experimentally determined excitation probabilities.<sup>[88]</sup> Whereas electronic friction theory fails in explaining the vibrational excitation probabilities, the experiment is more accurately reproduced by IESH. Recently, an almost complete experimental data set for the scattering of NO at Au (111) has been obtained: The translational inelasticity in low- $v$  NO/Au(111) surface scattering has been analyzed by quantum-state-resolved time-of-flight techniques resulting in a detailed picture of the coupling between the different molecular degrees of freedom.<sup>[17,89]</sup> In addition, the important role of molecular orientation has been investigated in the vibrational relaxation of NO( $v_1 = 3$ ). Here, a dramatic enhancement of vibrational relaxation is found if the molecule is oriented with the N-atom towards the surface.<sup>[90,91]</sup> The dependence of the vibrational relaxation probability on incident vibrational and translational energy has been examined in reference [6]. Figure 2.12 shows the central findings of this work. As can be seen in Figure 2.12a), the vibrational relaxation is promoted by both incidence translational as well as vibrational energy. Furthermore, N-atom down orientation is favorable for vibrational relaxation as long as the relaxation probability does not approach unity. See Figure 2.12b).

Following ideas developed earlier, the multi-quantum vibrational relaxation is explained as proceeding via the transient formation of the anion and subsequent excitation of an electron in the metal, thus involving two electron transfers in the mechanism.<sup>[11]</sup> Figure 2.12c) shows that this is possible because the anionic species becomes stabilized at the surface due to image charge stabilization. Figure 2.12d) shows that the anion can serve as a mediator between neutral potential energy surfaces, allowing the conversion of vibrational energy into electronic excitation. As the dynamics evolve on the anionic diabats the system can undergo several nonadiabatic transitions. That means that the molecule/surface system stays on the anionic diabats such that finally the transition back to a neutral potential energy surface corresponding to less vibrational energy and higher electronic excitation can occur. More incidence translational energy allows the molecule to approach closer to the surface such that the formation of the anion and thus vibrational relaxation becomes more likely. However, both IESH theory and MDEF fail to reproduce the incidence translational energy dependence of the relaxation process.<sup>[7]</sup> Moreover, a detailed comparison between the predictions of the IESH theory and the experimental observations revealed severe problems with the adiabatic potential energy surface used as the basis for the description of nonadiabatic dynamics in the IESH program.<sup>[16]</sup> Here, I would like to point out that the Monte Carlo wave packet study<sup>[87]</sup> deserves more recognition since it successfully predicts the promoting role of incidence translational energy on vibrational relaxation. It would



be interesting to test the prediction of this method for the available experimental data on excitation.

In the study presented here, remaining gaps in the available dataset for the NO/nobel metal surface scattering system are filled. The following questions are addressed: First, do the rotational state distributions in multi-quantum relaxation of initially highly vibrationally excited NO contain valuable information on the nonadiabatic interactions? Second, can we understand the coupling between the different molecular degrees of freedom in collisions of highly vibrationally excited NO? And last, how do surface properties influence the scattering process?

#### 2.5.4. Polyatomic molecule-surface scattering

In contrast to the available experimental data on diatomic molecule-surface scattering available data on quantum-state-resolved polyatomic molecule-surface scattering are sparse. Several of these studies provide insight into the mode-specific reactive sticking of molecules such as H<sub>2</sub>O<sup>[92]</sup> or CH<sub>4</sub><sup>[93]</sup> on Ni(111) surfaces.

In addition to the reactive sticking of molecules at surfaces it is also possible to study translational energy and internal state distribution of molecules scattered nonreactively from surfaces. These experiments are demanding since a state-resolved detection method is needed and the number of states involved in the collision increases with molecular complexity. As a consequence reports on polyatomic molecule-surface scattering achieving rotational resolution are up to now limited to few molecules for example the linear acetylene (C<sub>2</sub>H<sub>2</sub>), the spherical methane, and the prolate top ammonia.

For the scattering of the linear acetylene molecule at Au(111) the translational inelasticity, the rotational state distributions, and the amount of vibrational excitation in mode 4 (trans-bend mode) have been determined over the incidence translational energy range between 0.34 and 0.65 eV.<sup>[94]</sup> The rotational state distributions were found to be non-thermal, however describable by a Boltzmann distribution, and the rotational excitation increases with increasing incidence translational energy. The single quantum vibrational excitation in mode 4 increases linearly with incidence translational energy such that at 0.65 eV the branching ratio between the vibrationally excited state and the vibrational ground state is 30 %. The threshold for vibrational excitation is by extrapolation found to be 0.15 eV (0.07 eV above the vibrational spacing<sup>[95]</sup> which is  $\approx$  0.08 eV). The excitation of two quanta in mode 4 is found to be much less likely (< 1 %) in the examined incidence translational energy range.

In scattering experiments of ammonia from Au(111) the vibrational excitation<sup>[96]</sup> as well

## 2. Scientific context

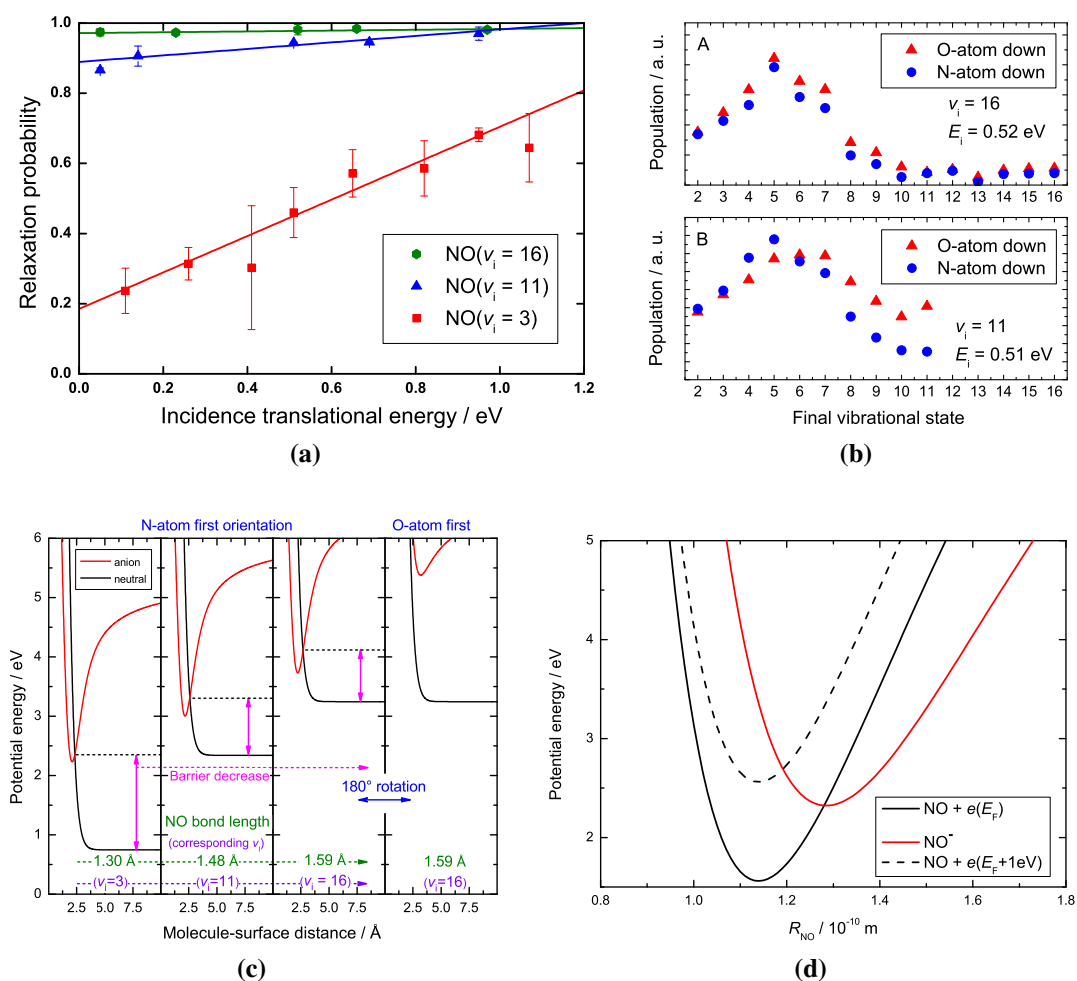


**Figure 2.12.:** a) Vibrational relaxation probabilities in NO/Au(111) surface scattering for three different incidence vibrational states of NO as a function of the incidence translational energy. The incidence vibrational state is indicated by  $v_i$  in the plot legend. b) The final vibrational state distributions are shown for two scattering experiments on NO in the initial vibrational states  $v_i = 11$  (panel A) and  $v_i = 16$  (panel B). The blue circles represent the vibrational state distribution for N-atom down orientation whereas the reversed orientation is represented by the red triangles. Figure a) and b) are taken from reference [6] and adapted with permission from Wiley-VCH Verlag GmbH & Co. KGaA, Weinheim (Copyright 2014). c) Relevant diabatic potentials of the anion and neutral molecule as a function of the molecule-surface distance. The molecular geometry is fixed at the outer turning point corresponding to the vibrational states 3, 11, and 16. d) The diabatic potentials for the anionic (red, solid line) and neutral species (black, solid line) at a distance of 2 Å from an hcp-site are plotted as a function of the NO bond length. In order to depict an electronic excitation in the metal the neutral curve has been shifted by 1 eV (black, dotted line). The potentials are taken from reference [52].

as the rotational state distributions<sup>[81]</sup> have been investigated. The vibrational excitation in the umbrella mode ( $\approx 800 \text{ cm}^{-1}$ ) increases linearly with incidence translational energy in the examined range (0.1 eV-0.35 eV) setting in at a translational energy threshold close to the energy needed for vibrational excitation. The maximum probability for single quantum vibrational excitation observed is 14 %. Overtones with two and three quanta of excitation in the umbrella mode are also observed. Here, the excitation probabilities are  $\approx 5 \%$  for both the first and second overtone at the fastest incidence translational energy. The rotational state distributions in the vibrational ground state of the oblate top molecule ammonia have been examined at a single incidence translational energy of 0.24 eV and an incidence angle of  $45^\circ$ . A large propensity of scattering into rotational states with low  $K$  is found. This means that tumbling is favored over spinning about the symmetry axis of the molecule. In addition, the extraordinary strong population of  $J = 0$  is attributed to a rotational rainbow.

The studies on ammonia and on acetylene have both been conducted using REMPI for detection. In contrast, methane scattering at LiF(100)<sup>[97]</sup> has been studied using a bolometric detection method. The experimental apparatus limits the study to low incidence translational energies. The incidence angle is  $60^\circ$  and the incidence translational energy is 0.075 eV. The rotational state distribution of directly scattered molecules has been detected at an scattering angle of  $60^\circ$ . It can be described by a Boltzmann distribution at 240 K.



## 3. Experimental setup

The experimental setup has been described in detail previously.<sup>[44]</sup> Over the course of the experimental work for this thesis the experimental setup has been modified to fulfill the requirements for the respective experiments. In this chapter, the general setup is described only very briefly whereas modifications made are explained in detail. Section 3.1 presents the scattering apparatus, and Section 3.2 presents the laser systems used in the experiments.

### 3.1. Surface scattering apparatus

The apparatus consists of three differentially pumped chambers. All of them are pumped by turbomolecular pumps. The source chamber has a base pressure of  $10^{-6}$  to  $10^{-5}$  mbar and houses the nozzle for generating a pulsed supersonic molecular beam. For experiments with nitric oxide a piezoelectric valve (1 mm  $\varnothing$  nozzle, 10 Hz, 3 Atm. stagnation pressure) is used whereas for experiments with formaldehyde a homebuilt, heatable Even-Lavie type nozzle is operated at a repetition rate of 10 Hz. See Section 3.1.1 for a detailed description of the nozzle. The differentially pumped chamber is connected to the source chamber by a 2 mm electro-formed skimmer (Ni Model 2, Beam Dynamics, Inc.). Further downstream, molecules enter the surface scattering chamber through an aperture (2 mm). The base pressure in the scattering chamber is  $\approx 1 \cdot 10^{-10}$  mbar. Under operation of the molecular beam it increases to  $\approx 1 \cdot 10^{-9}$  mbar. The surface is mounted on a manipulator, which allows it to be moved between the scattering chamber and the sample preparation chamber. The preparation chamber is equipped with an argon ion gun (LK Technologies, Bloomington India, Model NGI 3000-SE, beam voltage 3.0 kV, emission current 20 mA) for sputtering, an Auger spectrometer (Staib, ESA 100) in order to check the cleanliness of the surface, and a residual gas analyzer (SRS, RGA 200).

The geometry of the detection region is shown in Figure 3.1. The molecular beam impinges on the surface close to normal incidence. Laser beams can enter the scattering chamber perpendicular to the molecular beam axis through the windows located on the two sides of the chamber.

### 3. Experimental setup

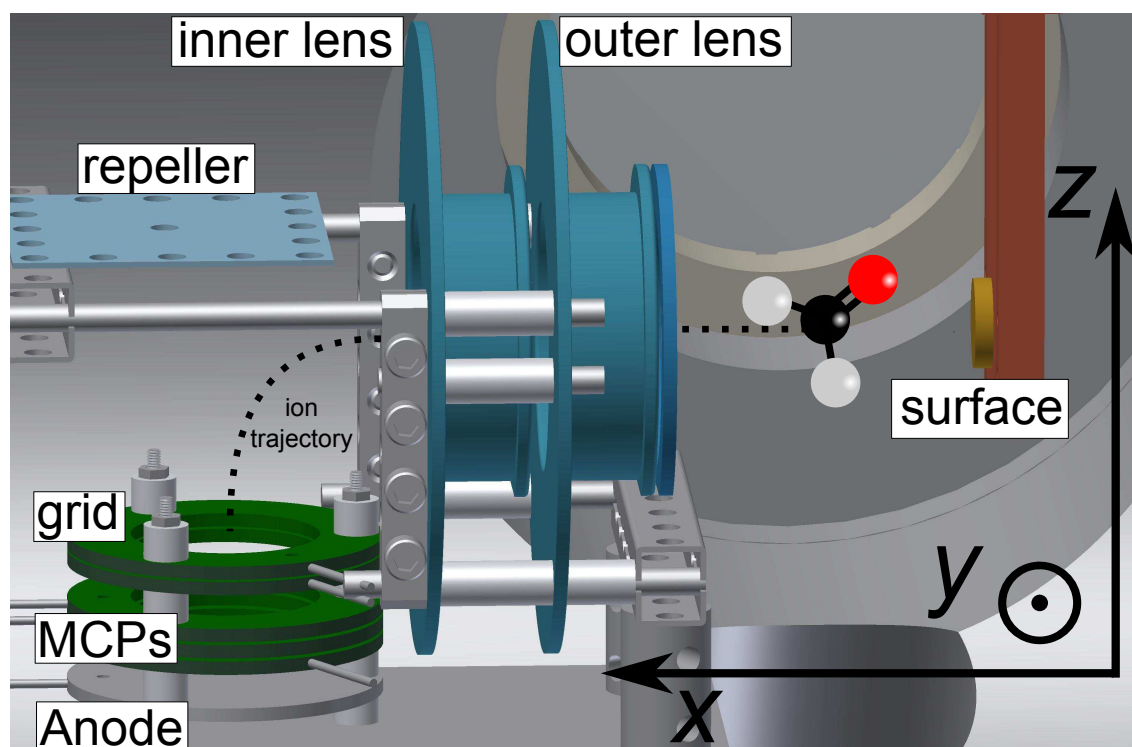


**Figure 3.1.:** Setup of the detector.

$\text{CaF}_2$  windows are mounted whenever vacuum ultraviolet (VUV) radiation is used. If VUV is not required, UV fused silica windows are installed. The detector consists of ion optics, multichannel plates, and an anode which can be connected to an oscilloscope to record the signal. The ion optics guide ions produced in the detection region onto multichannel plates. Note that the extraction occurs parallel to the propagation axis of the incoming beam. See Section 3.1.2 for a detailed description.

Note that experiments on the rotational state distribution in highly vibrationally excited NO/Au(111) surface scattering were determined using an older version of the setup with two relevant modifications to the setup described above. First, the detector consists only of a combination of MCP and anode. Ions are extracted perpendicular to the molecular beam axis. Second, an orientation electrode is mounted close to the surface, which allows the generation of a strong electric field (33 kV/cm) in the scattering region in front of the surface. See reference [44] for more details.

#### 3.1.1. A heatable nozzle

For the production of supersonic beams of formaldehyde a new nozzle design by Prof. Dirk Schwarzer is used. Under the presence of traces of water, monomeric formaldehyde

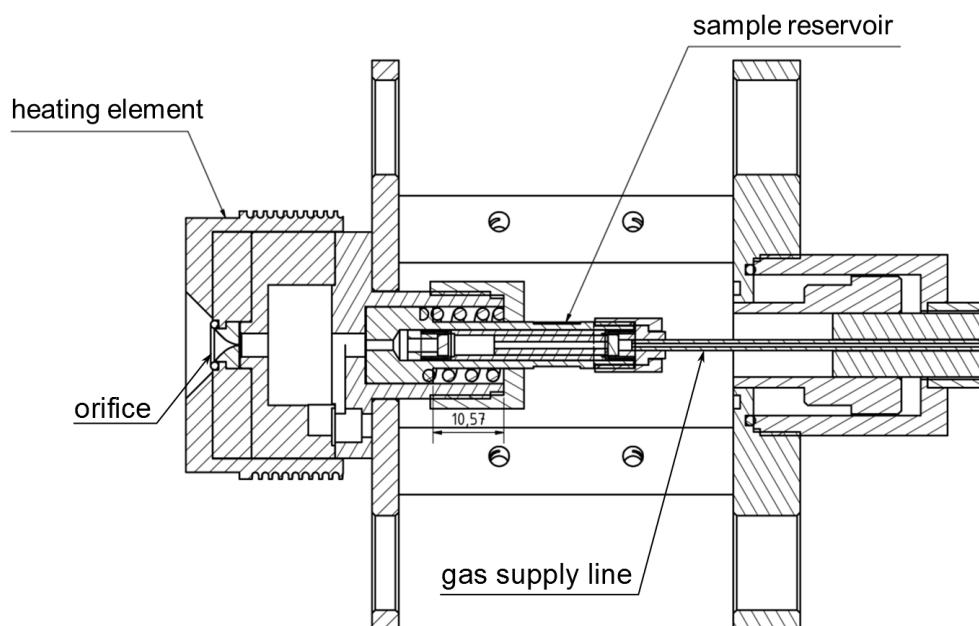


**Figure 3.2.:** Drawing of the nozzle design.

is unstable and forms polymeric paraformaldehyde. The monomeric formaldehyde can be obtained by heating paraformaldehyde to temperatures above 70 °C. Following the method reported in reference [98] the cracking process is performed in close proximity to the orifice of the nozzle in order to avoid repolymerization of formaldehyde. The nozzle design itself is based on the Even-Lavie design.<sup>[99]</sup> The tip of the nozzle is encapsulated by a copper block which can be resistively heated. The nozzle is equipped with a sample reservoir, which is located in the gas supply line just in front of the tip of the nozzle. See Figure 3.2 for a detailed drawing. The reservoir has sintered stainless steel filters to prevent solids from leaving the reservoir. In addition to the paraformaldehyde (97 % purity) the reservoir also contains  $\text{MgSO}_4$  which acts as a drying agent for the water produced in the cracking process. The reservoir is only passively heated via heat conduction from the copper block at the tip of the nozzle such that the temperature gradient in the direction of the gas flow is always positive. Experimentally, it has been found that a tip temperature of 120 °C results in a temperature of 75 °C in the reservoir which ensures sufficient production of formaldehyde.

The monomeric formaldehyde is expanded in different carrier gas mixtures consisting of  $\text{H}_2$ , He, and  $\text{N}_2$ . The optimum backing pressure is found to be between 4 and 12 bar and

### 3. Experimental setup

varies with the composition of the carrier gas mixture. This is explained in Section 7.3.1.

#### 3.1.2. Using the MCP detector

Figure 3.1 shows the ion and electron detector designed by Dr. Nils Bartels.<sup>[44]</sup> Under operating conditions the surface is located in front of the outer ion lens as shown in the figure. The second inner ion lens and the repeller guide the ions/electrons towards the grid and the two MCPs (Hamamatsu F1049-01, 20 mm effective diameter) in Chevron assembly located below the repeller. For ion detection the anode is directly connected to an oscilloscope. Electron detection is achieved capacitively with the anode at a high positive voltage. The voltages applied to the ion optics and the MCP are given in Table 3.1. The surface serves as an electrode in this detector configuration and stays grounded.

For ion detection the back of the MCP is grounded via an RC-circuit ( $R = 10 \text{ k}\Omega$ ,  $C = 3.3 \text{ nF}$ ). Often the voltage applied to the front of the MCP assembly is pulsed from a low voltage to a higher voltage, at the time when the desired signal is expected. This way, undesired signal due to scattered laser light is reduced.

Due to the geometry an ion that is produced from a molecule that has been moving towards the detector has a slightly shorter time-of-flight to the MCP than an ion produced from a molecule that has been moving away from the detector. See Figure 3.3 for a detailed explanation. Thus, the detector provides a rough velocity resolution which permits the differentiation between incoming molecules (component A) and directly scattered molecules (component B). This can be achieved by integrating the ion signal in a narrow arrival time window such that only component A or B is taken into account.

**Table 3.1.:** Voltages applied to the ion optics.

part	positive ion detection	electron detection
inner lens	-900 V	+500 V
outer lens	-200 V	+40 V
repeller	+100 V	-100 V
grid	-2000 V	+200 V
MCP front	pulsed from -1000 V up to -(1000-2000) V	+100 V
MCP back	grounded via RC-circuit	+1800 V
anode	grounded via oscilloscope	+2400 V



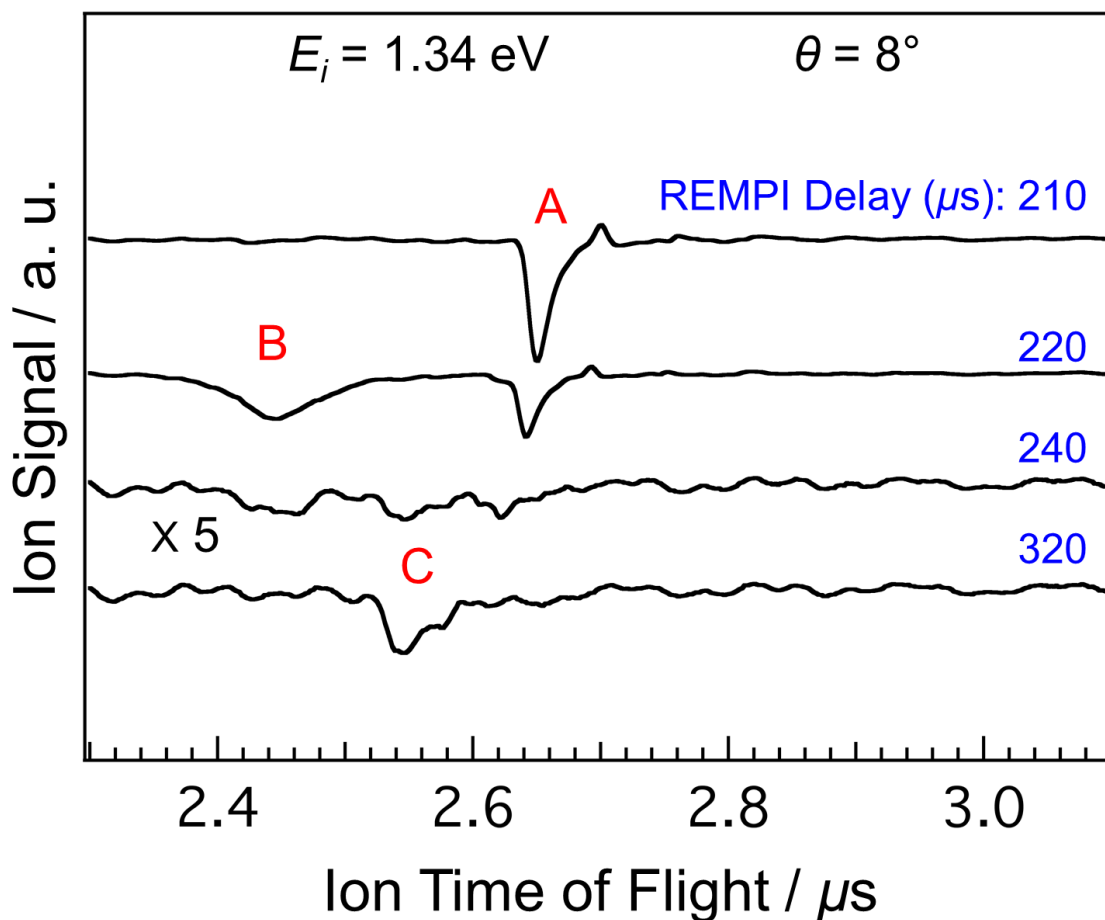


**Figure 3.3.:** Velocity resolution of the MCP detector. As a test formaldehyde is scattered from a Au(111) surface and detected using 2+1 REMPI spectroscopy (see Section 4.2.2) at a position of  $\approx 13$  mm away from the surface and 1.8 mm above the center of the molecular beam axis which corresponds to a scattering angle of  $8^\circ$ . The incidence translational energy is 1.34 eV. Note that due to the spatial profile of the molecular beam the ion signal corresponding to scattered molecules and the incoming beam is comparable in intensity. The four ion time-of-flight traces correspond to four different delays between the nozzle opening and the laser firing. At small delays the incoming beam arrives at the probe position and a signal at long ion time-of-flight indicated by A appears. At longer delays a second peak appears labeled by B which can be attributed to directly scattered molecules. Increasing the delay further makes the peaks A and B disappear. Depending on the scattering conditions a third peak may appear labeled as C. In this example, this can be attributed to a buildup of background gas by probing the molecule arrival time distribution at different probe positions. However, at the ion time-of-flight labeled by C ions created from scattered molecules with a low final speed are also expected.

### 3. Experimental setup

## 3.2. Lasers

In this work, the pulsed molecular beam and nanosecond lasers used for the preparation and characterization of molecules in the incoming and scattered beam are operated at 10 Hz repetition rate. The different laser systems used in the scattering experiments are described briefly below. For noncommercial and nonstandard laser systems references providing a detailed description are given in the respective section.

### 3.2.1. Dye lasers

#### Precision Scan

The "blue" dye laser (Sirah, Precision Scan, PRSCDA-24) is used to produce radiation in the range from 420 nm to 560 nm with a bandwidth of  $0.06 \text{ cm}^{-1}$  (90 mm grating, 2400 l/mm). It is pumped by the third harmonic generation of a Nd:YAG laser (Spectra Physics, Quanta Ray PRO-270-10). The output of the dye laser can be doubled in a BBO crystal to obtain radiation in the UV.

#### Cobra-Stretch SL

The Nd:YAG (Continuum, Powerlite 7010) pumped "red" dye laser (Sirah, Cobra-Stretch SL) supplies radiation from 550 nm bis 800 nm with a bandwidth of  $0.06 \text{ cm}^{-1}$  (90 mm grating, 1800 l/mm). The output is doubled in a BBO crystal.

### 3.2.2. Sunlite Ex OPO with FX 1 UV frequency extension

The commercially available solid state laser Sunlite Ex OPO with FX 1 UV frequency extension (Continuum) is used to generate UV radiation in the range between 230 nm and 450 nm with a pulse energy of  $\approx 4 \text{ mJ/pulse}$  and a bandwidth of  $0.075 \text{ cm}^{-1}$  in the visible (the UV output is expected to have a bandwidth of  $0.15 \text{ cm}^{-1}$ ).

### 3.2.3. Homebuilt optical parametric oscillators

Two homebuilt injection seeded optical parametric oscillators<sup>[100]</sup> (OPOs) are used to generate narrow-bandwidth radiation in the near IR. Both OPOs are pumped by an injection seeded Nd:YAG Laser (Spectra Physics Lab 170-10, 532 nm, FWHM 8-10 ns). The ring cavity contains two rotatable KTP crystals (KTP,  $\text{KTiOPO}_4$ , Altechna Co. Ltd.,  $67.4^\circ$ ) for frequency conversion to the desired signal and idler wavelength. In order to obtain a

narrow bandwidth, the OPO is seeded by a continuous wave external cavity diode laser at the desired wavelength (ECDL, Toptica Photonics, DL Pro 100, 875-940 nm). In addition, the cavity is actively stabilized by adjusting the voltage applied to a piezoelectric transducer (PZT, Piezomechanik GmbH, HPSt 150/200/12 VS35) to obtain the optimal position of the movable cavity mirror. In this way, the cavity length can be matched with the seed laser wavelength by monitoring the continuous wave output power of the cavity with a photodiode (PD, Thorlabs). The minimum output power corresponds to the optimal cavity length. Stabilization of the cavity is achieved using a Labview program which controls a data acquisition card.

The output of the OPOs is then used for sum frequency generation together with the second or fourth harmonic generation of the seeded Nd:YAG Laser, which yields narrow-bandwidth ( $\approx 0.007 \text{ cm}^{-1}$ ) radiation in the UV. In this work the OPOs are used for stimulated emission pumping of NO via the  $A^2\Sigma(v = 2, J = 0.5)$  state to the  $X^2\Pi_{1/2}(v = 11, J = 0.5)$  state. The laser radiation required for the pump step (dump step) is generated by setting the OPO to 887.146 nm (912.081 nm) and adding the fourth harmonic generation (second harmonic generation) of the Nd:YAG in a BBO crystal, Altechna Co. Ltd.,  $\theta = 58.3^\circ$  (Cstech,  $\theta = 23.6^\circ$ ). Note that the OPOs are tunable over a narrow wavelength range by changing the seed frequency. This allows the compensation of thermal drifts in the Nd:YAG laser frequency, such that the radiation for the pump and dump step can be kept at a constant frequency.

### 3.2.4. Fluorine laser

The molecular fluorine laser (EX350 EXCIMER LASER, GAM Laser) supplies pulsed VUV radiation (FWHM 20-26 ns) on two laser lines at 157.52 nm and 157.63 nm each with a bandwidth of  $8 \text{ cm}^{-1}$  and a pulse energy of typically 10 mJ/pulse. The optical path of the VUV radiation has to be evacuated. Thus, a custom beamline is used that is kept at a pressure of  $2 \cdot 10^{-2}$  Torr. The beamline can be connected to adapters at the windows on both sides of the surface scattering chamber. See Figure 3.4 for a drawing of the VUV beamline connected to the molecular beam surface scattering apparatus. The laser beam is passed through a small chamber which is equipped with a feedthrough for a detector that can be used to measure the pulse energy of the laser. In most cases a  $\text{CaF}_2$  lens ( $f = 775 \text{ mm}$  at 157 nm) is used to focus the laser beam into the detection region of the surface scattering chamber. The lens is positioned such that the actual focus lies behind the detection region and mild focusing to an area of  $5.5 \text{ mm}^2$  is achieved. Two mounts equipped with dichroic mirrors (157 nm,  $45^\circ$ , Qioptics) are used to guide the laser beam

### 3. Experimental setup

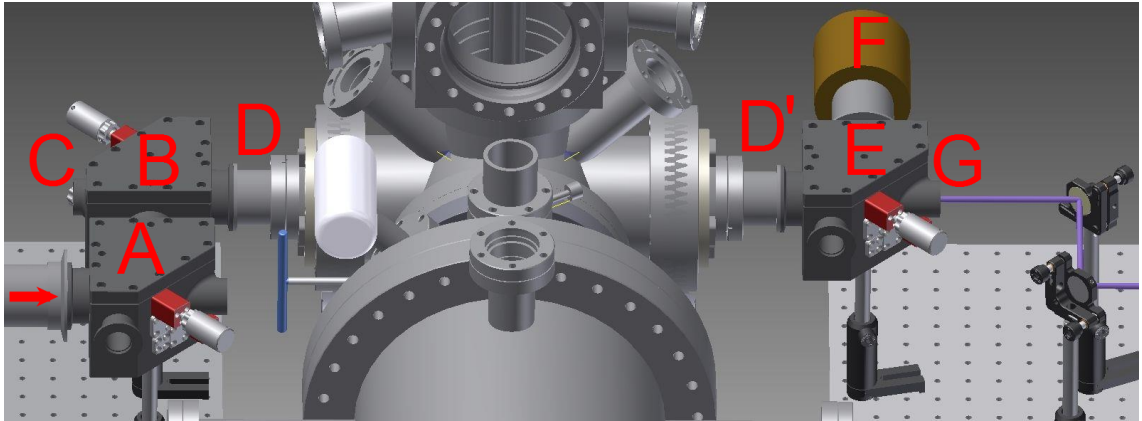


**Figure 3.4.:** Setup of the VUV beam line at the ultra-high vacuum (UHV) chamber. After a pass through a small chamber (not shown) used for pulse energy measurements of the incoming laser beam the VUV laser beam (propagation direction represented by the red arrow) is reflected at the dichroic mirror for radiation with a wavelength of 157 nm (Qioptics, 45°) in mirror mount A. After a second reflection at mirror mount B the beam is sent into the UHV chamber passing through a CaF<sub>2</sub> window located in the adapters D and D'. Just upstream of this adapter an iris is placed (not drawn). The VUV beam leaves the UHV chamber via an analogous adapter on the opposite side of the chamber. A third reflection at mirror mount E steers the beam onto a power detector F. The mirror mounts B and E are equipped with anti-reflection coated windows suitable for passing UV laser light at around 350 nm. The mounts for the dichroic mirrors are designed such that the UV laser light can pass from the entrance window G to the exit window C.

into the surface scattering chamber. In addition, an iris is located directly in front of the viewport. A third mirror mount at the rear of the chamber reflects the VUV light passed through the scattering chamber onto a power detector. The mirror mounts are equipped with windows such that additional laser beams can be collimated with the VUV laser beam and sent through the scattering chamber.

#### 3.2.5. Narrow-bandwidth IR-laser

A detailed description of the narrow-bandwidth IR-laser can be found in reference [101]. Briefly, the output of a cw Nd:YLF laser pumped ring-dye laser (Sirah Matisse DR, 20 MHz bandwidth) is pulse amplified in the PulsAmp 5X (Sirah) which is pumped by an injection-seeded Nd:YAG laser (Spectra Physics Quanta-Ray Pro-230). The pulsed light is then used together with the fundamental of the Nd:YAG laser in a difference frequency mixing process. The difference frequency is amplified in an OPA process which is pumped by the fundamental of the Nd:YAG laser. In this process signal and idler laser beams with

a nearly Fourier-transform limited bandwidth are obtained. In this thesis the idler beam at around  $2900\text{ cm}^{-1}$  ( $\approx 4\text{ mJ/pulse}$ ) is used.

In order to avoid reflection of UV/visible laser sources into the IR laser source when collimating the IR beam with counter propagating UV/visible laser beams the IR radiation can be sent through a germanium plate at the Brewster angle.



## 4. Experimental procedures

### 4.1. Experiments on nitric oxide scattering

Molecular beams of nitric oxide are prepared by expanding the gas together with different carrier gases. This seeding technique allows the adjustment of the incidence translational energy in a range from 0.05 eV up to  $\approx 1$  eV.

#### 4.1.1. Preparation of NO $X^2\Pi_{\frac{1}{2}}(\nu = 11)$

Highly vibrationally excited NO  $X^2\Pi_{\frac{1}{2}}(\nu = 11, J = 0.5)$  with negative parity is prepared following the Pump-Dump-Sweep approach<sup>[102]</sup> which is an extension to stimulated emission pumping.<sup>[103]</sup> The OPO system described in Section 3.2.3 supplies the radiation for the Pump step (204.708 nm) and Dump step (336.101 nm). The Pump (Dump) laser beam size was reduced to a beam diameter of 3 mm (4 mm) and the pulse energy was adjusted to 0.5 mJ (1 mJ). Both laser beams are collimated and overlapped with the molecular beam. The delay between the Pump and the Dump laser beam is adjusted to 3 ns via extension of the beam path of the Dump laser. A third so-called Sweep laser pulse (450.87 nm, 8 mJ/pulse, 5 mm diameter) is used to deplete the residual population in the excited electronic state. The Sweep laser pulse is supplied by the Sirah Precision Scan laser system. It is collimated with the other laser beams but fired at a delay of 13 ns with respect to the Pump pulse.

#### 4.1.2. 1+1 REMPI via the A state as a detection for surface scattered ground electronic state NO

1+1 REMPI spectroscopy via the A state at wavelengths between 230-320 nm is used to detect incoming and scattered ground electronic state NO in various rovibrational states. The output of the Sunlite Ex OPO with FX 1 UV frequency extension ( $\approx 1$  mJ/pulse, 2 mm diameter) is used to probe the molecules at different positions relative to the surface.

#### 4. Experimental procedures

For this purpose a periscope mounted on a translational stage is used. It is equipped with an additional translational stage to be able to adjust the laser position along the  $z$ -axis. The spectra is recorded at a fixed laser timing and position by scanning the Sunlite OPO continuously in wavelength at a speed of 0.005 nm/s. Alternatively, for detection of a single quantum state the laser can be set to a fixed wavelength. The wavelength of the Sunlite OPO is monitored by coupling a small portion of the output into a high-precision wavemeter (HighFinesse, WS7). The laser power is monitored by a detector positioned at the back of the chamber.

1+1 REMPI of surface scattered NO is recorded as follows. The molecules are prepared by the Pump-Dump-Sweep method and then scattered from the surface. The probe laser is positioned close to the surface ( $d = 3$  mm) at normal scattering angle. The delay of the probe laser is set to the maximum of the arrival time distribution. Then the laser is scanned in intervals of 5 nm between 230-320 nm. The ion signal and the laser pulse energy is recorded as the probe laser is scanned. A background spectrum is recorded with the Dump laser blocked such that scattering products originating exclusively from NO  $X^2\Pi_{\frac{1}{2}}(v = 11)$  can be identified.

##### 4.1.3. Time-of-flight experiments on NO $X^2\Pi_{\frac{1}{2}}(v = 11)$

Time-of-flight experiments are conducted to record arrival time distributions of the incoming and scattered beam. In Figure 4.1 the geometry of the experiment is shown for both measurements in the incoming and scattered beam. At the indicated position (red) highly vibrationally excited molecules are prepared. The preparation of NO  $X^2\Pi_{\frac{1}{2}}(v = 11, J = 0.5)$  is implemented as described in Section 4.1.1. However, the beam diameters are reduced to the following values: Pump 1 mm, Dump 2 mm, Sweep 3 mm. The Probe laser used for detection via 1+1 REMPI as described in Section 4.1.2 is reduced to a beam diameter of 1 mm. The probe positions in the incoming and scattered beam are marked in green and blue.

As shown in panel A), preparation and probe position in the incoming beam are separated along the  $x$ -axis by  $d_i$ . Typically,  $d_i = 20$  mm is used. The probe laser wavelength is set to a REMPI transition corresponding to the detection of NO  $X^2\Pi_{\frac{1}{2}}(v = 11, J = 0.5)$ . The ion signal is recorded as the delay of the probe laser pulse is varied with respect to the laser pulses used for preparation employing delay generators (Stanford Research Systems, DG535). The absolute delay between preparation and probe laser pulses is determined using a fast photo diode. Measurements for scattered molecules are performed analogously. Here, the preparation is located close to the surface ( $d_{ps} = 2$  mm). The probe



position is located at a distance of 10-20 mm from the surface. In order to detect different rovibrational states produced in the collision the probe laser wavelength can be set to a suitable REMPI transition. During the experiment the wavelength can be monitored by a high-precision wavemeter (HighFinesse, WS7). The correct wavelength for a particular rovibronic transition belonging to the X-A-transition band system is calculated as described in Section 2.1. In some cases it is necessary to record an additional “background” trace in order to account for the scattering of states populated due to fluorescence out of the A state. In these cases the arrival time distribution is recorded twice: once with Dump laser blocked and once with Dump laser unblocked. The desired arrival time distribution assignable to incoming  $\text{NO } X^2\Pi_{1/2}(v = 11, J = 0.5)$  is obtained by subtracting the two traces from each other.

In these experiments the knowledge of the flight distances is critical. A method for their determination is described below. The  $x$ -position of a laser beam can be most accurately determined by the use of the surface manipulator. The laser beam pulse energy is monitored on the rear of the chamber while a micrometer screw is used for manipulating the  $x$ -position of the surface. When only half of the full laser beam pulse energy is transmitted through the chamber the surface clips half of the laser beam. Thus, in this configuration the micrometer screw will show the  $x$ -position of the center of the laser beam. The  $z$ -position is determined in two steps. First the ion signal corresponding to population of  $\text{NO } X^2\Pi_{1/2}(v = 11, J = 0.5)$  in the incoming beam is recorded as a function of the  $z$ -position of the laser beam. The recorded maximum ion signal indicates the center of the molecular beam whose position can be read out at the micrometer screw. This position is then used as the origin of the  $z$ -axis and the laser beam can be moved to other  $z$ -positions, which can be easily determined by the reading of the micrometer screw on the periscope. In this way the distances  $l_i$ ,  $l_{ps}$ , and  $l_s$  shown in Figure 4.1 are accessible from simple geometrical considerations.

Once  $d_{ps}$ , the arrival time of the incoming beam at  $x = l_{ps}$ , and the incoming beam velocity are known the arrival time of the incoming beam at the surface can be calculated.

## 4.2. Experiments on formaldehyde scattering

Molecular beams of formaldehyde are prepared by expanding the cracked monomer together with different carrier gases. Since the nozzle reservoir is heated the molecule’s incidence translational energy can be adjusted up to 1.3 eV.

4. Experimental procedures

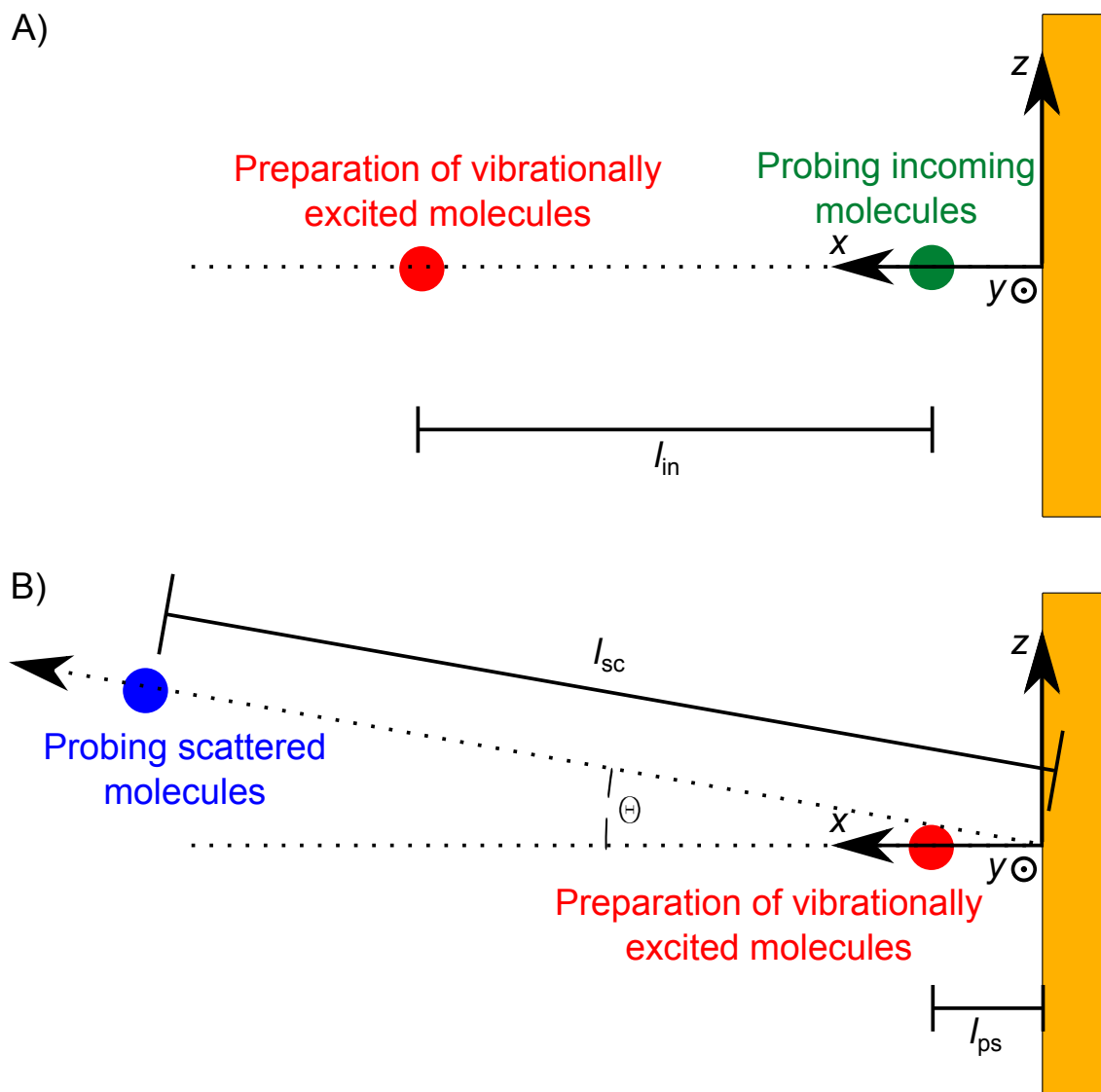


**Figure 4.1.:** Time-of-flight geometry used in the scattering of highly vibrationally excited nitric oxide. Panel A) shows the geometry for the experiment in the incoming beam. Panel B) shows the geometry for the experiment in the scattered beam.

### 4.2.1. 1+1' REMPI of formaldehyde via the $\tilde{A}$ state

The 1+1' REMPI of formaldehyde via the  $\tilde{A}^1A_2$  state<sup>[104]</sup> as a detection method has been established as a part of this thesis. Two laser pulses are used. The doubled output of the dye laser (Cobra-Stretch SL) at a wavelength around 353 nm (FWHM 8 ns) is used to excite molecules into the  $\tilde{A}^1A_2$  state. A VUV photon at 157 nm supplied by a fluorine laser (EX350 EXCIMER LASER, GAM Laser) is used for ionization of this state. The laser beams are collimated in the detection region. The timing of the laser pulses can be adjusted by means of delay generators (Stanford Research Systems, DG535). The delay between the laser pulses can most easily be measured by detecting the corresponding scattered laser light with the MCP detector. Irises can be used for both lasers.

The following settings are usually used in scattering experiments. The UV pulse energy is typically adjusted to  $\approx 4$  mJ/pulse. The beam diameter is reduced by a factor of two using a telescope to 3 mm and overlapped with the VUV laser which is delayed by 30 ns and focused as described in Section 3.2.4. At incidence translational energies below 0.4 eV the incidence beam and scattered molecules cannot be resolved by the ion time-of-flight. Thus scattered molecules are detected at  $x = 9$  mm measured from the surface and  $z = 3$  mm above the center of the incoming beam which excludes contributions of the incoming beam in the spectra of scattered molecules. Spectra of scattered molecules above 0.4 eV incidence translational energy can be acquired at a distance of 3 mm from the surface since incoming and scattered signal can be resolved in the ion time-of-flight. See Section 3.1.2. The delay of the lasers with respect to the nozzle opening is set to the maximum of the arrival time distribution. The ion signal for scattered molecules is recorded as the dye laser is scanned with a scan speed of 0.002 nm/s.

### 4.2.2. 2+1 REMPI of formaldehyde via the $3p_x$ Rydberg state

2+1 REMPI of formaldehyde via the  $3p_x^1A_2$  Rydberg state<sup>[25]</sup> is used in this work as a detection method for ground electronic state formaldehyde and is applied in non-state resolved time-of-flight experiments. The UV output of the Cobra-Stretch SL laser with doubling unit at around 295 nm ( $\approx 5$  mJ/pulse) is focused using a lens with a focal length of 500 mm.

In most of the experiments the laser is set to  $33866.6\text{ cm}^{-1}$ . According to a simulation with the spectroscopic constants taken from reference [105] the detected signal corresponds to transitions from many different  $J''$  values but only  $K_a'' = 0$  and  $K_a'' = 1$ . Thus, the REMPI signal should be approximately proportional to the population of the two  $K_a''$  manifolds

#### 4. *Experimental procedures*

but should not be affected by population of higher  $K_a''$ .

The arrival time distribution of the incoming or scattered beam can be measured as follows. The laser beam is moved to a certain set of  $x$  and  $z$  coordinates. The REMPI signal is recorded as the delay between laser firing and nozzle opening is scanned using a delay generator (Stanford Research Systems, DG535).

##### **4.2.3. Preparation of formaldehyde in vibrationally excited states**

The focused ( $f = 1000$  mm) or unfocused output of the narrow-bandwidth IR-laser ( $\approx 4$  mJ, beamdiameter  $\approx 4$  mm) is overlapped with the molecular beam and collimated with the dye laser and  $F_2$  laser used for  $1+1'$  REMPI spectroscopy as described in Section 4.2.1. The delay of the laser pulses is adjusted such that the IR pump pulse precedes the dye laser pulses by 10 ns. Excitation of  $2_14_1$  or  $2_16_1$  is probed via  $1+1'$  REMPI detection (see Section 4.2.1) of the vibrational ground and the vibrationally excited state.

### **4.3. Temperature programmed desorption**

The temperature programmed desorption experiments have been performed in a UHV apparatus described in reference [106]. Monomeric formaldehyde is produced following the procedure described in reference [107]. The 20 K Au(111) surface is dosed with formaldehyde via a homebuilt surface doser. It is important to note that the formaldehyde must be carefully evaporated. Then the surface is heated at a constant rate of 0.5 K/s in front of a modified residual gas analyzer recording the partial pressure at a mass-to-charge-ratio of 30 u.

Before each temperature programmed desorption experiment the surface is sputtered at a neon pressure of  $2.5 \times 10^{-7}$  Torr and subsequently annealed at 900 K. The desorption experiment is repeated for different exposure times of the clean surface to the formaldehyde gas.

## 5. Analysis

The analysis section is split into two parts. Section 5.1 describes the spectral analysis. The experiments probe which quantum states (vibrational and rotational) are populated after the surface collision. The major task is to quantitatively understand the REMPI scheme used for the detection of NO and formaldehyde. Section 5.2 deals with the analysis of time-of-flight experiments on the incoming and scattered molecules. It is shown how the velocities of incoming and scattered molecules are obtained from the measured arrival time distributions

### 5.1. Spectral analysis

#### 5.1.1. Nitric oxide

1+1 REMPI spectroscopy via the A state of NO has been shown to be a reliable tool for obtaining population distribution in the ground electronic state of NO over the quantum states characterized by the rotational quantum number  $J$ ,  $\Omega$  and the vibrational quantum number  $\nu$ .<sup>[27]</sup> Recently, this method has been successfully applied to the characterization of vibrational relaxation in NO surface scattering.<sup>[91]</sup> Neglecting effects of alignment in the laboratory frame the 1+1 REMPI spectrum  $S_{\text{NO}}$  can be simulated according to Equation 5.1.

$$S_{\text{NO}}(\tilde{\nu}) = \sum_0^{\nu_{\text{max}}} \sum_{0.5}^{J_{\text{max}}} \sum_{\Delta\nu} \sum_{\Delta F} \sum_{\Delta J=-1}^{\Delta J=+1} x(\nu, J, \Omega) f(\nu, J, \Omega, \Delta\nu, \Delta J, \Delta F) g(\tilde{\nu}, \tilde{\nu}_0(\nu, J, \Omega, \Delta\nu, \Delta J, \Delta F)) \quad (5.1)$$

In this equation,  $x(\nu, J, \Omega)$  is the population factor for a specific quantum state in the ground electronic state of NO characterized by the quantum numbers  $\nu$ ,  $J$ , and  $\Omega$ .  $f(\nu, J, \Omega, \Delta\nu, \Delta J, \Delta F)$  is the detection efficiency of a quantum state in the ground electronic state via a certain rovibronic transition specified by  $\Delta\nu$ ,  $\Delta J$ , and  $\Delta F$  and is composed of a rotational and vibrational part is shown later in this section.  $\Delta\nu$  ( $\Delta J$ ) specifies the change

## 5. Analysis

of vibrational (rotational) quanta in the first excitation step of the REMPI scheme and  $\Delta F$  describes the change of the spin label.  $g(\tilde{\nu}, \tilde{\nu}_0(\nu, J, \Omega, \Delta\nu, \Delta J, \Delta F))$  is the line shape function which depends on the center wavenumber  $\tilde{\nu}_0$  for a specific electronic transition. In order to obtain the whole spectrum all transitions from vibrational and rotational states belonging to the ground electronic state in the wavenumber range of the spectrum have to be taken into account. Thus, all vibrational bands and the respective rotational branches are considered by summation over  $\Delta J$ ,  $\Delta\nu$ , and  $\Delta F$ , where F can take the value  $F_1$  and  $F_2$ . The task of calculating  $S_{\text{NO}}(\tilde{\nu})$  can be separated into two problems: 1. The center wavenumber  $\tilde{\nu}_0$  for every relevant transition has to be known precisely. 2. The detection efficiency  $f$  has to be calculated for all transitions included in the simulation.

Both tasks have already been solved as described in reference [44]. This is why in the following, the procedure is described only briefly with the focus on recent modifications. First, the calculation of line positions is described. Second, the method for deriving detection efficiencies is discussed. Reference [44] provides the script for a MATHEMATICA notebook for the calculation of the transition wavenumbers  $\tilde{\nu}_0$ . The script is based on the effective Hamiltonian for the A and X state described in Section 2.1. The  $q_{\Lambda}$  and  $p_{\Lambda}$  parameters for the X state and all parameters for the A state are taken from reference [32]. All other parameters for the X state are taken from reference [30]. The MATHEMATICA notebook has been modified for this work such that spin splitting in the A state is taken into account, which is neglected in reference [44]. The terms that give rise to spin-splitting are given in Equation 2.7 and 2.8 of this work. Note that in reference [29] a minus sign is missing in the relevant matrix element for the  $F_2$  component which becomes obvious by a comparison to reference [108]. A Lorentzian lineshape profile is used. By a fit to various resolved REMPI transitions a FWHM of  $1 \text{ cm}^{-1}$  was found to resemble the line broadening.

The detection efficiency  $f(\nu, J, \Omega, \Delta\nu, \Delta J, \Delta F)$  is composed of a vibrational part  $w$  and a rotational part  $r$  ( $f = w \cdot r$ ). If only the resonant step influences the detection efficiency and no saturation effects are present  $w(\nu, \Delta\nu)$  corresponds to a Franck-Condon factor and  $r(J, \Delta J, \Delta F)$  corresponds to a Hönl-London factor. In reference [44], an experiment is described which allows  $w(\nu, \Delta\nu)$  to be measured. Briefly, a well determined vibrational distribution of NO molecules is produced in the ground electronic state by electronic excitation and subsequent fluorescence back to the ground state. A REMPI spectrum is recorded and the ion signal that is obtained for the different bands  $i_{\nu, \Delta\nu}$  is compared to the expectations for the population  $p_{\nu}$  of the vibrational state in the ground electronic state calculated from the Einstein A coefficients.  $w(\nu, \Delta\nu)$  is then

determined by  $w(v, \Delta v) = p_v/i_{v, \Delta v}$ . The calculation of  $r(J, \Delta J, \Delta F)$  is performed as described in reference [27] and successfully applied to highly vibrationally excited NO surface scattering as mentioned in reference [91].

Finally the population of a certain quantum state  $P$  can be obtained from a successful simulation of the REMPI spectrum. Note that each spectral region is recorded twice once with dump laser on and once with dump laser blocked which is necessary to discriminate real scattering signal originating from the desired initial state against background. Prior to the fit of the simulation to the spectra, both of these spectra are corrected for laser pulse energy assuming a linear dependence which has been found for all transition for which a laser pulse energy dependence has been obtained. If the recorded REMPI spectrum is not too dense and the number of states is not too high a whole experimental spectrum can be fitted minimizing the difference between experiment and simulation by adjusting the population factors  $x(v, J, \Omega)$  serving as fit parameters. The population of a certain quantum state  $P$  is then given by Equation 5.2 using the optimized population factors.

$$P(v, J, \Omega) = \frac{x(v, J, \Omega)}{\sum_0^{v_{\max}} \sum_0^{J_{\max}} \sum_{\Omega=0.5}^{\Omega=1.5} x(v, J, \Omega)} \quad (5.2)$$

In order to correct for background the population factors obtained for the analysis of the two spectra with dump laser unblocked and blocked are subtracted from each other. In certain cases when the spectrum is partially unresolved or the number of states in the simulation is too high it is necessary to split the analysis into two parts. In a first step, less dense parts of the spectrum containing only several vibrational bands are analyzed which yields the rotational state distributions. The whole spectrum is then fitted with fixed rotational state distributions such that the population of vibrational states can be derived.

### 5.1.2. Formaldehyde

In the following, a method for the analysis of rotationally resolved 1+1' REMPI spectra of ground electronic state formaldehyde using the  $\tilde{A} \leftarrow \tilde{X} 4_0^1$  band is described. The relevant spectroscopy for the  $\tilde{A} \leftarrow \tilde{X}$  transition is described in Section 2.2. A 1+1' REMPI spectrum  $S_{\text{form}}$  can be simulated following Equation 5.3. A MATLAB code for the simulation is provided in Section A.1.

$$S_{\text{form}}(\tilde{\nu}) = \sum_{J, K_a, K_c, J', K'_a, K'_c} x_{\text{form}}(J, K_a, K_c) f_{\text{form}}(J, K_a, K_c, J', K'_a, K'_c) g_{\text{form}}(\tilde{\nu}, \tilde{\nu}_0(J, K_a, K_c, J', K'_a, K'_c)) \quad (5.3)$$

## 5. Analysis

Here,  $x_{\text{form}}(J, K_a, K_c)$  are the population factors,  $f_{\text{form}}(J, K_a, K_c, J', K'_a, K'_c)$  are the line strength factors and  $g_{\text{form}}(\tilde{\nu}, \tilde{\nu}_0(J, K_a, K_c, J', K'_a, K'_c))$  is the line shape function. The sum indicates that various  $\tilde{A} \leftarrow \tilde{X}$  rotational transitions have to be taken into account. Following the selection rule 2.18 only transitions with  $\Delta K_a = \text{odd}$  are allowed. The calculations of line strength suggests that  $\Delta K_a = 1$  transition dominate. However, also  $\Delta K_a = 3$  and even higher values up to  $\Delta K_a = 9$  are taken into account for the simulation. The center wavenumber for each rovibronic transition  $\tilde{\nu}_0(J, K_a, K_c, J', K'_a, K'_c)$  is calculated from the asymmetric top Hamiltonian in the Wang basis. The line shape function used in the simulation has been determined by a fit to resolved rovibronic transitions and is given in Equation 5.4.

$$f_{\text{form}} = A_L \frac{\Gamma^2}{(\tilde{\nu} - \tilde{\nu}_0)^2 + \Gamma^2} + A_G \exp\left(\frac{-(\tilde{\nu} - \tilde{\nu}_0)^2}{\sigma^2}\right) \quad (5.4)$$

For the simulation of spectra of scattered molecules in this work the parameters  $\Gamma = 0.1 \text{ cm}^{-1}$ ,  $\sigma = 0.4 \text{ cm}^{-1}$ ,  $A_L = 0.3$ , and  $A_G = 0.7$  are used. If no saturation effects are present and the efficiency of the ionization step does not depend on the initial and intermediate state the intensity of a 1+1' REMPI transition is proportional to the transition dipole moment squared. Equation 2.24 gives the relevant matrix element for the calculation of the transition dipole moment. The matrix element can be split into a vibronic and a rotational part. Since in this work only the rotational state distribution in the ground state has been probed the vibronic part is the same for all analyzed transitions and can be used as a constant factor to match the integrated ion signal over the whole band. The rotational part can be solved by evaluation of Equation 2.24. The central part of this task is the calculation of direction-cosine matrix elements, which are tabulated in reference [109]. All the calculations mentioned above are included in the MATLAB code given in the Appendix A.1.

## 5.2. Time-of-flight analysis

The scattering experiments on nitric oxide and formaldehyde differ fundamentally in the way the starting point of the time-of-flight experiment is defined. In the scattering of highly vibrationally excited nitric oxide only direct-scattering is observed. The narrow angular distribution simplifies the analysis. Furthermore, the starting point is defined by the nanosecond laser preparation step in a small part of the molecular beam and thus the initial beam of vibrationally excited molecules can be approximated as a point source. This is clearly not the case in the formaldehyde ground state scattering since the initial



distribution is given by the whole molecular beam pulse which is on the order of ten microseconds and depends on the seeding conditions. Moreover, for the formaldehyde scattering broad angular distributions are observed in some cases, which indicates that an analysis must include velocity components parallel to the laser beam used for detection ( $y$ -axis). Thus the analysis of the two experiments is discussed separately in the following two sections.

### 5.2.1. Nitric oxide

The analysis described in the following has been developed following the methods described in reference [101]. The procedure for time-of-flight experiments on surface scattering of highly vibrationally excited NO surface scattering including the positioning of preparation and probe lasers is described in Section 4.1.3. First, the analysis of time-of-flight experiments in the incoming beam is described. Second, the analysis of time-of-flight experiments for scattered molecules is described. The flight distance  $l_{\text{in}}$  between pump and probe laser can be determined following the methods described in Section 4.1.3. The arrival time of the Pump laser pulse serves as the starting point  $t = 0$  in the time-of-flight experiment. By delaying the probe laser with respect to the preparation lasers the time-of-flight of the molecules from the preparation position to the probe position  $t_{\text{in}}$  can be varied precisely. The probe laser is set to a fixed wavelength for the detection of a single quantum state characterized by the rotational and vibrational quantum numbers  $J$ ,  $\Omega$ , and  $\nu$  via 1+1 REMPI spectroscopy. The ion signal  $I_{\text{ion}}$  is recorded as a function of the time-of-flight  $t_{\text{in}}$ . In general it has been shown that the flux velocity distribution  $F(v)$  in a molecular beam can be described by a floating Maxwell Boltzmann distribution given in Equation 5.5.<sup>[110]</sup>

$$F(v)dv = N_1 \cdot v^3 \exp\left(-\left(\frac{v - v_0}{\alpha}\right)^2\right) dv \quad (5.5)$$

In this equation  $N_1$  is a normalization factor,  $v$  is the velocity, and  $v_0$  is the center velocity. The parameter  $\alpha$  describes the width of the velocity distribution. Since in the time-of-flight experiment the velocity of a single molecule is constant the relation  $v = l_{\text{in}}/t$  holds. We can transform Equation 5.5 into a flux arrival time distribution  $F(t)$  by multiplying with the Jacobian  $\frac{dv}{dt} = -\frac{l}{t^2}$  since  $F(t) = F(v)\frac{dv}{dt}$ .

$$F(t_{\text{in}})dt_{\text{in}} = N_2 \cdot \frac{l_{\text{in}}}{t_{\text{in}}^2} \left(\frac{l_{\text{in}}}{t_{\text{in}}}\right)^3 \exp\left(-\left(\frac{l_{\text{in}}/t_{\text{in}} - v_0}{\alpha}\right)^2\right) dt_{\text{in}} \quad (5.6)$$

## 5. Analysis

In the experiment the molecules are detected in a small volume by a nanosecond laser pulse (probe laser diameter 1 mm). Because the velocity of the molecule is on the order of  $10^2 - 10^3$  m/s the molecules are approximately stationary during the laser pulse. For a realistic estimate of the velocity spread (10 %) and a flight length of  $l_{\text{in}} = 20$  mm the spatial dimension of the molecular beam pulse will be larger than the dimension of the detection region. Thus, under the conditions of the experiment the recorded ion signal is proportional to the density, which means that slower molecules are detected more efficiently than faster molecules. Similarly, the preparation step also selects a higher number of slower molecules. Since the density can be converted into flux by multiplying with the velocity the relationship between the ion signal recorded in the experiment and the flux is given by  $I_{\text{ion,in}}(t_{\text{in}}) \propto \frac{F(t_{\text{in}})}{v^2}$ . Equation 5.7 gives an expression for  $I_{\text{ion,in}}(t_{\text{in}})$ .

$$\begin{aligned} I_{\text{ion,in}}(t_{\text{in}})dt_{\text{in}} &= N_3 \cdot \left(\frac{t_{\text{in}}}{l_{\text{in}}}\right)^2 \frac{l_{\text{in}}}{t_{\text{in}}^2} \left(\frac{l_{\text{in}}}{t_{\text{in}}}\right)^3 \exp\left(-\left(\frac{l_{\text{in}}/t_{\text{in}} - v_0}{\alpha}\right)^2\right) dt_{\text{in}} \\ &= N_3 \cdot \frac{l_{\text{in}}^2}{t_{\text{in}}^3} \exp\left(-\left(\frac{l_{\text{in}}/t_{\text{in}} - v_0}{\alpha}\right)^2\right) dt_{\text{in}} \end{aligned} \quad (5.7)$$

The parameters  $N_3$ ,  $v_0$ , and  $\alpha$  can be fitted to the experimental arrival time distributions. The determination of the best fit parameters allows the extraction of relevant quantities like the average velocity in the incoming beam  $\langle v \rangle_{\text{in}}$  according to Equation 5.8.

$$\langle v \rangle_{\text{in}} = \int_0^{\infty} F(v)v dv = \int_0^{\infty} N_1 \cdot v^4 \exp\left(-\left(\frac{v - v_0}{\alpha}\right)^2\right) dv \quad (5.8)$$

The normalization factor can be obtained from  $\frac{1}{N_1} = \int_0^{\infty} v^3 \exp\left(-\left(\frac{v-v_0}{\alpha}\right)^2\right) dv$ .

The velocity distribution in the scattered beam is derived in a similar manner. However, the velocity of the molecules in the incoming beam has to be known in order to derive the time of the collision with the surface. Since the preparation step takes place very close to the surface it is justified to approximate that there is no spread of the beam pulse during the short flight length between preparation position and surface. In this case the time difference between the laser preparation step and the collision is given by  $\Delta t = \langle v \rangle_{\text{in}} d_{\text{ps}}$ . The relevant time-of-flight for scattered molecules  $t_{\text{sc}}$  can be calculated from the delay between probe and preparation laser pulses  $t_{\text{Laser}}$  by  $t_{\text{sc}} = t_{\text{Laser}} - \Delta t$ . The function used to describe the recorded ion signal for scattered molecules  $I_{\text{ion,sc}}$  is from a mathematical point of view identical to the one used for the incoming beam and given in Equation 5.9. The relationship between recorded ion signal and flux  $I_{\text{ion,sc}}(t_{\text{in}}) \propto \frac{F(t_{\text{sc}})}{v^2}$  still holds because

the directly scattered molecule's velocity is determined by the incidence velocity of the molecule. Equation 5.9 is used to fit the arrival time distributions obtained for scattered molecules.

$$I_{\text{ion,sc}}(t_{\text{sc}})dt_{\text{sc}} = N_3 \cdot \frac{l_{\text{sc}}^2}{t_{\text{sc}}^3} \exp\left(-\left(\frac{l_{\text{sc}}/t_{\text{sc}} - v_0}{\alpha}\right)^2\right) dt_{\text{sc}} \quad (5.9)$$

The average scattered velocity can be extracted in analogy to Equation 5.8.

### 5.2.2. Formaldehyde

In the following discussion of the analysis it is helpful to remember the chosen coordinate system given in Figure 4.1. The most probable velocity of formaldehyde in the molecular beam can be measured experimentally by a simple method. The arrival time distribution of the molecules in the incoming beam  $I_{\text{ion,in}}(x, z, t_0)$  is measured at different positions on the  $x$ -axis along the propagation direction of the incoming beam by delaying the probe laser firing with respect to the nozzle opening. Then the probe position  $x$  can be plotted against the maximum point  $t_{\text{max,in}}$  of the arrival time distribution at the respective position. The slope of this plot yields the most probable velocity in the incoming beam  $v_{\text{mp,in}}$ . The intersection with the  $t$ -axis yields the time of the collision with the surface. One can also analyze the arrival time distributions for scattered molecules following a similar approach. Again one can extract the most probable scattered velocity  $v_{\text{mp,sc}}$  from the slope of a plot of the flight length  $l = x^2 + z^2$  against the most probable arrival time  $t_{\text{max,sc}}$ . This method neglects the  $y$ -coordinate and is only applicable if the distribution over the scattering angle  $\theta$  is very narrow. For direct-scattering this requirement is fulfilled. However, for trapping-desorption this is not the case and another approach described below is more reliable in extracting the velocity distribution.

In the following an expression for the expected ion signal for desorbing formaldehyde molecules detected at a position defined by the coordinates  $x, y$  and  $z$  will be derived. The flight distance from the surface to the probe position is defined by  $d = (x^2 + y^2 + z^2)^{0.5}$ . The flux velocity distribution of molecules desorbing from a surface can be described by Equation 5.10.<sup>[110]</sup>

$$F(v)dv = N_4 \cdot v^3 \exp\left(-\frac{mv^2}{2k_B T}\right) \cos(\theta)dv \quad (5.10)$$

As long as effects of detailed balance are unimportant the effective temperature  $T$  is equal to the surface temperature  $T_{\text{surf}}$ . With the substitutions  $v = d/t$  and  $\cos(\theta) = x/d$  we

## 5. Analysis

obtain

$$F(t)dt = N_4 \cdot \frac{d^3x}{t^5} \exp\left(-\frac{md^2}{2k_B T t^2}\right) dt \quad (5.11)$$

The measured ion signal for a single starting point in time  $I_{\text{ion,td}}$  can now be related to the flux by taking into account that the detector is sensitive to the velocity along the  $xz$ -plane  $v_{xz} = (x^2 + y^2)^{0.5}/t$ . Thus, the ion signal is proportional to the density:  $I_{\text{ion,td}} \propto F(v)/v_{xz}$ . Following this argument  $I_{\text{ion,td}}$  can be described by Equation 5.12.

$$I_{\text{ion,td}}dt = N_5 \cdot \frac{x(x^2 + y^2 + z^2)^{3/2}}{(x^2 + y^2)^{1/2}t^4} \exp\left(-\frac{m(x^2 + y^2 + z^2)}{2k_B T t^2}\right) dt \quad (5.12)$$

Under the laser focusing conditions applied in the experiment the ion detector is sensitive to all formaldehyde molecules between  $y_0 = 1.5$  cm and  $y_1 = -1.5$  cm with a sharp cutoff for higher and lower values for  $y$ . Thus, we have to integrate over the  $y$ -coordinate in order to obtain a reasonable description of the arrival time distribution. In addition, the FWHM of the molecular beam pulse at the surface is on the order of ten microseconds. Thus, the simulation of the ion signal for a single starting point in time is convoluted with the temporal profile of the incoming beam at the position of the surface  $I_{\text{ion,in}}(0, 0, t_0)$ . This can be accurately measured by moving the surface out of the detection region. Equation 5.13 describes a simulation of the observable arrival time distribution taking the two considerations mentioned above into account.

$$I_{\text{ion,td,conv}}(t) = N_5 \int_{-\infty}^{+\infty} dt_0 \int_{y_0}^{y_1} dy \frac{x(x^2 + y^2 + z^2)^{3/2}}{(x^2 + y^2)^{1/2}(t - t_0)^4} \exp\left(-\frac{m(x^2 + y^2 + z^2)}{2k_B T (t - t_0)^2}\right) I_{\text{ion,in}}(0, 0, t_0) \quad (5.13)$$

The parameters  $N_5$  and  $T$  can be varied to optimize the fit of the simulation to the observed arrival time distribution. The difference between simulation and experimental observation is minimized in a nonlinear least-square fitting procedure: The integrals in Equation 5.13 are solved numerically and subsequently the simulation is compared to the experimental observation.

# 6. Scattering of highly vibrationally excited NO – results and discussion

## 6.1. Scattering from Au(111)

The scattering of highly vibrationally excited NO from Au(111) as a function of the incidence translational energy and orientation has already been reported in reference [44]. The central findings are given in Section 2.5.3, and Figure 2.12 shows the key observations. In a single collision with a Au(111) surface, NO( $v_i = 11$ ) molecules are very likely to lose a large part of their initial vibrational energy to the metal surface. The most probable scattering channel involves the loss of 5-6 vibrational quanta. Vibrational relaxation is more likely if the molecule points with the N-atom towards the surface. However, the rotational state distributions accompanying multi-quantum relaxation were only analyzed for a limited number of states.

### 6.1.1. Rotational state distributions as fingerprints of dynamical effects in NO( $v_i = 11$ )/Au(111) scattering

#### Results

The refined analysis of the 1+1 REMPI spectra for NO( $v_i = 11$ )/Au(111) reported in the present work in Section 5.1.1 allows us to obtain a more complete picture of the rotational state distributions. Instead of evaluating only nonoverlapping transitions large parts of the available spectra can be simulated with rotational resolution. Following this approach, information on the population of more final rovibrational states is available. Furthermore, the flux-equivalent population can be obtained by correcting the measured density by the velocities of the scattered molecules. These are accessible from time-of-flight measurements on highly vibrationally excited NO/surface scattering and reported in this work for the first time. A typical REMPI spectrum recorded for scattered NO molecules in NO( $v_i = 11$ )/Au(111) surface scattering is shown in Figure 6.1. The vibrational bands

## 6. Scattering of highly vibrationally excited NO – results and discussion

listed in Table 6.1 have been used for an analysis of the rotational state distribution in the respective vibrational state. Note that additional vibrational bands were taken into account in the simulation. The spectra have been recorded for three samples differing in

**Table 6.1.:** Overview of the vibrational bands used in the rotational state distribution analysis.

$\nu$ in $X^2\Pi_{\Omega}$	$\nu$ in $A^2\Sigma^+$
11	3
9	2
8	1
7	1
6	1
6	0
5	1
4	1

the distribution over the orientation angle  $\theta$ .  $\theta$  is taken as the angle between the surface normal and the internuclear axis and is defined as zero for an orientation where the O-atom points towards the surface. Figure 6.2 visualizes the degree of orientation achieved in the experiment which is close to the quantum mechanical limit. In the following, the terms “O-atom down”, “isotropic”, and “N-atom down” refer to the initial orientations as shown in this figure.

Figure 6.3 displays the final rotational state distributions at an incidence translational energy of 0.51 eV. The rotational state distributions vary strongly with orientation and the vibrational energy loss experienced in the collision. The rotational state distribution for vibrationally elastic scattering has a pronounced maximum at high rotational quantum numbers ( $J \approx 35.5$ ). This feature gradually diminishes for increasing vibrational energy loss. In turn a broad feature at low rotational quantum numbers ( $J \approx 13.5$ ) becomes more and more important when increasing the vibrational inelasticity and dominates the rotational state distribution for final vibrational states lower than  $\nu_s = 7$ . The incidence orientation strongly influences the rotational state distributions for  $\nu_s > 6$ . It can be seen that the maximum at high- $J$  is strongly enhanced if the incident molecules are oriented with the O-atom towards the surface. However, the influence of the orientation on the final rotational state distribution diminishes with increasing vibrational energy loss and is essentially absent for  $\nu_s = 4$ . Figure 6.4 shows the rotational state distributions for vibrationally elastic scattered molecules at three different incidence translational energies. The maximum of the rotational state distribution moves towards higher  $J$  as the incidence translational energy is increased. As an overview, Figure 6.5 provides the mean rotational

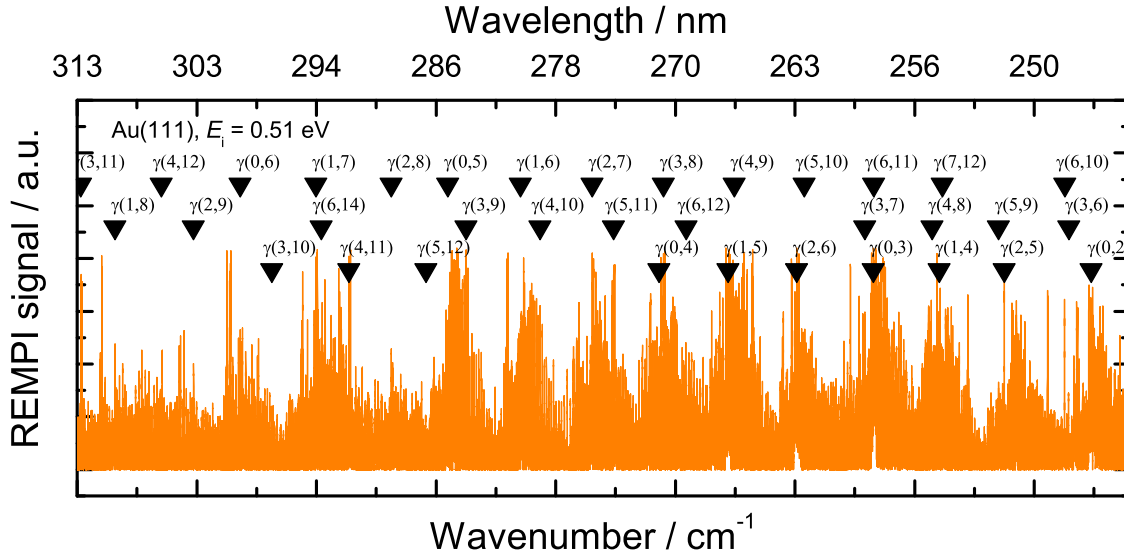


**Figure 6.1.:** Typical 1+1 REMPI spectrum for NO/Au(111) surface scattering. The recorded ion signal is shown as a function of the wavenumber and wavelength. The incidence orientation of the sample is isotropic and the incidence translational energy is 0.51 eV. The triangles indicate the expected positions of the vibrational band heads belonging to the  $\gamma$ -band system. For instance,  $\gamma(3, 11)$  marks the position of the  $A^2\Sigma^+(v = 3) \leftarrow X^2\Pi_{\Omega}(v = 11)$  band.

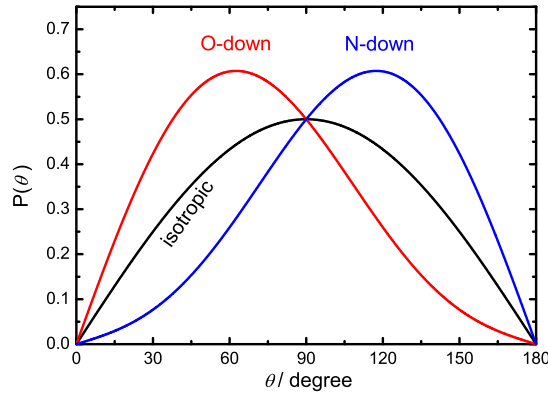


**Figure 6.2.:** Initial orientation distribution in the scattering experiment. The probability for a certain orientation is plotted as a function of the orientation angle  $\theta$ . The black line shows the isotropic experiment when no orientation field is applied. Nonisotropic orientation in the laboratory frame can be achieved using an orientation field  $|E| = 33$  kV/cm. When using a positive voltage at the orientation electrode the selected negative parity state NO( $v_i = 11, J_i = 0.5$ ) will orient with the O-atom down to the surface. Switching the polarity of the electric field results in N-atom down orientation. Figure adapted from reference [44].

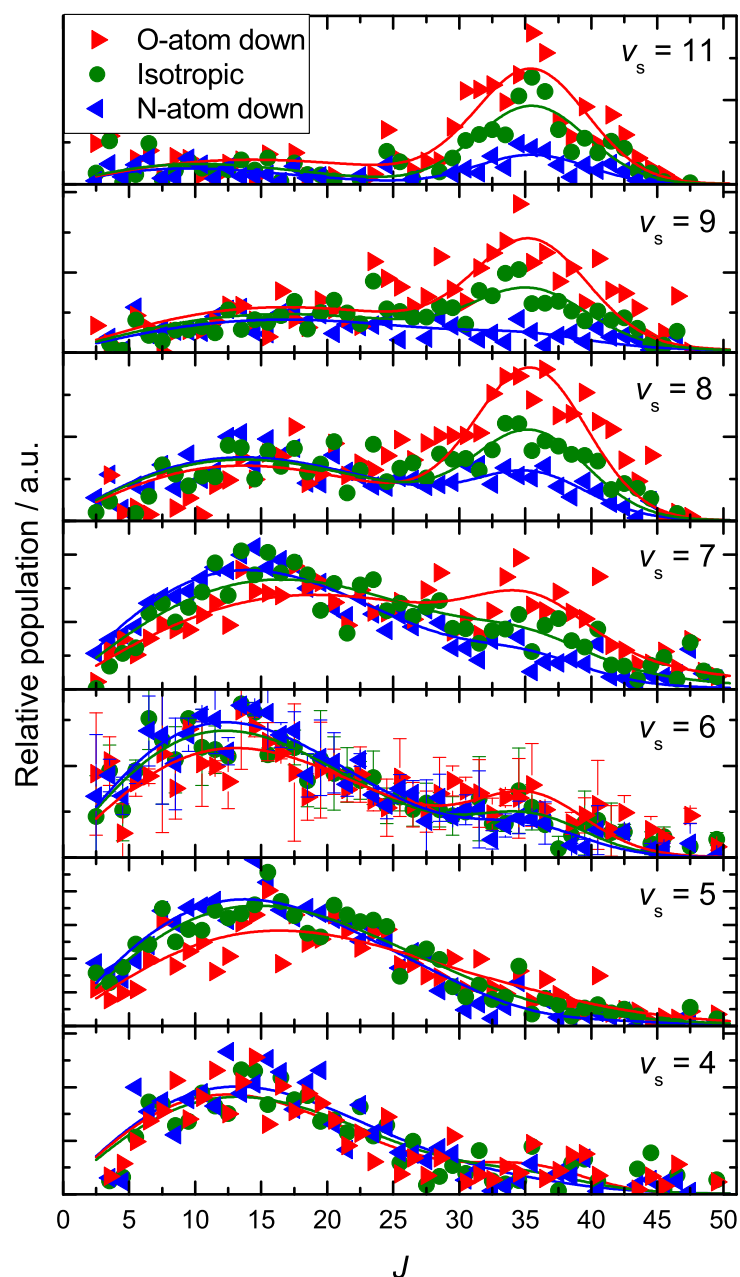


**Figure 6.3.:** Final rotational state distributions obtained from  $\text{NO}(v_i = 11, J_i = 0.5)/\text{Au}(111)$  surface scattering as a function of the vibrational energy loss and orientation. The incidence translational energy is 0.51 eV. The rotational state distributions derived from an analysis of 1+1 REMPI spectra are plotted for the final vibrational states  $v_s = 4 - 11$  with  $\Omega = \frac{1}{2}$ . The three different initial orientation distributions are indicated by red triangles (O-atom down orientation), green circles (isotropic), and blue triangles (N-atom down orientation). The error bars for the population of states belonging to the final vibrational state  $v_s = 6$  are calculated based on the two available datasets from the analysis of the independent vibrational bands  $\gamma(0, 6)$  and  $\gamma(1, 6)$ . The solid lines are drawn to guide the reader's eye. Figure taken from reference [111] - published by the PCCP Owner Societies.



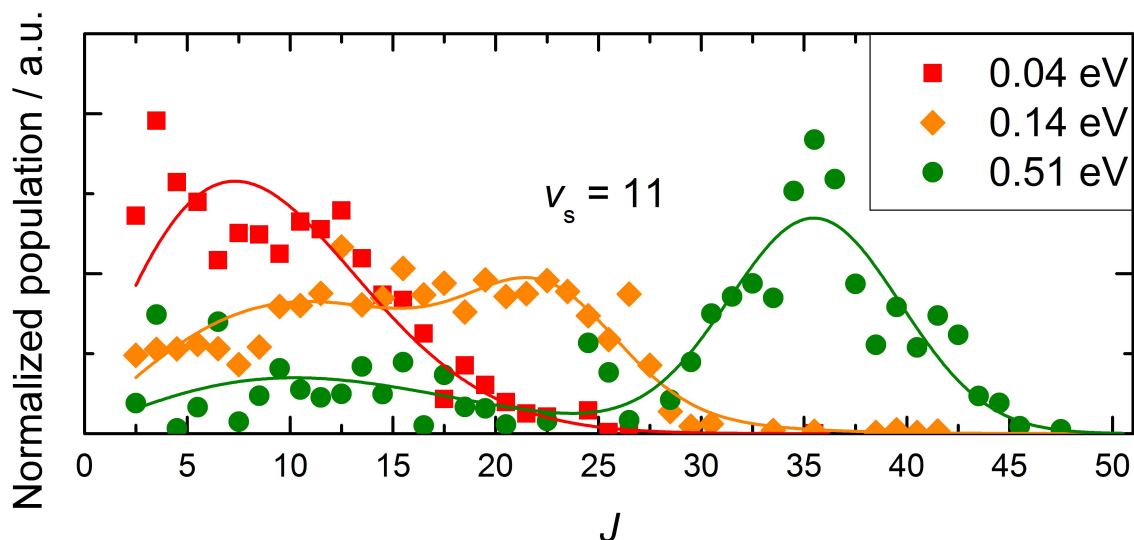


**Figure 6.4.:** Final rotational state distributions obtained from  $\text{NO}(v_i = 11, J_i = 0.5)/\text{Au}(111)$  surface scattering as a function of the incidence translational energy. The rotational state distributions for vibrationally elastic scattering are plotted at three different incidence translational energies given in the legend of the plot.

energy of scattered NO molecules as a function of the final vibrational state. Figure 6.5a) includes data for four different incidence translational energies whereas Figure 6.5b) shows the effect of orientation at an incidence translational energy of 0.51 eV. Figure 6.5a) shows that regardless of the vibrational energy loss during the collision rotational excitation is promoted by incidence translational energy. At high incidence translational energies the mean rotational energy tends to decrease with increasing vibrational energy loss. In contrast, at low incidence translational energy the vibrational energy loss does not have a large influence on the mean rotational energies. Figure 6.5b) shows that at an incidence translational energy of 0.51 eV O-atom down orientation leads to increased mean rotational energies. However, the effect diminishes for higher vibrational inelasticity.

### Discussion

As pointed out earlier, a preliminary analysis and discussion of the rotational state distribution accompanying vibrational multi-quantum relaxation in  $\text{NO}(v = 11)/\text{Au}(111)$  surface scattering has already been reported in reference [44]. The filtering model used for the interpretation of the limited dataset is found to agree with the larger dataset reported in this work. In the following the filtering model is explained. However, the emphasis of this section is on a conclusion on dynamical steering that becomes obvious from the results of

## 6. Scattering of highly vibrationally excited NO – results and discussion

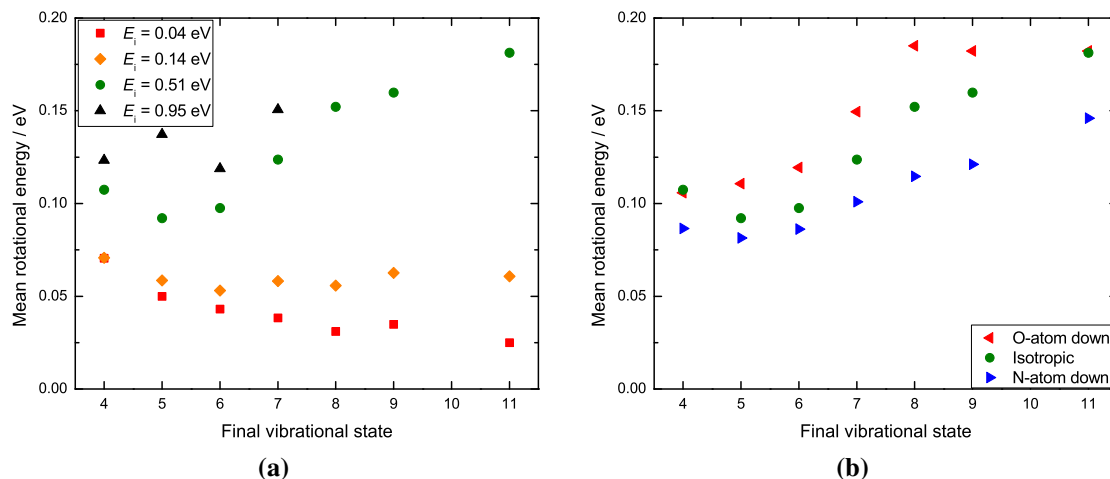


**Figure 6.5.:** Mean rotational energies as a function of the final vibrational state, incidence translational energy, and incidence orientation. Initially NO is prepared in  $v_i = 11, J_i = 0.5$ . The mean rotational energy is plotted against the final vibrational state. a) The rotational state distributions are probed at four different incidence translational energies indicated by the markers given in the legend of the figure. b) The rotational state distributions are probed at an incidence translational energy of 0.51 eV and three different incidence orientations indicated by the markers given in the legend of the figure.

the refined analysis.

Bimodal rotational state distributions are observed in the vibrational ground state NO/Ag(111) surface scattering.<sup>[68,75]</sup> The results have been interpreted in terms of a double rainbow picture.<sup>[78]</sup> Experimentally, it has been verified that the high- $J$  rainbow is caused almost exclusively by molecules initially oriented with the O-atom towards the surface whereas the low- $J$  rainbow is dominated by initial orientations of the molecules in which the N-atom points towards the surface.<sup>[76]</sup> See Section 2.5.2 for a detailed description. Recently, it was shown that this behavior is more general and can also be found in the scattering of vibrationally excited NO( $v_i = 3$ )/Au(111).<sup>[90,91]</sup> Also, for the NO( $v_i = 3$ )/Au(111) system it has been experimentally shown that the high- $J$  part of the rotational state distribution is caused by O-atom down orientation whereas the low- $J$  part is dominated by N-atom down orientation. Moreover, population in the high- $J$  part could only be observed for the vibrationally elastic scattering and not for molecules undergoing relaxation to  $v_s = 2$ . In addition, the probability for relaxation is found to be drastically increased when the incidence orientation distribution is changed from O-atom down to N-atom down. These observations have led to the conclusion that the vibrational relaxation event can act as a filter for the rotational state distribution. Since O-atom down

orientations do not lead to vibrational relaxation the rotational state distribution for vibrationally relaxed molecules reflects the absence of these orientations by the lack of the high- $J$  rainbow. Thus, the shape of the rotational state distribution allows conclusions on the orientation just before the collision process happens.

The double rainbow interpretation is also valid for the NO( $v_i = 11, J_i = 0.5$ ) system which is evident from two observations. First, the orientation experiment at 0.51 eV incidence translational energy clearly shows that the population in the high- $J$  part is significantly enhanced for O-atom down orientation. See Figure 6.3. Second, the position of the maximum at high- $J$  shifts to higher  $J$  when the incidence translational energy is increased which is a common finding in rotational rainbow scattering of NO at metal surfaces<sup>[112]</sup>. See Figure 6.4. Both observations verify that the maximum at high- $J$  in the rotational state distribution can be attributed to a rotational rainbow caused by O-atom down orientation.

Unlike in NO( $v_i = 3$ ) scattering where vibrational relaxation is only possible with N-atom down orientation, in NO( $v_i = 11$ ) scattering O-atom down orientation at the surface may lead to vibrational relaxation. This can be seen in the rotational state distributions in Figure 6.3 for  $v_s = 6-9$  where the high- $J$  rainbow can be clearly identified. Thus, for highly vibrationally excited NO/surface scattering the requirements concerning the orientation for relaxation are less strict than for NO( $v_i = 3$ ). As pointed out in reference [6] this trend can be explained by the more favorable energetics for electron transfer for highly vibrationally excited NO( $v_i = 11$ ) such that the orientation is less crucial to the relaxation process. Nevertheless, the energetically favorable N-atom down orientation does lead to more relaxation and a higher average loss of vibrational quanta. The filter effect of vibrational relaxation acting as a filter on the rotational state distributions explains why the high- $J$  rainbow associated with O-atom down orientations is found in the rotational state distribution belonging to the final vibrational states  $v_s = 6 - 11$  and partially why it diminishes with increasing vibrational energy loss. However, the observation that the effect of orientation vanishes with increasing vibrational energy loss cannot be explained by only considering the filter effect which becomes clear by a closer look at the rotational state distributions for  $v_s = 4 - 5$ . There is a high and constant population of low- $J$  states and no sign for a high- $J$  rotational rainbow regardless of the initial orientation distribution. This observation might be interpreted as a fingerprint of dynamical steering. The dynamical steering effect has been predicted by the IESH theory.<sup>[8]</sup> In the beginning of the collision the NO molecule is thought to be steered into its energetically favorable configuration such that efficient vibrational relaxation can take place. This means that the molecules

## 6. Scattering of highly vibrationally excited NO – results and discussion

undergoing dynamical steering hit the repulsive wall of the molecule-surface interaction with the N-atom pointing towards the surface regardless of their orientation prior to the collision. Thus, molecules undergoing dynamical steering will all be oriented such that they experience less rotational excitation, which is an agreement with the observed rotational state distributions.

### 6.1.2. Translational inelasticity accompanying multi-quantum vibrational relaxation at Au(111)

#### Results

The translational inelasticity accompanying multi-quantum vibrational relaxation of NO( $v_i = 11, J_i = 0.5$ ) at Au(111) is revealed using time-of-flight experiments as described in Section 4.1.3. The incidence angles used are  $5 - 8^\circ$  in all cases. The arrival time distribution of scattered molecules is probed at the maximum of the angular distribution. In all scattering channels narrow angular distributions are observed. A typical distribution is shown in Figure 6.6a). Within the experimental uncertainty all angular distributions peak at the specular angle. A typical outcome of a time-of-flight experiment is shown in Figure 6.6b). The arrival time distributions are narrow and strongly affected by the incidence translational energy. In some cases a well separated second maximum with low intensity could be observed in the arrival time distribution at very late arrival times ( $50 \mu\text{s}$ ). This effect can be attributed to an artifact which results from additional collisions with parts of the ion detector as discussed in Section 6.1.3. In that section, it is also shown that the results described below are not affected by the artifact because of the separation of the two peaks in the arrival time distribution.

The detection laser wavelength is adjusted such that a single quantum state defined by  $v, J,$  and  $\Omega$  can be probed. This is a difficult due to the congested nature of the spectra of scattered molecules (see Figure 6.1 for an example). Ideal probing wavelengths are obtained by searching the line list of the complete spectrum for nonoverlapping rovibronic transitions that are separated by at least  $1 \text{ cm}^{-1}$  from a neighboring transition. The line list can be obtained by an evaluation of Brown's Hamiltonian as described in Section 2.1. In addition, the rotational energy and vibrational energy of the probed state can be obtained. The following investigation on the effect of rotational excitation and vibrational relaxation on the translational inelasticity is limited to the  $X^2\Pi_{\Omega=1/2}$  state.

The average final translational energy  $\langle E_f \rangle$  is extracted from the calculation of the expectation value using the flux-velocity distribution in Equation 5.5 and the best fit parameters

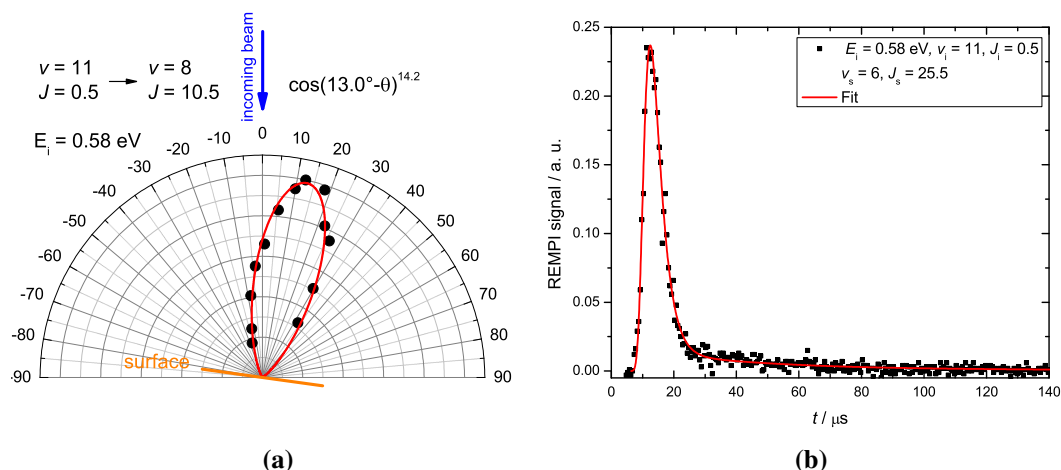


**Figure 6.6.:** Typical characteristics of  $\text{NO}(v_i = 11, J_i = 0.5)/\text{Au}(111)$  surface scattering. The incidence translational energy is 0.58 eV and the surface tilted at  $5 - 8^\circ$  from the incoming beam axis. a) Angular distribution for scattered molecules in  $v_s = 8, J_s = 10.5$ . The function  $\cos(\phi - \theta)^n$  is fitted to the distribution. The best fit is shown as a red line. b) Arrival time distribution recorded for scattered molecules in  $v_s = 6, J_s = 25.5$ . The red line shows the best fit using the fitting function given by Equation 5.7.

derived from a fit of the function in Equation 5.7 to the experimentally measured arrival time distribution. Figure 6.7 shows the correlation between final incidence translational energy of the scattered molecule and vibrational energy loss during the surface collision.  $\langle E_f \rangle$  is found to increase linearly with vibrational energy loss. The slope of this increase depends on the incidence translational energy of the molecules. The coupling between translational energy gain and vibrational energy loss increases with incidence translational energy.

Figure 6.8 shows the dependence of final translational energy on rotational excitation experienced during the collision for the two different scattering channels  $v_i = 11 \rightarrow v_s = 11$  and  $v_i = 11 \rightarrow v_s = 6$ . In general, it is found that there is a negative correlation between rotational excitation and final translational energy. The more the molecule is rotationally excited during the collision the less translational energy is retained after the collision. A linear dependence between the final translational and rotational energy is found. The slope depends on the incidence translational energy and varies between  $-0.3$  and  $-0.8$  in the investigated energy range. The slope at a given incidence translational energy is remarkably similar for the vibrationally elastic and inelastic scattering channels shown in panel (a) and (b), respectively.

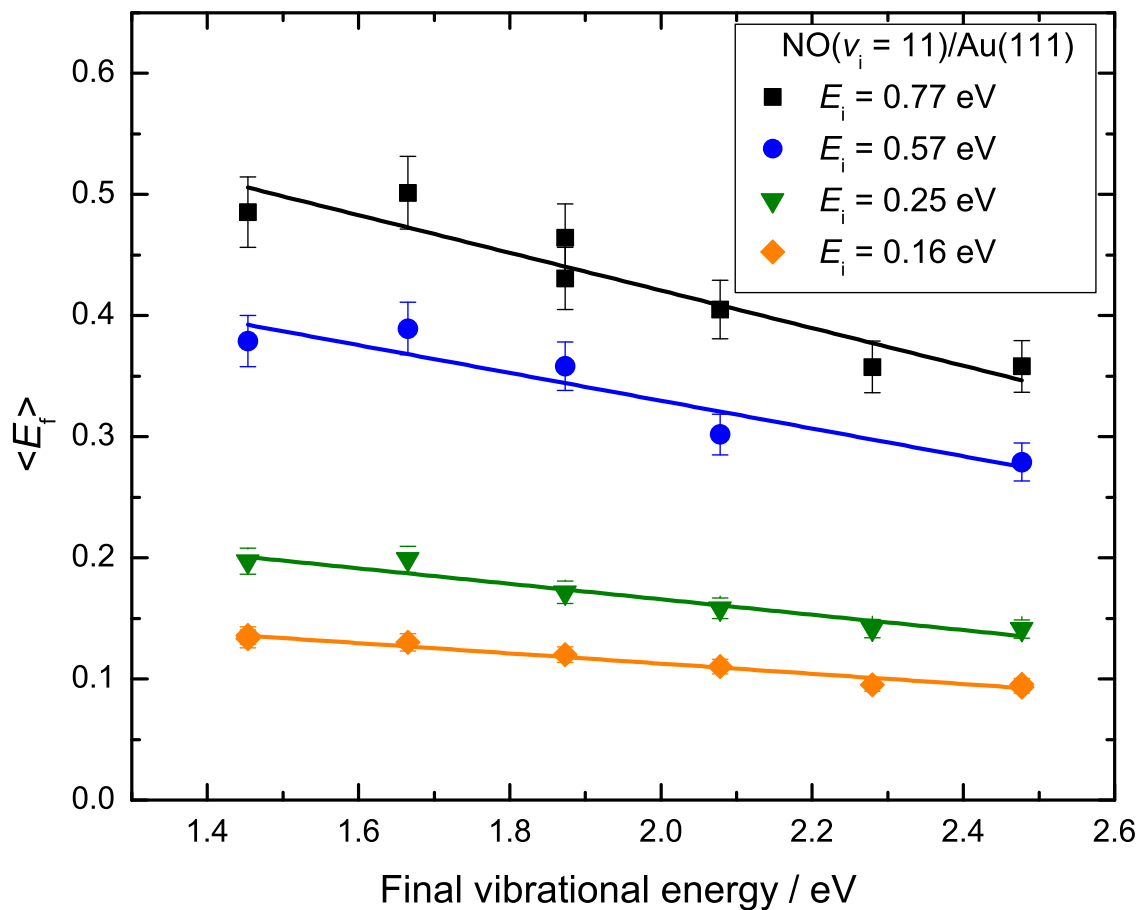


**Figure 6.7.:** Mean final translational energy  $\langle E_f \rangle$  as a function of the final vibrational energy in NO( $v_i = 11, J_i = 0.5$ )/Au(111) surface scattering. The scattered molecules are detected in rotational states ranging from  $J = 9.5$  to  $J = 15.5$ . Four different incidence translational energies are investigated as indicated in the plot legend. The solid lines represent the best linear fits to the data.

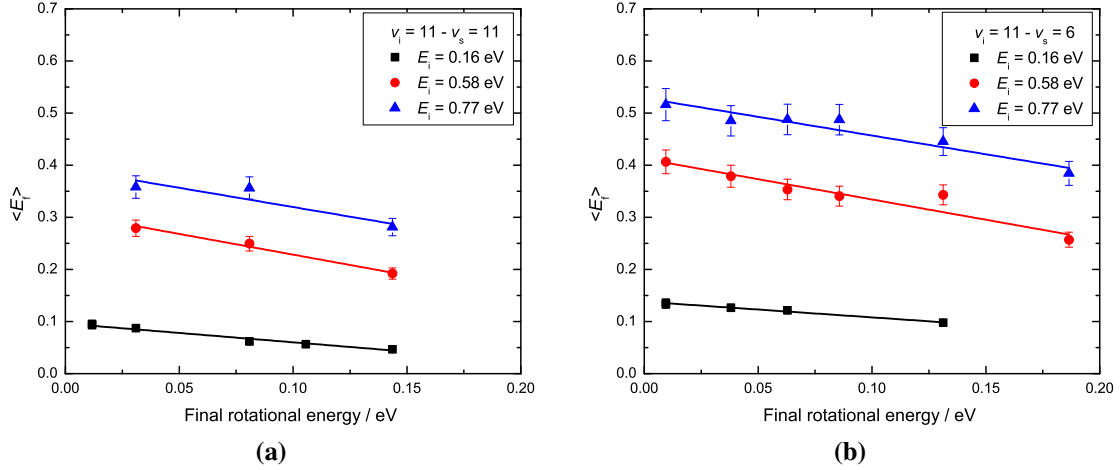


**Figure 6.8.:** Mean final translational energy  $\langle E_f \rangle$  as a function of the final rotational energy in NO( $\nu_i = 11, J_i = 0.5$ )/Au(111) surface scattering. Three different incidence translational energies are investigated as indicated in the plot legends. The solid lines represent the best linear fit to the data. The dependence of average final translational energy on final rotational energy is shown a) for the vibrationally elastic channel and b) for the loss of 5 vibrational quanta ( $\nu_i = 11 \rightarrow \nu_s = 6$ ).

## Discussion

Figure 6.8 displays the dependence of the translational inelasticity on rotational excitation for vibrationally elastic and inelastic scattering processes. Since the dependence is found to be linear, an extrapolation to zero rotational excitation allows the investigation of the translational inelasticity in the absence of rotational excitation. In Figure 6.9 the intercepts of the best linear fits to the experimental data  $E_f(E_{\text{rot}} = 0)$  are plotted as a function of the incidence translational energy. Regardless of the vibrational energy loss during the collision a linear dependence between final and incidence translational energy is found. This can be interpreted as a fingerprint of the underlying direct-scattering mechanism as discussed in Section 2.5.1. The Baule limit is plotted for comparison. The Baule limit considers the collision process as a purely impulsive central collision of two hard spheres without any attraction. The translational inelasticity is then determined by the mass ratio between the impinging molecule and the surface atom mass. For NO scattered at Au, the Baule limit is  $E_f = 0.54E_i$ . The observed behavior for the vibrationally elastic scattering channel is well described by the Baule limit. This puzzling agreement with the oversimplified model has also been observed in previous investigations on NO( $\nu = 3$ )/Au(111) scattering<sup>[101]</sup> and even earlier work on NO ground vibrational state/Ag(111) scattering<sup>[68]</sup>. As the Baule limit model does not include attraction between

## 6. Scattering of highly vibrationally excited NO – results and discussion

molecule and surface, the question arises, why there is absolutely no visible influence of the molecule-surface attraction on the translational inelasticity. The red dotted line in Figure 6.9 represents the prediction of a hard cube model that includes an acceleration of the molecule by the attractive interaction between molecule and surface and a subsequent collision with a hard wall. The attractive interaction has been estimated assuming that the desorption energy of 0.24 eV<sup>[113]</sup> determined by TPD equals the binding energy. The model underestimates the amount of translational energy retained in the molecule. A possible explanation might be that the effective molecule-surface attraction felt by molecules experiencing little rotational excitation is much less than the desorption energy that resembles the molecule-surface attraction in the most favorable molecular orientation. However, it is questionable whether this effect can account for the observed deviation.

For the further discussion of effects concerning the coupling between translational energy, rotational energy, and vibrational energy in multi-quantum vibrational relaxation, it is helpful to compare to the tremendous amount of available experimental data obtained for the scattering of NO( $v = 3$ )<sup>[17,89,101]</sup>. Figure 6.7 shows that the coupling between vibrational energy loss and final translational energy previously referred to as V-T coupling increases with the incidence translational energy of the molecule. The slopes of fitted lines in this plot  $\Delta\langle E_f \rangle / \Delta E_{\text{vib}}$  can be taken as a measure of the coupling between the two quantities. The slopes express how much of the vibrational energy lost in the process is converted to final translational energy of the molecule. Figure 6.10 shows the dependence of the coupling strength  $\Delta\langle E_f \rangle / \Delta E_{\text{vib}}$  on the incidence translational energy. For NO( $v_i = 11, J_i = 0.5$ ) the coupling strength increases linearly with incidence translational energy. As a comparison the coupling strengths obtained for NO( $v_i = 3$ ) scattering taken from reference [101] are given as well. In that study, only two scattering channels involving vibrational relaxation could be probed. Thus, the linear dependence between vibrational energy loss and incidence translational energy gain has not been reported before.<sup>[101]</sup> However, the  $\Delta\langle E_f \rangle / \Delta E_{\text{vib}}$  values have been reported for each channel separately. The agreement between the coupling strengths  $\Delta\langle E_f \rangle / \Delta E_{\text{vib}}$  for NO( $v_i = 3$ ) and NO( $v_i = 11$ ) scattering is remarkable. Furthermore, the plot suggests that the linear dependence between vibrational energy loss and translational energy gain is also present for NO( $v_i = 3$ ) scattering. In order to explain the V-T coupling effect, Golibrzuch *et al.*<sup>[89]</sup> considered three possible mechanisms: 1. Image charge acceleration of the transiently formed anion. 2. A “mixed” adiabatic/nonadiabatic behavior. 3. Vibration-translation coupling mediated by electron-hole pairs. Explanations 1. and 2. could be easily ruled out by examining the effect of incidence translational energy and surface temperature on



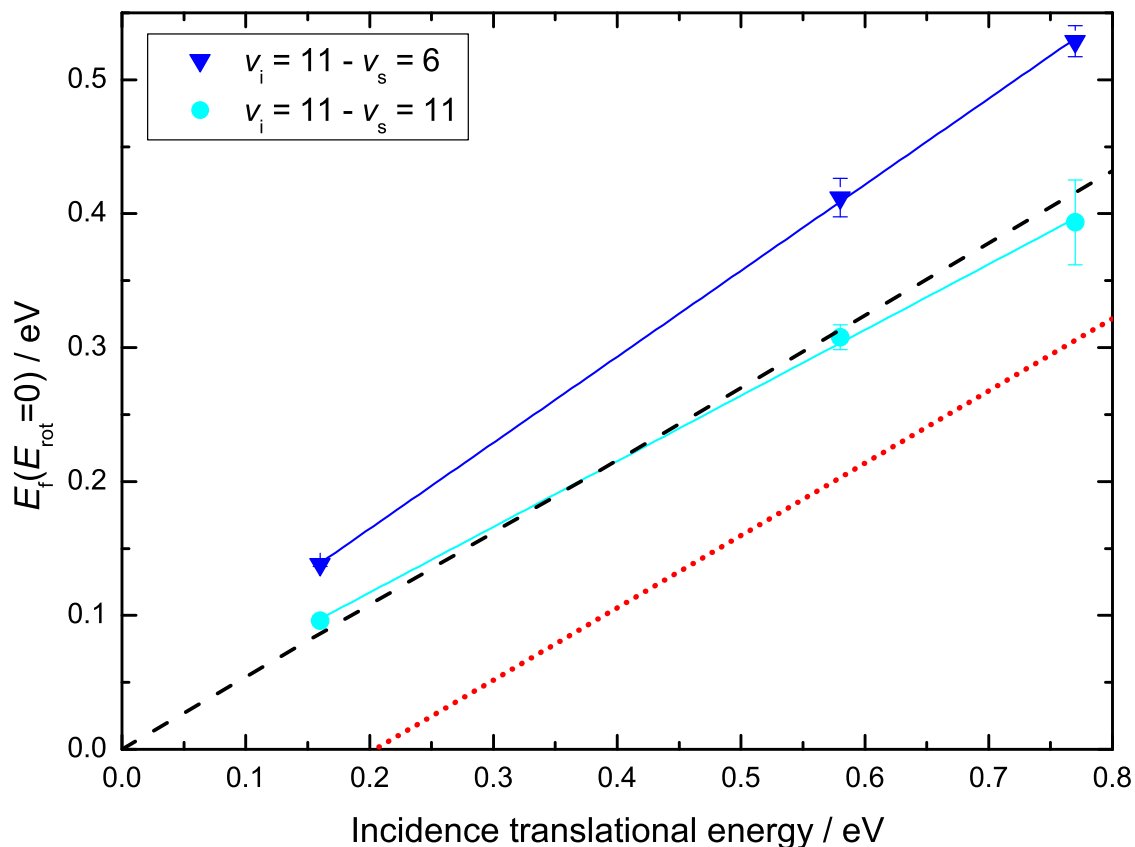


**Figure 6.9.:** Translational inelasticity for vibrationally elastic and inelastic scattering. The translational inelasticity of a molecule experiencing no rotational excitation  $E_f(E_{\text{rot}} = 0)$  is plotted against the incidence translational energy.  $E_f(E_{\text{rot}} = 0)$  is derived from the intercept at  $E_{\text{rot}} = 0$  in the plots shown in Figure 6.8. The vibrationally elastic scattering channel  $v_i = 11 \rightarrow v_s = 11$  is shown as light blue circles whereas the inelastic channel  $v_i = 11 \rightarrow v_s = 6$  is shown as blue triangles. The dashed black line represents the Baule limit. The red dotted line represents the prediction of the hard cube model with an attractive well of 0.24 eV corresponding to the desorption energy<sup>[113]</sup> measured by TPD.

## 6. Scattering of highly vibrationally excited NO – results and discussion

the coupling strength. Explanation 3. has been considered as likely where the incidence translational energy dependence of the V-T coupling has been explained by stronger non-adiabatic coupling in regions only accessible with higher incidence translational energy. Here, it is important to add that the nonadiabatic coupling relevant for energy transfer between electron-hole pairs and the final translational energy of the molecule depends on the velocity along the surface normal. This provides an additional explanation for the incidence translational energy dependence of the V-T coupling. Summarizing, the V-T coupling could proceed as follows. The vibrational energy lost in the collision is transferred to the excitation energy of electron-hole pairs. At a given incidence translational energy a constant fraction of the electronic excitation can be transferred to the translational energy of the molecule. This nonadiabatic energy transfer will depend on the incidence translational energy of the molecule.

In addition to the V-T coupling in NO( $v_i = 11, J_i = 0.5$ )/Au(111) surface scattering, a further coupling between translation energy loss in the collision and rotational excitation previously referred to as T-R coupling is found in an analysis of the quantum-state-resolved time-of-flight experiments. Figure 6.8 shows the observed dependence of the final translational energy on rotational excitation. The more rotational excitation is experienced by a molecule during the collision the less final translational energy is retained in the molecule. The T-R coupling strength can be described by the slope of the linear dependence found between final rotational and final translational energy of the molecule  $\Delta\langle E_f \rangle / \Delta E_{\text{rot}}$ . These slopes are plotted against the incidence translational energy for vibrationally elastic and inelastic scattering channels as shown in Figure 6.11. As a comparison, data for NO( $v_i = 3$ ) scattering<sup>[89]</sup> is also given in the same plot. For both NO( $v_i = 11$ ) and NO( $v_i = 3$ ) scattering it is observed that at incidence translational energies above 0.4 eV the slopes are between  $-0.5$  and  $-0.8$ . For low incidence translational energies the slopes increase. Following the explanations in reference [89] the meaning of these values can be best clarified by considering the limiting cases of  $\Delta\langle E_f \rangle / \Delta E_{\text{rot}} = -1$  and  $\Delta\langle E_f \rangle / \Delta E_{\text{rot}} = 0$ .  $\Delta\langle E_f \rangle / \Delta E_{\text{rot}} = -1$  means that the energy for rotational excitation is exclusively supplied by the translational energy of the molecule and thus the translational energy transfer to the surface is constant and independent of the rotational excitation experienced. In contrast,  $\Delta\langle E_f \rangle / \Delta E_{\text{rot}} = 0$  means that the energy for rotational excitation is supplied by surface degrees of freedom. The values found in the experiment between  $-1$  and  $0$  have been interpreted by the very likely assumption that the translational energy transfer to the surface as well as the rotational excitation experienced in the collision depend on the orientation of the molecule prior to the surface. Thus, the condition for  $\Delta\langle E_f \rangle / \Delta E_{\text{rot}} = -1$  —the

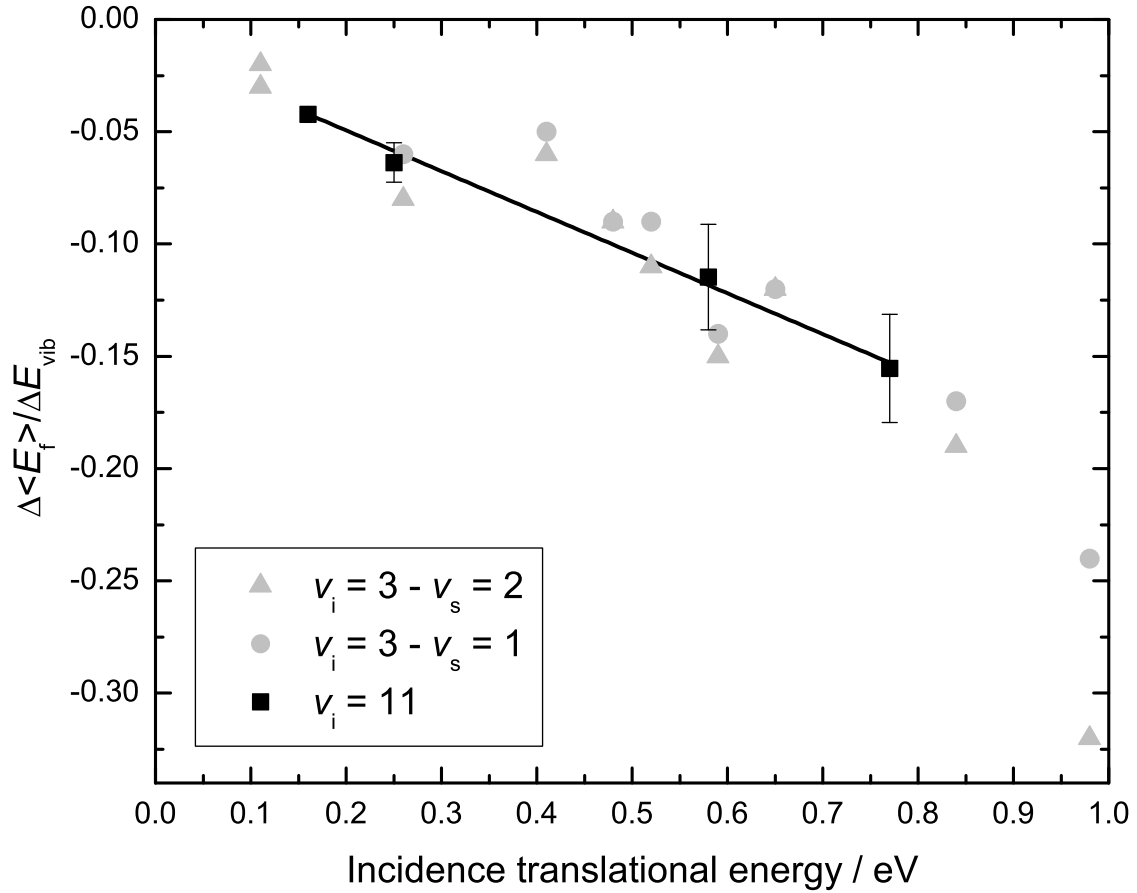


**Figure 6.10.:** Efficiency of translation to vibration coupling in  $\text{NO}(v_i = 11, J_i = 0.5)$  and  $\text{NO}(v_i = 3)/\text{Au}(111)$  surface scattering. The values  $\Delta\langle E_f \rangle / \Delta E_{\text{vib}}$  are derived from the slopes of the plots in Figure 6.7 and are given as black squares. The solid line represents the best linear fit to the data. The data for  $\text{NO}(v_i = 3)/\text{Au}(111)$  surface scattering is taken from reference [101]. A linear dependence between vibrational energy loss and incidence translational energy gain was not noted in reference [101]. However, the  $\Delta\langle E_f \rangle / \Delta E_{\text{vib}}$  values have been reported for each relaxation channel separately and are given as grey triangles and circles. The plot legend indicates the incidence vibrational state as  $v_i$  and the final vibrational state as  $v_s$ .

## 6. Scattering of highly vibrationally excited NO – results and discussion

translational energy transfer to the surface is independent of the rotational excitation—is not fulfilled. The slopes found in the experiment in the range of  $0 > \Delta\langle E_f \rangle / \Delta E_{\text{rot}} > -1$  can be interpreted as an anti-correlation between rotational excitation and phonon excitation. In Section 6.1.1 it has already been discussed that the rotational excitation experienced in the collision is determined by the initial orientation of the molecule. The anti-correlation between phonon and rotational excitation can be rationalized considering that orientations that lead to a high amount of phonon excitation cause little rotational excitation and vice versa.<sup>[114]</sup> In reference [89] a deviation in the T-R coupling between vibrationally elastic and inelastic scattering channels has been reported for incidence translational energies below 0.4 eV and even values for  $\Delta\langle E_f \rangle / \Delta E_{\text{rot}} > 0$  have been observed for vibrationally inelastic scattered molecules. This is also shown in Figure 6.10. As an explanation dynamical steering leading to a (re-)orientation at low incidence translational energies has been invoked. The data obtained for NO( $v_i = 11$ ) does not support this idea since the T-R coupling is remarkable similar for vibrationally elastic and inelastic channels at all incidence translational energies investigated. The rotational state distributions suggest that for the channel  $v_i = 11 \rightarrow v_s = 6$  dynamical steering is present even at incidence translational energies as high as 0.51 eV. However, even at small incidence translational energies  $\Delta\langle E_f \rangle / \Delta E_{\text{rot}}$  for the vibrationally inelastic channel is clearly  $< 0$  for  $v_i = 11 \rightarrow v_s = 6$ .

### 6.1.3. Artifact resulting from collisions with a detector part

When measuring arrival time distributions in NO/Au(111) surface scattering as described in Section 4.1.3, a second weak maximum at late arrival times is observed in some cases. This observation is shown in Figure 6.12a). The arrival time distribution is probed at three different positions differing by the distance to the position of the collision at the crystal surface as shown in Figure 6.12b). The real scattering signal shifts to later arrival times if the distance between surface and probe position is increased. This can be seen by a look at the falling edge of the first intense peak in the arrival time distribution. However, the second peak does behave differently: It shifts to earlier arrival times if the surface probe position distance is increased. Thus the molecules associated with this signal must travel from the detector part in the direction of the surface. This interpretation is supported by the observation that the intensity of the second peak decreases when the probe position is moved away from the detector part.

In order to reduce this artifact the detector has been placed as far as possible from the surface. However, in the detection geometry of the current setup the occurrence of this

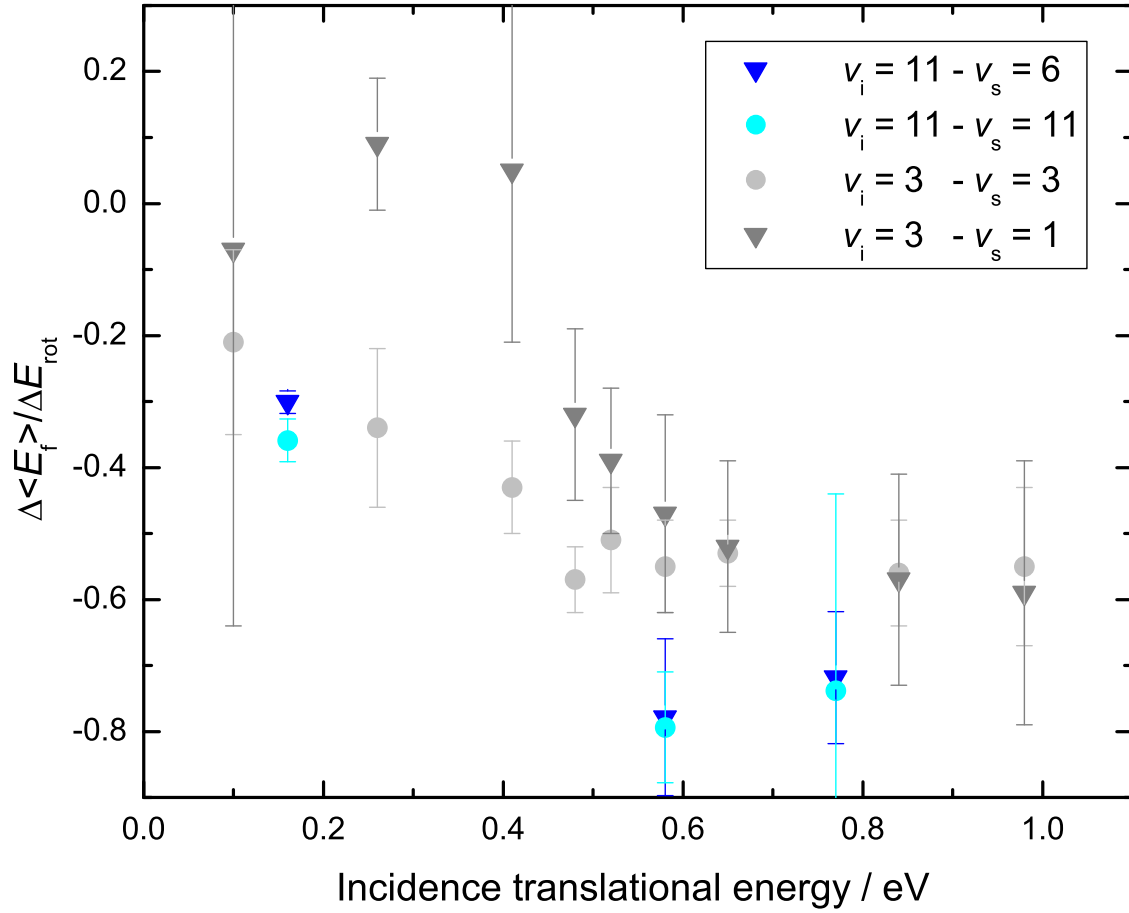


**Figure 6.11.:** Efficiency of translation to rotation coupling in  $\text{NO}(v_i = 11, J_i = 0.5)$  and  $\text{NO}(v_i = 3)/\text{Au}(111)$  surface scattering. The values  $\Delta\langle E_f \rangle / \Delta E_{\text{rot}}$  are derived from the slopes of the plots in Figure 6.8. The data for  $\text{NO}(v_i = 3)/\text{Au}(111)$  surface scattering is taken from reference [101].

## 6. Scattering of highly vibrationally excited NO – results and discussion

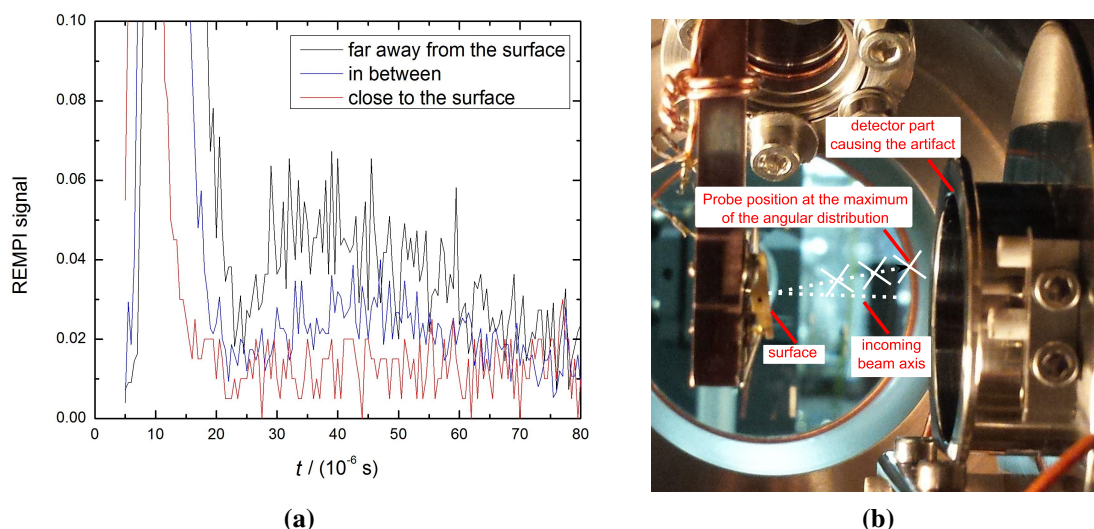


**Figure 6.12.:** Characterization of the artifact. a) The measured arrival time distribution for scattered  $\text{NO}(v_s = 6, J_s = 6.5)$  at three different probe positions along a line corresponding to the same scattering angle are shown as indicated in the plot legend. The first intense maximum attributed to the real scattering signal is cut in order to show the second maximum at 40-50  $\mu\text{s}$  more clearly which is attributed to an artifact produced by additional collisions of molecules at detector parts. b) A photo of the detection region is shown. The probe positions are indicated by the white crosses.

artifact cannot be excluded completely. Figure 6.12a) shows that the real direct-scattering signal and the artifact can be resolved with the setup. Thus, the occurrence of the artifact does not affect the analysis of the direct-scattering channel. However, it potentially limits the capability of the apparatus of detecting small amounts of scattering products with low final velocity.

### 6.1.4. Effect of the surface temperature on multi-quantum vibrational relaxation

The effect of the surface temperature on the translational inelasticity is only spot-checked. A relaxation process of NO at the Au(111) surface involving the loss of 3 vibrational quanta and moderate rotational excitation ( $v_i = 11, J_i = 0.5 \rightarrow v_s = 8, J_s = 10.5$ ) is investigated in the temperature range between 300 K and 700 K. The mean final translational energy is found to increase slightly with the surface temperature. See Figure 6.13. A linear fit to the observed behavior yields a slope of  $0.15 \pm 0.03$  meV/K. This value can be compared to earlier work on  $\text{NO}(v_i = 2)$  scattering.<sup>[17]</sup> For the relaxation event  $v_i = 2 \rightarrow v_s = 1$ , a slope of  $0.12 \pm 0.03$  meV/K has been reported. Thus, the temperature dependence

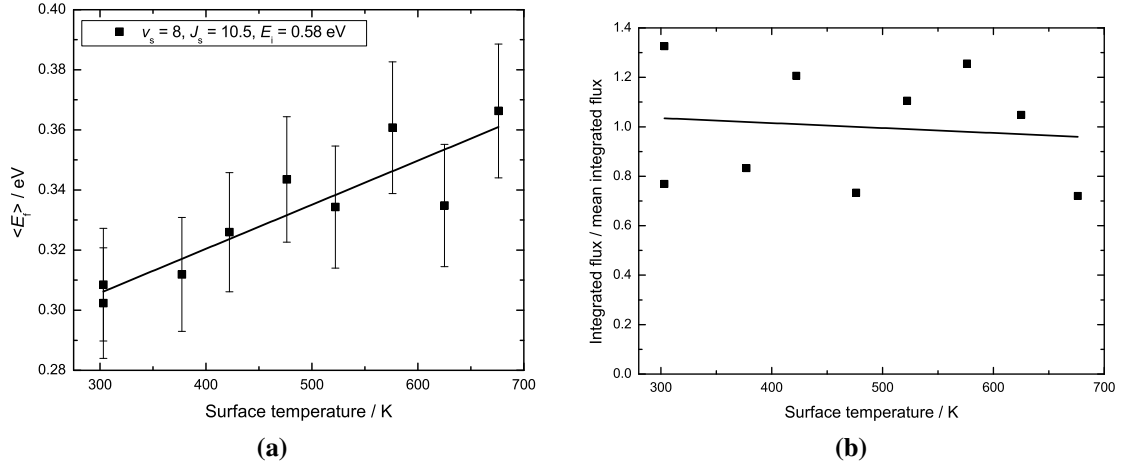


**Figure 6.13.:** Effect of surface temperature on multi-quantum vibrational relaxation. a) Effect of the surface temperature on the translational inelasticity in  $\text{NO}(\nu_i = 11, J_i = 0.5)/\text{Au}(111)$  surface scattering. The scattered NO is detected in  $\nu_s = 8, J_s = 10.5$ . b) Effect of surface temperature on the relaxation probability into  $\nu_s = 8, J_s = 10.5$ . The integrated flux for scattered  $\text{NO}(\nu_s = 8, J_s = 10.5)$  molecules normalized to the mean integrated flux measured for all investigated temperatures is plotted against the surface temperature. The solid line represents the best linear fit to the data.

for the inelasticity in the two relaxation channels is quite similar but clearly differs from the observation for the vibrationally elastic channel  $\nu_i = 2 \rightarrow \nu_s = 2$  where a slope of only 0.07 meV/K has been reported. Mechanical mechanisms and the influence of electron-hole pairs have been considered as possible causes of this effect but no complete explanation could be given.<sup>[17]</sup> The finding that the temperature dependence for the two channels  $\nu_i = 2 \rightarrow \nu_s = 1$  and  $\nu_i = 11 \rightarrow \nu_s = 8$  is quite similar makes it questionable if nonadiabatic effects can be the origin of the difference in temperature dependence between vibrationally elastic and inelastic collisions. In the multi-quantum relaxation process the molecule's trajectory should sample regions with stronger nonadiabatic couplings than in single quantum relaxation processes. However, an alternative explanation is still missing.

In addition, the integration of the arrival time distributions for the  $\nu_i = 11, J_i = 0.5 \rightarrow \nu_s = 8, J_s = 10.5$  relaxation process at different temperatures allows the calculation of the change of the probability for this process with surface temperatures. Figure 6.13b) shows the integrated flux in the investigated temperature range. The values are normalized by the mean flux for the scattering channel over the investigated temperature range. The linear fit to the data shows that within the experimental fluctuation there is no systematic change with the surface temperature. Admittedly, studying only one process out of the various proceeding scattering channels does not allow a general statement to be made. However,

in contrast to nonadiabatic vibrational excitation at metal surfaces<sup>[12,86]</sup> the studied multi-quantum vibrational relaxation process does not exhibit a strong temperature dependence. This observation is in agreement with theoretical predictions of Li *et al.*<sup>[87]</sup>

## 6.2. Scattering from Ag(111)

### 6.2.1. Multi-quantum vibrational relaxation at Ag(111): The vibrational state distribution

#### Results

In order to study the role of surface properties on multi-quantum vibrational relaxation of NO at metal surfaces the scattering experiments described in Section 4.1.2 and 4.1.3 are performed at a Ag(111) surface. The results can be directly compared to previous experiments on highly vibrationally excited NO/Au(111) surface scattering which can be found in reference [44] and in the Sections 6.1.1-6.1.4 of this work. The NO molecule is prepared in  $v_i = 11, J_i = 0.5$  and scattered from the (111) surface of the Ag crystal. The Ag crystal is kept at a temperature of 670 K. This ensures that the surface stays clean for several hours of operation of the molecular beam, which enables consistent relaxation probabilities from the clean surface to be obtained. Figure 6.14 shows a comparison between the 1+1 REMPI spectrum recorded for the NO molecules scattered from the Ag and the Au surface at the same incidence translational energy. The difference between the spectra is obvious. The vibrational bands that probe the ground-state vibrational levels  $v_s = 2$  and  $v_s = 3$  dominate the spectrum recorded at the Ag(111) surface, whereas the bands that probe  $v_s = 4$ - $v_s = 8$  dominate the spectrum recorded at the Au(111) surface. An analysis according to Section 5.1.1 of the spectra taken at the Ag(111) at two different incidence translational energies yields the final relative populations of the vibrational states. The results are given in Figure 6.15. Regardless of the incidence translational energy (0.14 eV or 0.51 eV), no vibrationally elastically scattered molecules are detected. The highest relative population is measured for  $v_s = 2$ . Note that the population in  $v_s = 1$  and  $v_s = 0$  cannot be probed because of “background” signal arising from vibrationally elastic and inelastic scattering of NO( $v_i = 0$ ) molecules at the surface. As a comparison a vibrational state distribution obtained from the scattering experiment with 0.51 eV incidence translational energy at Au(111) is also shown. The differences are obvious: First, the relaxation probability at the Ag(111) surface is unity whereas at Au(111) there is a small but clearly nonzero probability that NO( $v_i = 11$ ) survives the



collision in the incidence vibrational state. Second, the average vibrational energy loss is 1.1 eV at Au(111) whereas at Ag(111) it is probably larger than the lower bound 1.8 eV determined from the available data because population in the states  $\nu_s = 0$  and  $\nu_s = 1$  not observable in the experiment is likely.

## Discussion

The effects of the molecular degrees of freedom on multi-quantum vibrational relaxation are qualitatively well explained by considering the formation of the nitric oxide anion as a mediator for energy transfer from the molecular vibration to the excitation of electrons.<sup>[6]</sup> The mechanism leading to vibrational relaxation includes at least two electron transfer events as explained in Section 2.5.3. Vibrational energy can be lost because of nonadiabatic transitions allowing the molecule/surface system to stay on a certain diabatic potential energy curve which enables the mediator function of the anion as shown in Figure 2.12c). Thus, vibrational relaxation becomes more efficient with stronger nonadiabatic coupling. The nonadiabatic coupling is strong close to the crossing between neutral and anionic diabats. As a consequence, both the likelihood and the magnitude of vibrational relaxation scale with the ability of the molecule to reach the crossing seam. The potential energy surfaces for the NO/Au(111) and NO/Ag(111) systems are given in Figure 6.16. The NO/Au(111) potential is based on DFT calculations to which a model Hamiltonian has been fitted.<sup>[52]</sup> This model Hamiltonian contains a parameter representing the work function. In order to obtain an approximation for the potential energy surface for NO/Ag(111) this parameter has been changed to the value of the work function of Ag(111) reported in reference [56]. This approach is less crude than it seems since the electronic structure and the lattice constants<sup>[56]</sup> in the Au and Ag crystal (407.86 pm and 408.62 pm, respectively) are quite similar. A slice of these potentials at a NO bond length of 1.49 Å is shown in Figure 6.16a). This corresponds to the classical outer turning point of NO( $\nu = 11$ ) in the gas phase. The difference between anionic and neutral diabats at infinite molecule-surface distance is given by the workfunction  $\Phi$  and the vertical electron binding energy  $VEBE$ .  $VEBE$  is the difference between neutral and anionic potential at a given bond length in the gas phase. As shown in the figure, the lower work function of the Ag surface leads to a smaller separation between neutral and ionic curves far away from the surface. Thus, the crossing between the potentials occurs at longer molecule-surface distances. Figure 6.16 also shows the 2-dimensional potential energy surface of the adiabatic ground state as a function of the molecule-surface distance and the NO bond length for NO/Au(111) (b) and NO/Ag(111) (c). The crossing seam between the diabats is indicated by a red line. The

6. Scattering of highly vibrationally excited NO – results and discussion

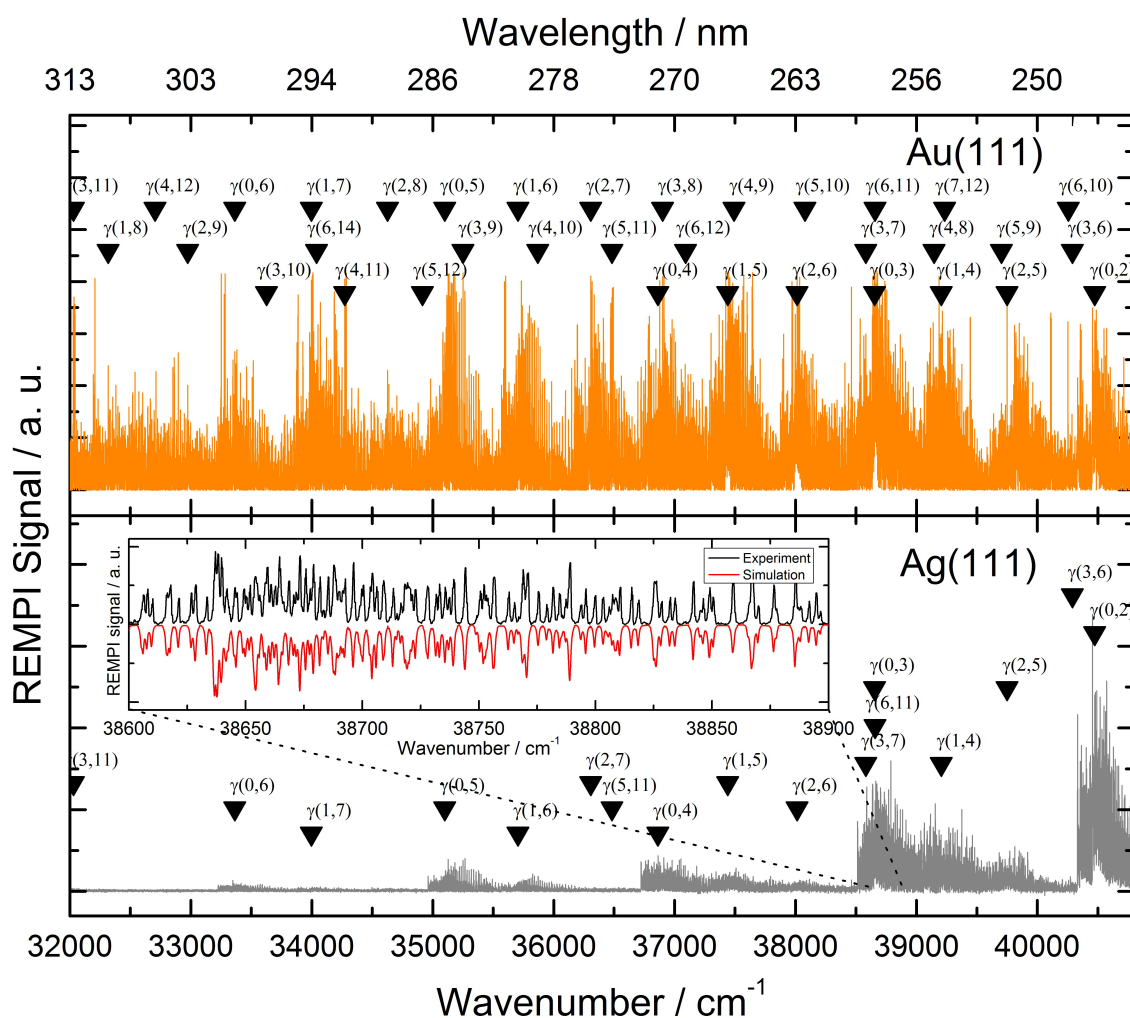


**Figure 6.14.:** 1+1 REMPI spectra recorded of scattered NO in  $\text{NO}(v_i = 11, J_i = 0.5)/\text{Au}(111)$  and  $\text{Ag}(111)$  surface scattering. The two main panels show the REMPI spectra. The black triangles indicate the positions of the band heads of the vibrational bands. For instance,  $\gamma(3,11)$  marks the position of the  $\text{A}^2\Sigma^+(v = 3) \leftarrow \text{X}^2\Pi_{\Omega}(v = 11)$  band. The inset shows a part of the experimental spectrum obtained at the  $\text{Ag}(111)$  surface in black and the simulation following the analysis described in Section 5.1.1 in red. The figure is taken with permission from reference [115]. Copyright (2016) American Chemical Society.

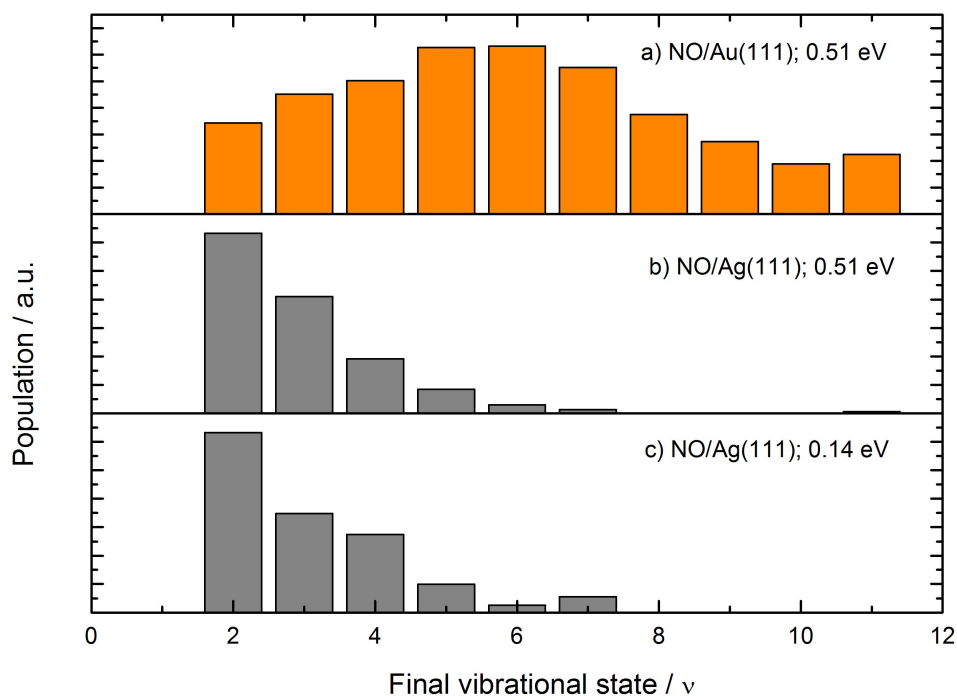


**Figure 6.15.:** Vibrational state distribution resulting from multi-quantum vibrational relaxation at Au(111) and Ag(111). The NO molecules are prepared in  $\nu_i = 11, J_i = 0.5$ . The relative population is plotted against the final vibrational state. The data for Au is taken from reference [6]. The incidence translational energy is given in each panel. The figure is taken with permission from reference [115]. Copyright (2016) American Chemical Society.

## 6. Scattering of highly vibrationally excited NO – results and discussion

contours show the energetically allowed area for the vibrational states 0-16. The contour for  $\text{NO}(v = 11)$  is highlighted in green. By a comparison of the two plots one can see that at the  $\text{Ag}(111)$  surface the crossing seam is accessible at larger molecule-surface distances. In a classical picture the vibrational motion at the crossing seam is characterized by a higher velocity at the  $\text{Ag}(111)$  than at the  $\text{Au}(111)$  surface because the crossing occurs in general at lower potential energy. Thus, because of the higher velocity nonadiabatic transitions giving rise to electronic excitation via transfer of vibrational energy are more likely which explains the more efficient vibrational relaxation at the  $\text{Ag}(111)$  surface. Summarizing, the work function dramatically changes the stability of the anion at the surface. A lower work function causes a stabilization of the anion which leads to more efficient vibrational relaxation.

This idea is supported by theoretical calculations employing the IESH program, which uses a potential energy surface derived from *ab initio* calculations for the  $\text{NO}/\text{Au}(111)$  system.<sup>[8]</sup> In the IESH program the parameter for the work function and the surface atom mass were changed to reproduce the properties of a  $\text{Ag}(111)$  surface. The outcome of the calculation is shown in Figure 6.17. For both surfaces far too little vibrational relaxation is predicted. Note that problems concerning the IESH potential energy surface have been reported.<sup>[16]</sup> Nevertheless, the theory qualitatively reproduces the increased efficiency of vibrational relaxation when the work function is increased.

In reference [115] it is also mentioned that the transition state to dissociation of NO might influence the vibrational inelasticity. The barrier to dissociation is calculated to be 3.1 eV at  $\text{Ag}(111)$  and 3.6 eV at  $\text{Au}(111)$ . The total energy of the molecule in  $v_i = 11$  at an incidence translational energy of 0.51 eV is 3.0 eV. In the experiment no reaction products could be detected on the surface. However, it is possible that trajectories probe the region close to the transition state which might enhance the vibrational inelasticity for two reasons. First, the stretched geometry of the molecule favors the formation of the anion and thus promotes vibrational relaxation via an anion mediated mechanism. Second, in the vicinity of the transition state vibrational energy might be lost adiabatically by coupling between vibrational and translational motion as experimentally found for  $\text{H}_2/\text{Cu}(111)$ .<sup>[116]</sup> However, it is questionable if the second effect can be significant because the authors in reference [116] mention that the coupling is only strong relatively close to the top of the barrier. For the  $\text{NO}(v_i = 11)/\text{Ag}(111)$  system, the vibrational relaxation efficiency for a translational energy of 0.14 eV and 0.51 eV is similar though in the first case the molecules' total energy is 2.6 eV which is 0.5 eV lower than the calculated barrier for dissociation.

Summarizing, it is questionable if the effect of the dissociative transition state can be

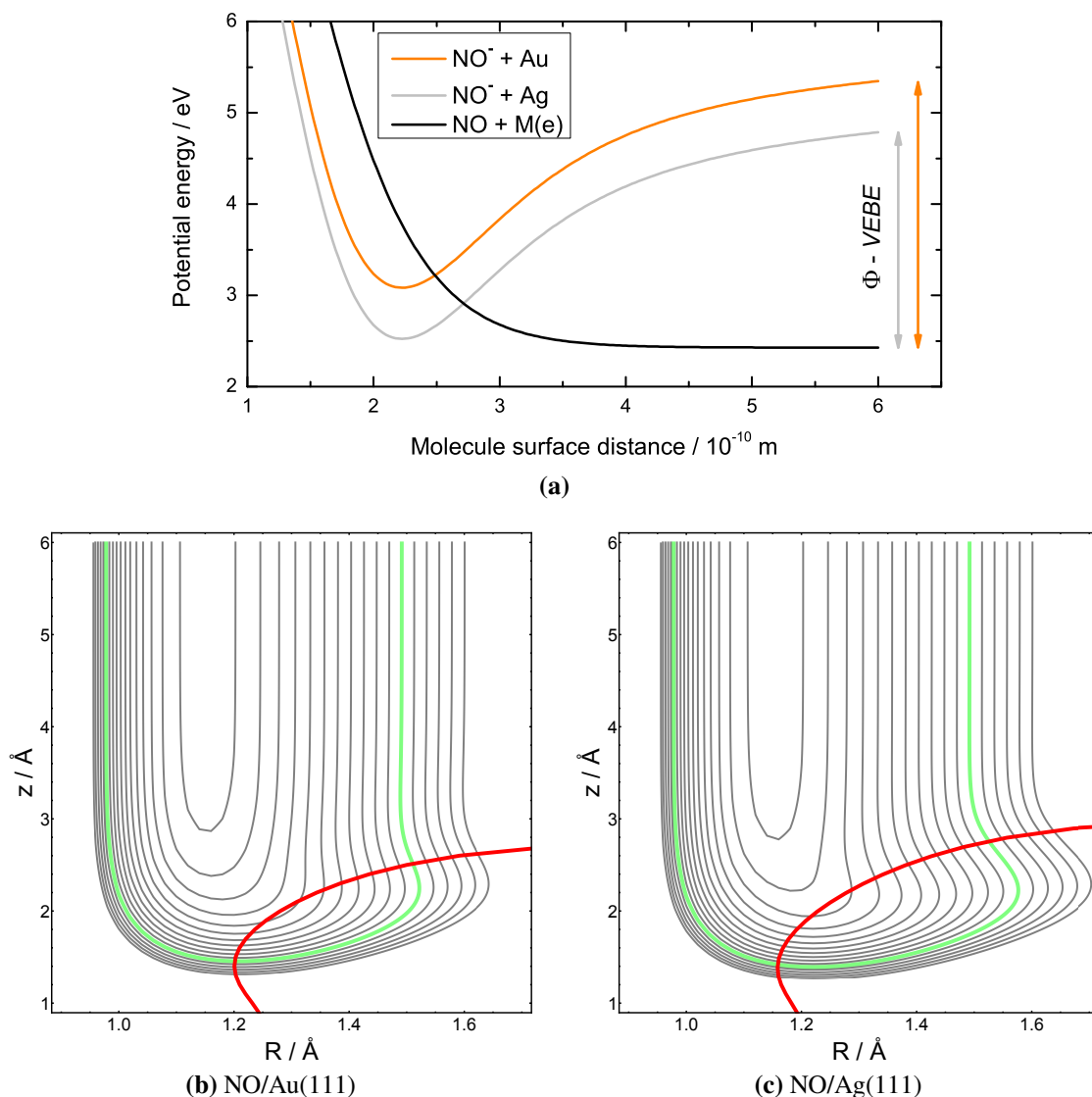


**Figure 6.16.:** Potential energy surfaces for the NO/Au(111) and NO/Ag(111) system in the two state picture. The potential energy surfaces are calculated according to reference [52]. The potential energy surfaces for the NO/Ag(111) system are obtained by changing the work function parameter to the value reported in reference [56]. The molecule is located over an hcp site of the surface. The orientation is chosen such that the N-atom points towards the surface. a) The diabatic potential energy curves are shown for the neutral species in black and the anionic species in gold and silver indicating the potential for the respective surface. The NO bond length is  $1.49 \text{ \AA}$ . The difference at infinitely large molecule-surface separation is given by the difference between the work function  $\Phi$  and the vertical electron binding energy  $\text{VEBE}$ . b) c) The adiabatic ground state potential energy surface is shown for the NO/Au(111) system (b) and the NO/Ag(111) system (c). The contours indicate the classically allowed region for NO in its vibrational states  $v_s = 0 - v_s = 16$ . The relevant contour for  $\text{NO}(v = 11)$  is highlighted in green. The red line displays the crossing seam between neutral and anionic diabatic potential energy surface. At large molecule-surface distances  $z$  and small NO bond lengths  $R$ , the adiabatic ground state has a neutral character. On the opposite side of the red line the adiabatic ground state mainly has ionic character.

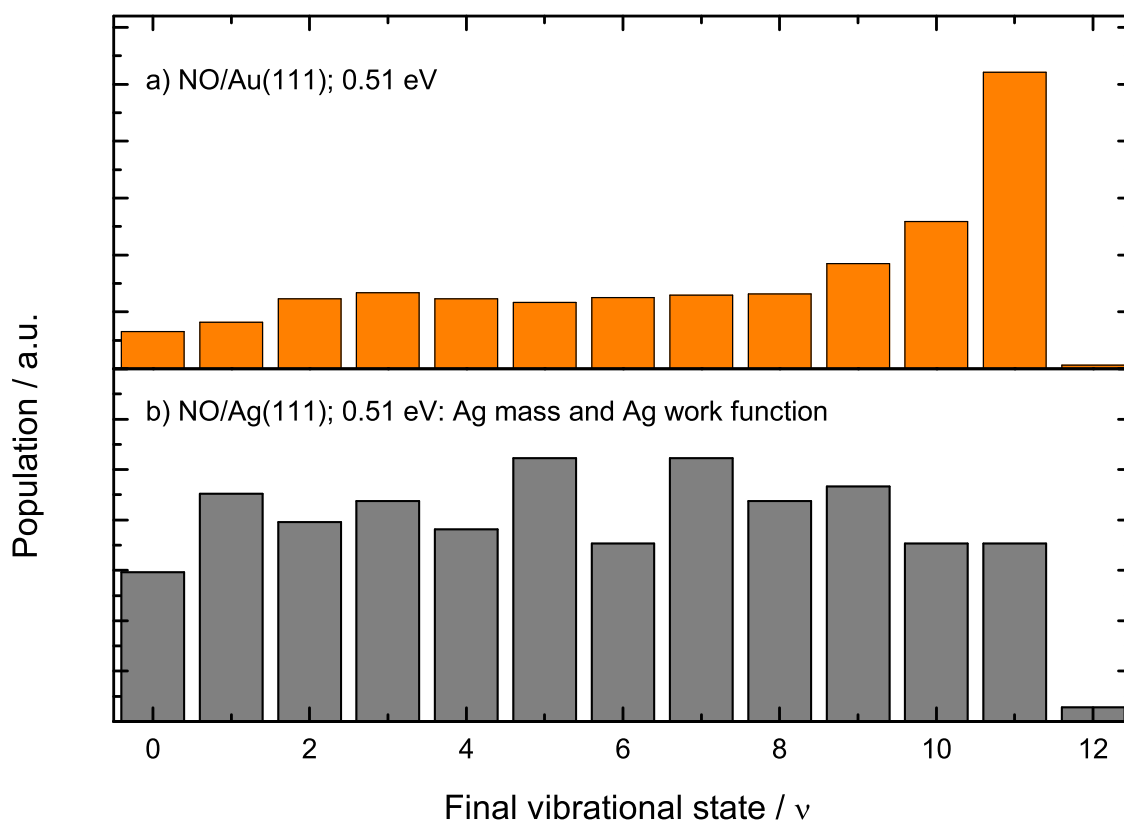


**Figure 6.17.:** The vibrational state distributions predicted by IESH theory. The incidence parameters are: translational energy 0.51 eV, vibrational energy corresponding to  $\nu = 11$ , and an isotropic initial orientation distribution. The vibrational energy distribution is collected into histogram bins centered at the vibrational eigenstate energies. The population is plotted against the final vibrational state. Upper panel: at Au(111), lower panel: at Ag(111).

separated from the effect of the work function since both effect stabilize the molecule at large NO bond length and lead to an increase of vibrational relaxation. For NO/metal surface systems a lower work function will stabilize the anion with respect to the neutral species. The anion favors a stretched bond geometry, thus the potential energy at large NO bond lengths is decreased which lowers the barrier to dissociation.

### 6.2.2. Multi-quantum vibrational relaxation at Ag(111): The rotational state distributions

The rotational state distributions are derived from an analysis (see Section 5.1.1) of 1+1 REMPI spectra. A typical spectrum is shown in Figure 6.14. Figure 6.18a) shows the rotational state distributions in the final vibrational states  $\nu_s = 2-5$  at two different incidence translational energies. Two trends can be identified. First, as the incidence translational energy is increased the maximum of the rotational state distributions in all scattering channels shifts to higher  $J$ . This indicates that rotational excitation in the collision is caused by the conversion of translational energy into rotational energy. This effect can be interpreted as a signature of direct-scattering. Furthermore, the population of high  $J$  states tends to increase with vibrational energy loss, regardless of the incidence translational energy. In general, the rotational state distributions can be described by a Boltzmann distribution. Representative data for the final vibrational state  $\nu_s = 3$  is shown in Figure 6.18b). The effective rotational temperatures are not related to the surface temperature. There are no observable rotational rainbow features at high  $J$  observable. A Boltzmann analysis of the distributions yields the mean rotational energies shown in Figure 6.18c). The mean rotational energies tend to increase with vibrational energy lost during the collision.

In contrast, rotational rainbows are observed in the vibrational ground state NO/Ag(111) surface scattering where the high- $J$  rainbow can be attributed to initial O-atom down orientations.<sup>[68,75,76,78]</sup> In the following it will be discussed why they are absent in the scattering of initially highly vibrationally excited NO/Ag(111) surface scattering.

A comparison of the rotational state distributions observed at Ag(111) with the distributions observed at Au(111) (see Section 6.1.1) reveals two major deviations. First, the rotational rainbows dominating the rotational state distribution for moderate vibrational relaxation in scattering from Au are completely absent in the distributions observed at Ag. Second, at Au(111) the mean rotational energy decreases (or remains approximately constant) with increasing vibrational energy loss, whereas at Ag(111) the mean rotational

6. Scattering of highly vibrationally excited NO – results and discussion

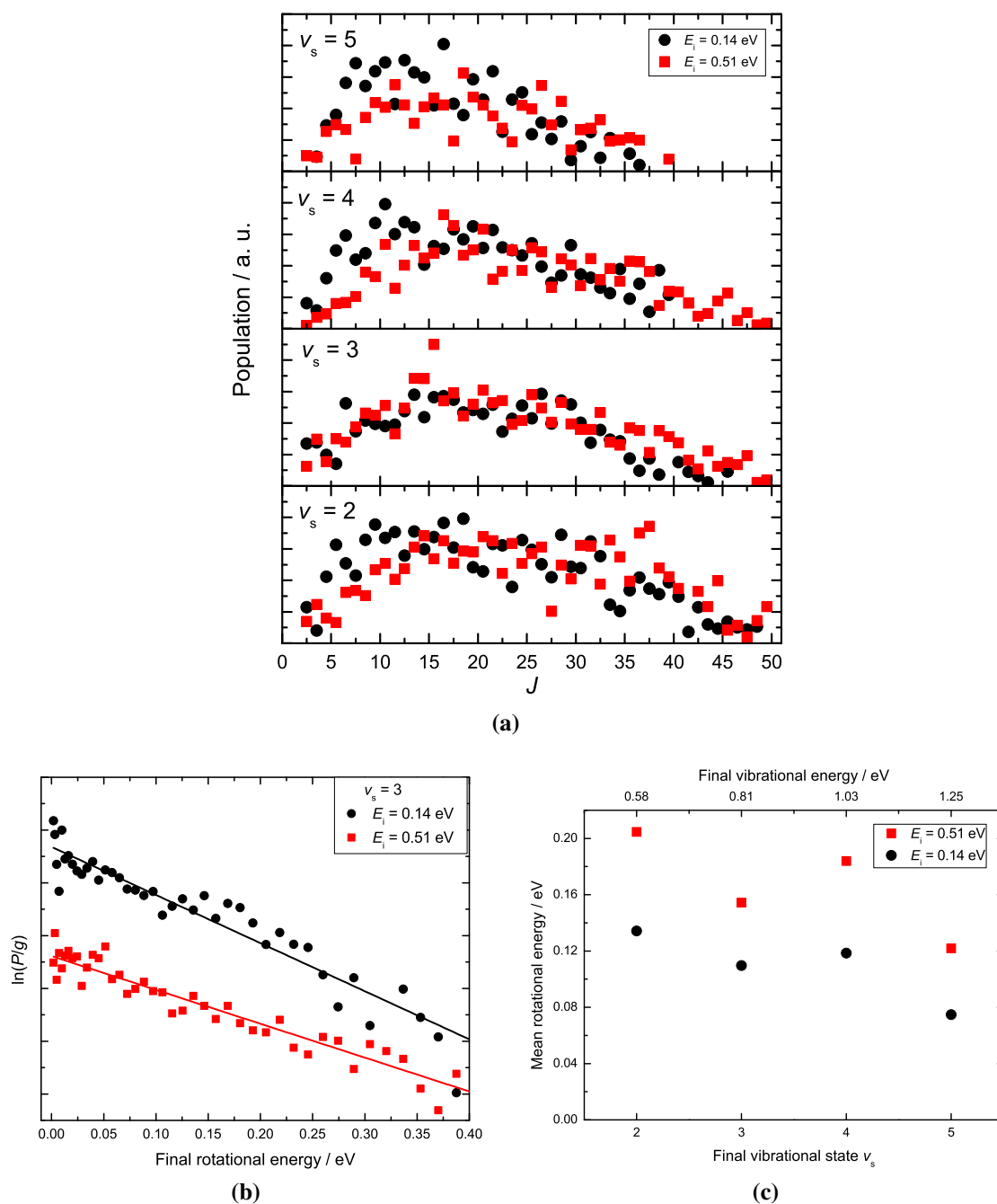


**Figure 6.18.:** Rotational state distributions in multi-quantum vibrational relaxation at Ag(111). NO is prepared in  $v_i = 11, J_i = 0.5$ . The experiment is performed at two different incidence translational energies as indicated in the plot legends. a) The panels show the final rotational state distributions in the final vibrational state  $v_s = 2 - 5$  with  $\Omega = \frac{1}{2}$ . b) Boltzmann plot for the rotational state distributions observed in the vibrational state  $v_s = 3$  at two different incidence translational energies.  $\ln(P/g)$  is plotted against the final rotational energy. Here  $P/g$  denotes the normalized population divided by the degeneracy of the respective rotational state. The best linear fits to the data are visualized by the solid lines. c) The mean rotational energies obtained from a Boltzmann-analysis of the rotational state distributions shown in a) are plotted against the final vibrational state.



energy increases with increasing vibrational energy loss. It is important to note that as a consequence of the more efficient vibrational energy loss, lower final vibrational states are predominantly populated at the Ag(111) surface than at the Au(111) surface. The rotational state distributions in the final vibrational states that could be analyzed on both surfaces ( $v_s = 4$  and  $v_s = 5$ ) are qualitatively similar. At an incidence translational energy of 0.51 eV the mean rotational energy in  $v_s = 5$  is 0.09 eV at Au(111) and 0.13 eV at Ag(111). For scattering from Au(111) at an incidence translational energy of 0.51 eV the high- $J$  rotational rainbow vanishes for increasing vibrational energy loss and is essentially absent for the final vibrational states  $v_s = 4$  and  $v_s = 5$ . The absence of the rotational rainbow for these scattering channels is interpreted to be a consequence of efficient dynamical steering that causes the molecule to be oriented with the N-atom towards the surface when it hits the repulsive part of the molecule-surface potential. As pointed out in reference [8] dynamical steering, strong nonadiabatic coupling, and efficient vibrational energy loss are strongly correlated. The complete absence of a high- $J$  rotational rainbow in the scattering of NO( $v_i = 11$ ) at Ag(111) suggests that the dynamical steering effect is always strong enough to achieve an orientation of the N-atom towards the surface which is consistent with the extremely large vibrational energy loss observed. It is unclear why the mean rotational energies increase as the vibrational energy loss increases from 1.2 eV ( $v_s = 5$ ) to 1.9 eV ( $v_s = 2$ ). A speculative explanation is that acceleration due to image charge attraction effectively increases the collision energy leading to higher rotational energies. This is supported by the potential energy surfaces shown in Figure 6.16b) and c). The region where the adiabatic ground state has dominantly anionic character is larger for Ag than for Au.

### 6.2.3. Multi-quantum vibrational relaxation at Ag(111):

#### Translational inelasticity

The translational inelasticity accompanying multi-quantum vibrational relaxation of NO( $v_i = 11$ ,  $J_i = 0.5$ ) at Ag(111) is revealed using time-of-flight experiments as described in Section 4.1.3. The incidence angles used are  $< 3^\circ$  in all cases. The arrival time distributions of scattered molecules are probed at the maximum of the angular distribution. In all scattering channels narrow angular distributions are observed. A typical distribution is shown in Figure 6.19a). Within the experimental uncertainty all angular distributions peak at the specular angle. A typical outcome of a time-of-flight experiment is shown in Figure 6.19a). As described in Section 6.1.2, NO can be detected in a single quantum

## 6. Scattering of highly vibrationally excited NO – results and discussion

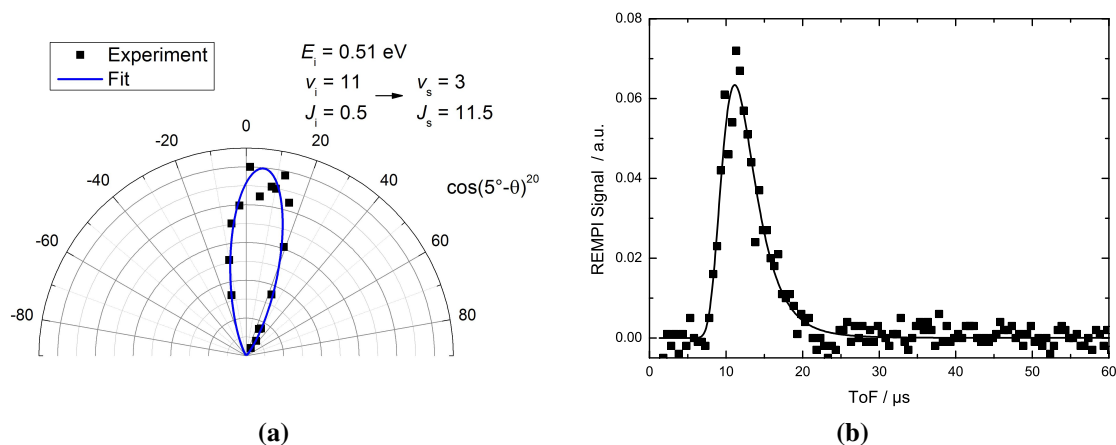


**Figure 6.19.:** Typical characteristics of NO( $v_i = 11, J_i = 0.5$ )/Ag(111) surface scattering. The incidence translational energy is 0.51 eV and the surface tilted at  $< 3^\circ$  from the incoming beam axis. a) Angular distribution for scattered molecules in  $v_s = 3, J_s = 11.5$ . The function  $\cos(\phi - \Theta)^n$  is fitted to the distribution. The best fit is shown as a blue line. b) Arrival time distribution recorded for scattered molecules in  $v_s = 3, J_s = 11.5$ . The black line shows the best fit using the fitting function given by Equation 5.7.

state characterized by  $v, J, \Omega$  and the average final translational energy can be obtained from the calculation of the expectation value analogously to Equation 5.9 after fitting the function in Equation 5.7 to the experimental measured arrival time distribution.

The correlation between final translational and vibrational energy is shown in Figure 6.20 for three different incidence translational energies. The final translational energies scale with the incidence translational energy, which is as a fingerprint of a direct-scattering mechanism. Furthermore, the mean final translational energy increases with vibrational energy loss experienced during the collision as shown in Figure 6.20a). The observation is qualitatively similar to the analogous scattering experiment at the Au(111) surface. See Section 6.1.2 for a detailed discussion of the origin of this V-T coupling. Assuming that the Baule model holds for a hypothetical vibrationally elastic scattering events at Ag(111) the V-T coupling strength given by  $\Delta\langle E_f \rangle / \Delta E_{\text{vib}}$  is  $-18 \pm 5\%$  at 0.51 eV incidence translational energy. At the same incidence translational energy at Au(111)  $-12 \pm 2\%$  is determined. Within the error of the experiment the V-T coupling strength does not differ significantly at Ag(111) and Au(111).

Figure 6.20 b) shows the translational inelasticity as a function of the rotational excitation experienced for an incidence translational energy of 0.51 eV and the final vibrational state  $v_s = 3$ . The mean translational energies decrease with rotational excitation experienced in the collision. A detailed discussion of the T-R anti-correlation can be found

### 6.3. Scattering of highly vibrationally excited NO( $v_i = 11$ ) from Ge(111)

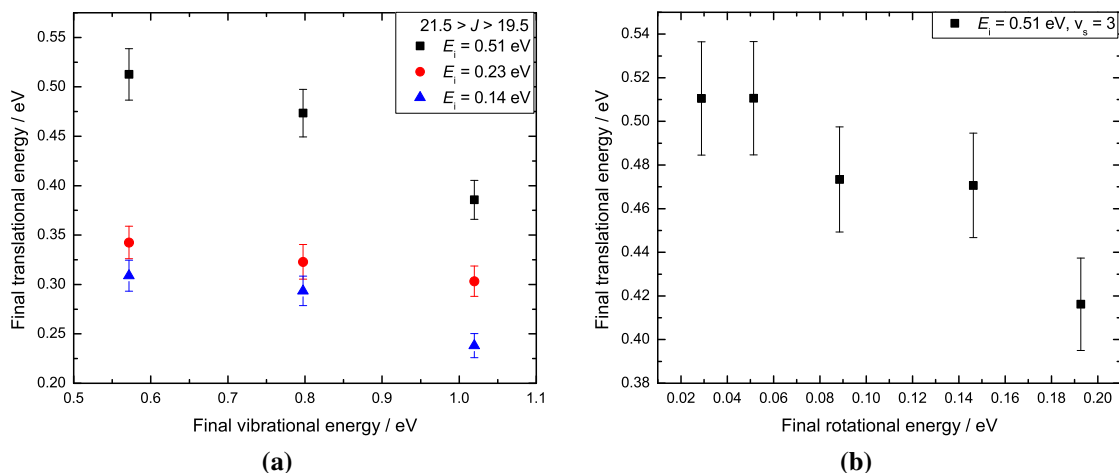


**Figure 6.20.:** Translational inelasticity in NO( $v_i = 11, J_i = 0.5$ )/Ag(111) surface scattering. a) The average final translational energy is plotted against the final vibrational energy. The scattered molecules are detected in rotational states ranging from  $J = 19.5$  to  $J = 21.5$ . Three different incidence translational energies are investigated as indicated in the plot legend. b) The average final translational energy is plotted against the final rotational energy. The scattered molecules are detected in the vibrational state  $v_s = 3$ . The incidence translational energy is 0.51 eV.

in Section 6.1.2. The observed slope  $\Delta\langle E_f \rangle / \Delta E_{\text{rot}} = -0.54 \pm 0.11$  derived from a linear interpolation to the data shown in Figure 6.20 b) is similar to the observations for NO( $v_i = 3$ )<sup>[89]</sup> and NO( $v_i = 11$ )/Au(111) surface scattering (see Figure 6.7).

In summary, the coupling between the molecular degrees of freedom, namely the V-T coupling and the T-R anti correlation, in the collision of NO( $v_i = 11$ ) at Au(111) and Ag(111) do not differ significantly. However, it is worth noting that the average vibrational energy loss is much larger on the Ag surface than on the Au surface such that the most probable observed scattering channel at Ag(111) involves the loss of 9 vibrational quanta. Due to V-T coupling these molecules scattered back in  $v_s = 2$  are effectively accelerated during the collision such that molecules experiencing little rotational excitation have a higher final translational energy than prior to the collision.

### 6.3. Scattering of highly vibrationally excited NO( $v_i = 11$ ) from Ge(111)

The scattering experiments of NO( $v_i = 11, J_i = 0.5$ ) at Ge(111) were often complicated by failure of the laser systems. The amount of reliable data obtained for this system is little

## 6. Scattering of highly vibrationally excited NO – results and discussion

but it is presented in this section with the intention to serve as a starting point for possible future investigations of this system. In the following, a few requirements are listed for performing scattering experiments on a clean germanium surface. The surface needs to be kept above 400 °C. Otherwise residual NO<sub>2</sub> as an impurity in the NO gas leads to oxidation of germanium as reported in reference [117]. At the elevated surface temperature GeO constantly evaporates which ensures a clean surface. H<sub>2</sub> cannot be used as a seeding gas. If NO is co-expanded with this gas the scattered flux in a specific quantum state in NO( $v_i = 11, J_i = 0.5$ ) surface scattering changes over time. The flux for the vibrationally elastic scattered molecules increases with exposure to such a molecular beam until it gets saturated. This behavior is absent for a beam of NO in He which indicates that exposure to H<sub>2</sub> changes the surface properties. It is likely that H/Ge(111) is formed. An efficient way of producing it is to generate H-atoms via a hot filament in the vicinity of the bare Ge surface.<sup>[118]</sup> In our experiment, the germanium crystal has been heated resistively via tungsten wires. When the filament is exposed to the molecular beam containing H<sub>2</sub>, it very likely serves as a H-atom source may lead to hydrogenation of the germanium surface. Thus the following experiments were performed with expansion mixtures of NO and He.

### The rotational and vibrational state distributions

The 1+1 REMPI spectrum with dump laser on shown in Figure 6.21 is obtained for scattering of NO( $v_i = 11, J_i = 0.5$ ) from Ge(111) at an incidence translational energy of 0.4 eV. It is recorded as described in Section 4.1.2. An analysis according to Section 5.1.1 allows the relative population of the final vibrational states to be derived. Due to difficulties with the laser systems the spectrum could only be obtained between 31700 cm<sup>-1</sup> and 35400 cm<sup>-1</sup>, which is sufficient to derive the relative population in the vibrational states  $v_s = 5$ - $v_s = 11$ . The spectrum is dominated by vibrational bands associated with population of  $v_s = 11$ . An exception is the region around 33300 cm<sup>-1</sup>. Here, the  $\gamma(0, 6)$  band is intense. However, this is also true for this band in the background spectrum recorded for the dump laser blocked whereas for all other bands the observed background level is much lower. Thus, by correcting for the background the relative population in  $v_s = 6$  is determined to be much lower than in  $v_s = 11$ . This large amount of background can be very likely attributed to a failure of the laser system used for the sweep step in the laser preparation method described in Section 4.1.1. An analysis of the  $\gamma(3, 11)$  band yields the rotational state distribution in  $v_s = 11$  shown in Figure 6.22a). The distribution is well characterized by a Boltzmann distribution with an effective rotational temperature of 960 K. Note that this is significantly higher than the surface temperature (637 K), which

### 6.3. Scattering of highly vibrationally excited $\text{NO}(v_i = 11)$ from $\text{Ge}(111)$

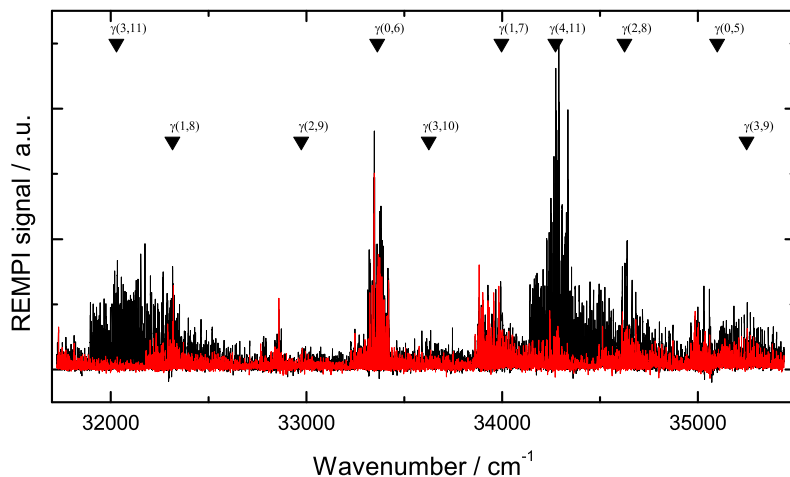


**Figure 6.21.:** 1+1 REMPI spectrum of scattered  $\text{NO}(v_i = 11, J_i = 0.5)$  at  $\text{Ge}(111)$ . The incidence translational energy is 0.4 eV. The black line shows the spectrum with dump laser unblocked and the red line shows the spectrum with dump laser blocked. The black triangles indicate the positions of the vibrational band heads of the vibrational bands. For instance,  $\gamma(3, 11)$  marks the position of the  $\text{A}^2\Sigma^+(v = 3) \leftarrow \text{X}^2\Pi_\Omega(v = 11)$  band.

means that a clearly non-thermal distribution is observed. The determination of rotational state distributions for other vibrational states is not reliable because the intensities of the corresponding bands in the spectrum are low and in some cases the bands overlap with the strong bands originating from  $v_s = 11$ . Thus, in the analysis of the complete spectrum it was assumed that the rotational state distribution does not change with the final vibrational state. This yields the relative populations of vibrational states shown in Figure 6.22b). Vibrationally elastic scattering dominates the scattering process. The population of vibrational states associated with vibrational energy loss is in general small but nonzero. The branching ratio between vibrational relaxation events to the final vibrational states 5-10 and the vibrationally elastic scattering channel is much smaller at the germanium surface than at the metal surfaces. Under the assumption that the states  $v_s = 0-5$  are not populated in the collision at the semiconductor the relaxation probability is much lower at the semiconductor than at the metal surfaces (see Section 6.2.1). The Debye frequency for Ge is  $260 \text{ cm}^{-1}$  [56] which is higher than for the two metals. Nevertheless, there is a large difference to the fundamental frequency of NO which is  $1876 \text{ cm}^{-1}$ . Based on this comparison phonon mediated vibrational relaxation is very unlikely at least for scattering channels involving the loss of more than one vibrational quanta. At the metal surfaces vibrational relaxation via coupling to electrons is considered to be the dominant mechanism. See Section 2.5.3 and 6.2.1. In this mechanism the transiently formed nitric oxide anion serves as a mediator for transfer of vibrational energy to electronic excitation.

## 6. Scattering of highly vibrationally excited NO – results and discussion

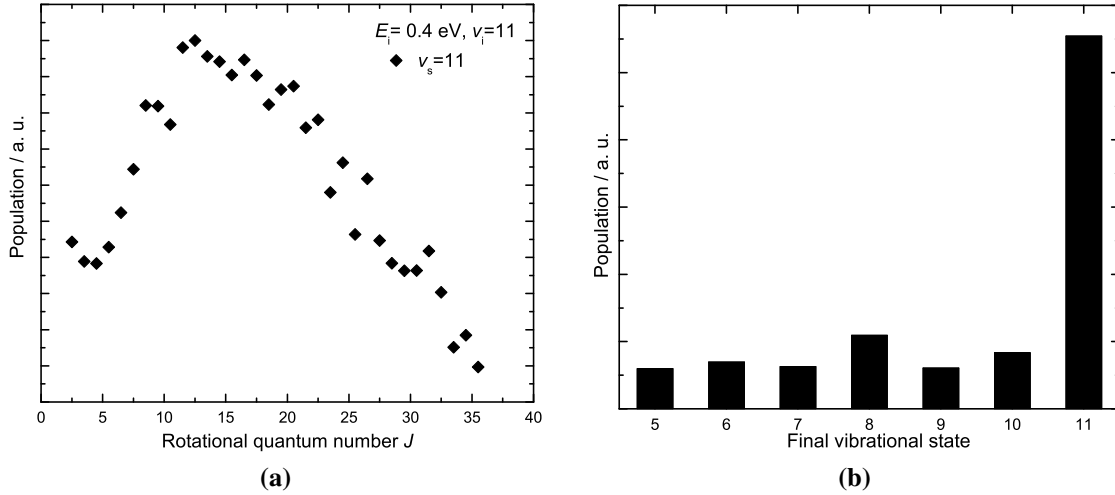


**Figure 6.22.:** Rotational (a) and vibrational (b) state distributions in NO( $v_i = 11$ ,  $J_i = 0.5$ )/Ge(111) surface scattering. The incidence translational energy is 0.4 eV. a) The rotational state distribution is shown for the vibrationally elastic scattering channel.

In the following, the influence of the electronic properties of the germanium surface on the efficiency of vibrational relaxation is discussed. Central to the relaxation process via coupling to electrons is the stabilization of the nitric oxide anion at the surface with respect to the neutral species. In general, the anion is destabilized by an increase of the work function and stabilized by image charge stabilization. The work function of Ge(111) is 4.8 eV<sup>[57]</sup>, which is close to the value for the Ag(111) surface, 4.74 eV<sup>[56]</sup>, and lower than the work function of Au(111), 5.33 eV<sup>[56]</sup>. The direct band gap of germanium at the crystal temperature (673 K) used in the scattering experiment is 0.6 eV.<sup>[59]</sup> In the intrinsic semiconductor the Fermi energy is located in the middle of the gap, which means that the electronic states in the valence band are located  $\approx 0.3$  eV below the Fermi energy. According to calculations on the charge carrier concentration following the remarks in reference [119] the population of the conduction band is many orders of magnitude ( $\approx 10^6$  at 673 K) smaller than in a metal. This makes it questionable if the electrons in the conduction band can significantly contribute to vibrational relaxation. In addition, the image charge stabilization must be estimated. The potential energy of a charged particle with the charge  $e$  at a distance  $z$  from a dielectric surface can be described by Equation 6.1.<sup>[120]</sup>

$$V_{\text{Im}} = \left( \frac{1}{4\pi\epsilon_0} \right) \left( \frac{\epsilon_r - 1}{\epsilon_r + 1} \right) \left( \frac{e^2}{4z} \right) \quad (6.1)$$

### 6.3. Scattering of highly vibrationally excited $\text{NO}(v_i = 11)$ from $\text{Ge}(111)$

In this equation  $\epsilon_r$  is the dielectric constant for a specific material. For metals,  $\epsilon_r = \infty$  and the expression for the image charge stabilization simplifies to  $e^2/16\pi\epsilon_0z$ . For the semiconducting germanium the dielectric constant is  $\epsilon_r = 15.8$ .<sup>[56]</sup> This means that the image charge stabilization at a germanium surface is only  $(15.8 - 1)/(15.8 + 1) = 88\%$  of the image charge stabilization at a metal surface. Assuming that the NO molecule can approach the Ge surfaces as close as the Au surface the maximal achievable stabilization of the anion is  $\approx 0.3$  eV less than at Au(111). Summarizing, the energetic conditions are quite similar for germanium and gold. The work function for Ge(111) is by 0.5 eV smaller than for Au(111) but the valence band of Ge lies  $\approx 0.3$  eV below the Fermi level and the image charge stabilization is  $\approx 0.3$  eV less at the semiconductor. However, the main difference is that there are no available empty bulk electronic states in the band gap of germanium. Thus, an electron in the valence band can only be excited by a higher energy than the band gap energy of 0.6 eV. These considerations have led to speculation about whether vibrational relaxation channels in  $\text{NO}(v_i = 11, J_i = 0.5)/\text{Ge}(111)$  surface scattering involving the loss of less than three quanta corresponding to  $< 0.6$  eV vibrational energy loss are suppressed but relaxation events with a higher vibrational energy loss than the band gap are possible. This would also contribute to the discussion of whether the vibrational energy lost in the nonadiabatic mechanism is transferred to a single electron or rather transferred to excitation of multiple electrons. However, in the experiment it is unclear whether the small population in the vibrational states  $v = 9$  and  $v = 10$  are attributable to an adiabatic or a nonadiabatic mechanism because empty electronic states in the band gap do exist at the surface.<sup>[61]</sup> This is why based on the observed vibrational state distribution the speculative idea mentioned above cannot be verified.

#### **Translational inelasticity**

The translational inelasticity accompanying multi-quantum vibrational relaxation of  $\text{NO}(v_i = 11, J_i = 0.5)$  at  $\text{Ge}(111)$  is revealed using time-of-flight experiments as described in Section 4.1.3. The incidence angles used are  $< 3^\circ$  in all cases. The arrival time distribution of scattered molecules is probed at the maximum of the angular distribution. As described in Section 6.1.2 NO can be detected in a single quantum state characterized by  $v, J$ , and  $\Omega$  and the average final translational energy can be obtained from the calculation of the expectation value analogously to Equation 5.9 after fitting the function in Equation 5.7 to the experimental measured arrival time distribution.

Figure 6.23a) shows the mean final translational energy of vibrationally elastic scattered  $\text{NO}(v_i = 11)$  as a function of the rotational excitation experienced at an incidence

## 6. Scattering of highly vibrationally excited NO – results and discussion

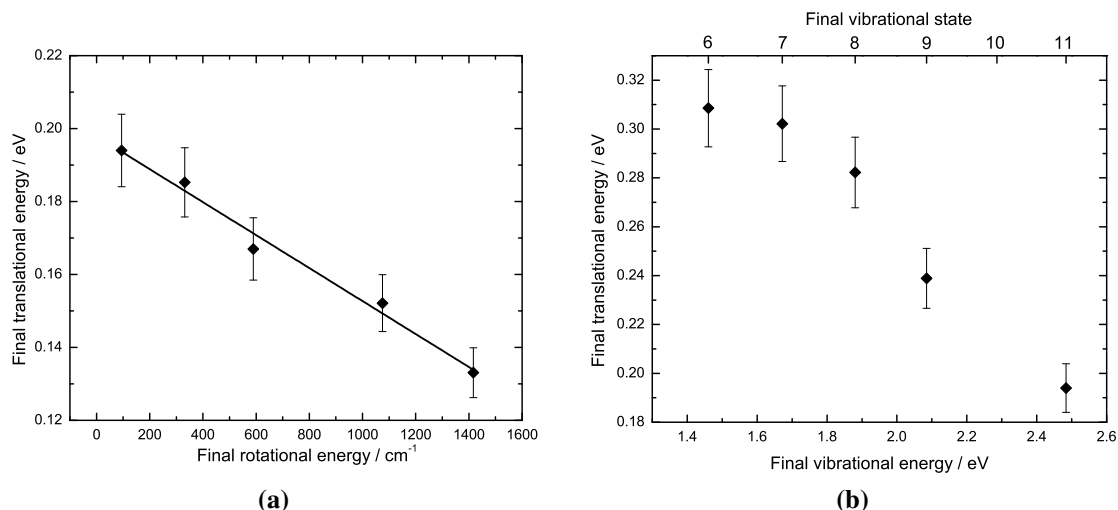


**Figure 6.23.:** Translational inelasticity in NO( $v_i = 11$ ,  $J_i = 0.5$ )/Ge(111) surface scattering. The incidence translational energy is 0.33 eV. a) The average final translational energy is plotted against the final rotational energy. The scattered molecules are detected in the vibrational state  $v_s = 11$ . b) The average final translational energy is plotted against the final vibrational energy. The scattered molecules are detected in rotational states  $J = 10.5$  except for  $v_s = 11$  where  $J = 7.5$  is detected.

translational energy of 0.33 eV. The final translational energy is found to decrease with increasing rotational excitation experienced in the collision. An extrapolation to zero rotational excitation yields 0.20 eV final translational energy. Thus, the ratio between final and incidence translational energy is 0.6 which does not agree with the Baule limit for the surface atom mass of one Ge atom mass which is 0.17. The fraction of 0.6 at 0.33 eV incidence translational energy found in highly vibrationally excited NO/Ge(111) scattering is higher than 0.46, which was determined in NO ground vibrational state/Ge(111) surface scattering at an incidence translational energy of 0.73 eV.<sup>[117]</sup> However, a more detailed investigation at different incidence translational energies of both ground state and vibrationally excited NO/Ge(111) surface scattering is needed to clearly identify a difference in the translational inelasticity. The decrease of translational energy with increasing rotational excitation can be attributed to the conversion of translational energy to rotational energy. The slope of a linear fit yields  $\Delta\langle E_f \rangle / \Delta E_{\text{rot}} = -0.36$  which is close to the value observed for NO( $v_i = 3$ )/Au(111) surface scattering.<sup>[89]</sup> See Figure 6.11. As discussed in Section 6.1.2, the deviation in the slope from  $-1$  originates in an anti-correlation between phonon and rotational excitation.

Figure 6.23b) shows the effect of vibrational energy loss on the translational inelasticity



### 6.3. Scattering of highly vibrationally excited $\text{NO}(v_i = 11)$ from $\text{Ge}(111)$

in  $\text{NO}(v_i = 11, J_i = 0.5)/\text{Ge}(111)$  surface scattering. The arrival time distribution for scattered NO in the final vibrational states  $v_s = 11-6$  is probed. The rotational quantum number is  $J_s = 10.5$  except for  $v_s = 11$  where  $J_s = 7.5$  is probed. The mean final translational energy increases with vibrational energy loss. A linear interpolation of the data shown yields  $\Delta\langle E_f \rangle / \Delta E_{\text{vib}} = -0.12$ . This value is remarkably close to the V-T coupling strength obtained for  $\text{NO}(v_i = 3)$  and  $\text{NO}(v_i = 11)/\text{Au}(111)$  surface scattering. A possible origin of the V-T coupling at the  $\text{Au}(111)$  surface is discussed in Section 6.1.2. The nonadiabatic mechanism is thought to involve transfer of vibrational energy to electron hole pairs and subsequent retransfer of a fraction of this energy to the final translational motion of the molecule. The very similar V-T coupling strength observed at  $\text{Au}(111)$  and  $\text{Ge}(111)$  gives rise to the speculation if this nonadiabatic mechanism is also present at  $\text{Ge}(111)$ . As a consequence the relaxation process  $v_i = 11 \rightarrow v_i = 9$  would have to be attributed to coupling to electrons because a clear increase of incidence translational energy compared to vibrationally elastic scattering is observed. However, the vibrational energy lost in this process is below the band gap of Ge. This means that the vibrational energy is either transferred to the very small amount of electrons in the conduction band or it is transferred to electrons in the valence states which are excited to electronic states in the band gap. Based on the small number of electrons in the conduction band (see discussion above in this section) and the presence of surface states in the band gap the second hypothesis seems more plausible.



# 7. Formaldehyde at Au(111) – results and discussion

## 7.1. Temperature programmed desorption

Temperature programmed desorption experiments on formaldehyde at Au(111) are performed as described in Section 4.3. The partial pressure at a mass to charge ratio of 30 u/e is recorded as a function of the surface temperature at different initial formaldehyde coverages. Figure 7.1 shows the desorption rates at different formaldehyde doses. The increase of the  $\alpha$  peak is saturated by increasing the formaldehyde dose whereas the  $\beta$  peak increases uniformly. This allows the  $\alpha$  peak to be assigned to monolayer desorption and the  $\beta$  peak to be assigned to overlayer desorption. Following this assignment the partial pressure measured in the experiment can be converted to the desorption rates shown on the ordinate. The conversion factor is obtained using the relationship that the integrated monolayer desorption peak in the saturation limit corresponds to a coverage of one monolayer. The desorption rate  $r$  at the leading edge of the monolayer desorption peak can be described using the Polanyi Wigner relation and assuming a zeroth-order process. In this case the desorption rate is described by Equation 7.1.

$$r = A \cdot \exp\left(\frac{-E_{\text{des},0}}{k_{\text{B}}T}\right) \quad (7.1)$$

Here,  $A$  is the Arrhenius prefactor,  $E_{\text{des},0}$  is the zeroth-order desorption energy and  $T$  is the surface temperature. The best fit to the data shown by the brown line in Figure 7.1 yields  $E_{\text{des},0} = 0.325 \pm 0.02$  eV and  $A = (7 \pm 5)10^{13} \text{ s}^{-1}$ . Alternatively, the whole monolayer peak can be simulated. The simplest model that can describe the observed behavior considers the desorption process as a first order process and the desorption energy as linearly dependent on coverage. In this case, the desorption rate is described by Equation 7.2.<sup>[121]</sup>

$$r = \Theta \frac{A}{k} \cdot \exp\left(\frac{-E_{\Theta=0} - W\Theta}{k_{\text{B}}T}\right) \quad (7.2)$$

## 7. Formaldehyde at Au(111) – results and discussion

In this equation,  $\Theta$  is the coverage,  $E_{\Theta=0}$  is the desorption energy at zero coverage, and  $W$  is the interaction energy in the monolayer. The differential equation is solved numerically and the simulation is fitted to the desorption rates observed in the experiment. The inset of Figure 7.1 compares the simulation obtained for the best fit parameters to the experimental data. Assuming a prefactor derived from the leading edge analysis, the simulation of the first order process yields  $E_{\Theta=0} = 0.31 \pm 0.02$  eV and  $W = 0.015 \pm 0.002$  eV ML<sup>-1</sup>. Though two different kinetic models were used to describe the temperature programmed desorption experiments the desorption energy is in both cases was determined to be around 0.32 eV.

At Au(110) the desorption energy of formaldehyde is 0.43 eV.<sup>[122]</sup> This is significantly higher than 0.32 eV and consistent with the observation that (111) surfaces in general exhibit less interaction with adsorbates than the other low index surfaces. See for instance reference [123] for the NO/Pt system. Furthermore, a comparison of the desorption experiment at the Au(111) surface to analogous experiments on formaldehyde/Ag(111) shows remarkable similarities in the measured desorption rates. Assuming a prefactor of 10<sup>13</sup> s<sup>-1</sup> Fleck *et al.*<sup>[124]</sup> determined the desorption energy and the interaction energy as  $E_{\Theta=0} = 0.27$  eV and  $W = 0.022$  eV ML<sup>-1</sup>. Considering the uncertainty arising from the prefactor these parameters do not differ significantly for desorption at Au(111) and Ag(111). The binding energy of formaldehyde at Au(111) calculated by DFT theory as 0.24 eV<sup>[125]</sup> shows that this theory slightly underestimates the attractive interaction between formaldehyde and Au(111) determined in the experiment.

### 7.2. 1+1' REMPI of formaldehyde via the $\tilde{A}$ state

In this work the first rotationally-resolved tunable REMPI scheme for formaldehyde applicable to state-specific scattering experiments is characterized. 1+1' REMPI via the  $\tilde{A}$  state was first demonstrated in reference [127]. The motivation for this scheme is to benefit from the long lifetime of the  $\tilde{A}$  state which allows rotational state resolution in the well characterized  $\tilde{A}^1A_2 \leftarrow \tilde{X}^1A_1$  resonant step of this scheme. The laser radiation for the resonant step is supplied by the frequency-doubled output of a conventional dye laser (see Section 3.2.1). Typically, 3-7 mJ/pulse are collimated to an area of 3 mm<sup>2</sup> using a telescope. Molecules are ionized from the  $\tilde{A}$  state by a single photon of 157 nm VUV radiation, which is supplied by a F<sub>2</sub> laser and is sufficient to overcome the ionization potential of 10.87 eV<sup>[128]</sup>. See Section 3.2.4 for a description of the laser. In the experiment presented below the two counter-propagating laser pulses (FWHM: dye laser 8-10 ns, F<sub>2</sub>

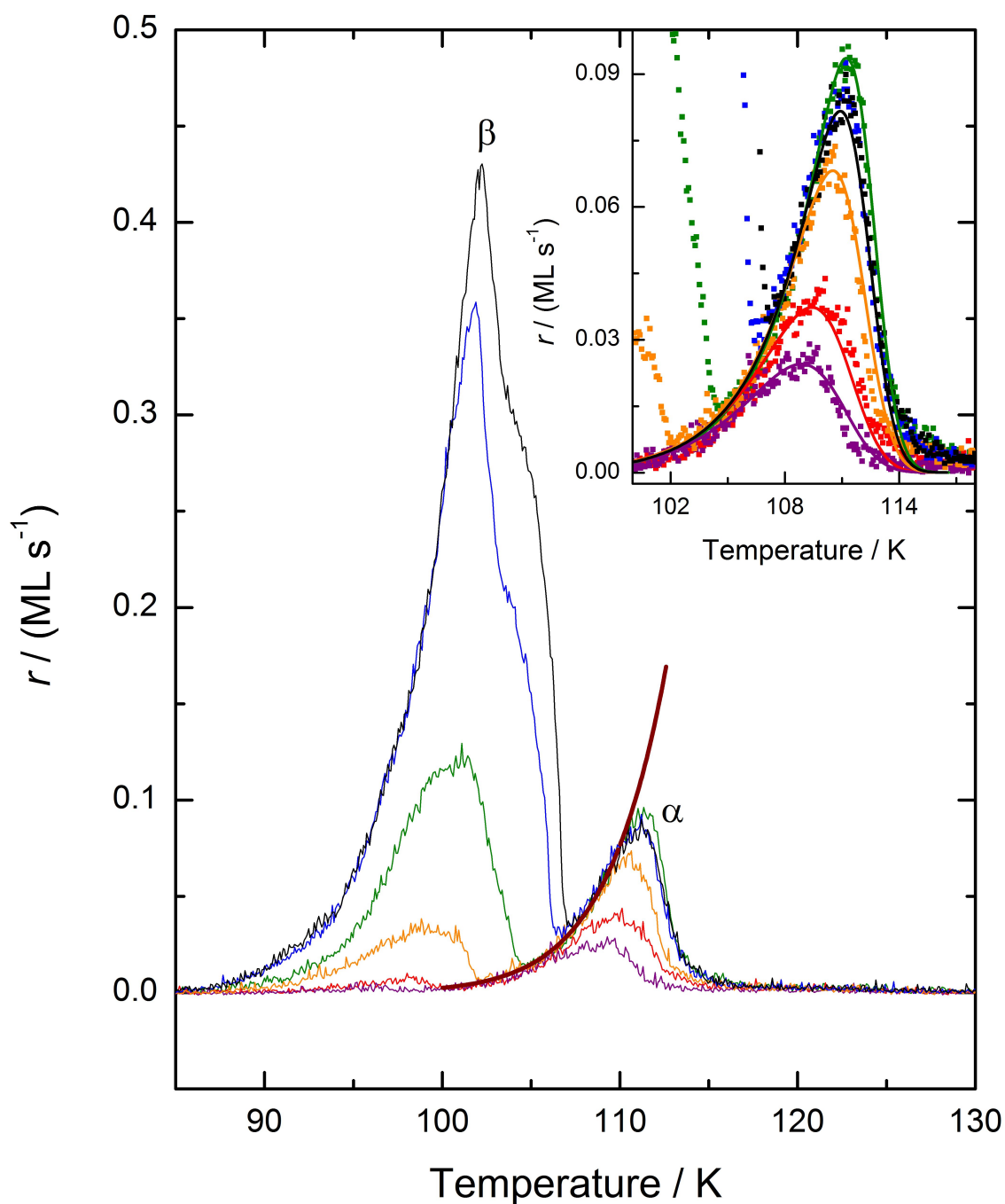


**Figure 7.1.:** Temperature programmed desorption experiment on formaldehyde adsorbed at Au(111). The heating rate is 0.5 K/s. The thin lines in different colors represent the desorption rate in experiments at different formaldehyde doses. The brown thick line corresponds to the best fit following the leading edge analysis. The labels  $\alpha$  and  $\beta$  indicate the monolayer desorption peak and the overlayer desorption peak, respectively. The inset shows the traces in the temperature region of the monolayer desorption between 100 K and 116 K. The experimental data for different coverages is represented by the plot markers in different colors. The simulations of the desorption rates are performed employing Equation 7.2 using the best fit parameters obtained as described in the text. These are shown as the colored lines. Figure reproduced from reference [126] with permission from the PCCP Owner Societies.

## 7. Formaldehyde at Au(111) – results and discussion

laser 20-26 ns) are spatially overlapped with the molecular beam. The geometry of the setup is described in Section 3.2.4. The dye laser is tuned to resonant transitions of the  $\tilde{A} \leftarrow \tilde{X} (4_0^1)$  band at  $\approx 353$  nm (3.5 eV). The laser fluence dependence of the REMPI signal on both lasers is characterized in Section 7.2.1. The effect of rotationally-dependent pre-dissociation rates on the REMPI signal is characterized in Section 7.2.2.

### 7.2.1. Laser fluence dependence

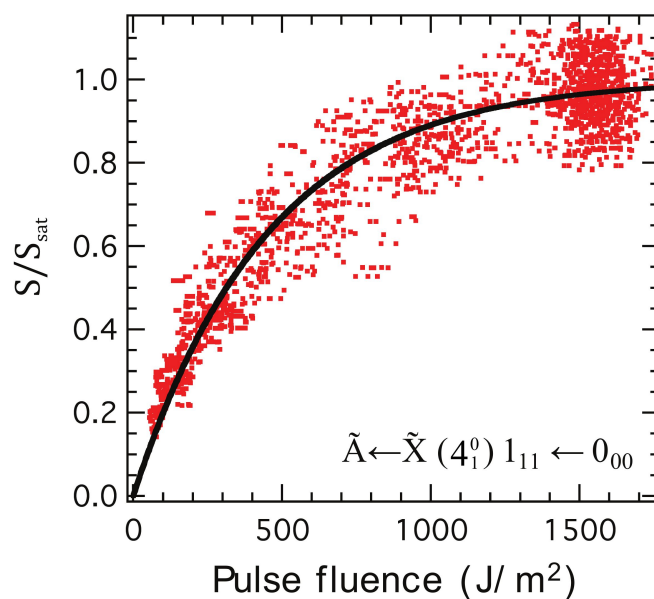
#### Results

In a first experiment, the dye laser frequency is set to the  $\tilde{A} \leftarrow \tilde{X} (4_0^1, 1_{11} \leftarrow 0_{00})$  transition denoting the transition  $\tilde{A} \leftarrow \tilde{X} \left( (\text{mode})_{v'''}', J'_{K_a'K_c'} \leftarrow J''_{K_a''K_c''} \right)$ . The  $F_2$  laser pulse arrives 30 ns after the dye laser pulse. The REMPI signal is monitored while the pulse energy is varied using a neutral density filter (Thorlabs NDC-50C-2M). Figure 7.2a) shows the dependence of the REMPI signal  $S$  normalized to the maximum achievable signal  $S_{\text{sat}}$  on the dye laser pulse fluence used in the experiment.  $S/S_{\text{sat}}$  goes into saturation for high pulse fluence and can be described by Equation 7.3. For this experiment the dye laser pulse energy has been measured at the exit window of the VUV beam line.

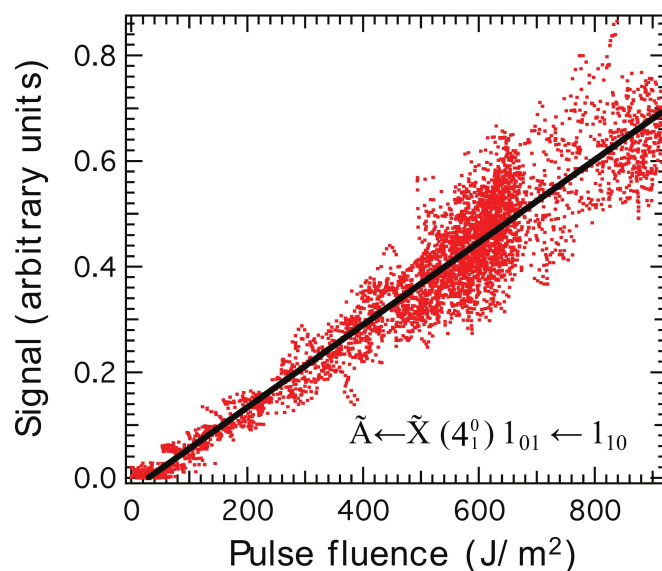
$$\frac{S}{S_{\text{sat}}} = 1 - \exp\left(\frac{-F}{F_0}\right) \quad (7.3)$$

In this equation,  $F$  is the laser fluence and  $F_0$  the saturation parameter. A best fit of Equation 7.3 yields  $F_0 = 450 \pm 20 \text{ Jm}^{-2}$ . The error is derived from the fit. The absolute error is expected to be larger since the characterization of the beam profile and focussing conditions is difficult.

The pulse fluence is varied by slowly leaking air into the VUV laser beam line. The oxygen in the air absorbs light at 157 nm. Thus, the VUV light is attenuated due to absorption of light in the beam path  $l_1$  in front of the chamber according to Beer's law. However, the VUV pulse fluence obtained from a measurement at the back of the scattering chamber is lower than the actual fluence in the scattering chamber, because the VUV light is also attenuated due to absorption of light in the beam path  $l_2$  at the back of the chamber. The beam paths  $l_1$  and  $l_2$  can be identified in Figure 3.4.  $l_1$  describes the 135 cm long path from the exit window of the laser to the  $\text{CaF}_2$  window in the adapter D.  $l_2$  describes the 38.5 cm long path from the  $\text{CaF}_2$  window in the adapter D' to the detector F. Since both beam paths are connected by a tube and the air is leaked in slowly the beam paths are at the same pressure. The actual pulse fluence  $F(p_{\text{O}_2})$  at a certain  $\text{O}_2$  partial pressure can



(a) Resonant step



(b) Ionization step

**Figure 7.2.:** The 1+1' REMPI signal as a function of the laser fluence used in the resonant and ionization step. The rovibronic transition used as the resonant step is indicated in the respective plot. a) The REMPI signal  $S$  is normalized to the maximum achievable REMPI signal  $S_{\text{sat}}$  at the chosen rovibronic transition and at an  $F_2$  laser pulse energy of 7.1 mJ used for ionization.  $S/S_{\text{sat}}$  is plotted against the pulse fluence of the resonant laser. The black curve represents a best fit of Equation 7.3 to the experimental data shown in red. b) The REMPI signal is plotted against the pulse fluence of the ionization laser. The pulse energy of the dye laser used in the resonant step is kept at 5.3 mJ. The experimental data are shown in red. The best linear fit is given by the black line. Figures taken from reference [104] and modified with permission - published by the PCCP Owner Societies.

## 7. Formaldehyde at Au(111) – results and discussion

be related to the pulse fluence  $F_B(p_{O_2})$  obtained from a measurement at the back of the chamber using the fluence  $F_0$  for an oxygen-free VUV beam path via Equation 7.4.

$$F(p_{O_2}) = F_0 \left( \frac{F_B(p_{O_2})}{F_0} \right)^{\left(1 - \frac{I_2}{I_1 + I_2}\right)} \quad (7.4)$$

Following the method described above, the dependence of the REMPI signal on the ionization laser fluence is obtained. Figure 7.2b) shows that in the range of fluences studied the REMPI signal depends linearly on the ionization laser fluence. The black line represents the best fit to the data shown in red.

### Discussion

The dependence of the REMPI signal on the dye laser fluence shown in Figure 7.2a) indicates that at the maximum investigated laser fluence the resonant  $\tilde{A} \leftarrow \tilde{X} (4_0^1, 1_{11} \leftarrow 0_{00})$  transition is saturated. At 300 K an integrated cross section of  $1.23 \cdot 10^{-11} \text{ m}^2 \text{ molecule}^{-1} \text{ s}^{-1}$  has been reported for the  $4_0^1$  band in reference [129]. By a consideration of the population weights at 300 K this can be related to an Einstein coefficient of  $1.05 \cdot 10^{15} \text{ m}^3 \text{ J}^{-1} \text{ s}^{-2}$  for the  $1_{11} \leftarrow 0_{00}$  transition. This yields a saturation parameter of  $69 \text{ J m}^{-2}$  which is within an order of magnitude of the value obtained in this work. As pointed out earlier the determination relies on an exact absolute pulse fluence determination. This is experimentally challenging because focus conditions, beam profile and pulse energy have to be measured precisely. Thus, the order-of-magnitude agreement between the value obtained here and the reported absorption cross section is reasonable.

The observed laser pulse fluence dependence for the ionization step shown in Figure 7.2b) indicates that saturation effects are absent in the investigated pulse fluence range. This is expected since transitions to the ionization continuum are typically weak. The ionization cross section out of the  $\tilde{A}$  state of formaldehyde is unknown. Assuming a typical value of  $10^{-19} \text{ cm}^2$  [130] saturation effects are expected to be unimportant up to a laser fluence that is more than two orders of magnitude higher than the maximum fluence investigated in the experiment.

### 7.2.2. 1+1' REMPI spectra of formaldehyde in a cold molecular beam

As a test of the 1+1' REMPI scheme, the REMPI spectra of formaldehyde in a supersonic molecular beam expansion are compared to spectra obtained via laser induced fluorescence (LIF). The LIF setup and the spectra acquisition are described in reference [131]. Figure 7.3



shows a comparison of spectra acquired under similar cooling conditions in the molecular beam. The spectra are recorded at laser fluences that exclude saturation effects. The REMPI spectrum is recorded with a delay of 3 ns between the resonant and ionization laser. It mostly resembles the LIF spectrum. However, some transitions marked in the REMPI spectrum exhibit much stronger relative intensities than in the LIF spectrum. A comparison to time-resolved LIF experiments<sup>[132]</sup> reveals that the rotational levels in the  $\tilde{A}$  state associated with these transitions exhibit a short lifetime. The 1+1' REMPI scheme presented here provides an alternative method for measuring the lifetimes of the rotational levels in the  $\tilde{A}$  state. This can be achieved by monitoring the REMPI signal while scanning the delay between the ionization laser and the resonant laser.

Figure 7.4 shows the typical outcome of such an experiment for two final rotational states with comparatively short lifetime. An exponential fit to the measured decay of the REMPI signal allows the excited state lifetimes in the  $\tilde{A}$  state to be extracted. Table 7.1 provides an overview of the lifetimes of shortlived rotational levels in the  $\tilde{A}$  state determined by REMPI (this work) and LIF (reference [132]). The results mostly agree. In three cases

**Table 7.1.:** Lifetimes of short-lived rotational levels in the  $\tilde{A}$  state. The rotational levels in the  $\tilde{A}$  state are given together with the lifetimes determined by REMPI and LIF. Additionally the  $\tilde{A} \leftarrow \tilde{X}(4_0^1)$  transitions used are stated.

$\tilde{A}$ state level	examined transition	$\tau_{\text{REMPI}} / \text{ns}$ (this work)	$\tau_{\text{LIF}} / \text{ns}$ (Ref. [132])
3 <sub>03</sub>	${}^{\text{P,R}}\text{R}_{1,2}(2)$	$51 \pm 4$	100
1 <sub>10</sub>	${}^{\text{r,P}}\text{Q}_{0,1}(1)$	$10 \pm 4$	818
3 <sub>12</sub>	${}^{\text{r,P}}\text{Q}_{0,3}(3)$	$25 \pm 2$	< 100
3 <sub>21</sub>	${}^{\text{r,P}}\text{R}_{1,2}(2)$	$36 \pm 3$	< 100
4 <sub>22</sub>	${}^{\text{r,P}}\text{R}_{1,3}(3)$	$45 \pm 4$	< 100

the LIF technique provides only an upper limit of < 100 ns whereas the REMPI approach yields values on the order of ten nanoseconds. A major disagreement is observed for the lifetime of the 1<sub>10</sub> level in the  $\tilde{A}$  ( $4_1$ ) state, which is determined to be 10 ns by REMPI. However, a lifetime of 818 ns has been reported in reference [132]. This likely relies on an incorrect spectral assignment of the two only partially resolved transitions  ${}^{\text{r,P}}\text{Q}_{0,1}(1)$  and  ${}^{\text{r,P}}\text{Q}_{0,2}(2)$ . Thus, the comparatively long lifetime of 818 ns should be attributed to the 2<sub>11</sub> instead of the 1<sub>10</sub> level. In general, the lifetimes of rotational levels in the  $\tilde{A}$  state vary dramatically in a pseudo-random way. For instance, in reference [133] lifetimes between 66 ns and 4.2  $\mu\text{s}$  have been reported. This observation has been interpreted in terms of a sequential coupling mechanism via the ground electronic state of formaldehyde to the  $\text{H}_2+\text{CO}$  dissociation continuum. Short lifetimes are attributed to resonance effects. The

## 7. Formaldehyde at Au(111) – results and discussion

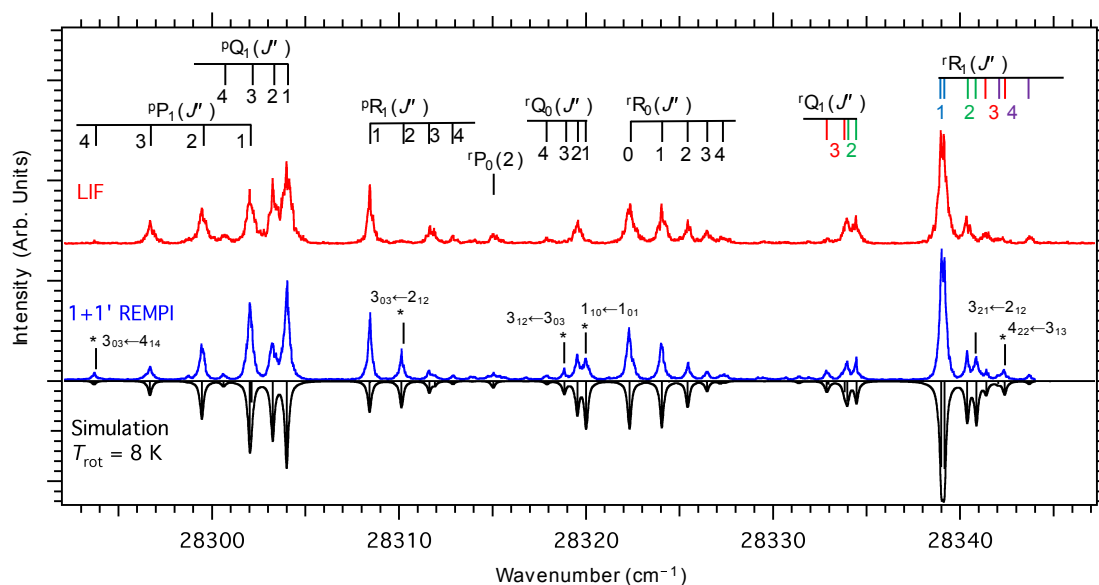


**Figure 7.3.:** Comparison between LIF and 1+1' REMPI spectra. The 1+1' REMPI signal is plotted against the wavenumber (blue line). The delay between the two laser pulses used in the REMPI process is set to  $\approx 3$  ns such that the resonant laser is fired first. The spectrum is acquired in a supersonic molecular beam expansion using 12 bar  $H_2$  as the seeding gas. As a comparison the LIF spectrum is shown in red. The fluorescence of formaldehyde is integrated in a 100 ns wide window starting at a delay of 45 ns with respect to the laser excitation. Here, formaldehyde is expanded together with 0.5 bar He and the LIF spectrum is acquired in the source chamber of the molecular beam scattering apparatus used in this work. The assignment to the different rotational branches is given in the top of the figure. Here, the notation  $\Delta K_a \Delta J_{K_a''}(J'')$  is used. Transitions that are much more intense in the 1+1' REMPI spectrum than in the LIF spectrum are labeled with an asterisk and the notation  $J_{K_a' K_c'} \leftarrow J_{K_a'' K_c''}$  is used to specify the transition. The black line represents a simulation of an unsaturated adsorption spectrum at a rotational temperature of 8 K assuming a Lorentzian line shape with a FWHM of  $0.12 \text{ cm}^{-1}$ . Figures taken from reference [104] and modified with permission - published by the PCCP Owner Societies.

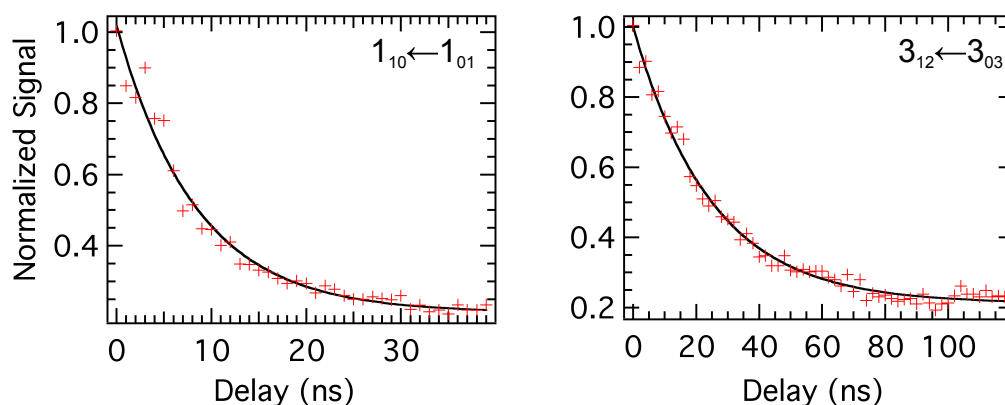


**Figure 7.4.:** Lifetime measurements using the 1+1' REMPI scheme. The REMPI signal is plotted against the delay between the two laser pulses used in the REMPI approach. The resonant laser is set to a rovibronic transition belonging to the  $\tilde{A} \leftarrow \tilde{X}(4_0^1)$  band as indicated in the respective plot. The signal does not decay to zero because the transition is not completely resolved from neighboring rovibronic transitions with much larger lifetime ( $\approx 1\mu\text{s}$ ). The black line represents the best single exponential fit to the measured REMPI signal decay. Figure taken from reference [104] and modified with permission - published by the PCCP Owner Societies.

overview of lifetimes of rotational levels in the  $\tilde{A}(v_4 = 1)$  state provided in reference [132] shows that the states picked in Table 7.1 exhibit rather exceptional short lifetimes. For most of the rotational levels the lifetime is longer than 100 ns.

The short lifetime of particular rotational levels explains the deviation between the LIF and REMPI spectrum shown in Figure 7.3. The total fluorescence yield drastically decreases with decreasing pre-dissociative lifetime. In addition, due to experimental limitations caused by scattered laser light the fluorescence traces can only be integrated starting at 45 ns with respect to the laser excitation. Thus, states with a shorter lifetime are invisible in the LIF spectrum. The intensities of transitions involving extremely short-lived intermediate states like the  $\tilde{A}(4_1, 1_{10})$  level are also potentially attenuated in the REMPI spectrum. However, the REMPI spectrum is affected much less by effects of the intermediate state lifetime because the delay between the two laser pulses can be chosen as short as several nanoseconds. Thus, the method is limited by the temporal width of the ionization laser pulse, which has a FWHM of 20-26 ns. This is demonstrated by the good agreement between the REMPI spectrum and a simulation of an unsaturated absorption spectrum (see Figure 7.4). The simulation neglects any effects arising from ionization and intermediate state lifetime. A Boltzmann analysis of the REMPI spectrum allows the determination of the rotational temperature in the supersonic beam expansion. Figure 7.5

## 7. Formaldehyde at Au(111) – results and discussion

shows a plot of  $\ln(SQ/\mu^2gP)$  against the rotational energy in the  $\tilde{X}$  state above the rotational ground state of the respective nuclear spin isomer  $E_{\text{rot}} - E_0$ . Here,  $S$  is the integrated REMPI signal of a specific rovibronic transition and  $Q$  the partition function,  $g$  is the degeneracy and  $\mu$  is the relative rotational transition moment. The three latter quantities can be calculated using the MATLAB code given in the Appendix A.1. In the analysis the ortho and para states are treated completely separately, because a consideration of the rates for interconversion<sup>[134]</sup> shows that the nuclear spin states cannot be converted during the molecular beam expansion. Thus, a population weight  $P$  is introduced that is 1 for para states and 3 for ortho states which reflects the high temperature distribution between both nuclear spin isomers. Following this idea, the population of both the ortho and para manifolds follow a Boltzmann distribution at a rotational temperature of  $8.7 \pm 0.4$  K which is derived from a linear fit represented by the black line in Figure 7.3. In summary, the 1+1' REMPI scheme allows the extraction of the population of single rotational states in the  $\tilde{X}$  state. As a test the rotational temperature of a molecular beam expansion using 12 bar H<sub>2</sub> and formaldehyde is determined as 8.7 K indicating efficient rotational cooling. In the molecular beam the rotational states with  $K_a = 0$  and 1 and  $J = 0 - 2$  dominate the rotational distribution.

### 7.2.3. Applying the REMPI scheme to surface scattering

The nice agreement between rotationally resolved experimental REMPI spectra acquired in a supersonic molecular beam and simulated absorption spectra demonstrated in Section 7.2.2 is encouraging. However, the requirements for the 1+1' REMPI scheme as a detection method in molecule-surface scattering are even more demanding: First, due to the available energy from the collision or the thermal energy at the surface the number of accessible states is much higher than in the cold molecular beam. Thus, a narrow line width is crucial to maintain rotational resolution. Second, due to the excitation of many internal states as well as the dilution of the molecules in space the absolute density of scattered molecules in a certain quantum state will be much lower than that of molecules in the incoming beam. This is why a high detection efficiency is needed.

As a first test case, formaldehyde is scattered from an adsorbate-covered Au(111) surface. In this experiment the surface was not cleaned after exposure to air, which means that it is probably covered with water and carbon impurities. The detection lasers are centered at a position of  $x = 7$  mm away from the surface and  $z = 3$  mm above the center of the incoming beam. Apart from the modified laser positions, the spectrum of scattered molecules is recorded as described in Section 4.2.1. The “dirty” Au(111) surface

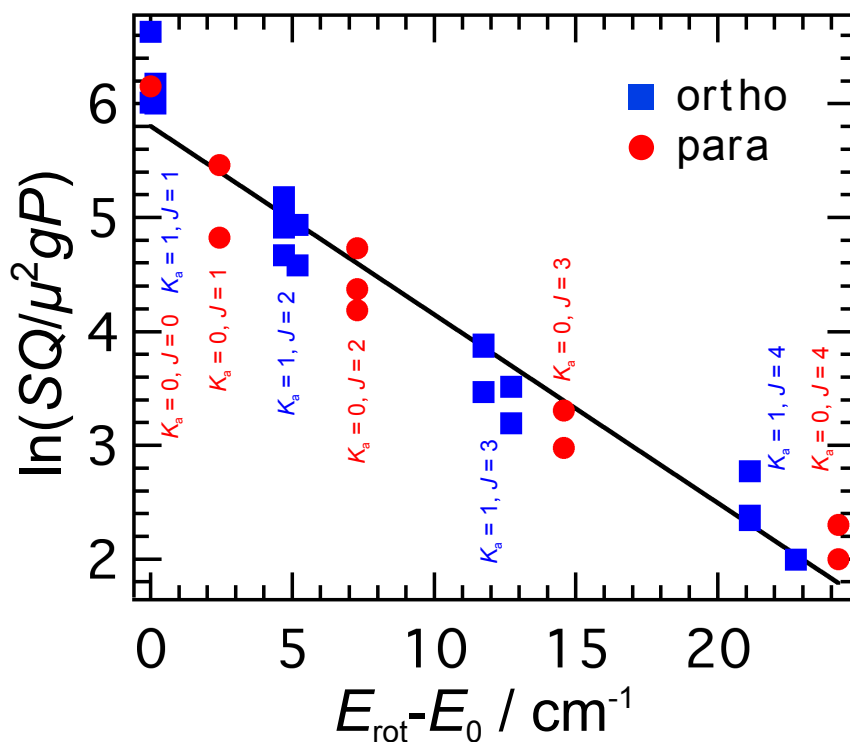


**Figure 7.5.:** Boltzmann plot derived from the 1+1' REMPI spectrum of formaldehyde in a supersonic molecular beam expansion.  $\ln(SQ/\mu^2gP)$  is plotted against the rotational energy in the  $\tilde{X}$  state referenced to the rotational ground state of the respective nuclear spin isomer,  $E_{\text{rot}} - E_0$ .  $S$  is the integrated REMPI signal. The rotational quantum numbers  $K_a$  and  $J$  for the  $\tilde{X}$  state are given for the para (red labels) and ortho spin isomer (blue labels) in the plot. In the analysis para and ortho states are treated separately.  $Q$  is the partition function.  $\mu$  is the relative rotational transition moment.  $g$  is the degeneracy and  $P$  is a population factor which is 1 for para states and 3 for ortho states reflecting the absence of interconversion between nuclear spin states in the expansion process. The values obtained for ortho (para) states are indicated by blue squares (red circles). The best linear fit to the data represented by the black line yields a rotational temperature of 8.7 K. Figure taken from reference [104] and modified with permission - published by the PCCP Owner Societies.

## 7. Formaldehyde at Au(111) – results and discussion

favors trapping-desorption which is also consistent with the final speed of the scattered molecules obtained by time-of-flight experiments. Thus, neglecting effects of detailed balance it is expected that the rotational state distribution is well described by a Boltzmann distribution at the surface temperature (300 K). Figure 7.6 shows a comparison between the observed 1+1' REMPI spectrum (red) and a simulated absorption spectrum with a rotational temperature of 300 K (blue). The spectral region shown in Figure 7.6 is a part of the  $\tilde{A} \leftarrow \tilde{X}(4_0^1)$  band. The agreement is satisfactory. The stick spectrum shown in black illustrates how many single rovibronic transitions contribute to the spectrum. Clearly, the spectrum contains many only partially resolved rovibronic transitions. Nevertheless, a lot of rotational structure can be observed and even lines belonging to single rovibronic transitions can be identified in the spectrum. The good agreement between experiment and simulation shows that effects of extremely short-lived intermediate states discussed in Section 7.2.2 and resonances in the ionization continuum on the 1+1' REMPI spectrum are negligible for the investigated vibronic band since neither effects is considered in the simulation. Extremely short-lived rotational levels in the  $\tilde{A}(v_4 = 1)$  state seem to be rare, which is consistent with the reported lifetimes for these states.<sup>[135]</sup> Furthermore, measurements on the single VUV photon absorption cross section suggest that the region of the ionization continuum probe in our experiment is structureless<sup>[128,136]</sup> which allows the ionization cross section to be neglected in the simulation of the  $\tilde{A} \leftarrow \tilde{X}(4_0^1)$  1+1' REMPI spectrum.

## 7.3. Scattering of formaldehyde from Au(111)

### 7.3.1. Characterization of the incoming beam

In this section, supersonic molecular beam pulses of formaldehyde in different carrier gases are characterized. These are produced using the heatable nozzle described in Section 3.1.1. 2+1 REMPI detection (described in Section 4.2.2) is used to measure the arrival time distribution of the molecular beam pulse in the scattering chamber. For each seeding gas mixture, the backing pressure and the duration of the electrical trigger to the nozzle  $\tau_{el}$  are optimized in order to maximize the peak intensity in the arrival time distribution and obtain a near Gaussian pulse shape minimizing the temporal width of the distribution. The duration of the electrical trigger is indirectly related to the opening duration of the nozzle. The longer the electrical trigger the stronger the driving force for the displacement of the poppet which leads to a longer opening duration of the nozzle.

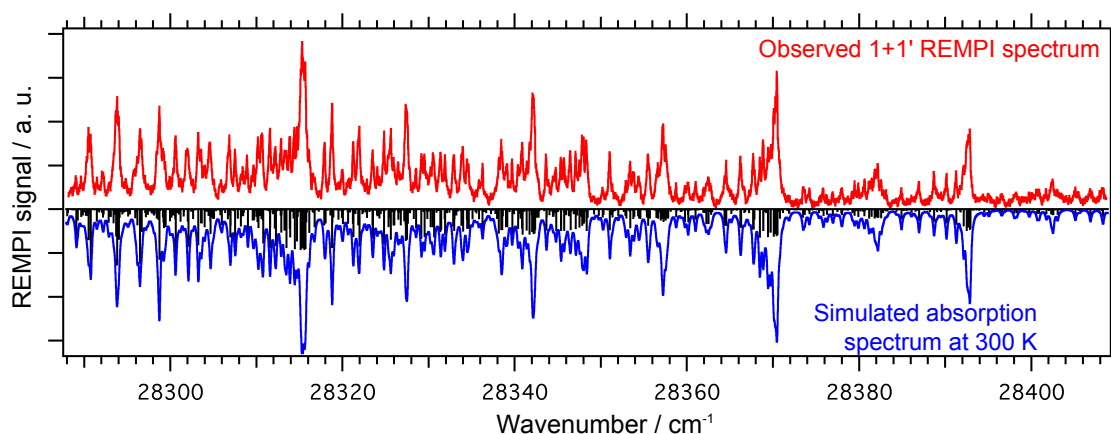


**Figure 7.6.:** Applying the 1+1' REMPI scheme to surface scattering. The experimentally observed REMPI spectrum obtained for scattered formaldehyde from an adsorbate covered 300 K Au(111) surface is shown in red. The delay between the resonant and ionization laser is 5 ns. As a comparison a simulated absorption spectrum with a rotational temperature of 300 K is plotted in blue assuming a Lorentzian line shape with a FWHM of  $0.15 \text{ cm}^{-1}$ . The corresponding stick spectrum is shown in black. Figure taken from reference [104] and modified with permission - published by the PCCP Owner Societies.

For most of the seeding gas mixtures a “sweet spot” in both settings is found providing the maximum peak intensity at the narrowest temporal width possible. If this is not the case the setting is chosen such that the width of the distribution is minimized at an affordable peak intensity. The parameters shown in Table 7.2 can be taken as a guideline for future usage of the nozzle. However, it was found that after servicing of the nozzle in some cases slight adjustments to the electrical trigger duration had to be made in order to regain the optimum molecular beam pulse. It is found that the electrical trigger duration is a critical parameter to the pulse shape for this nozzle design and should be checked frequently. In general, it is found that  $\tau_{el}$  has to be increased if the expanded gas mixtures contain heavier atoms/molecules. This might be attributed to an increased viscosity of the gas mixtures that increases according to the kinetic theory of gases with the square root of the mass.

The most probable velocity in the incoming beam can be derived by probing the arrival time distribution at different positions along the propagation axis of the incoming beam. The delay between nozzle opening and laser firing is varied while the REMPI signal is recorded. Figure 7.7a) shows a typical data set of such a measurement. The arrival time distribution can be in a good approximation described by a Gaussian function. The FWHM does not vary significantly along the 2 cm probe position range. For the data shown in the figure (using 10.8 bar in He as a seeding gas) it is  $29 \mu\text{s}$ . As the probe position is moved from the nozzle towards the surface the molecular beam pulse arrives at later delays

**Table 7.2.:** Relevant parameters for the heatable Even-Lavie type nozzle. The gas mixtures are given with the optimized backing pressure  $p_{\text{back}}$  and the nozzle opening duration as well as the resulting incidence translational energy of formaldehyde in the molecular beam.

gas mixture	$p_{\text{back}} / \text{bar}$	$\tau_{\text{el}} / \mu\text{s}$	$E_i / \text{eV}$
pure H <sub>2</sub>	12	26.5	1.34
50% H <sub>2</sub> +50%He	12	27	0.90
pure He	10.8	29.5	0.59
10% N <sub>2</sub> +90% H <sub>2</sub>	12	28.5	0.48
15% N <sub>2</sub> +85% H <sub>2</sub>	12	29	0.43
25% N <sub>2</sub> +75% H <sub>2</sub>	12	29.5	0.32
pure N <sub>2</sub>	4	31	0.12

between nozzle opening and laser firing. The arrival time at the maximum of the arrival time distribution can be plotted against the probe position used in the measurement as shown in the inset of Figure 7.7a). The slope of a linear fit to this data yields the most probable velocity in the incoming beam. These values are used to calculate the incidence translational energy of formaldehyde. The  $z$ -profile of the molecular beam perpendicular to its propagation axis is investigated by setting the laser-nozzle delay to the maximum of the arrival time distribution and recording the REMPI signal as a function of the  $z$ -position of the probe laser. The typical result of such a measurement is shown in Figure 7.7b). The distribution with a flat maximum and a rather sharp cutoff shows a FWHM of  $\approx 2$  mm regardless of the seeding gas mixture used. The observed shape is consistent with the restricting 2 mm aperture located between the differentially pumped chamber and the surface scattering chamber.

For the optimized nozzle parameters the rotational state distributions in the cold molecular beam are probed following the method described in Section 7.2.2. The rotational temperatures are in the range between 2 K and 13 K and no conversion between ortho and para states in the expansion is found. This means that for every seeding gas mixture expanded almost exclusively rotational states with  $K_a = 0$  and  $K_a = 1$  are populated in the beam.

### 7.3.2. Manipulation of the incoming beam - preparation of vibrationally excited formaldehyde

In this section, results on the preparation of vibrationally excited formaldehyde in the incoming beam are presented. The experimental procedure is described in Section 4.2.3. It will be demonstrated that formaldehyde can be efficiently excited to the vibrational



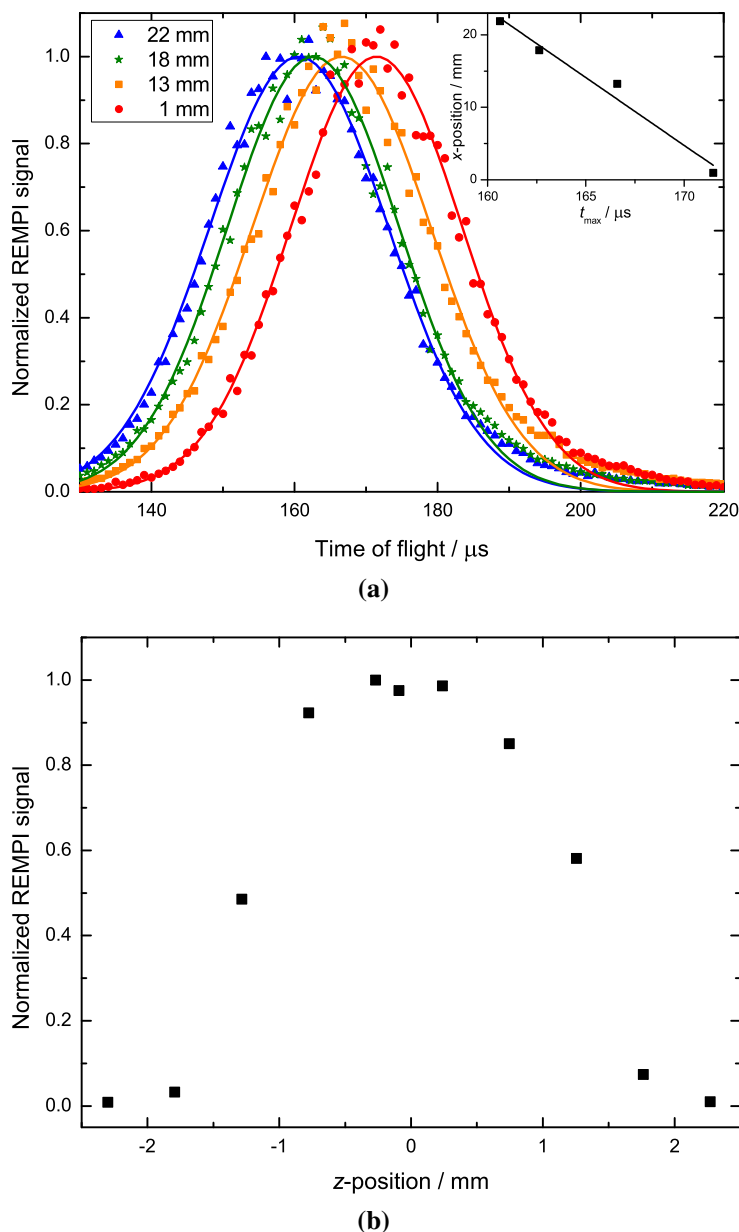


**Figure 7.7.:** Characteristics of the incoming beam. a) The arrival time distribution of the molecular beam pulse in the surface scattering chamber is probed using 2+1 REMPI spectroscopy. The REMPI signal is plotted against the time-of-flight corresponding to the delay between laser firing and nozzle opening. The experimental data is shown for different positions along the propagation axis of the molecular beam. In the plot legend the distance of the probe position to the surface  $x$  is stated. The colored lines represent the best fit of a Gaussian to the observed arrival time distribution at the respective probe position. In the inset the center of the Gaussian is plotted against the probe position (black squares). A linear fit (black line) to the data yields the most probable speed in the incoming beam as the slope. b) The  $z$ -profile of the molecular beam perpendicular to its propagation axis is shown. The REMPI signal observed at the maximum of the arrival time distribution is plotted against the  $z$ -position of the laser.

## 7. Formaldehyde at Au(111) – results and discussion

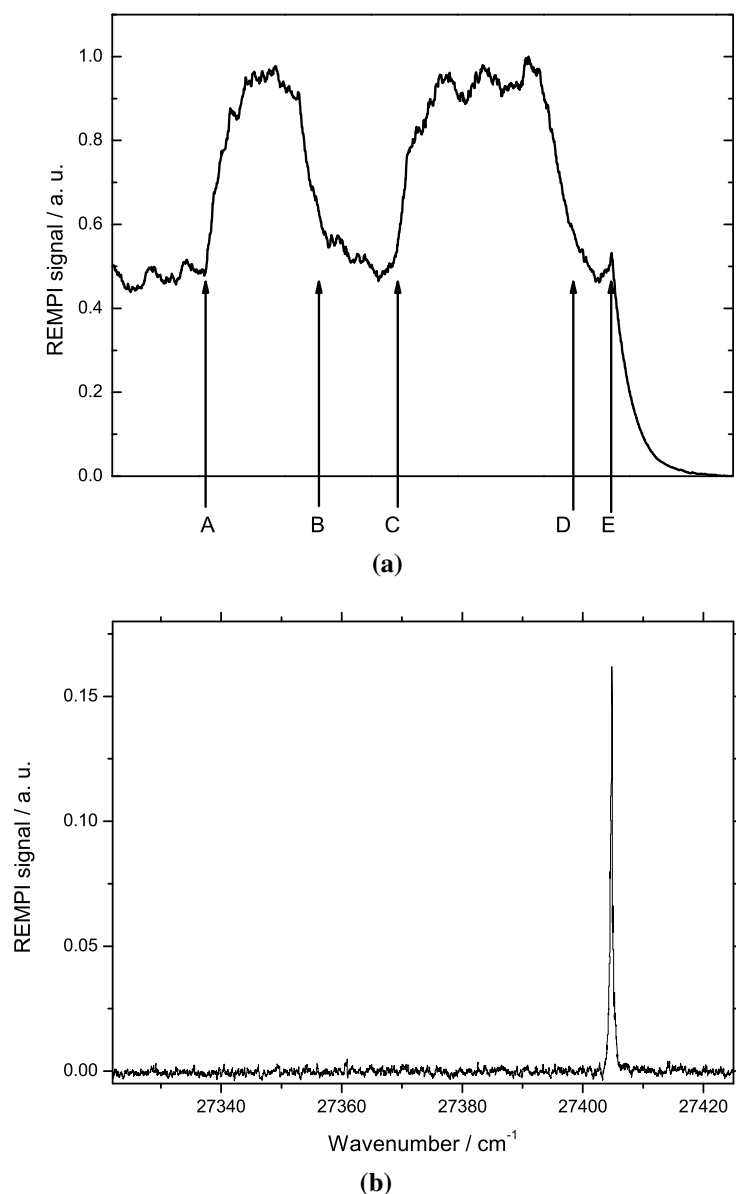


**Figure 7.8.:** Production of vibrationally excited formaldehyde in the incoming beam. The IR laser is set to the  $2_0^1 6_0^1 P, P P_{11}(1)$  transition at  $2989.5269 \text{ cm}^{-1}$ . a) The REMPI signal is shown during the course of the experiment. The dye laser is set to  $28302.02 \text{ cm}^{-1}$  probing vibrational ground state formaldehyde via the  $\tilde{A} \leftarrow \tilde{X} (4_0^1) P, P P_{1,1}(1)$  transition. In the beginning all three lasers (IR laser, dye laser,  $F_2$  laser) are unblocked and the molecular beam is running. At the point in time A the IR laser is blocked and unblocked at the point in time B again. This is repeated as indicated by C and D. At E the molecular beam is turned off. The REMPI signal does not change instantaneously because the oscilloscope is set to average multiple shots. b) The  $1+1'$  REMPI signal in the range between  $27320 \text{ cm}^{-1}$  and  $27430 \text{ cm}^{-1}$  is shown. Only one peak at  $27404.9 \text{ cm}^{-1}$  is present in the spectrum corresponding to formaldehyde in the  $\tilde{X}(2_1 6_1)$  state probed via the  $\tilde{A}(2_1 4_1 6_1) \leftarrow \tilde{X}(2_1 6_1) R, R R_{0,0}(0)$  transition.

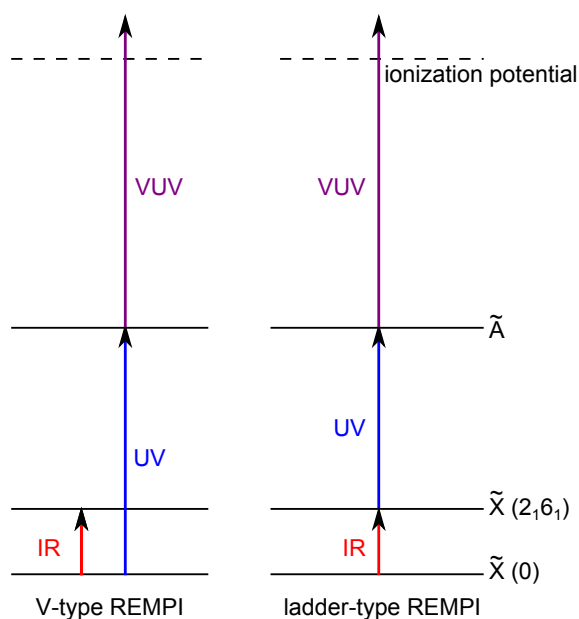


**Figure 7.9.:** V-type and ladder-type REMPI experiment. The diagram is not drawn to scale.

states  $2_14_1$  and  $2_16_1$  using a narrow-bandwidth IR laser source (see Section 3.2.5 for the characteristics of this laser system). Three lasers are used in the experiment described in the following: an IR laser source for pumping and a dye laser as well as an  $F_2$  laser for probing using  $1+1'$  REMPI spectroscopy. Figure 7.8 a) shows the outcome of a V-type double resonance experiment (see Figure 7.9 for a schematic). The IR laser is set to the  $2_0^16_0^1 P,P P_{1,1}(1)$  transition at  $2989.5269 \text{ cm}^{-1}$  agreeing with the transition wavenumber reported in the database described in reference [137].  $1+1'$  REMPI spectroscopy is used to detect the ground state  $\tilde{X}(0, 1_{11})$ . In the beginning all lasers are on. The label “A” indicates when the IR laser is blocked which leads to an increase of the REMPI signal by a factor of two. At “B” the IR laser is unblocked and the cycle is repeated as indicated by “C” and “D”. At “E” the molecular beam is turned off. The experiment shows that the ground state bleach originating from the IR laser is  $\approx 50\%$  which means that the pump transition can be saturated at an IR pulse energy of  $4 \text{ mJ/pulse}$  using a  $1000 \text{ mm}$  focusing lens. This is even true if the lens is removed and an unfocused laser beam with a beam diameter of  $4 \text{ mm}$  is used. In a second experiment the vibrationally excited state is directly probed employing a ladder-type REMPI experiment (see Figure 7.9 for a schematic). Figure 7.8 b) shows a  $1+1'$  REMPI spectrum scanning the dye laser in the range between  $27320 \text{ cm}^{-1}$  and  $27430 \text{ cm}^{-1}$ . The observed peak at  $27404.9 \text{ cm}^{-1}$  is assigned to excited formaldehyde in  $\tilde{X}(2_16_1, 0_{00})$  probed via the  $\tilde{A}(2_14_16_1) \leftarrow \tilde{X}(2_16_1)^{R,R} R_{0,0}(0)$  transition. Note that there is

## 7. Formaldehyde at Au(111) – results and discussion

only one peak because  $J'' = 0$  is probed and only the R-branch is allowed. The peak is completely absent if the IR laser is blocked.

In a similar experiment the vibrationally excited state  $2_14_1$  is produced. For this vibrational state two IR transitions are examined as pump transitions. At the wavenumber of  $2895.26861\text{ cm}^{-1}$  given for the  $2_0^14_0^1\text{P,QP}_{10}(1)$  transition in the database in reference [137] no REMPI signal or ground state bleach could be detected in the ladder-type and V-type REMPI experiment. However, at a wavenumber of  $2895.257\text{ cm}^{-1}$  (according to the High-Finesse WS 7 wavemeter used) a weak REMPI signal could be observed when probing the  $\tilde{X}(2_14_1, 0_{00})$  level in the ladder-type experiment via the  $\tilde{A}(0) \leftarrow \tilde{X}(2_14_1)^{\text{R,R}}\text{R}_{0,0}(0)$  transition at  $25292.2\text{ cm}^{-1}$ . The reason for the discrepancy is unclear.

In contrast, a strong REMPI signal could be observed when using the  $2_0^14_0^1\text{R,QR}_{11}(1)$  transition for pumping and the  $\tilde{A}(0) \leftarrow \tilde{X}(2_14_1)^{\text{R,P}}\text{R}_{21}(2)$  transition for probing. The optimum IR laser wavenumber is consistent with the transition wavenumber of  $2932.22854\text{ cm}^{-1}$  reported in the database described in reference [137]. In addition, a strong ground state bleach could be observed for this pump transition.

In conclusion, efficient preparation of the vibrational states  $2_14_1$  and  $2_16_1$  can be achieved using the  $2_0^14_0^1\text{R,QR}_{11}(1)$  and  $2_0^16_0^1\text{P,P}P_{11}(1)$  transition whereas the  $2_0^14_0^1\text{P,QP}_{10}(1)$  seems to be inappropriate for this purpose. So far this approach has not been successfully applied to scattering experiments, probably because the overall density of formaldehyde in the molecular beam is too low. An estimation based on measurements with a mass spectrometer shows that with the used heatable nozzle the fraction of formaldehyde seeded in  $\text{H}_2$  in an expansion with a total backing pressure of 12 bar is only  $\approx 1\%$  corresponding to a partial pressure of 0.1 bar formaldehyde in the nozzle. This is only a small fraction of the vapor pressure of formaldehyde which is 2.2 bar at  $0\text{ }^\circ\text{C}$ <sup>[56]</sup> and potentially even larger at the elevated temperatures in the nozzle. It is unclear why the limit of the vapor pressure is not reached. From an experimental point of view a change of the nozzle design regarding three characteristics might enhance the formaldehyde production. First, the sample compartment should be enlarged allowing the cracking of formaldehyde in a larger volume. Second the sample compartment could be heated directly in order to increase the cracking temperature and in this way the cracking rate. Third, a more efficient drying agent can be used to prevent repolymerization caused by the presence of water.

### 7.3.3. Translational inelasticity in the scattering of formaldehyde from Au(111)

#### Results

The translational inelasticity in formaldehyde/Au(111) surface scattering is studied using 2+1 REMPI detection described in Section 4.2.2. The relevant information on the time-of-flight methods is given in Section 5.2.2. The experiments described in this section are performed with the REMPI laser wavenumber fixed to  $33866.6 \text{ cm}^{-1}$ . This method allows the detection of vibrational and electronic ground state formaldehyde in the  $K_a = 0$  and  $K_a = 1$  manifold regardless of  $J$ . In the incidence molecular beam states with  $K_a = 0$ ,  $K_a = 1$  and  $J = 0 - 2$  dominate (see Section 7.3.1). Assuming no para to ortho conversion in the collision process, this means that the investigated scattering processes involve no rotational excitation about the  $a$ -axis of the formaldehyde molecule but may involve rotational excitation about the  $b$ - and  $c$ -axis. The section is structured such that first results for low incidence translational energies of the molecule are presented and subsequently the results for higher incidence translational energies are presented.

Figure 7.10 provides an overview of the arrival time distributions measured at an incidence translational energy of 0.11 eV. The scattering geometry is given in Figure 4.1. The incidence angle is normal to the surface. The arrival time distributions are obtained at different scattering angles as indicated in the figure. This is achieved by positioning the REMPI laser at  $x = 13 \text{ mm}$  and varying the  $z$ -position such that different scattering angles are probed. The observed arrival time distributions are consistent with a simulation of the arrival time distribution assuming a Maxwell-Boltzmann velocity distribution at the surface temperature (300 K) according to the procedure described in Section 5.2.2. Integration of the experimentally determined arrival time distribution yields the angular distribution represented by the black points in the inset of the figure. The angular distribution shown in the figure is consistent with a  $\cos(\theta)^n$  distribution with  $n = 1$ . An analysis of the angular distributions derived from all available datasets for this incidence translational energy yields  $n$  ranging from 1 to 2. The observations of arrival time distributions that are well described by assuming complete equilibration of the translational degrees of freedom with the surface as well as the broad angular distribution can be interpreted as a “fingerprint” of trapping-desorption.

As the incidence translational energy is increased to 0.33 eV the observed arrival time distributions clearly change with respect to those observed at the lower incidence translational energy. Figure 7.11 shows the observed changes. The measured arrival

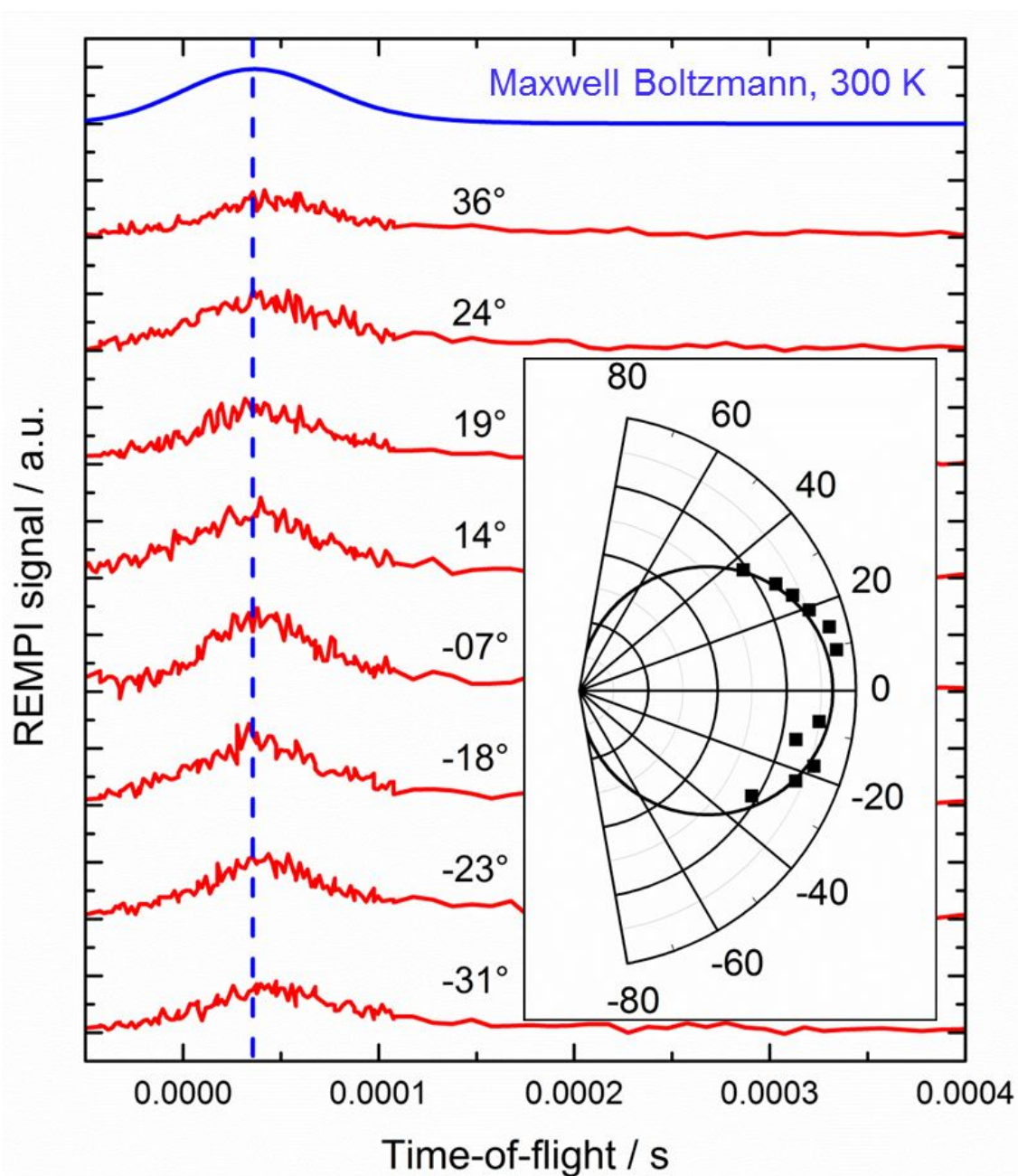


**Figure 7.10.:** Arrival time distributions of formaldehyde scattered from Au(111) at 0.11 eV incidence translational energy. The REMPI signal is shown as a function of the time-of-flight of the scattered molecules for different scattering angles as indicated in the figure (red lines). As a comparison, a simulation of the arrival time distribution assuming a Maxwell-Boltzmann velocity distribution at the temperature of the 300 K Au crystal is shown in blue. The inset shows the angular distribution derived from integration of the arrival time distributions. Figure reproduced from reference [126] with permission from the PCCP Owner Societies.

time distributions are shown in red. At large absolute scattering angles the arrival time distributions are still well described by the expectation for complete equilibration with the surface. At scattering angles close to the normal the maximum of the distribution shifts to earlier arrival times. In addition, the integration of the arrival time distributions yields an increase of molecules scattered at scattering angles close to the normal with respect to large absolute scattering angles. These observations suggest that the arrival time distributions are composed of two components, one originating from trapping-desorption and a second component that will be shown to originate from direct-scattering. In order to separate the two components it is assumed that desorption dynamics do not change when the incidence translational energy is increased. Following this idea we obtain the arrival time distributions for the second component shown in black by subtracting the expected arrival time distribution for desorbing formaldehyde. This assumes that desorption follows a  $\cos(\theta)$  angular distribution as observed at lower incidence translational energy and that the flux at absolute scattering angles  $> 35^\circ$  can be attributed exclusively to trapping-desorption. An analysis of the arrival time distributions for the second component indicates that the scattered molecules must be faster than the desorbing molecules since the arrival time distribution is shifted to earlier arrival times. In addition, the angular distribution for the second component shown in the inset of Figure 7.11 is narrow and can be described by a  $\cos(\theta)^{22}$  distribution. Both observations are consistent with direct-scattering as the mechanism for the second component.

As the incidence translational energy is increased further the overall angular distribution becomes narrower. In addition, the maximum in the arrival time distribution at scattering angles close to the surface normal shifts to an even earlier arrival time. The most probable speed of molecules scattered at these angles  $|\theta| \leq 10^\circ$  can be obtained by probing the arrival time distribution at a constant angle but at different distances from the surface. Figure 7.12 shows the method used. As shown the maximum points of the arrival time distribution of the incoming beam and scattered beam at different probe positions are obtained from an analysis of the measured arrival time distributions. The slope of a plot of the maximum points of the arrival time distribution against the probe position yields the most probable velocity of the incoming and scattered molecules. From these values the incidence translational energy and final translational energy can be calculated. Figure 7.13 shows the dependence of the final translational energy on the incidence translational energy. The final translational energy increases linearly with the incidence translational energy. The red line represents the best linear fit to the data. Within the error of the experiment this does not differ from the expectation of a simple Baule model represented by the dashed

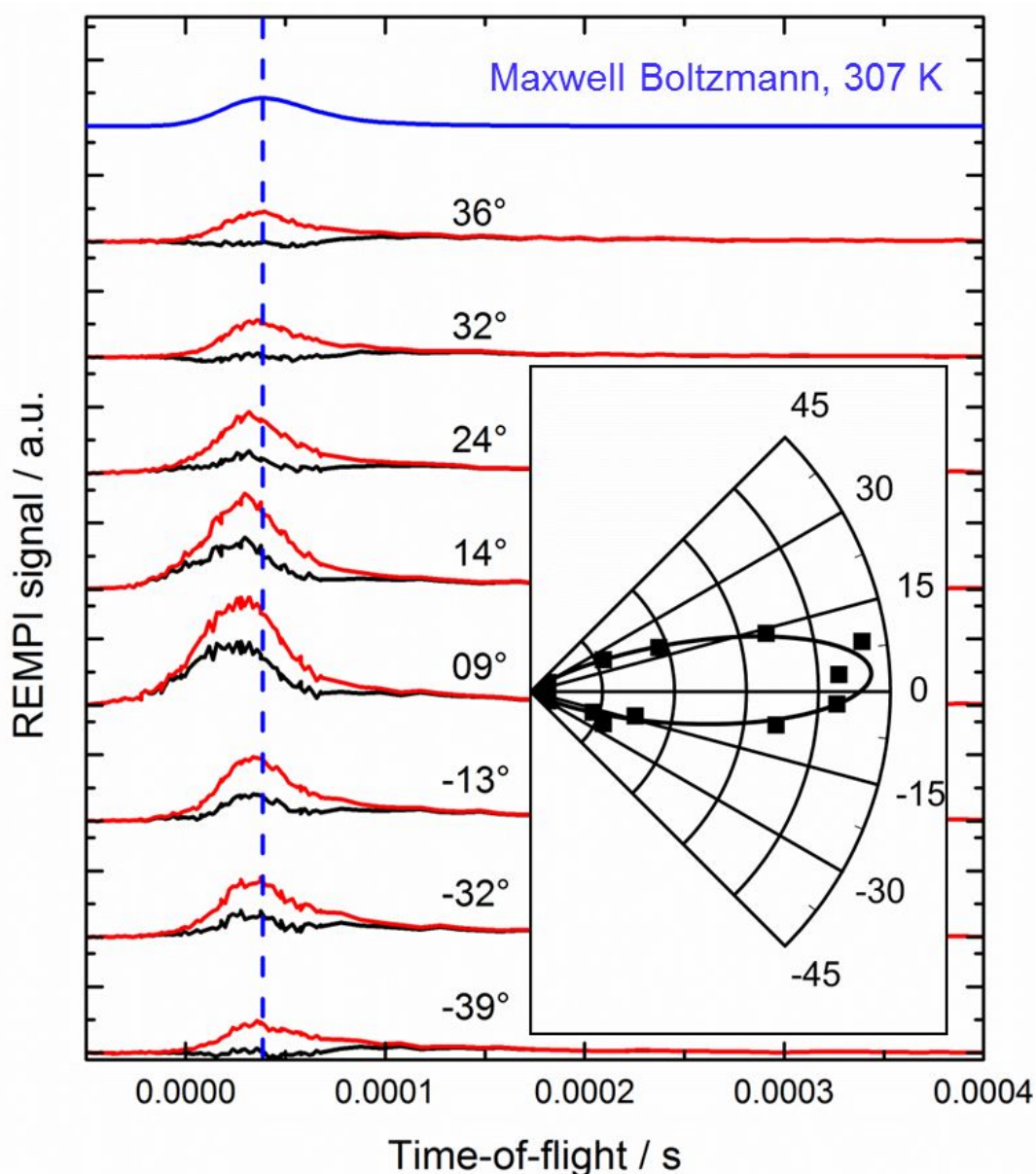


**Figure 7.11.:** Arrival time distributions of formaldehyde scattered from Au(111) at 0.33 eV incidence translational energy. The REMPI signal is shown as a function of the time-of-flight of the scattered molecules for different scattering angles as indicated in the figure (red lines). As a comparison a simulation of the arrival time distribution assuming a Maxwell-Boltzmann velocity distribution at the temperature of the Au crystal is shown in blue. The black traces are obtained by subtracting the expectation for the contribution of desorbing molecules from the arrival time distributions and represent a second component in the arrival time distribution. This analysis assumes that desorption follows a  $\cos(\theta)$  angular distribution as observed at lower incidence translational energy and that the flux at absolute scattering angles  $> 35^\circ$  can be attributed exclusively to trapping-desorption. The inset shows the angular distribution derived from integration of the arrival time distributions for the second component. Figure reproduced from reference [126] with permission from the PCCP Owner Societies.



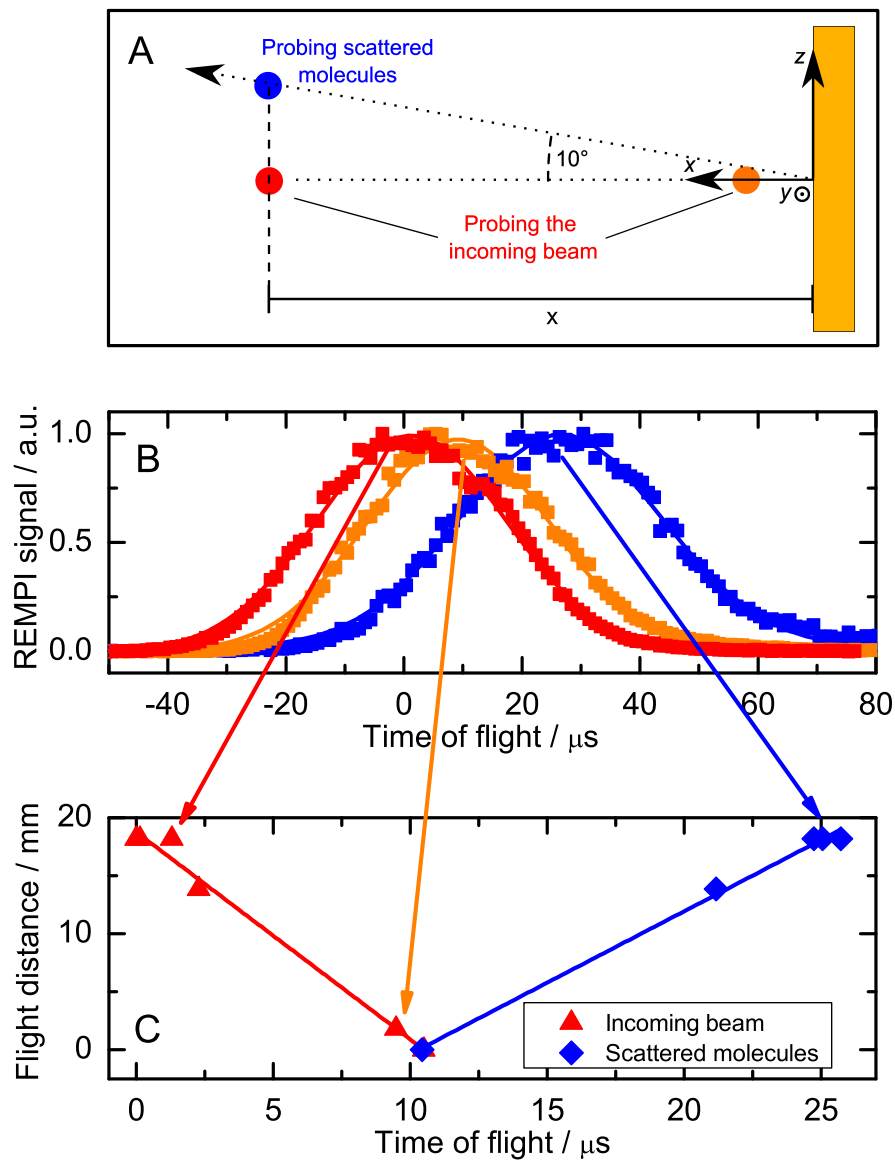


**Figure 7.12.:** Derivation of the most probable speeds of the incoming and scattered molecules. Panel A shows the scattering geometry used. The incoming beam propagates along the  $x$ -axis towards the surfaces. Its arrival time distribution is probed at several probe positions along this axis. Scattered molecules are probed at a constant scattering angle but at different distances from the position of the surface collision. Panel B shows the arrival time distributions for the incoming beam (red and orange squares) and the scattered beam (blue squares). The maximum points of the arrival time distributions can be obtained from Gaussian fits shown by the colored curves. These maximum points are plotted against the probe position as shown in panel C. The red line represents a linear fit to the data for the incoming beam (red triangles). This yields the most probable speed in the incoming beam. An extrapolation to zero flight distance allows the determination of the time of the collision. The time of the collision is included in the analysis of the data for the scattered molecules (blue squares). A linear fit represented by the blue line yields the most probable velocity of scattered molecules.

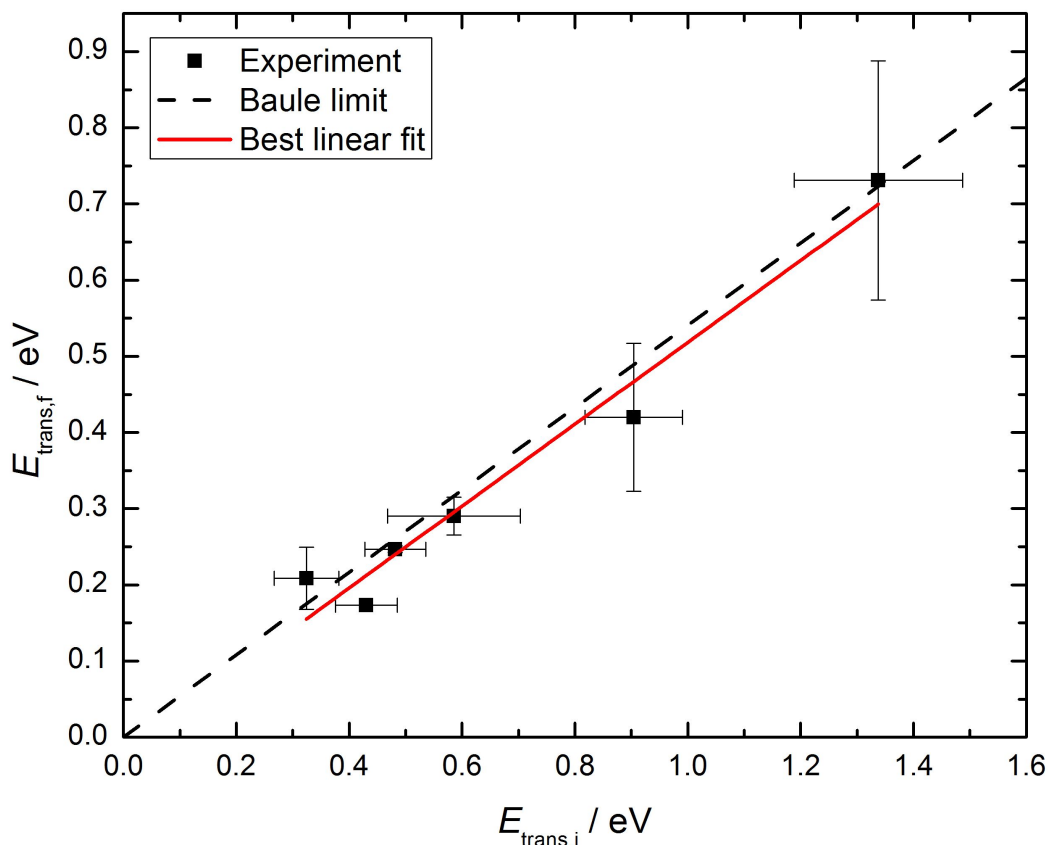


**Figure 7.13.:** Translational inelasticity in direct-scattering of formaldehyde from Au(111). The final translational energy of formaldehyde is plotted against the incidence translational energy. The experimental data is shown as black squares. The best linear fit to the data is represented by the red line. The dashed line shows the expectation for a simple Baule model. Figure adapted from reference [126] with permission from the PCCP Owner Societies.

line. This model assumes that the collision can be described by an impulsive collision between two cubes at the mass of formaldehyde and the mass of a Au-atom. Energy and momentum conservation yield  $(m_{\text{Au}} - m_{\text{H}_2\text{CO}})^2 / (m_{\text{Au}} + m_{\text{H}_2\text{CO}})^2 = 0.54$  for the ratio between final and incidence translational energy. This observation reflects the “memory effect” that is a characteristic of direct-scattering which means that the molecules’ final properties are directly influenced by the incidence parameters.

At incidence translational energies above 0.6 eV only direct-scattering can be clearly identified. Figure 7.14 shows the arrival time distributions for direct-scattering at 1.3 eV. In the presence of a dominating fast scattering channel the sensitivity for detection of a possible minor trapping-desorption channel is limited by the occurrence of an artifact

shown at the top of the figure in green. The maximum of this artifact clearly appears later in the molecule time-of-flight than would be expected for desorbing molecules. The artifact is identified by probing the arrival time distribution at different probe positions as discussed in Section 6.1.3. The artifact appears to be caused by secondary collisions with parts of the ion detector. It is present under conditions where the final translational energy in the direct-scattering channel is fast. Due to the velocity resolution of the MCP detector, this artifact can be easily discriminated in the ion time-of-flight from signal of the directly scattered molecules as shown in Section 3.1.2. However, due to the small velocity difference it is not resolvable from desorbing molecules in the ion time-of-flight. Although the maximum of the arrival time distribution of the artifact occurs later than the expected arrival of desorbing molecules, the rising edge of the artifact interferes with possible signal from desorbing molecules. Based on this observation it cannot be excluded that a trapping-desorption channel exists at incidence translational energies above 0.6 eV. Based on a comparison of the REMPI signal observed for the artifact at the expected arrival time of desorbing molecules and the direct-scattering signal, the branching ratio for trapping-desorption should be well below 10 %.

A comparison of the angular distribution for directly scattered molecules at 0.33 eV and 1.3 eV (see inset in Figure 7.11 and 7.14) shows that the distribution becomes even narrower if the incidence translational energy is increased. In general the distributions can be fitted using Equation 7.5.

$$N(\theta) = A \cos(\theta - \theta_0)^n \quad (7.5)$$

Here,  $N$  is the normalized flux obtained by integrating the observed arrival time distributions at a specific angle and  $\theta_0$  is the angle at the maximum  $N$ . The fit parameter  $n$  is directly related to the width of the distribution and  $A$  reflects the maximum integrated flux observed. Table 7.3 provides an overview of the best fit parameters derived for the different incidence translational energies.

**Table 7.3.:** The best fit parameters obtained from a fit to the angular distributions measured for directly scattered molecules are given for four incidence translational energies  $E_i$ .

$E_i / \text{eV}$	$n$	FWHM / °	$\theta_0 / ^\circ$
1.33	52.9	18.5	3.0
0.90	32.1	23.4	0.7
0.58	26.7	26.0	2.6
0.32	22.2	28.5	3.0

In summary, it is shown that both trapping-desorption and direct-scattering are present

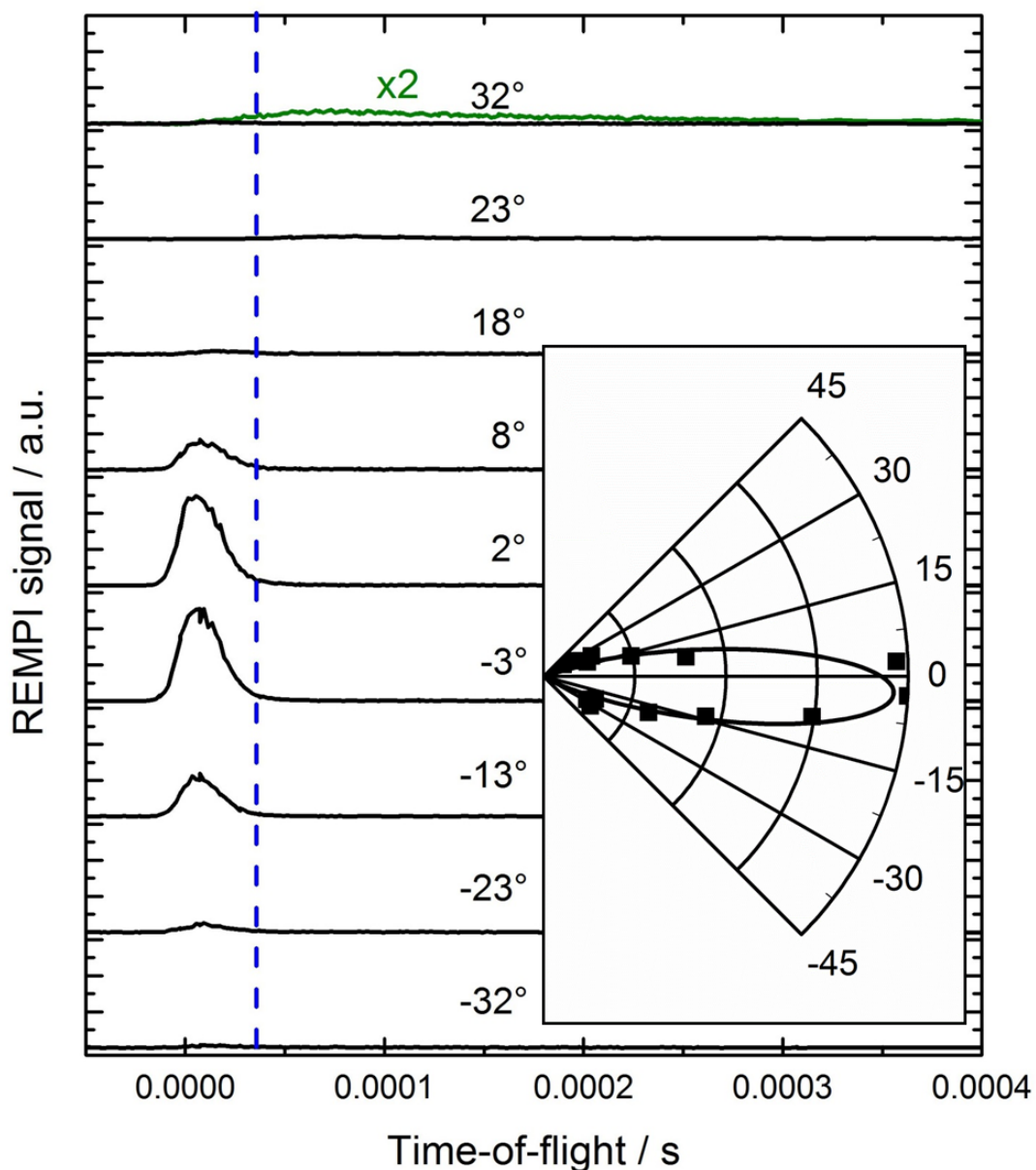


**Figure 7.14.:** Arrival time distributions of formaldehyde scattered from Au(111) at 1.3 eV incidence translational energy. The REMPI signal is shown as a function of the time-of-flight of the directly scattered molecules (black lines) as indicated in the figure. The REMPI signal is obtained by only integrating the signal at early ion time-of-flight associated with direct-scattering (peak B, see Figure 3.3 in Section 3.1.2). The blue line indicates the expectation for the maximum of the arrival time distribution assuming desorption after complete equilibration with the surface. The green line shows the arrival time distribution when integrating only the artifact (peak C, see Figure 3.3 in Section 3.1.2). The trace is enlarged by a factor of two and does not change strongly with the detection angle. The inset shows the angular distribution derived from integration of the arrival time distributions for the directly scattered molecules.

in the scattering of formaldehyde at Au(111). The branching ratio changes with incidence translational energy such trapping-desorption dominates the scattering process at low incidence translational energies, whereas direct scatter dominates at high incidence translational energies.

## Discussion

The angle-resolved arrival time distribution and the achieved separation between the direct-scattering and trapping-desorption channel using the different angular distributions and velocity distributions associated with these channels allows an estimation of the trapping probability. The trapping probability is defined as the ratio between the flux of the molecules undergoing trapping-desorption and the total scattered flux. The derivation of the trapping probabilities from the experimentally determined arrival time distributions uses the following assumptions and approximations. First, vibrational excitation is assumed to be negligible in the scattering process. The population of one quanta in mode 4 which is the lowest energy vibration has been probed by REMPI spectroscopy. However, there is no clear sign for vibrational excitation in the collision. Second, the assumptions used to separate direct-scattering from trapping-desorption applied in the section above have to hold. Namely, trapping-desorption follows a  $\cos(\theta)$  angular distribution regardless of the incidence translational energy and it dominates the scattering process at very large absolute scattering angles. Third, the measured density can be converted into flux by correcting by the velocity for the respective scattering channel as discussed in Section 5.2.2. Fourth, the REMPI scheme detects only molecules in  $K_a = 0$  and  $K_a = 1$  regardless of  $J$ . Thus, the calculation includes a correction for the measured distributions over  $K_a$  that is dramatically different for direct-scattering and trapping-desorption (see Section 7.3.4). The integration over all arrival times and scattering angles for both scattering channels gives the total flux of the respective channel. The calculations are performed using the angular distributions for direct-scattering given in Table 7.3. As already stated above the trapping probability can then be obtained as the ratio between the flux for trapping-desorption and the total flux.

Figure 7.15 shows the experimentally derived trapping probability as red squares for three different incidence translational energies. As discussed in the section above the occurrence of an artifact prevents the determination of the trapping probability at incidence translational energies above 0.6 eV. The trapping probability decreases with incidence translational energy. As a comparison the prediction of a hard cube model including a well depth<sup>[69]</sup> is shown (red line). The model is described in Section 2.5.1. The well

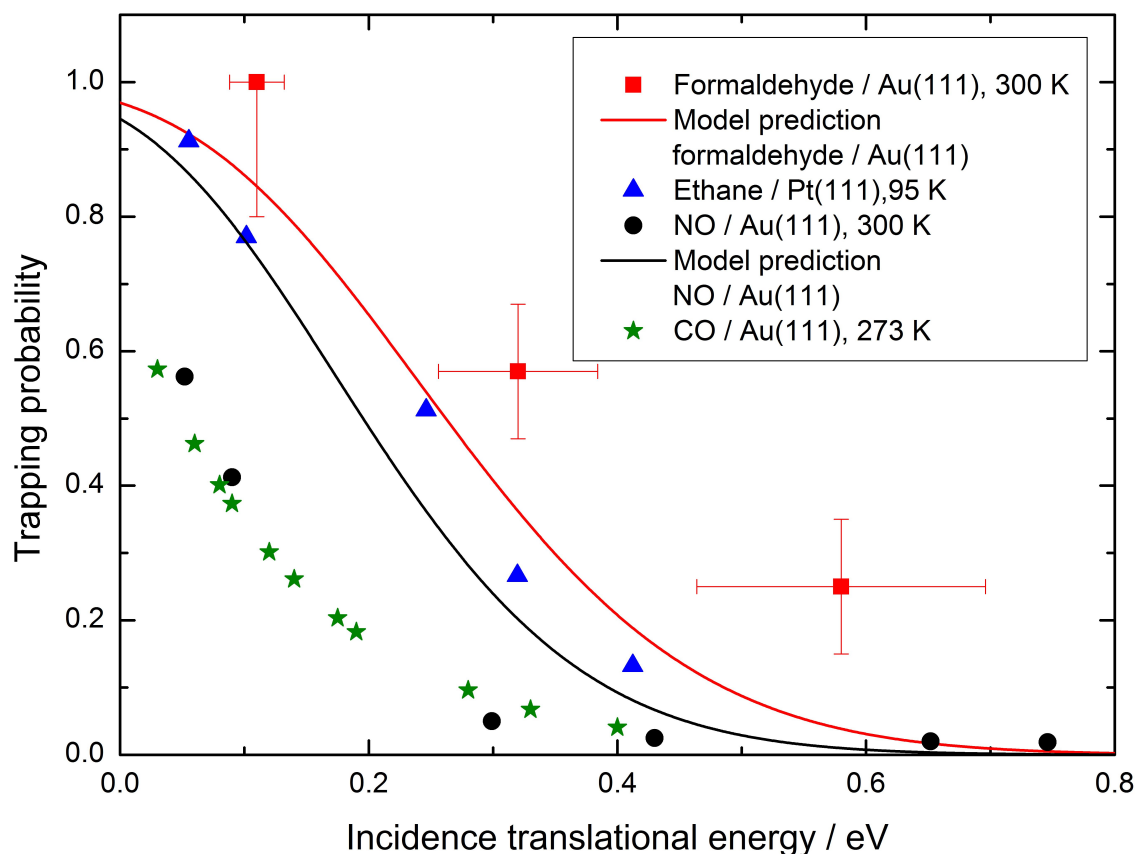


**Figure 7.15.:** Trapping probabilities as a function of the incidence translational energy. The experimentally derived trapping probability for formaldehyde at Au(111) (red squares) is plotted against the incidence translational energy. The prediction of a hard cube model with a well depth of 0.32 eV is shown as the red line. In addition, trapping probabilities determined for molecule/surface systems with similar masses and binding energies are plotted. Those are ethane/Pt(111)<sup>[71]</sup>, NO/Au(111)<sup>[64]</sup>, and CO/Au(111)<sup>[63]</sup>. For the NO/Au(111) surface system also the prediction of the hard cube model is shown as a black line. This model uses the desorption energy determined by TPD<sup>[113]</sup> as the well depth of the potential. Figure reproduced from reference [126] with permission from the PCCP Owner Societies.

### 7.3. Scattering of formaldehyde from Au(111)

depth is chosen as 0.32 eV resembling the desorption energy determined by temperature programmed desorption (see Section 7.1). The comparison shows that the model predicts less trapping than observed in the experiment. In addition, trapping probabilities for molecule/surface systems with molecular and surface atom masses as well as binding energies very similar to the formaldehyde/Au(111) system are plotted. It can be seen that the trapping probabilities for the diatomic molecules CO and NO at Au(111) are lower than the trapping probabilities observed for polyatomic molecules namely ethane at Pt(111) and formaldehyde at Au(111). This observation cannot be attributed to a mass effect since the masses of the projectiles and the surface atoms are very similar for these systems:  $m(\text{NO}) = m(\text{H}_2\text{CO}) = 30 \text{ u}$ ,  $m(\text{CO}) = 28 \text{ u}$ ,  $m(\text{Au}) = 197 \text{ u}$   $m(\text{Pt}) = 195 \text{ u}$ . Also the slightly higher binding energies observed for the polyatomic molecules cannot explain this effect. This is illustrated by a comparison of the prediction of the hard cube model for formaldehyde and NO/Au(111) surface scattering. The desorption energies used as the well depth are 0.24 eV for NO<sup>[113]</sup> and 0.32 eV for formaldehyde. The predicted trapping probabilities (red and black curve in Figure 7.15) differ only slightly which means that the large deviation does not originate from the different binding energies. The increased trapping probabilities observed for polyatomic molecules rather indicate that excitation of internal degrees of freedom are important in the trapping process. If initial translational energy is converted into excitation of internal degrees of freedom the molecule might lose its translational energy efficiently such that trapping is facilitated. This idea has already been mentioned in reference [72] where the trapping probabilities obtained in molecular beam studies for projectile/surface systems with atomic, diatomic, and polyatomic projectiles have been compared. As a practical descriptor for the efficiency of the trapping process the ratio  $E_{\text{trap},50\%}/\epsilon$  can be used to compare the different systems.  $E_{\text{trap},50\%}$  is the incidence translational energy at which 50 % of the molecules are trapped at the surface and  $\epsilon$  is the well depth, in most cases determined by TPD. Comparing the systems Ar/Pt(111), N<sub>2</sub>/W(100) and ethane/Ir(110)-(1x2) the authors found that  $E_{\text{trap},50\%}/\epsilon$  increases systematically from 38 % obtained for atom/surface scattering (Ar/Pt(111)) to 95 % obtained for polyatomic molecule scattering (ethane/Ir(110)-(1x2)) though the mass effect would favor trapping in the system with the atomic projectile. This supports the idea that excitation of internal degrees of freedom are important in the trapping process. The ratio  $E_{\text{trap},50\%}/\epsilon$  for the formaldehyde/Au(111) system is even 115 % illustrating the efficient trapping observed.

However, in the formaldehyde/Au(111) surface scattering experiment vibrational excitation could not be observed which makes it questionable if vibrational excitation can

significantly contribute to the trapping process. The important role of rotational excitation in the trapping process has been demonstrated in several diatomic/surface scattering experiments. In the scattering of oriented samples of NO at Ag(111) the trapping probabilities are enhanced if the O-atom points towards the surface. This is interpreted as a consequence of the larger amount of rotational excitation experienced in a collision where the O-atom points towards the surface compared to the reverse orientation.<sup>[138]</sup> Also in CO/Ni(111) surface scattering rotational excitation has been found to be important in the trapping process which has been referred to as rotational trapping.<sup>[74]</sup> An analysis of the rotational state distributions observed in the direct-scattering of formaldehyde suggests that a comparatively large amount rotational excitation, especially about the *a*-axis, can be observed. This will be shown in Section 7.3.4. Thus, the efficient trapping of formaldehyde at the Au(111) surface might be attributed to efficient transfer of initial translational energy to rotational energy.

### 7.3.4. Rotational state distributions

The rotational state distributions in formaldehyde/Au(111) surface scattering are derived from an analysis of the 1+1' REMPI spectra of scattered formaldehyde for different incidence translational energies of the molecule. The experimental procedure is described in Section 4.2.1. The spectra is acquired using laser fluences at which saturation effects in the REMPI signal as discussed in Section 7.2.2 can be neglected. The spectral analysis is described in Section 5.1.2. General information on the spectroscopy of the  $\tilde{A} \leftarrow \tilde{X} (4_0^1)$  band investigated is given in Section 2.2. The code for a MATLAB program used for the simulation of the  $\tilde{A} \leftarrow \tilde{X} (4_0^1)$  spectra is given in the Appendix A.1.

#### Low incidence translational energy

Figure 7.16 shows 1+1' REMPI spectra of scattered formaldehyde at an incidence translational energy of 0.11 eV (red line). The Au crystal temperature is maintained at the values  $T_s$  given in the figure. The simulated absorption spectra with a rotational state distribution described by a Boltzmann distribution at the surface temperature are plotted for comparison. The agreement for the three higher surface temperatures is convincing. A fit of a simulation using a Boltzmann distribution as the population model yields rotational temperatures that agree within the experimental error with the temperature of the surface. However, at  $T_s = 140$  K there are some disagreements between experiment and simulation. These are most likely caused due to a poor signal-to-noise ratio in the recorded



spectra. Nevertheless the agreement observed between the experimental spectrum and the simulation for the other surface temperatures can be interpreted as nearly complete equilibration of the molecular rotational degrees of freedom with the surface degrees of freedom. This is consistent with the arrival time distributions and angular distribution observed at 0.11 eV incidence translational energy indicating that the scattering process is governed by trapping-desorption.

### Rotationally resolved REMPI spectra in the direct-scatter regime

The experimental conditions for the acquisition of spectra are chosen such that directly scattered molecules dominate the signal. Considering the difference in angular distributions for the direct-scattering and trapping-desorption channel reported in Section 7.3.3 the probe positions used corresponding to narrow scattering angles and the short laser nozzle delay set to the peak of the arrival time distribution allow the detection of dominantly directly scattered molecules as long as the probability for direct-scattering and trapping-desorption are on the same order of magnitude.

Thus, the 1+1' REMPI spectra of the  $\tilde{A} \leftarrow \tilde{X} (4_0^1)$  band shown in Figure 7.17 correspond to spectra of directly scattered formaldehyde. The spectra are shown for incidence translational energies between 0.3-1.2 eV. At a first glance, an evolution of the spectra starting from the bottom of the figure (low incidence translational energies) to the top of the figure (high incidence translational energies) in two parts of the spectra is obvious. Firstly, the rise of the band heads at large wavenumbers becomes more pronounced as the incidence translational energy is increased. The band heads at the high wavenumber originate from  $K_a'' = 12 - 14$  corresponding to comparatively high rotational energies ( $\approx 1300 - 1900 \text{ cm}^{-1}$ ) which can be seen in detail in Figure 7.18. Thus, the population of these states associated with high  $a$ -axis rotational energy increases with incidence translational energy. In addition, the band is found to extend further to lower wavenumbers as the incidence translational energy is increased. This reflects that rotational excitation increases with incidence translational energy since many high- $J$  transitions are located in this spectral region. The analysis of the spectra is performed using a simple model with a small number of parameters for the rotational state distribution instead of employing a model with one parameter for the population of every rotational state. The population model is used for the simulation of REMPI spectra (see Section A.1). Finally, the parameters in the population model are optimized to yield the best agreement between experimental observation and simulation. This procedure has the advantage that the fit converges more easily and it prevents misinterpretation of congested spectral regions. One of the simplest models

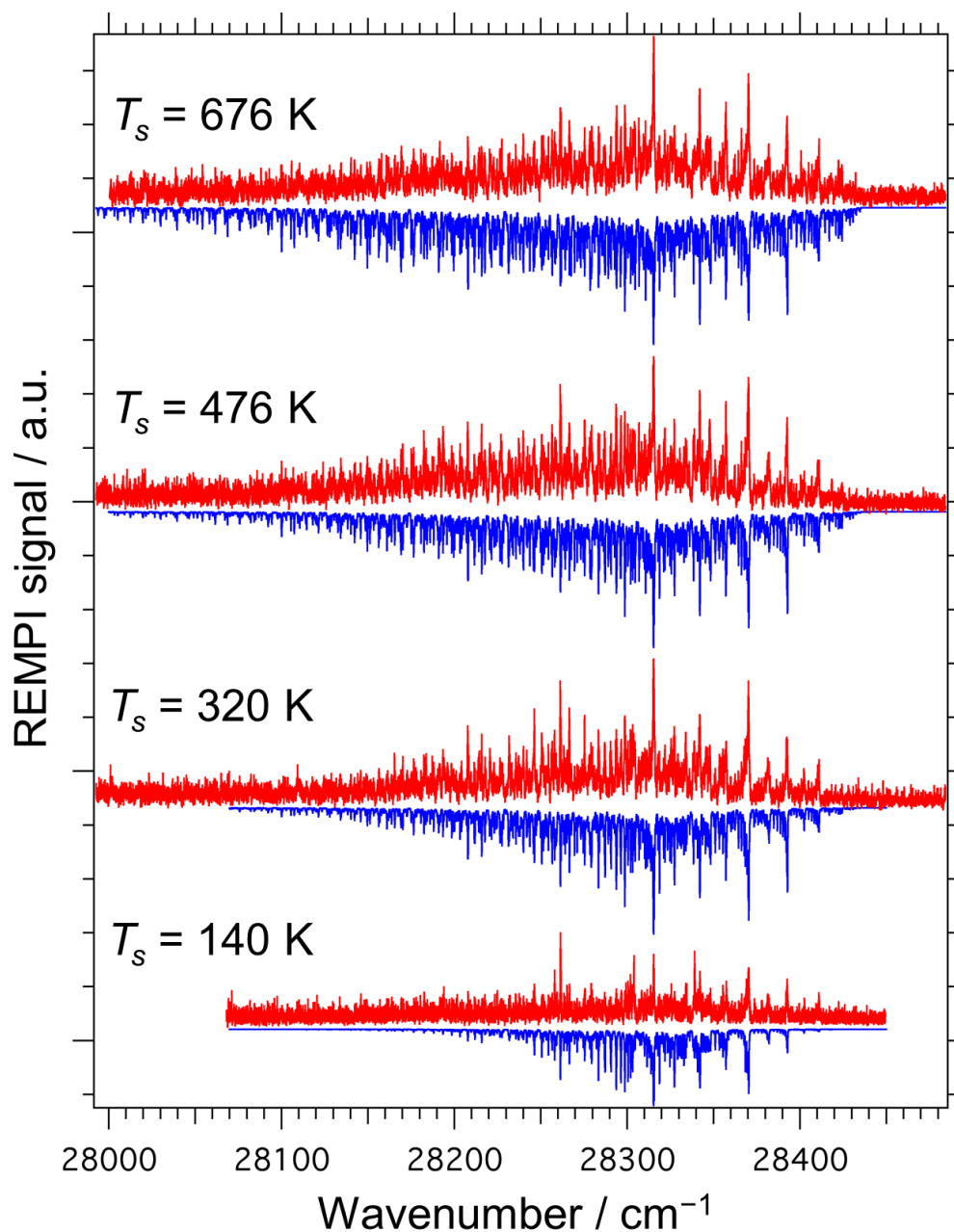


**Figure 7.16.:** 1+1' REMPI spectra of the  $\tilde{A} \leftarrow \tilde{X} (4_0^1)$  band at 0.11 eV incidence translational energy. The 1+1' REMPI spectra are shown (red curves) at different surface temperatures as indicated in the plot by  $T_s$ . A simulation of an absorption spectrum assuming a rotational temperature equal to the surface temperature is shown for each temperature in blue.

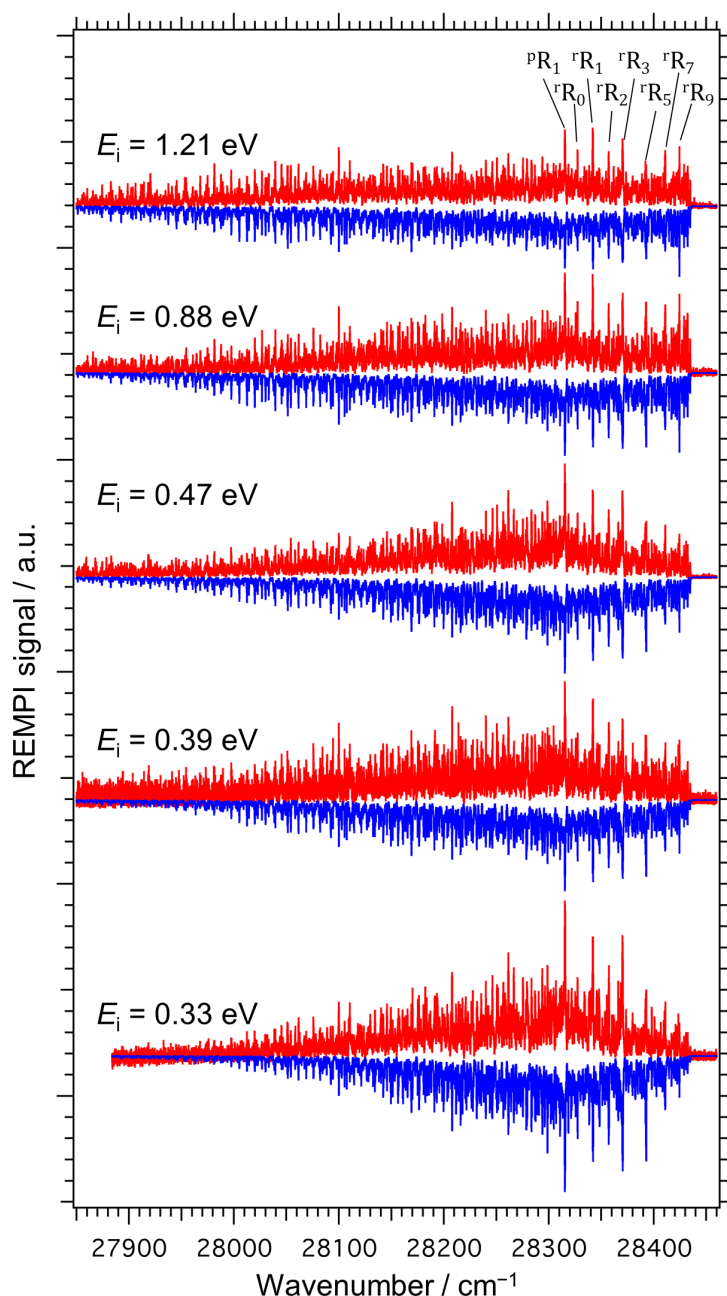


**Figure 7.17.:** 1+1' REMPI spectra of the  $\tilde{A} \leftarrow \tilde{X} (4_0^1)$  band corresponding to spectra of directly scattered formaldehyde at incidence translational energies between 0.3 eV and 1.2 eV. The experimentally observed spectra are shown in red. The incidence translational energy  $E_i$  is given for each spectrum in the figure. The simulations of absorption spectra of the  $\tilde{A} \leftarrow \tilde{X} (4_0^1)$  band are shown in blue. The simulations use the rotational state distribution described by Equation 7.6. The parameters in the rotational state distribution are derived from a fit to the experimentally observed spectra. In the fit procedure the constraints  $T_a = T_{bc}$  and  $\sigma_a = 850 \text{ cm}^{-1}$  are used. The prominent band heads of the  $\Delta K_a \Delta J_{K_a}$  branches are labeled in the spectrum recorded at 1.21 eV incidence translational energy. Figure taken from reference [139] - published by the PCCP Owner Societies.

## 7. Formaldehyde at Au(111) – results and discussion

is a Boltzmann distribution with an effective rotational temperature used as a fit parameter to account for the rotational excitation at different incidence parameters. However, in the following it will be shown that this model is insufficient to reproduce the observed spectra. Figure 7.18 shows the recorded REMPI spectra in the region of the  $^R R$  band heads (upper panel, red curve) at the highest incidence translational energy 1.21 eV. The disagreement with the simulation (lower panel, green curve) assuming a Boltzmann distribution at an effective rotational temperature is the largest. The best-fit effective rotational temperature to the whole spectrum is 1082 K. However, the comparison between the simulation and the observed spectrum in the band head region shows that transitions originating from comparatively high  $K_a''$  are dramatically underrepresented in the simulation. In order to account for the relative intensity observed for  $K_a'' = 10 - 15$  the rotational temperature would have to be increased by a factor of 3. However, this high rotational temperature is inconsistent with the overall band shape observed and in particular with the low intensity observed for transitions corresponding to states with high rotational quantum number  $J$  and low  $K_a$ . Thus, a model for the rotational state distribution has to include the possibility of different distributions over  $K_a$  and  $J$ . Motivated by the observation and treatment of non-Boltzmann distributions in diatomic<sup>[75]</sup> and linear polyatomic molecule<sup>[94]</sup> surface scattering the model used in this work describes the distribution over  $K_a$  as a sum of a Boltzmann component and a Gaussian term at high rotational energy. In this model the population  $P_i(J, K_a, K_c)$  of a certain rotational state  $i$  is described by Equation 7.6.

$$P_i(J, K_a, K_c) = N \cdot g_i \cdot \exp\left(\frac{-E_{bc,i}}{k_B T_{bc}}\right) \left( \exp\left(\frac{-E_{a,i}}{k_B T_a}\right) + S \cdot \exp\left(\frac{(E_0 - E_{a,i})^2}{\sigma_a^2}\right) \right) \quad (7.6)$$

Here,  $E_{a,i}$  and  $E_{bc,i}$  denote the rotational energy of a particular rotational state  $i$  about the  $a$ -axis, respectively the total rotational energy about the  $b$ - and  $c$ -axis. The effective rotational temperatures for the different axes  $T_a$  and  $T_{bc}$  are used as fit parameters. The Gaussian contribution is described by a scaling factor  $S$ , the center energy  $E_0$ , and a width parameter  $\sigma_a$  that can also be used as fit parameters.  $g_i$  is a degeneracy factor including  $M_J$  degeneracy and nuclear spin degeneracy. Finally,  $N$  is a normalization factor and is used as a fit parameter. The rotational energy about the  $a$ -axis can be approximated with a very small error as  $E_a \approx AK_a^2$ . In this approximation the rotational energy about the  $b$ - and  $c$ -axes is given by  $E_{bc} \approx E_{\text{tot}} - AK_a^2$ . If the constraints  $T_a = T_{bc}$  and  $S = 0$  are used, Equation 7.6 becomes a Boltzmann distribution. When the observed spectrum is fit to a simulation based on the population model of Equation 7.6, a high degree of correlation between the fit parameters is obtained. In order to reduce this correlation the

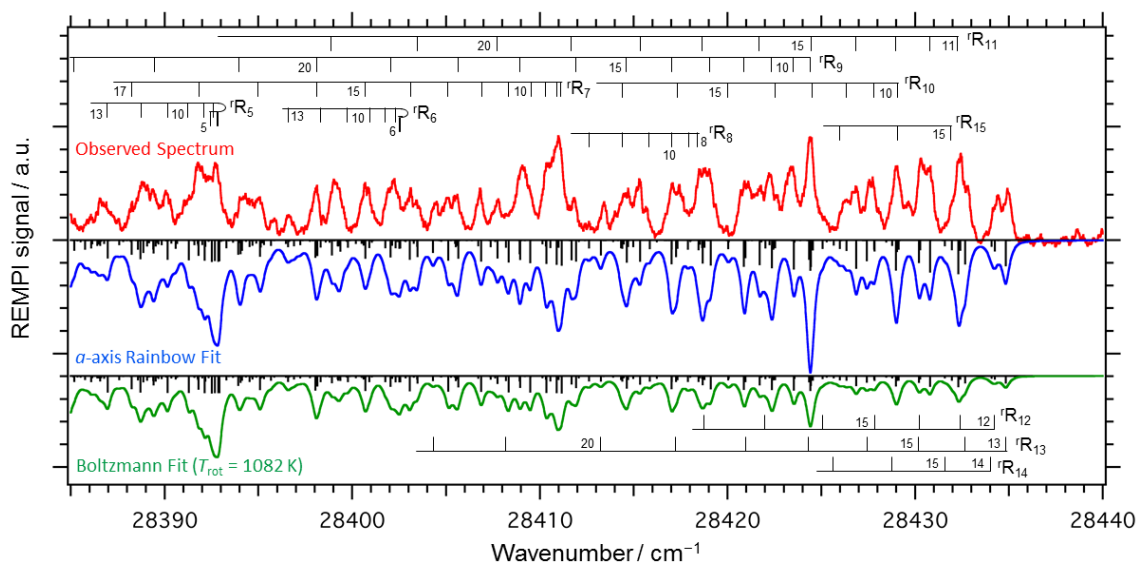


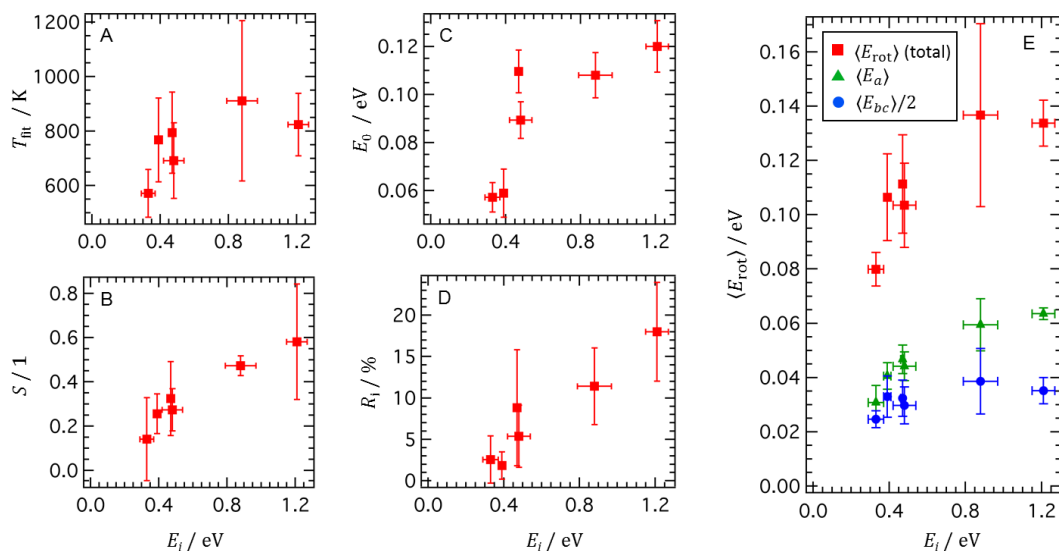
**Figure 7.18.:**  $1+1'$  REMPI spectrum of the  $\tilde{A} \leftarrow \tilde{X} (4_0^1)$  band in the band head region. The experimental spectrum at an incidence translational energy of 1.21 eV is represented by the red curve in the upper panel. The blue and green curve (middle and lower panel) represent simulations relying on the rotational state distribution described by two different models with the best fit parameters determined for a fit to the experimentally observed spectrum. The models for the population of the rotational states are based on Equation 7.6. Blue curve: In the fit procedure, the constraints  $T_a = T_{bc}$  and  $\sigma_a = 850 \text{ cm}^{-1}$  are used.  $E_0$ ,  $S$  and  $T_{bc}$  are used as fit parameters. Green curve: the model corresponds to a simple Boltzmann distribution which follows from Equation 7.6 by using the constraints  $T_{\text{rot}} = T_a = T_{bc}$  and  $S = 0$ . Figure taken from reference [139] - published by the PCCP Owner Societies.

## 7. Formaldehyde at Au(111) – results and discussion

following constraints are used. First, the effective rotational temperatures  $T_a$  and  $T_{bc}$  are set equal to another. Second, the width parameter for the Gaussian contribution is fixed at  $\sigma_a = 850 \text{ cm}^{-1}$  which is determined from a fit at an incidence translational energy of 1.21 eV. This model will be referred to below as the Gaussian model. The simulation based on the constrained population model using the best fit parameters yields a good overall agreement with the experimentally observed spectra regardless of the incidence translational energy (see Figure 7.17). In particular at high incidence translational energies the band head region is much better reproduced using the Gaussian model than using a Boltzmann distribution with a single effective rotational temperature (see Figure 7.18). An evaluation of the population model using the best fit parameters yields the average rotational energy about a specific axis  $q$  via Equation 7.7.

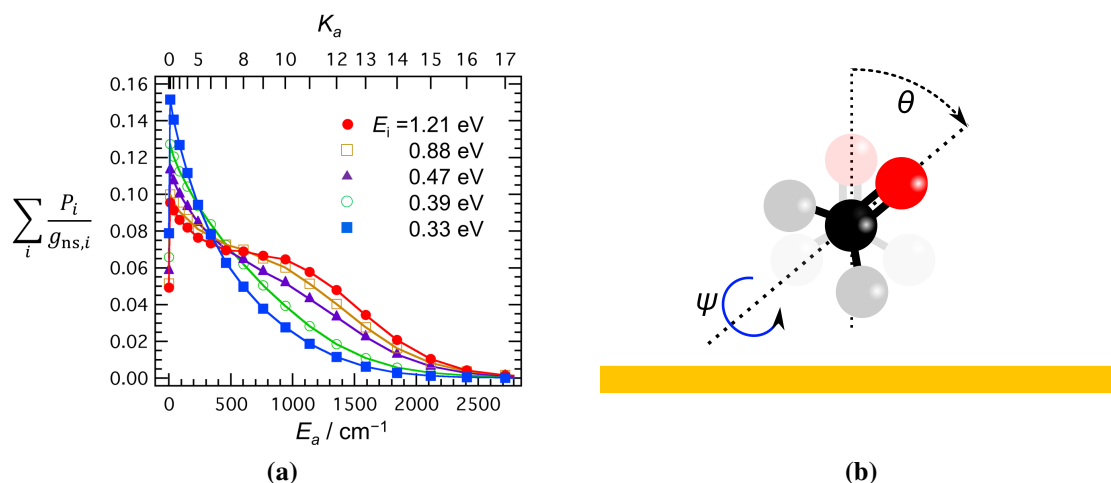
$$\langle E_q \rangle = \sum_i P_i E_{q,i} \quad (7.7)$$

Figure 7.19 provides an overview of the best fit parameters obtained and the derived average rotational energies as a function of incidence translational energy. The parameters are also given in the Appendix A.2. Firstly, the results of the fit confirm the conclusion obtained from the qualitative analysis of the spectra above that the average rotational energy increases with incidence translational energy. See panel E. This increase in rotational energy originates both from an increase of the effective rotational temperature  $T_{\text{fit}} = T_a = T_{bc}$  (see panel A) as well as the increasing importance of the Gaussian contribution. This is expressed by the increase of  $E_0$  and  $S$  with incidence translational energy (panel B and C). A comparison of the rotational excitation observed about the different axes reveals that regardless of the incidence translational energy on average more rotational excitation is experienced about the  $a$ -axis of the molecule than about either of the other two axes. The parameter  $R_i$  shown in panel D reflects the degree of improvement in the root mean square error (RMSE) if instead of using a Boltzmann model the Gaussian model is used.  $R_i$  can be calculated from the RMSE  $\Delta_G$  for a fit based on the Gaussian model and the RMSE  $\Delta_B$  for a fit based on the Boltzmann model via  $R_i = (\Delta_B - \Delta_G)/\Delta_B$ . The observed increase in  $R_i$  is consistent with the qualitative observation that the disagreement between the simulation using the Boltzmann distribution and the experimentally observed spectra in the band head region becomes more severe when the incidence translational energy is increased. This confirms that the distribution over  $K_a$ , shown in in Figure 7.20 a), cannot be described by a Boltzmann distribution especially at high incidence translational energies.



**Figure 7.19.:** Best fit parameters characterizing the rotational state distribution and derived mean rotational energies as a function of the incidence translational energy. Panel A: The effective rotational temperature  $T_{\text{fit}} = T_a = T_{bc}$  is plotted against the incidence translational energy  $E_i$ . Panel B: The scaling factor for the Gaussian term  $S$  is shown at different incidence translational energies. Panel C: The center rotational energy of the Gaussian term  $E_0$  is plotted against the incidence translational energy. Panel D: The degree of improvement in the root mean square error  $R_i$  when employing the Gaussian model instead of a Boltzmann model is plotted against the incidence translational energy. Panel E: The derived total average rotational energy  $\langle E_{\text{rot}} \rangle$  as well as the average rotational energy about the  $a$ -axis  $\langle E_a \rangle$  and the average rotational energy about the  $b$ - and  $c$ -axes per axis  $\langle E_{bc} \rangle / 2$  is shown at the different incidence translational energies investigated. Figure taken from reference [139] - published by the PCCP Owner Societies.

## 7. Formaldehyde at Au(111) – results and discussion



**Figure 7.20.:** a)  $K_a$  state distributions at different incidence translational energies. The  $K_a$  state distributions are calculated according to Equation 7.6 using the best fit parameters derived from a fit of the simulation to the experimental observed spectrum. Figure taken from reference [139] - published by the PCCP Owner Societies. b) Relevant Euler angles for the orientation of formaldehyde at a flat and structureless surface. The angle  $\theta$  defines the orientation of the C-O bond with respect to the surface normal. The angle  $\psi$  rotates the molecule about its  $a$ -axis. The configuration at  $\theta = \psi = 0^\circ$  is indicated by the transparent molecule.

A closer examination of the evolution of the best fit parameter  $E_0$  describing the center rotational energy of the Gaussian contribution to the  $K_a$  distribution reveals interesting dynamics. As the incidence translational energy is increased the center rotational energy increases. The observed component at high  $K_a$  in the  $K_a$  distribution and its incidence translational energy dependence are similar to the observations for rotational rainbows in the  $J$  distribution in diatomic molecule-surface scattering, for instance NO/Ag(111)<sup>[75]</sup> scattering. The rotational rainbows originate from maxima in the function describing the dependence of the final rotational angular momentum on the initial orientation angle.<sup>[78]</sup> As explained in Section 2.5.2, such a maximum causes many different orientations to result in the same final rotational state leading to a maximum in the  $J$  state distribution. In formaldehyde/Au(111) surface scattering a similar effect might be responsible for the  $K_a$  distribution. However, as a consequence of the asymmetric top nature of the formaldehyde molecule the process is more complex and even at a flat and structureless surface at least two Euler angles have to be considered, which are shown in Figure 7.20 b).  $\theta$  describes the angle between the C-O bond axis and the surface normal. The angle  $\psi$  describes the rotation of the molecule about its  $a$ -axis. The  $K_a$  distribution exhibiting the rainbow-like behavior describes the rotational excitation about this axis, which is stronger than the



excitation about the other two axes regardless of incidence translational energy. In the rainbow picture roots in the partial derivative of  $\partial \mathbf{J}_a / \partial \psi$  will cause a large population at the corresponding value of  $K_a$ . Here,  $\mathbf{J}_a$  denotes the  $a$ -axis projection of the classical angular momentum. These roots in the partial derivative of  $\partial \mathbf{J}_a / \partial \psi$  are related to extrema in the gradient of a potential energy surface describing formaldehyde/Au(111) surface scattering  $\partial V / \partial \psi$ . In the experiment a pronounced Gaussian contribution is observed suggesting that the rainbow  $a$ -axis rotational energy is similar over a wide range of  $\theta$ . Thus, also the gradients in the potential energy surface  $\partial V / \partial \psi$  should be similar for a large range of different  $\theta$ .

#### **The impact of rotational excitation on the trapping of formaldehyde**

As already discussed in Section 7.3.3, formaldehyde is efficiently trapped at the Au(111) surface. This is best visualized by a comparison to the NO/Au(111) system. Whereas a hard cube model overestimates the trapping probability in NO/Au(111) surface scattering it underestimates the probability for trapping in formaldehyde/Au(111) surface scattering. The trapping probability of NO at Au(111) drops to 50 % at an incidence translational energy corresponding to 23 %<sup>[64]</sup> of the desorption energy determined by TPD<sup>[113]</sup>. On the other hand, the trapping probability of formaldehyde at Au(111) drops to 50 % at an incidence translational energy corresponding to 115 % of the desorption energy determined by TPD. In Section 7.3.3 it was speculated whether rotational excitation promotes the trapping process by efficient conversion of translational energy into rotational excitation and subsequent equilibration at the surface. Clearly, this process cannot be monitored directly with the available experimental techniques. However, the rotational energy distributions observed in direct-scattering show at least how efficiently a molecule is rotationally excited at the surface. Figure 7.21 shows the rotational energy distribution in the direct-scattering of formaldehyde and NO from Au(111) at similar incidence translational energies at around 0.5 eV. These are derived from the experimentally determined rotational state distributions by adding the population weights for states in a certain rotational energy window with a size of 0.02 eV. The rotational state distribution for NO/Au(111) surface scattering is taken from reference [12]. As shown in the figure formaldehyde experiences much more rotational excitation than nitric oxide at the Au(111) surface. This is consistent with the idea that the enhanced trapping probability of formaldehyde at Au(111) is caused by efficient conversion of translational energy into rotational excitation.

## 7. Formaldehyde at Au(111) – results and discussion

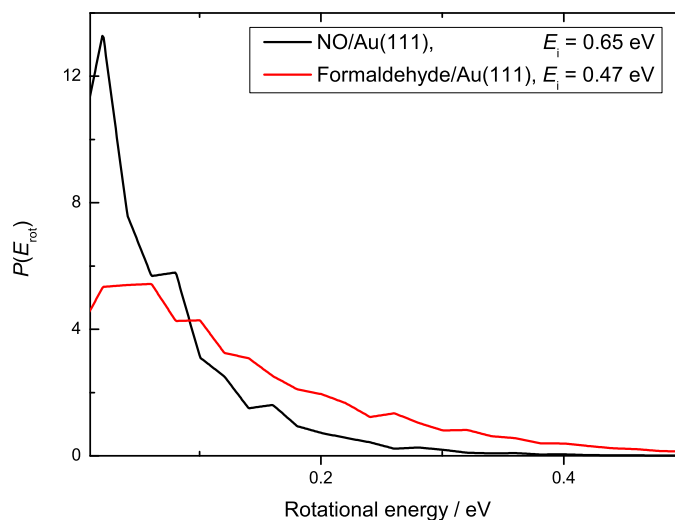


**Figure 7.21.:** Final rotational energy distributions observed in formaldehyde and NO/Au(111) surface scattering. The normalized rotational energy distributions  $P(E_{\text{rot}})$  are shown for formaldehyde (red) and NO scattering (black). The incidence translational energy  $E_i$  is indicated in the plot legend. The distributions are derived from the rotational state distributions as described in the text. The data for NO/Au(111) surface scattering is taken from reference [12].

### 7.3.5. Comparison of experimentally derived rotational state distributions to predictions of classical trajectory calculations

In order to gain insight into the dynamical behavior causing the rotational state distributions observed in the experiment, classical trajectory calculations on the formaldehyde-Au collisions are performed using a MATHEMATICA notebook given in the Appendix A.3. In these calculations formaldehyde is assumed to be a rigid rotor with the geometry given in reference [140]. Two different potential energy surfaces are used. In a first approach the interaction between the surface and the molecule is treated as the repulsion between a hard wall and a molecule consisting of hard spheres located at the position of the atoms with the radii corresponding to the van der Waals radii of the atoms. In a second approach the interaction is described by Lennard-Jones potentials between the atoms in the formaldehyde molecule and an Au atom at the surface. The Lennard-Jones parameters are taken from reference [141]. However, the  $\epsilon$  parameter for Au is scaled by a factor of 1800 such that the global minimum of the potential energy surface resembles the desorption energy measured in the TPD experiment. This potential is referred to below as the LJ-potential. The surface motion is modeled by a surface harmonic oscillator in which the force constant is calculated from the Debye frequency of gold. This oscillator is

driven by the force perpendicular to the surface resulting from the repulsion or attraction of the molecule at the surface.

Initially, the molecule is set to a randomly determined distance between 10 Å and 12 Å from the surface. The molecule's initial velocity is perpendicular to the surface and can be adjusted to correspond to different incidence translational energies. The initial orientation distribution is isotropic and the molecule's incidence rotational energy is set to zero. The motion of the surface at a finite temperature is modeled by providing an energy of  $1/2k_B T$  for the motion of the surface harmonic oscillator perpendicular to the surface where  $T = 300$  K is used. A trajectory is calculated by numerical solution of the equations of motion in steps of 1 fs over a total integration time of 2400 fs. In total, 10000 trajectories are calculated per incidence translational energy. Trajectories in which the final center of mass of the molecule is at distances less than 8 Å are counted as trapped and are discarded from the analysis.

Final rotational energy distributions are obtained by binning the trajectories according to their rotational energy with a bin size of 0.02 eV. Note that during the torque-free motion that occurs after the molecule-surface interaction, the total rotational energy is conserved. However, the rotational energy about the different axes will be time dependent according to Equations 7.8-7.10 for torque-free motion.<sup>[142]</sup>

$$I_{aa}\dot{\omega}_a = \omega_b\omega_c(I_{bb} - I_{cc}) \approx 0 \quad (7.8)$$

$$I_{bb}\dot{\omega}_b = \omega_c\omega_a(I_{cc} - I_{aa}) \quad (7.9)$$

$$I_{cc}\dot{\omega}_c = \omega_a\omega_b(I_{bb} - I_{cc}) \quad (7.10)$$

Here,  $\omega_i$  is the angular velocity about a certain axis of the molecule and  $I_{ii}$  are the corresponding moments of inertia. For formaldehyde the moments of inertia are  $I_{cc} \approx I_{bb} \gg I_{aa}$ . In the approximation  $I_{cc} \approx I_{bb}$ , the change of the angular velocity about the  $a$ -axis is zero and thus the rotational energy about the  $a$ -axis  $E_a$  is conserved. However,  $\omega_b$  and  $\omega_c$  are time-dependent such that only  $E_{\text{tot}} - E_a = E_b + E_c$  is conserved.<sup>[142]</sup> In the following, the rotational energy about the  $a$ -axis  $E_a$  and the average rotational energy about the  $b$ - and  $c$ -axes  $(E_b + E_c)/2$  will be compared. Figure 7.22 provides an overview of the results obtained from the classical trajectory calculations using the LJ-potential. In Figure 7.22a) the distribution over the rotational energy about the  $a$ -axis  $E_a$  is shown for three different incidence translational energies. As the incidence translational energy is increased an increasing number of trajectories lead to high final rotational energies about

## 7. Formaldehyde at Au(111) – results and discussion

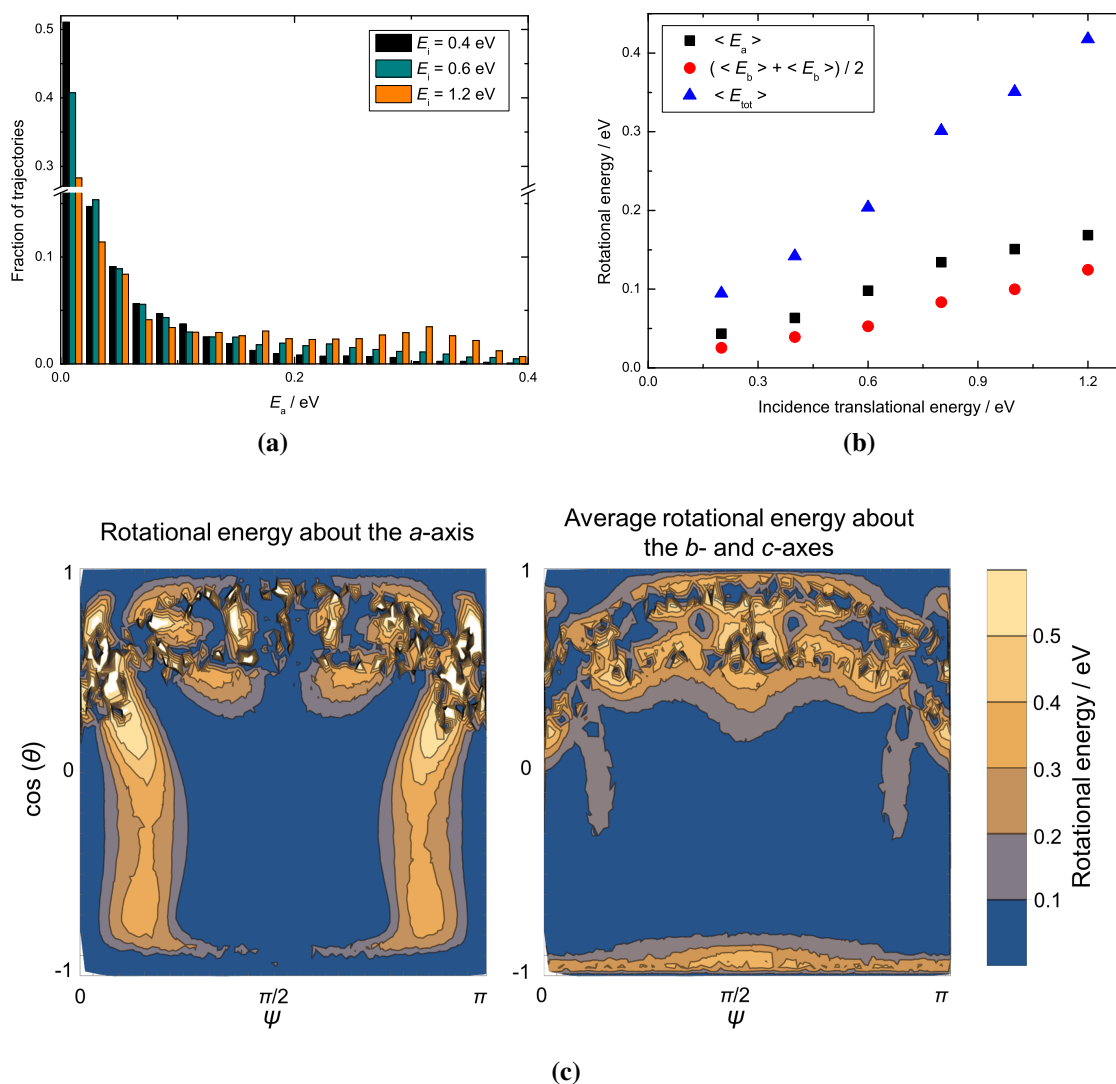


**Figure 7.22.:** Results of the classical trajectory calculations using the LJ-potential. a) The distribution for the rotational energy about the  $a$ -axis is plotted for three different incidence translational energies as indicated in the plot legend. b) The mean total rotational energy  $\langle E_{tot} \rangle$  as well as the mean rotational energy about the  $a$ -axis  $\langle E_a \rangle$  and the mean average rotational energy about the  $b$ - and  $c$ -axes  $(\langle E_b \rangle + \langle E_c \rangle)/2$  are plotted against the incidence translational energy. c) The achieved rotational excitation for specific axes is plotted against the initial Euler angles  $\theta$  and  $\psi$ . The left panel shows the rotational energy about the  $a$ -axis. The right panel displays the time-averaged rotational energy about the  $b$ - and  $c$ -axes  $(E_b + E_c)/2$ . The incidence translational energy is 1.2 eV. The color code for the contour plots is given on the right side of the figure.

the  $a$ -axis such that at incidence translational energies above 0.6 eV a second maximum can be clearly identified in the distribution. In contrast, no such second maximum can be identified in the distribution over  $(E_b + E_c)/2$  in the investigated range of incidence translational energies between 0.2 and 1.2 eV. Figure 7.22b) shows the mean rotational energies about the different axes as well as the mean total rotational energy as a function of the incidence translational energy. The rotational excitation about the  $a$ -axis is in general found to be larger than the average rotational excitation about the  $b$ - and  $c$ -axes. These results are qualitatively in agreement with the experimental observations. See Figures 7.19 and 7.20a). As in the simulation, in the experiment the rotational excitation about the  $a$ -axis is observed to be stronger than about the  $b$ - and  $c$ -axes and the distribution over  $K_a$  exhibits a non-Boltzmann behavior that becomes more pronounced when the incidence translational energy is increased. This qualitative agreement encourages an interpretation of the experimental data using information derived from the trajectory calculation. Figure 7.22c) shows the dependence of the final rotational energy about the different axes on the initial Euler angles describing the orientation of the molecule. The definition of the Euler angle used can be seen in Figure 7.20c).  $\theta$  describes the orientation of the C-O bond internuclear axis ( $a$ -axis) with respect to the surface normal. When  $\theta = 0$  ( $\cos(\theta) = 1$ ) the hydrogen atoms are pointing towards the surface.  $\psi$  describes the rotation about the  $a$ -axis. When  $\theta = \pi/2$  and  $\psi = 0$ , the  $b$ -axis, which lies in the plane of all atoms perpendicular to the C-O bond, is parallel to the surface normal. The left panel shows that a large amount of excitation about the  $a$ -axis is achieved if  $\psi$  is between  $15^\circ$  and  $35^\circ$ , relatively independent of  $\theta$ . The trajectory calculations show that these orientations dominate the second maximum in the distribution over the  $a$ -axis rotational energy. On the other hand, rotational excitation about the  $b$ - or  $c$ -axis occurs especially for orientations when  $\theta$  is close to  $\pi$  and if  $\theta$  is between 0 and  $\pi/2$  as shown in the right panel.

Thus, the trajectory calculations indicate that the non-Boltzmann nature of the  $a$ -axis rotational energy distribution observed in the experiment originates from a rotational rainbow that occurs over a large continuous range of different  $\theta$  due to roots in  $\partial \mathbf{J}_a / \partial \psi$ . Furthermore, both in the experiment and in the trajectory calculations the mean final rotational energy about the  $a$ -axis is higher than the average mean rotational energy about the  $b$ - and  $c$ -axes. This remains true even if a purely repulsive hard wall potential is used in the trajectory calculations. This indicates that the preferential excitation about the  $a$ -axis observed in the experiment is related to the “shape” of the molecule and should be largely insensitive to the molecule-surface attraction.

A quantitative comparison between the mean rotational energies determined in the

## 7. Formaldehyde at Au(111) – results and discussion

experiment and in the trajectory calculations shows that the rotational excitation observed in the experiment is largely overestimated in the calculation. This can also be seen by comparing the  $a$ -axis rotational energy distributions derived from the rotational state population model obtained in the experiment to the distribution obtained from the classical trajectory calculation shown in Figure 7.23. Note that the experimental  $a$ -axis rotational energy distribution is obtained from Equation 7.6 by using the best-fit parameters given in Table A.1, integrating over the rotational energy  $E_{bc}$ , dividing by the nuclear spin degeneracy, and transforming the distribution over  $K_a$  into an energy distribution using the Jacobian  $\frac{dK_a}{dE_a} \approx \frac{1}{2A} \sqrt{\frac{A}{E_a}}$ . The observed deviation between the experiment and the outcome of the classical trajectory calculation has two possible origins. First, the model potential might not be accurate enough. Second, the description of the surface atom motion as a harmonic oscillator might lead to an unreasonable high rotational excitation. In particular, a behavior observed in a comparatively high amount of trajectories is suspicious: A molecule is highly rotationally excited and at the same time loses a lot of its initial translational energy to the surface such that it stays for a longer time at the surface but suddenly leaves again. A possible explanation is that the surface oscillator is not damped such that energy can be transferred back to the molecules leading to an underestimation of trapping and an overestimation of rotational excitation. Even if trapping is not important this might lead to unphysically high excitation of molecular degrees of freedom with respect to the excitation of surface degrees.

Thus, based on the quantitative discrepancy described above a more detailed analysis of the results of the trajectory calculations regarding the trapping probabilities and the translational inelasticity will not lead to reliable results. A more accurate calculation based on an *ab initio* derived potential energy surface would be desirable to gain more insights into the origin of the high trapping probability and the rotational state distribution observed in the experiment. However, this is beyond the scope of this experimental work.

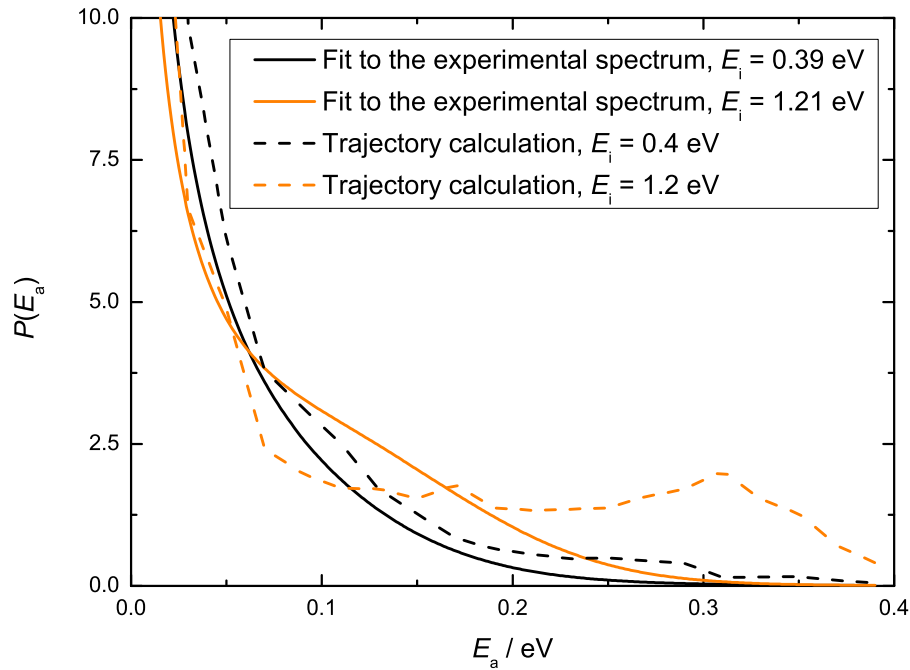


**Figure 7.23.:** Experimental and theoretical  $a$ -axis rotational energy distribution. The solid curves display the experimentally derived  $a$ -axis rotational energy distribution whereas the dashed curves display the results of the trajectory calculations. The incidence translational energies are given in the plot legend. The experimental distribution is derived from the population model given in Equation 7.6 using the best fit parameters provided in the Appendix A.2. Note that the Jacobian is used to transform the  $a$ -axis rotational state distribution to the  $a$ -axis rotational energy distribution shown in the figure. Here, the approximation  $\frac{dK_a}{dE_a} \approx \frac{1}{2A} \sqrt{\frac{A}{E_a}}$  is used.





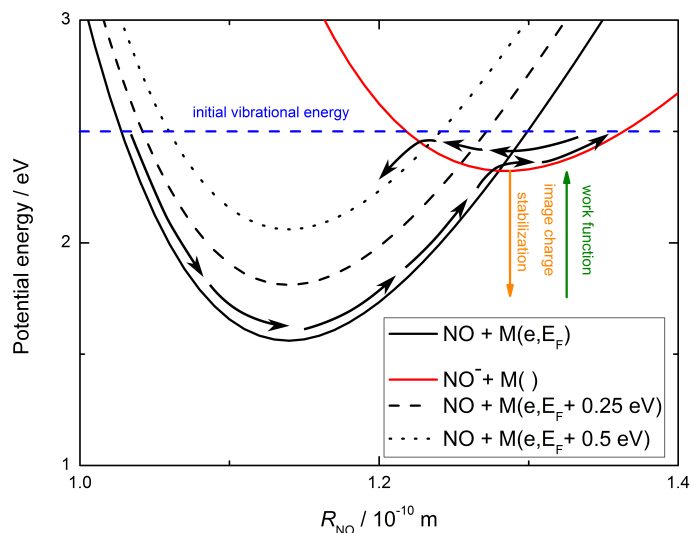
## 8. Conclusions and outlook

### Scattering of highly vibrationally excited nitric oxide

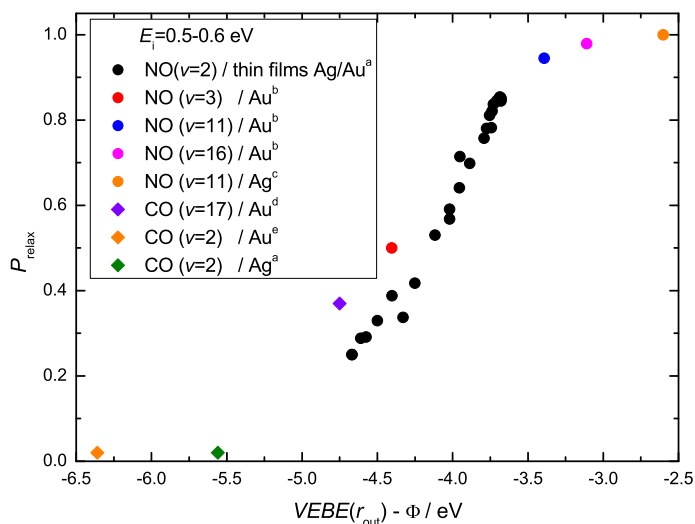
The time-of-flight experiments on highly vibrationally excited NO/Au(111) surface scattering accompanying vibrational multi-quantum relaxation presented in this work provide an important missing piece of information for this extensively studied showcase system for nonadiabatic effects. The coupling between final translational and rotational energy as well as the coupling between vibrational energy loss and the final translational energy in the surface scattering process are shown to be similar for initially highly vibrationally excited nitric oxide and moderately<sup>[89,101]</sup> vibrationally excited nitric oxide. However, the experiments presented in this work allow the investigation of scattering channels differing by a much larger amount of vibrational energy loss. This allows the conclusion that a constant fraction of the vibrational energy loss is transferred to final translational energy. The efficiency of this process is found to be enhanced by an increase of the incidence translational energy which is a strong indication that this process is mediated by electrons. Moreover, the knowledge of the coupling between the molecular degrees of freedom allows the calculation of the energy lost to the surface. In the following, this is shown for one of the most probable scattering processes in NO( $v_i = 11$ )/Au(111) surface scattering at an incidence translational energy of 0.58 eV: NO( $v_i = 11, J_i = 0.5$ )  $\rightarrow$  NO( $v_s = 6, J_s = 13.5$ ). The initial vibrational energy is 2.48 eV and the initial rotational energy is 0.00 eV. The molecule experiences rotational excitation corresponding to 0.04 eV and loses 1.03 eV vibrational energy. After the scattering event the molecule has a final translational energy of 0.38 eV. Thus an energy of 1.19 eV is converted from molecular degrees of freedom to surface degrees of freedom. Using the information on the translation-to-vibration coupling as well as the assumption that the phonon coupling is described by the Baule model, the energy lost in the collision can be divided into two parts. 0.31 eV is transferred to phonons and 0.88 eV to electrons.

Furthermore, a comparison of experiments of highly vibrationally excited NO/Ag(111) and Au(111) surface scattering reveals the influence of surface properties on the relaxation process. Vibrational relaxation is much more efficient at Ag(111) than at Au(111). Within

## 8. Conclusions and outlook



(a)



(b)

**Figure 8.1.:** a) Sketch of the nonadiabatic multi-quantum vibrational relaxation. The potentials<sup>[52]</sup> for the neutral (black) and anionic (red) species at a molecule-surface distance of 2 Å over an hcp site and an N-atom down orientation are shown as a function of the N-O bond length. An electronic excitation in the metal is sketched by shifting the neutral curve upwards by 0.25 eV (dashed line) and 0.5 eV (dotted line), respectively. The initially available vibrational energy is indicated by the blue dashed line. A possible trajectory is sketched by the black arrows. The effect of the work function and the image charge stabilization on the position of the anionic potential are indicated by the green and the orange arrow. b) Vibrational relaxation probabilities of NO and CO at noble metal surfaces. The incidence translational energy is 0.5-0.6 eV. The probability of vibrational relaxation for different molecule-surface systems is plotted against the parameter  $VEBE(r_{out}) - \Phi$ . The initial vibrational quantum number  $\nu$  is given in the plot legend for each experiment. The relaxation probabilities for the different systems are taken from references a:[19], b:[6], c: this work, d:[143], and e:[101].

the mechanistic picture developed in references [6, 11] this effect can at least in great part be ascribed to the effect of the work function of the surface. Figure 8.1a) sketches how the work function influences the vibrational energy loss. The black arrows in the figure show a possible pathway leading to vibrational relaxation via energy transfer to an electron. The diabatic potentials are shown as a function of the vibrational coordinate. In a first step the anion is formed. Then, the anion undergoes nonadiabatic transitions (the trajectory follows the anionic diabat). Finally, the electron is transferred back to an excited level of the metal, resulting in a neutral species with less vibrational energy. A lower work function leads to a shift of the anionic potential to lower energies. If the work function is lowered, the anion is formed with more energy in the vibrational coordinate which makes nonadiabatic transitions more likely. Hence, more efficient vibrational relaxation takes place, which explains the stronger relaxation at the Ag(111) surface. Following this concept, the magnitude of the relaxation probability as well as the amount of vibrational energy loss in scattering experiments of CO<sup>[19,101,143]</sup> and NO<sup>[6]</sup> in different initial vibrational states from noble metal surfaces can be understood considering the stabilization of the anion. This is shown in Figure 8.1b). The stabilization of the anionic species with respect to the neutral species can be quantified by the parameter  $VEBE(r_{\text{out}}) - \Phi$ . Here,  $\Phi$  is the work function of the surface. As discussed above, the lower the work function, the more the anion is stabilized.  $VEBE(r_{\text{out}})$  is the vertical electron binding energy corresponding to the potential difference between neutral and anionic species at the outer turning point of the neutral potential in the gas phase. This parameter expresses that the anion is in general more stable at larger N-O bond lengths and takes into account that molecules with high vibrational energy exhibit the maximum probability near the classical outer turning point. As shown in the figure the relaxation probability for the different systems is highly correlated with the parameter  $VEBE(r_{\text{out}}) - \Phi$ , which strongly suggests that the stabilization of the anion is crucial to the relaxation process.

Preliminary experiments at a germanium surface indicate much less efficient vibrational relaxation of initially highly vibrationally excited NO than observed at the two investigated metal surfaces, even though the work function of the Ge(111) surface is similar to the one of the Ag(111) surface. A part of this effect can be attributed to the lower image charge stabilization at the semiconductor surface, which is predicted by Equation 6.1 to be only 88 % of the image charge stabilization experienced at a metal surface. However, this finding is probably not sufficient to explain the observed differences in the vibrational relaxation efficiency. It remains an open question whether these differences are caused by the missing electronic states in the band gap of germanium. This emphasizes the need for

## 8. Conclusions and outlook

a quantitative *ab initio* theory correctly predicting multi-quantum vibrational relaxation at surfaces. However, it remains a challenge to obtain accurate potential energy surfaces, which are needed as a basis for these theories. Up to now, it could not be conclusively verified whether the IESH approach, designed for the treatment of nonadiabatic effects in multidimensional systems, provides an accurate description of vibrational relaxation of NO at metal surfaces.<sup>[16]</sup> In this context, the nice agreement between the experimental observations for highly vibrationally excited NO/Au(111) surface scattering and the theoretical predictions of a Monte Carlo wave packet study<sup>[87]</sup> on a model potential should be highlighted. It might be interesting to perform IESH calculations using this model potential to test whether the description of nonadiabatic effects by the IESH approach is correct.

### Formaldehyde

The 1+1' REMPI scheme, using the  $\tilde{A} \leftarrow \tilde{X}$  transition developed as a part of this work, enables rotationally resolved detection of ground electronic state formaldehyde. This detection method is successfully tested for formaldehyde samples with comparatively high amount of rotational excitation as observed for scattering processes with high incidence translational energy. Together with the presented time-of-flight experiments using 2+1 REMPI spectroscopy via the 3  $p_x$  Rydberg state, these techniques allow the trapping-desorption and direct-scattering channels in ground vibrational state formaldehyde/Au(111) surface scattering to be characterized. Though formaldehyde is weakly bound to the Au(111) surface (the desorption energy is determined to be  $0.32 \pm 0.02$  eV), trapping-desorption is found to dominate up to an incidence translational energy of  $0.37 \pm 0.07$  eV. This observation disagrees with the hard cube model. Together with the comparatively "hot" rotational state distribution observed in direct-scattering, this provides a strong indication that conversion of incidence translational energy into rotational energy is crucial in the trapping process of formaldehyde at elevated incidence translational energies. In this work the first state-resolved characterization of rotational dynamics in the surface scattering of an asymmetric top molecule is provided. With the help of trajectory calculations an axis-specific rotational rainbow could be identified in the rotational state distributions in direct-scattering.

The characterization of the scattering process for ground vibrational state formaldehyde can serve as a guideline for future experiments on vibrationally excited formaldehyde surface scattering. The direct-scattering of vibrationally excited formaldehyde potentially exhibits rich dynamical behavior. In particular, it would be interesting to examine if mode

specificity in the vibrational relaxation process can be observed. This is motivated by the observation that in resonant collisions of electrons with formaldehyde only excitation in the CO stretch (mode 2) can be observed.<sup>[144]</sup> This gives rise to the speculation whether nonadiabatic vibrational energy loss of formaldehyde at metal surfaces is specific to mode 2. In order to answer this question, an experiment on direct-scattering of vibrationally excited formaldehyde in the initial state  $2_1X_1$  is desirable. Here,  $X$  can be any other mode than 2. An investigation of the relaxation probability to  $2_0X_1$  and  $2_1X_0$  as a function of the incidence translational energy could potentially reveal the mechanism responsible for the relaxation of the two modes. In this work it has been demonstrated that the vibrational states  $2_14_1$  and  $2_16_1$  can be produced efficiently in the incoming beam using a narrow-bandwidth IR laser source. Furthermore, based on the vibrational ground state scattering data, direct-scattering of the vibrationally excited molecules should be clearly observable at incidence translational energies above  $0.37 \pm 0.07$  eV. At the same time, this experiment would reveal if nuclear spin isomers can be interchanged in a single collision with the metal surface since the preparation method using the narrow-bandwidth laser allows the exclusive population of only one of the existing two spin isomers. However, up to now scattering products for initially vibrationally excited molecules could not be detected probably because the produced densities of formaldehyde in the incoming beam are too low. As proposed in this work, the nozzle design could be changed as described in the following in order to increase the partial pressure of formaldehyde in the nozzle: enlargement of the sample compartment, installation of direct heating of the sample compartment, and usage of a more efficient drying agent. If the formaldehyde density in the molecular beam is successfully increased this will enable further interesting scattering experiments using vibrationally excited formaldehyde.



# A. Appendix

## A.1. MATLAB code for simulating 1+1' REMPI spectra

The simulation of 1+1' REMPI spectra of formaldehyde can be accomplished with the MATLAB code written by Dr. G. Barratt Park shown in the following sections. Section A.1 contains the main program. Here the population model is defined, all rovibronic transitions are calculated, the line strengths are calculated, and the spectrum is plotted. This program uses the eigenvalues and eigenvectors as well as transformation matrices calculated via the functions defined in Section A.1 and A.1, where also the used spectroscopic constants are given as an input. Section A.1 supplies the code for the calculation of direction-cosine matrix elements that are central to the derivation of line strength. Instead of evaluating the  $3j$  symbols in Equation 2.24 the code uses the evaluated form tabulated in reference [109].

## A. Appendix

### Main code

```
*****
% Defining Input Parameters
*****

Jmin=0;
Jmax=90;
Ta=886.3133653;
Tbc=Ta;

GA=0;
Gc=11.8643^2*9.4055242077;
Gw=1300;

A1=-0.672552407;
A2=-0.15890312;%A1*1.62921989/2.723766071;
BL=0;

data=load('directory input needed in order to compare to spectrum');
%data(:,1)=data(:,1)*2;
%data=data(1:10000,:);

eps0=8.854187817e-12;
h=6.62606957e-34;
c=299792458;

kTa=(1.3806488e-23)*(Ta)*(5.03445e22); %units = cm-1
kTbc=(1.3806488e-23)*(Tbc)*(5.03445e22); %units = cm-1

%Vibronic Symmetries
S=[+1,+1; %v=0, A1
   -1,-1]; %v4' B2

%Dipole moment operators
ux=1;
uy4_1=0; %
uy4_5=0;
ux6_1=0;
ux6_5=0; %
uz3_1=0;
uz3_4=0; %
uz2_1=0;

numlowerstates=1;
numupperstates=1;
numstates=numlowerstates+numupperstates;

%In ground state formaldehyde: ortho = odd Ka, para = even Ka.
*****
% DETERMINE ORTHO GROUND STATE ENERGY
*****
orthominJ=1;
[orthominbasisqnos, orthominV, orthominEnergies, Worthomin]=PerrinWangL(orthominJ);
%Make assignments for the minimum ortho J (which is 1)
%With the new version of PerrinWang, I am no longer using basis state
```



## A.1. MATLAB code for simulating 1+1' REMPI spectra

```

%overlaps. I am taking the order of the eigenvectors which should be
%already correctly sorted.
statein=1;
orthominassignment=zeros((2*orthominJ+1)*numstates,4);
for orthominKa=0:orthominJ
    if orthominKa==0
        orthominKc=orthominJ;
        orthominI=orthominJ+orthominKa-orthominKc+1;
        orthominassignment(orthominI,1)=statein;
        orthominassignment(orthominI,2)=orthominJ;
        orthominassignment(orthominI,3)=orthominKa;
        orthominassignment(orthominI,4)=orthominKc;
    else
        for orthominKc=[orthominJ-orthominKa+1,orthominJ-orthominKa]
            orthominI=orthominJ+orthominKa-orthominKc+1;
            orthominassignment(orthominI,1)=statein;
            orthominassignment(orthominI,2)=orthominJ;
            orthominassignment(orthominI,3)=orthominKa;
            orthominassignment(orthominI,4)=orthominKc;
        end
    end
end
for n=1:length(orthominassignment(:,1))
    if orthominassignment(n,1)==1 && ... %state = ground
        orthominassignment(n,2)==1 && ... %J=1
        orthominassignment(n,3)==1 && ... %Ka=1
        orthominassignment(n,4)==1 %Kc=0
        orthominindex=n;
    end
end
orthominEnergy=orthominEnergies(orthominindex);

```

---

```

*****
% Calculate Ortho and Para Partition Function
*****
tic
QOrtho=0;
QPara=0;
%You have to be careful about convergence. For T=1000, convergence occurs
%at about Jmax=60. However, the partition function goes haywire if you have
%Jmax > 90.
for braJ=0:90
    [brabasisqnos, braV, braEnergies, Wbra]=PerrinWangL(braJ);
    %brabasisqnos has columns: J, vibstatelabel, symm top K
    %Make bra assignments
    statein=1;
    braassignment=zeros((2*braJ+1)*numstates,4);
    for braKa=0:braJ
        if braKa==0
            braKc=braJ;
            braI=braJ+braKa-braKc+1;
            braassignment(braI,1)=statein;
            braassignment(braI,2)=braJ;
        end
    end
end

```

## A. Appendix

```

        braassignment(braI,3)=braKa;
        braassignment(braI,4)=braKc;
    else
        for braKc=[braJ-braKa+1,braJ-braKa]
            braI=braJ+braKa-braKc+1;
            braassignment(braI,1)=statein;
            braassignment(braI,2)=braJ;
            braassignment(braI,3)=braKa;
            braassignment(braI,4)=braKc;
        end
    end
end
for j=1:length(braEnergies)
    if mod(braassignment(j,3),2)==0 %if Ka is even, para. The *1 is
        %for para ns degeneracy.
        Energy=braEnergies(j);
        QPara=QPara+(2*braJ+1)*1*exp(-Energy/kTbc);
    elseif mod(braassignment(j,3),2)==1 %if Ka is odd, ortho. The *3 is
        %for ortho ns degeneracy.
        Energy=braEnergies(j);
        QOrtho=QOrtho+(2*braJ+1)*3*exp(-(Energy-orthominEnergy)/kTbc);
    end
end
end
toc

%%
%*****
% STEP THROUGH EACH J FROM JMIN TO JMAX AND CALCULATE A-X TRANSITIONS
%*****
tic
counter=1;
ll=zeros(900000,17);
for braJ=Jmin:Jmax
    [brabasisqnos, braV, braEnergies, Wbra]=PerrinWangL(braJ);
    %brabasisqnos has columns: J, vibstatelabel, symm top K
    %Make bra assignments
    statein=1;
    braassignment=zeros((2*braJ+1)*numlowerstates,4);
    %NOTE: This code is currently not designed for >1 lower state
    for braKa=0:braJ
        if braKa==0
            braKc=braJ;
            braI=braJ+braKa-braKc+1;
            braassignment(braI,1)=statein;
            braassignment(braI,2)=braJ;
            braassignment(braI,3)=braKa;
            braassignment(braI,4)=braKc;
        else
            for braKc=[braJ-braKa+1,braJ-braKa]
                braI=braJ+braKa-braKc+1;
                braassignment(braI,1)=statein;
                braassignment(braI,2)=braJ;
            end
        end
    end
end

```

### A.1. MATLAB code for simulating 1+1' REMPI spectra

```

        braassignment(braI,3)=braKa;
        braassignment(braI,4)=braKc;
    end
end
end
for ketJ=max(braJ-1,0):braJ+1
    %ketJ
    [ketbasisqnos, ketV, ketEnergies, Wket]=PerrinWangU(ketJ);
    %Make ket assignments
    ketassignment=zeros(numupperstates*(2*ketJ+1),4);
    for statein=1:numupperstates;
        for ketKa=0:ketJ
            if ketKa==0
                ketKc=ketJ;
                I=ketJ+ketKa-ketKc+1;
                ketassignment(I,1)=statein;
                ketassignment(I,2)=ketJ;
                ketassignment(I,3)=ketKa;
                ketassignment(I,4)=ketKc;
            elseif ketKa~=0
                for ketKc=[ketJ-ketKa+1,ketJ-ketKa]
                    I=ketJ+ketKa-ketKc+1;
                    ketassignment(I,1)=statein;
                    ketassignment(I,2)=ketJ;
                    ketassignment(I,3)=ketKa;
                    ketassignment(I,4)=ketKc;
                end
            end
        end
    end
end

%Now, create linelist, using assignments, eigenvectors, and
%eigenenergies
for braeigstate=1:length(braEnergies)
    brastate=braassignment(braeigstate,1);
    braKa=braassignment(braeigstate,3);
    braKc=braassignment(braeigstate,4);
    for keteigstate=1:length(ketEnergies)
        ketstate=ketassignment(keteigstate,1)+numlowerstates;
        ketKa=ketassignment(keteigstate,3);
        ketKc=ketassignment(keteigstate,4);
        %apply Ka/Kc selection rules
        %let ketstate==2 correspond to v4'. Want b-type. The
        %following two lines skip any transition where Delta Ka or
        %Delta Kc is even. The rest of the lines are historical
        %artifacts
        if ketstate==2 && mod(braKa+ketKa,2)==0 %mod tests for remainder
            %after division
        elseif ketstate==2 && mod(braKc+ketKc,2)==0
        elseif braEnergies(braeigstate)>ketEnergies(keteigstate)
        %
            elseif ketstate==3 && mod(braKa+ketKa,2)==0
        %
            elseif ketstate==3 && mod(braKc+ketKc,2)==0
        %
            elseif (ketstate==4 || ketstate==5) && mod(braKa+ketKa,2)==1
    end
end

```

## A. Appendix

```

%           elseif (ketstate==4 || ketstate==5) && mod(braKc+ketKc,2)==0
elseif brastate==0 %skip brastates not assigned to groundstate
    'bra unassigned'
    [braJ braeigstate]
elseif ketstate==0 %skip ketstates not assigned
    'ket unassigned'
    [ketJ keteigstate- (2*ketJ+1) ]
elseif brastate==1 && ketstate==1 %skip the microwave spectrum
%           elseif braEnergies(braeigstate)>10*kT
elseif abs(braKa-ketKa)>9
elseif abs(braKa-ketKa)>7 && braKa > 15
elseif abs(braKa-ketKa)>5 && braKa > 20
elseif abs(braKa-ketKa)>3 && braKa > 30
else
    braE=braEnergies(braeigstate);
    ketE=ketEnergies(keteigstate);
    freq = ketE-braE;
    Int=0;

    %nuclear spin weights
    if brastate==0
        gns=0; %skip anything not assigned to ground state
    elseif S(brastate,2)*(-2*mod(braKa,2)+1)<0
        gns=3;
    elseif S(brastate,2)*(-2*mod(braKa,2)+1) >= 0
        gns=1;
    end

%*****
% Population model
%*****

%note: the "extra" gns factor of 1 and 3 which I added
%at the front is for the
%relative total population of each species at high T.
if mod(braKa,2)==0 %if para state
% Simple Boltzmann fit
prefactor=1*(8*pi^3*freq)/(4*pi*eps0*3*h*c*QPara)*gns*...
    (1-exp(-freq/kTpara))*exp(-braE/kTpara);
% Gaussian model I
JaEnergy=braKa^2*9.4055242077;
JbcEnergy=braE;
popfactor=1/QPara*gns*...
    exp(-JbcEnergy/kT)*(1+GA*exp(-(JaEnergy-Gc)^2/Gw^2));
% Gaussian model II
JaEnergy=braKa^2*9.4055242077;
JbcEnergy=braE-JaEnergy;
popfactor=1/QPara*gns*...
    exp(-JbcEnergy/kTbc)*...
    (exp(-JaEnergy/kTa)+GA*exp(-(JaEnergy-Gc)^2/Gw^2));
elseif mod(braKa,2)==1 %if ortho state
% Simple Boltzmann
%prefactor=3*(8*pi^3*freq)/(4*pi*eps0*3*h*c*QOrtho)*gns*...
% (1-exp(-freq/kTortho))*exp(-braE/kTortho)*...

```

## A.1. MATLAB code for simulating 1+1' REMPI spectra

```

        exp(orthominEnergy/kTortho);
%
% Gaussian Model I
JaEnergy=braKa^2*9.4055242077;
JbcEnergy=braE;
popfactor=3/QOrtho*gns*...
        exp(-(JbcEnergy-orthominEnergy)/kT)*...
        (1+GA*exp(-(JaEnergy-orthominEnergy-Gc)^2/Gw^2));
% Gaussian Model II
JaEnergy=braKa^2*9.4055242077;
JbcEnergy=braE-JaEnergy;
popfactor=3/QOrtho*gns*...
exp(-(JbcEnergy-(orthominEnergy-1^2*9.4055242077))/kTbc)*...
(exp(-(JaEnergy-1^2*9.4055242077)/kTa)
+GA*exp(-(JaEnergy-1^2*9.4055242077-Gc)^2/Gw^2));
end

%*****
% Calculation of Line Strength
%*****

if braE>ketE
    display('for now, put the lower state in the bra')
end
braVecWANG=braV(:,braeigstate);
ketVecWANG=ketV(:,keteigstate);
%transform back to non-wang basis
braVec=Wbra*braVecWANG;
%The calculation is most easily performed
%in the symmetric top basis.
%Thus, transformation of the eigenvectors from the Wang basis
%into the symmetric top basis is necessary
ketVec=Wket*ketVecWANG;
for brabasisindex=1:(2*braJ+1)*numlowerstates
    for ketbasisindex=1:(2*ketJ+1)*numupperstates
        ketbasisstate=ketbasisqnos(ketbasisindex,2)+numlowerstates;
        brabasisstate=brabasisqnos(brabasisindex,2);
        ketK=ketbasisqnos(ketbasisindex,3);
        braK=brabasisqnos(brabasisindex,3);
        if ketbasisstate==2 %v4'
            Int=Int+ux*braVec(brabasisindex)*ketVec(ketbasisindex) ...
                *dircosJK(braJ,braK,ketJ,ketK,'b');
            %direction cosines are calculated in a separate program
            +uy4_5*braVec(brabasisindex)*ketVec(ketbasisindex) ...
            * (...
%0.5*dircosJK(braJ,braK,ketJ,ketK+1,'c')*(ketJ*(ketJ+1)-ketK*(ketK+1))^0.5 ...
%+0.5*dircosJK(braJ,braK,ketJ,ketK-1,'c')*(ketJ*(ketJ+1)-ketK*(ketK-1))^0.5 ...
%+0.5*dircosJK(braJ,ketK,ketJ,ketK,'c')*(braJ*(braJ+1)-ketK*(braK))^0.5*...
%(abs(braK-ketK)==1) ...
        );
%
% elseif ketbasisstate==3 %v6
% Int=Int+ux6_1*braVec(brabasisindex)*ketVec(ketbasisindex) ...
% *dircosJK(braJ,braK,ketJ,ketK,'b') ...

```

## A. Appendix

```

%      +ux6_5*braVec (brabasisindex) *ketVec (ketbasisindex) ...
%      * ( ...
%+0.5*dircosJK (braJ,braK,ketJ,ketK+1,'a') * (ketJ*(ketJ+1)-ketK*(ketK+1))^0.5 ...
%-0.5*dircosJK (braJ,braK,ketJ,ketK-1,'a') * (ketJ*(ketJ+1)-ketK*(ketK-1))^0.5 ...
% +0.5*dircosJK (braJ,ketK,ketJ,ketK,'a')*...
% (braJ*(braJ+1)-ketK*braK)^0.5*(braK==ketK+1) ...
%-0.5*dircosJK (braJ,ketK,ketJ,ketK,'a')*...
% (braJ*(braJ+1)-ketK*braK)^0.5*(braK==ketK-1) ...
%      );
%      elseif ketbasisstate==4 %v3
%      Int=Int+uz3_1*braVec (brabasisindex) *ketVec (ketbasisindex) ...
%      *dircosJK (braJ,braK,ketJ,ketK,'a') ...
%      +0.5*uz3_4*braVec (brabasisindex) *ketVec (ketbasisindex) ...
%      * ( ...
%      0.5*dircosJK (braJ,braK,ketJ,ketK+1,'b') * (ketJ*(ketJ+1)-ketK*(ketK+1))^0.5 ...
%-0.5*dircosJK (braJ,braK,ketJ,ketK-1,'b') * (ketJ*(ketJ+1)-ketK*(ketK-1))^0.5 ...
% -0.5*dircosJK (braJ,braK+1,ketJ,ketK,'b') * (braJ*(braJ+1)-braK*(braK+1))^0.5 ...
% +0.5*dircosJK (braJ,braK-1,ketJ,ketK,'b') * (braJ*(braJ+1)-braK*(braK-1))^0.5 ...
% -0.5*dircosJK (braJ,braK,ketJ,ketK+1,'c') * (ketJ*(ketJ+1)-ketK*(ketK+1))^0.5 ...
% -0.5*dircosJK (braJ,braK,ketJ,ketK-1,'c') * (ketJ*(ketJ+1)-ketK*(ketK-1))^0.5 ...
% -0.5*dircosJK (braJ,braK+1,ketJ,ketK,'c') * (braJ*(braJ+1)-braK*(braK+1))^0.5 ...
% -0.5*dircosJK (braJ,braK-1,ketJ,ketK,'c') * (braJ*(braJ+1)-braK*(braK-1))^0.5 ...
%      );
%      elseif ketbasisstate==5 %v2
%      Int=Int+uz2_1*braVec (brabasisindex) *ketVec (ketbasisindex) ...
%      *dircosJK (braJ,braK,ketJ,ketK,'a') ;
%      end
%      end
%      end

%M population weights
Mmax=min (braJ,ketJ);
rotstrength=Int;
for M=-Mmax:Mmax
    if braJ==ketJ+1
        phiJMJM=2*sqrt ((ketJ+1)^2-M^2);
    elseif braJ==ketJ
        phiJMJM=2*M;
    elseif braJ==ketJ-1
        phiJMJM=2*sqrt (ketJ^2-M^2);
    end

    muvibronic=1; %when you model more than one band, need to
    %have relative vibronic intensities here.
    murovibronic=rotstrength*phiJMJM*muvibronic;
    Intensity=popfactor*murovibronic^2; %This is written in
    %"S12" linestrength units, except that I've set mu to 1.
    %If you figure out vibronic strengths from literature,
    %convert to mu12 units and plug in above.

    rho=0.1;
    Fsat=popfactor*0.5*(1-exp (-2*murovibronic^2*rho));
    %here murovibronic^2 should really have conversion

```

## A.1. MATLAB code for simulating 1+1' REMPI spectra

```

%factors from mu^2 to Einstein B. rho represents
%the energy density times the pulse duration, but
%the units are currently left out.
ll(counter,1)=freq;
ll(counter,2)=Intensity;
ll(counter,3)=Fsat;
ll(counter,4)=murovibronic^2;
ll(counter,5)=popfactor;
ll(counter,6)=ketE;
ll(counter,7)=ketstate;
ll(counter,8)=ketJ;
ll(counter,9)=ketKa;
ll(counter,10)=ketKc;
ll(counter,11)=braE;
ll(counter,12)=1;
ll(counter,13)=braJ;
ll(counter,14)=braKa;
ll(counter,15)=braKc;
ll(counter,16)=M;
ll(counter,17)=phiJMJM;
counter=counter+1;
end
end
end
end
end
end
toc

%%
tic

ll=ll(1:counter-1,:);
%[B, I]=sort(ll(:,6));
%ll=ll(I,:);
toc
%*****
%Make llMsum matrix, in which M-components are added together.
%*****
tic
llMsum=zeros(10000,length(ll(1,:)));
counter=1;
llindex=1;
while llindex<=length(ll(:,1))
    dummy=0;
    llMsum(counter,:)=ll(llindex,:);
    llMsum(counter,16)=0;
    llMsum(counter,17)=0;
    dummy=dummy+1;
    if min(ll(llindex,8),ll(llindex,13))>0
        for llindex2=llindex+1:llindex+2*min(ll(llindex,8),ll(llindex,13))
            llMsum(counter,2)=llMsum(counter,2)+ll(llindex2,2);
        end
    end
    llindex=llindex+1;
end

```

## A. Appendix

```

        l1Msum(counter,3)=l1Msum(counter,3)+l1(l1index2,3);
        l1Msum(counter,4)=l1Msum(counter,4)+l1(l1index2,4);
        dummy=dummy+1;
    end
    end
    l1index=l1index+dummy;
    counter=counter+1;
end
l1Msum=l1Msum(1:counter-1,:);
toc

figure %Plot a stick spectrum
g = stem(l1Msum(:,1),l1Msum(:,2)*(A1+A2));
    set(g, 'Marker', 'none');
    xlim2=data(1,1);
    xlim1=length(data(:,1)),1);
    axis([xlim1 xlim2 -inf inf])

    hold on

% Plot spectrum with Gaussian/Lorentzian linewidths
% Gaussian
freqaxis=freqaxis=data(:,1);%in the range of the spectrum
Gwidth=.65;
GaussianSpectrum=zeros(length(freqaxis),1)';
for j=1:length(l1(:,1))
    GaussianSpectrum=GaussianSpectrum+l1(j,2)...
        *exp(-(freqaxis-l1(j,1)).^2./Gwidth^2);
end
figure
plot(freqaxis,GaussianSpectrum)

% %
% tic
% Gwidth=0.4;
% %A1=-0.3042;
% LFWHM2=0.1;
% %A2=-0.1523;
% freqaxis=data(:,1);
% LorenzianSpectrum=zeros(length(freqaxis),1);
% for j=1:length(l1Msum(:,1))
%     %x1=(l1(j,1)-freqaxis)/LFWHM1;
%     x2=(l1Msum(j,1)-freqaxis)/LFWHM2;
%     LorenzianSpectrum=LorenzianSpectrum+A1*l1Msum(j,2)*...
%     exp(-(freqaxis-l1Msum(j,1)).^2./Gwidth^2);
%     LorenzianSpectrum=LorenzianSpectrum+A2*l1Msum(j,2)*(1./(1+x2.^2));
% end
% LorenzianSpectrum=LorenzianSpectrum-BL;
% plot(freqaxis,LorenzianSpectrum)
% toc

plot(data(:,1),-data(:,2))

```



### Calculation of the Hamiltonian for the $\tilde{X}$ state

```

%*****
% Diagonalization for the Hamilton Matrix in the X state
%*****
function [qnos, Tconcat, Energiesconcat, W]=PerrinWangL(Jin)
%Parameters
%Perrin, Keller, Flaud, 2003 JMS, Vol 221, pg 192

numstates = 1;
v0=zeros(1,numstates);
A=v0;
B=v0;
C=v0;
DK=v0;
DJK=v0;
DJ=v0;
deltaK=v0;
deltaJ=v0;
HK=v0;
HKJ=v0;
HJK=v0;
HJ=v0;
phiK=v0;
phiJK=v0;
phiJ=v0;

%X Ground State
v0(1)=0;
A(1)=9.4055242077;
B(1)=1.2954312093;
C(1)=1.1341913215;
DK(1)=6.4761769E-4;
DJK(1)=4.3067094E-5;
DJ(1)=2.5125772E-6;
deltaK(1)=0.000034294225;
deltaJ(1)=3.48723783E-7;
HK(1)=1.35924E-7;
HKJ(1)=-2.5581E-9;
HJK(1)=1.08068E-9;
HJ(1)=3.2666E-12;
phiK(1)=4.9734E-8;
phiJK(1)=5.72463E-10;
phiJ(1)=1.48553E-12;
LK(1)=-2.025E-11;
LKKJ(1)=1.368E-12;
LJK(1)=-1.991E-13;
LJJK(1)=-5.3203E-14;
LKJ(1)=-2.852E-12;

% %v6
% v0(3)=1249.09468;
% A(3)=9.4022072;
% B(3)=1.29810167;

```

## A. Appendix

```
% C(3)=1.13212697;
% DK(3)=0.001081107;
% DJK(3)=0.00004547;
% DJ(3)=2.53628E-6;
% deltaK(3)=0.000039528;
% deltaJ(3)=3.8199E-7;
% HK(3)=1.35924E-7;
% HKJ(3)=-2.5581E-9;
% HJK(3)=1.08068E-9;
% HJ(3)=3.2666E-12;
% phiK(3)=4.9734E-8;
% phiJK(3)=5.72463E-10;
% phiJ(3)=1.48553E-12;
% LK(3)=-2.025E-11;
% LKKJ(3)=1.368E-12;
% LJK(3)=-1.991E-13;
% LJJK(3)=-5.3203E-14;
% lKJ(3)=-2.852E-12;
%
% %v3
% v0(4)=1500.17474;
% A(4)=9.4671592;
% B(4)=1.29429962;
% C(4)=1.12707430;
% DK(4)=0.000685886;
% DJK(4)=0.0000446903;
% DJ(4)=2.5580E-6;
% deltaK(4)=0.000034267;
% deltaJ(4)=3.7914E-7;
% HK(4)=1.35924E-7;
% HKJ(4)=-2.5581E-9;
% HJK(4)=1.08068E-9;
% HJ(4)=3.2666E-12;
% phiK(4)=4.9734E-8;
% phiJK(4)=5.72463E-10;
% phiJ(4)=1.48553E-12;
% LK(4)=-2.025E-11;
% LKKJ(4)=1.368E-12;
% LJK(4)=-1.991E-13;
% LJJK(4)=-5.3203E-14;
% lKJ(4)=-2.852E-12;
%
% %v2
% v0(5)=1746.00886;
% A(5)=9.3999000;
% B(5)=1.28790723;
% C(5)=1.12538522;
% DK(5)=0.000650704;
% DJK(5)=0.000043016;
% DJ(5)=2.45099E-6;
% deltaK(5)=0.000035955;
% deltaJ(5)=2.9901E-7;
% HK(5)=1.35924E-7;
```

## A.1. MATLAB code for simulating 1+1' REMPI spectra

```

% HJK(5)=1.08068E-9;
% HJ(5)=3.2666E-12;
% phiK(5)=4.9734E-8;
% phiJK(5)=5.72463E-10;
% phiJ(5)=1.48553E-12;
% LK(5)=-2.025E-11;
% LKKJ(5)=1.368E-12;
% LJK(5)=-1.991E-13;
% LJJK(5)=-5.3203E-14;
% lKJ(5)=-2.852E-12;
%
% %Perturbations
% h1A64=10.414368;
% h2A64=0.297598E-2; %
% h3A64=-0.4934E-4;
% h4A64=-0.30896E-3*0.5;%
% h5A64=-0.5791E-5; %
% h1Anh23=0.3245E-2;
% h1B34=1.887690;
% h3B34=-0.2501E-4;
% h1C36=-1.035081; %
% h2C36=-0.0207426;

J=Jin;
%J=1;
%List qnos of all states for given J
state=1;
if mod(J,2)==0
    dummy=1;
    for K=-J:2:J
        qnos_e(dummy,1:3)=[J state K];
        dummy=dummy+1;
    end
    dummy=1;
    for K=-J+1:2:J-1
        qnos_o(dummy,1:3)=[J state K];
        dummy=dummy+1;
    end
elseif mod(J,2)==1
    dummy=1;
    for K=-J:2:J
        qnos_o(dummy,1:3)=[J state K];
        dummy=dummy+1;
    end
    dummy=1;
    for K=-J+1:2:J-1
        qnos_e(dummy,1:3)=[J state K];
        dummy=dummy+1;
    end
end

%List qnos of all states for given J
dummy=1;
for state=1:numstates

```

## A. Appendix

```

        qnos(dummy,1:3)=[J state K];
        dummy=dummy+1;
    end
end
end
H_e=zeros(length(qnos_e(:,1)));
for braindex=1:length(qnos_e(:,1))
    for ketindex=1:length(qnos_e(:,1))
        brastate=qnos_e(braindex,2);
        ketstate=qnos_e(ketindex,2);
        braK=qnos_e(braindex,3);
        ketK=qnos_e(ketindex,3);
        %Diagonal matrix elements
        if brastate==ketstate && braK==ketK
            H_e(braindex,ketindex)=H_e(braindex,ketindex) ...
                +v0(brastate) ...
                +0.5*(B(brastate)+C(brastate))*J*(J+1) ...
                +(A(brastate)-0.5*(B(brastate)+C(brastate)))*braK^2 ...
                -DJ(brastate)*J^2*(J+1)^2 ...
                -DJK(brastate)*J*(J+1)*braK^2 ...
                -DK(brastate)*braK^4 ...
                +HJ(brastate)*J^3*(J+1)^3 ...
                +HJK(brastate)*J^2*(J+1)^2*braK^2 ...
                +HKJ(brastate)*J*(J+1)*braK^4 ...
                +HK(brastate)*braK^6 ...
                ... %+LJ(brastate)*J^4*(J+1)^4 ...
                +LJJK(brastate)*J^3*(J+1)^3*braK^2 ...
                +LJK(brastate)*J^2*(J+1)^2*braK^4 ...
                +LKKJ(brastate)*J*(J+1)*braK^6 ...
                +LK(brastate)*braK^8;
        end
        %Delta K = 2 matrix elements (diagonal in vibration)
        if brastate==ketstate && braK==ketK+2
            H_e(braindex,ketindex)=H_e(braindex,ketindex) ...
                + ( ...
                    0.25*(B(brastate)-C(brastate)) ...
                    -deltaJ(brastate)*J*(J+1) ...
                    -0.5*deltaK(brastate)*((ketK+2)^2+ketK^2) ...
                    +phiJ(brastate)*J^2*(J+1)^2 ...
                    +0.5*phiJK(brastate)*J*(J+1)*((ketK+2)^2+ketK^2) ...
                    +0.5*phiK(brastate)*((ketK+2)^4+ketK^4) ...
                    +0.5*1KJ(brastate)*(J*(J+1))*((ketK+2)^4+ketK^4) ...
                ) ...
                * ((J*(J+1)-ketK*(ketK+1))*(J*(J+1)-(ketK+1)*(ketK+2)))^0.5;
        end
        if brastate==ketstate && braK==ketK-2
            H_e(braindex,ketindex)=H_e(braindex,ketindex) ...
                + ( ...
                    0.25*(B(brastate)-C(brastate)) ...
                    -deltaJ(brastate)*J*(J+1) ...
                    -0.5*deltaK(brastate)*((ketK-2)^2+ketK^2) ...

```

### A.1. MATLAB code for simulating 1+1' REMPI spectra

```

+phiJ(brastate)*J^2*(J+1)^2 ...
+0.5*phiJK(brastate)*J*(J+1)*((ketK-2)^2+ketK^2) ...
+0.5*phiK(brastate)*((ketK-2)^4+ketK^4) ...
+0.5*1KJ(brastate)*(J*(J+1))*((ketK-2)^4+ketK^4) ...
) ...
*(J*(J+1)-ketK*(ketK-1))*(J*(J+1)-(ketK-1)*(ketK-2))^0.5;
end

%PERTURBATIONS
%h1A64 4/6 Coriolis Perturbation, (Term 1)
if brastate==2 && ketstate==3 && braK==ketK
    H_e(braindex,ketindex)=H_e(braindex,ketindex)+h1A64*braK;
end
if brastate==3 && ketstate==2 && braK==ketK
    H_e(braindex,ketindex)=H_e(braindex,ketindex)+h1A64*braK;
end
%h2A64 4/6 Coriolis Perturbation, (Term 2)
if brastate==3 && ketstate==2 && braK==ketK+2
    H_e(braindex,ketindex)=H_e(braindex,ketindex) ...
    +0.5*h2A64*((J*(J+1)-ketK*(ketK+1))*(J*(J+1)-(ketK+1)*(ketK+2)))^0.5;
end
if brastate==2 && ketstate==3 && braK+2==ketK
    H_e(braindex,ketindex)=H_e(braindex,ketindex) ...
    +0.5*h2A64*((J*(J+1)-braK*(braK+1))*(J*(J+1)-(braK+1)*(braK+2)))^0.5;
end
if brastate==3 && ketstate==2 && braK==ketK-2
    H_e(braindex,ketindex)=H_e(braindex,ketindex) ...
    -0.5*h2A64*((J*(J+1)-ketK*(ketK-1))*(J*(J+1)-(ketK-1)*(ketK-2)))^0.5;
end
if brastate==2 && ketstate==3 && braK-2==ketK
    H_e(braindex,ketindex)=H_e(braindex,ketindex) ...
    -0.5*h2A64*((J*(J+1)-braK*(braK-1))*(J*(J+1)-(braK-1)*(braK-2)))^0.5;
end
%h3A64 4/6 Coriolis Perturbation, (Term 3)
if ((brastate==2 && ketstate==3) || (brastate==3 && ketstate==2)) && braK==ketK
    H_e(braindex,ketindex)=H_e(braindex,ketindex) ...
    +h3A64*J*(J+1)*ketK;
end
%h4A64 4/6 Coriolis Perturbation, (Term 4)
if brastate==3 && ketstate==2 && braK==ketK+2
    H_e(braindex,ketindex)=H_e(braindex,ketindex) ...
    +0.5*h4A64*(2*ketK+2) ...
    *((J*(J+1)-ketK*(ketK+1))*(J*(J+1)-(ketK+1)*(ketK+2)))^0.5;
end
if brastate==2 && ketstate==3 && braK+2==ketK
    H_e(braindex,ketindex)=H_e(braindex,ketindex) ...
    +0.5*h4A64*(2*braK+2) ...
    *((J*(J+1)-braK*(braK+1))*(J*(J+1)-(braK+1)*(braK+2)))^0.5;
end
if brastate==3 && ketstate==2 && braK==ketK-2
    H_e(braindex,ketindex)=H_e(braindex,ketindex) ...
    +0.5*h4A64*(2*ketK-2) ...

```

## A. Appendix

```

        * ((J*(J+1) - ketK*(ketK-1)) * (J*(J+1) - (ketK-1)*(ketK-2))) ^0.5;
    end
    if brastate==2 && ketstate==3 && braK-2==ketK
        H_e(braindex,ketindex)=H_e(braindex,ketindex) ...
        +0.5*h4A64*(2*braK-2) ...
        * ((J*(J+1) - braK*(braK-1)) * (J*(J+1) - (braK-1)*(braK-2))) ^0.5;
    end
    %h5A64 4/6 Coriolis Perturbation, (Term 5)
    if brastate==3 && ketstate==2 && braK==ketK+2
        H_e(braindex,ketindex)=H_e(braindex,ketindex) ...
        +0.5*h5A64*((ketK+2)^2+ketK^2) ...
        * ((J*(J+1) - ketK*(ketK+1)) * (J*(J+1) - (ketK+1)*(ketK+2))) ^0.5;
    end
    if brastate==2 && ketstate==3 && braK+2==ketK
        H_e(braindex,ketindex)=H_e(braindex,ketindex) ...
        +0.5*h5A64*((braK+2)^2+braK^2) ...
        * ((J*(J+1) - braK*(braK+1)) * (J*(J+1) - (braK+1)*(braK+2))) ^0.5;
    end
    if brastate==3 && ketstate==2 && braK==ketK-2
        H_e(braindex,ketindex)=H_e(braindex,ketindex) ...
        -0.5*h5A64*((ketK-2)^2+ketK^2) ...
        * ((J*(J+1) - ketK*(ketK-1)) * (J*(J+1) - (ketK-1)*(ketK-2))) ^0.5;
    end
    if brastate==2 && ketstate==3 && braK-2==ketK
        H_e(braindex,ketindex)=H_e(braindex,ketindex) ...
        -0.5*h5A64*((braK-2)^2+braK^2) ...
        * ((J*(J+1) - braK*(braK-1)) * (J*(J+1) - (braK-1)*(braK-2))) ^0.5;
    end
    %h1B34 3/4 Coriolis Perturbation, (Term 1)
    if brastate==4 && ketstate==2 && braK==ketK+1
        H_e(braindex,ketindex)=H_e(braindex,ketindex) ...
        +0.5*h1B34*(J*(J+1) - ketK*(ketK+1)) ^0.5;
    end
    if brastate==2 && ketstate==4 && braK+1==ketK
        H_e(braindex,ketindex)=H_e(braindex,ketindex) ...
        +0.5*h1B34*(J*(J+1) - braK*(braK+1)) ^0.5;
    end
    if brastate==4 && ketstate==2 && braK==ketK-1
        H_e(braindex,ketindex)=H_e(braindex,ketindex) ...
        +0.5*h1B34*(J*(J+1) - ketK*(ketK-1)) ^0.5;
    end
    if brastate==2 && ketstate==4 && braK-1==ketK
        H_e(braindex,ketindex)=H_e(braindex,ketindex) ...
        +0.5*h1B34*(J*(J+1) - braK*(braK-1)) ^0.5;
    end
    %h3B34 3/4 Coriolis Perturbation, (Term 2)
    if brastate==4 && ketstate==2 && braK==ketK+1
        H_e(braindex,ketindex)=H_e(braindex,ketindex) ...
        +0.5*h3B34*J*(J+1) * (J*(J+1) - ketK*(ketK+1)) ^0.5;
    end
    if brastate==2 && ketstate==4 && braK+1==ketK
        H_e(braindex,ketindex)=H_e(braindex,ketindex) ...

```

## A.1. MATLAB code for simulating 1+1' REMPI spectra

```

+0.5*h3B34*J*(J+1)*(J*(J+1)-braK*(braK+1))^0.5;
end
if brastate==4 && ketstate==2 && braK==ketK-1
    H_e(braindex,ketindex)=H_e(braindex,ketindex) ...
    +0.5*h3B34*J*(J+1)*(J*(J+1)-ketK*(ketK-1))^0.5;
end
if brastate==2 && ketstate==4 && braK-1==ketK
    H_e(braindex,ketindex)=H_e(braindex,ketindex) ...
    +0.5*h3B34*J*(J+1)*(J*(J+1)-braK*(braK-1))^0.5;
end
%h1C36 3/6 Coriolis Perturbation, (Term 1)
if brastate==4 && ketstate==3 && braK==ketK+1
    H_e(braindex,ketindex)=H_e(braindex,ketindex) ...
    +0.5*h1C36*(J*(J+1)-ketK*(ketK+1))^0.5;
end
if brastate==3 && ketstate==4 && braK+1==ketK
    H_e(braindex,ketindex)=H_e(braindex,ketindex) ...
    +0.5*h1C36*(J*(J+1)-braK*(braK+1))^0.5;
end
if brastate==4 && ketstate==3 && braK==ketK-1
    H_e(braindex,ketindex)=H_e(braindex,ketindex) ...
    -0.5*h1C36*(J*(J+1)-ketK*(ketK-1))^0.5;
end
if brastate==3 && ketstate==4 && braK-1==ketK
    H_e(braindex,ketindex)=H_e(braindex,ketindex) ...
    -0.5*h1C36*(J*(J+1)-braK*(braK-1))^0.5;
end
%h2C36 3/6 Coriolis Perturbation (Term 2)
if brastate==4 && ketstate==3 && braK==ketK+1
    H_e(braindex,ketindex)=H_e(braindex,ketindex) ...
    +0.5*h2C36*(2*ketK+1)*(J*(J+1)-ketK*(ketK+1))^0.5;
end
if brastate==3 && ketstate==4 && braK+1==ketK
    H_e(braindex,ketindex)=H_e(braindex,ketindex) ...
    +0.5*h2C36*(2*braK+1)*(J*(J+1)-braK*(braK+1))^0.5;
end
if brastate==4 && ketstate==3 && braK==ketK-1
    H_e(braindex,ketindex)=H_e(braindex,ketindex) ...
    +0.5*h2C36*(2*ketK-1)*(J*(J+1)-ketK*(ketK-1))^0.5;
end
if brastate==3 && ketstate==4 && braK-1==ketK
    H_e(braindex,ketindex)=H_e(braindex,ketindex) ...
    +0.5*h2C36*(2*braK-1)*(J*(J+1)-braK*(braK-1))^0.5;
end
%h1Anh23 2/3 'Anharmonic' (?) Perturbation
if brastate==5 && ketstate==4 && braK==ketK+2
    H_e(braindex,ketindex)=H_e(braindex,ketindex) ...
    +0.5*h1Anh23*((J*(J+1)-ketK*(ketK+1))*(J*(J+1)-(ketK+1)*(ketK+2)))^0.5;
end
if brastate==4 && ketstate==5 && braK+2==ketK
    H_e(braindex,ketindex)=H_e(braindex,ketindex) ...
    +0.5*h1Anh23*((J*(J+1)-braK*(braK+1))*(J*(J+1)-(braK+1)*(braK+2)))^0.5;
end

```

## A. Appendix

```

if brastate==5 && ketstate==4 && braK==ketK-2
    H_e(braindex,ketindex)=H_e(braindex,ketindex) ...
    +0.5*h1Anh23*( (J*(J+1)-ketK*(ketK-1))*(J*(J+1)-(ketK-1)*(ketK-2)))^0.5;
end
if brastate==4 && ketstate==5 && braK-2==ketK
    H_e(braindex,ketindex)=H_e(braindex,ketindex) ...
    +0.5*h1Anh23*( (J*(J+1)-braK*(braK-1))*(J*(J+1)-(braK-1)*(braK-2)))^0.5;
end
end
end

if J~=0
H_o=zeros(length(qnos_o(:,1)));
for braindex=1:length(qnos_o(:,1))
    for ketindex=1:length(qnos_o(:,1))
        brastate=qnos_o(braindex,2);
        ketstate=qnos_o(ketindex,2);
        braK=qnos_o(braindex,3);
        ketK=qnos_o(ketindex,3);
        %Diagonal matrix elements
        if brastate==ketstate && braK==ketK
            H_o(braindex,ketindex)=H_o(braindex,ketindex) ...
                +v0(brastate) ...
                +0.5*(B(brastate)+C(brastate))*J*(J+1) ...
                +(A(brastate)-0.5*(B(brastate)+C(brastate)))*braK^2 ...
                -DJ(brastate)*J^2*(J+1)^2 ...
                -DJK(brastate)*J*(J+1)*braK^2 ...
                -DK(brastate)*braK^4 ...
                +HJ(brastate)*J^3*(J+1)^3 ...
                +HJK(brastate)*J^2*(J+1)^2*braK^2 ...
                +HKJ(brastate)*J*(J+1)*braK^4 ...
                +HK(brastate)*braK^6 ...
                ... %+LJ(brastate)*J^4*(J+1)^4 ...
                +LJJK(brastate)*J^3*(J+1)^3*braK^2 ...
                +LJK(brastate)*J^2*(J+1)^2*braK^4 ...
                +LKKJ(brastate)*J*(J+1)*braK^6 ...
                +LK(brastate)*braK^8;
        end
        %Delta K = 2 matrix elements (diagonal in vibration)
        if brastate==ketstate && braK==ketK+2
            H_o(braindex,ketindex)=H_o(braindex,ketindex) ...
                +( ...
                0.25*(B(brastate)-C(brastate)) ...
                -deltaJ(brastate)*J*(J+1) ...
                -0.5*deltaK(brastate)*((ketK+2)^2+ketK^2) ...
                +phiJ(brastate)*J^2*(J+1)^2 ...
                +0.5*phiJK(brastate)*J*(J+1)*((ketK+2)^2+ketK^2) ...
                +0.5*phiK(brastate)*((ketK+2)^4+ketK^4) ...
                +0.5*1KJ(brastate)*J*(J+1)*((ketK+2)^4+ketK^4) ...
                ) ...
                *((J*(J+1)-ketK*(ketK+1))*(J*(J+1)-(ketK+1)*(ketK+2)))^0.5;
        end
    end
end

```



## A.1. MATLAB code for simulating 1+1' REMPI spectra

```

end
if brastate==ketstate && braK==ketK-2
    H_o(braindex,ketindex)=H_o(braindex,ketindex) ...
        + ( ...
            0.25*(B(brastate)-C(brastate)) ...
            -deltaJ(brastate)*J*(J+1) ...
            -0.5*deltaK(brastate)*((ketK-2)^2+ketK^2) ...
            +phiJ(brastate)*J^2*(J+1)^2 ...
            +0.5*phiJK(brastate)*J*(J+1)*((ketK-2)^2+ketK^2) ...
            +0.5*phiK(brastate)*((ketK-2)^4+ketK^4) ...
            +0.5*1KJ(brastate)*J*(J+1)*((ketK-2)^4+ketK^4) ...
        ) ...
        * ((J*(J+1)-ketK*(ketK-1))*(J*(J+1)-(ketK-1)*(ketK-2)))^0.5;
end

%PERTURBATIONS
%h1A64 4/6 Coriolis Perturbation, (Term 1)
if brastate==2 && ketstate==3 && braK==ketK
    H_o(braindex,ketindex)=H_o(braindex,ketindex)+h1A64*braK;
end
if brastate==3 && ketstate==2 && braK==ketK
    H_o(braindex,ketindex)=H_o(braindex,ketindex)+h1A64*braK;
end
%h2A64 4/6 Coriolis Perturbation, (Term 2)
if brastate==3 && ketstate==2 && braK==ketK+2
    H_o(braindex,ketindex)=H_o(braindex,ketindex) ...
        +0.5*h2A64*((J*(J+1)-ketK*(ketK+1))*(J*(J+1)-(ketK+1)*(ketK+2)))^0.5;
end
if brastate==2 && ketstate==3 && braK+2==ketK
    H_o(braindex,ketindex)=H_o(braindex,ketindex) ...
        +0.5*h2A64*((J*(J+1)-braK*(braK+1))*(J*(J+1)-(braK+1)*(braK+2)))^0.5;
end
if brastate==3 && ketstate==2 && braK==ketK-2
    H_o(braindex,ketindex)=H_o(braindex,ketindex) ...
        -0.5*h2A64*((J*(J+1)-ketK*(ketK-1))*(J*(J+1)-(ketK-1)*(ketK-2)))^0.5;
end
if brastate==2 && ketstate==3 && braK-2==ketK
    H_o(braindex,ketindex)=H_o(braindex,ketindex) ...
        -0.5*h2A64*((J*(J+1)-braK*(braK-1))*(J*(J+1)-(braK-1)*(braK-2)))^0.5;
end
%h3A64 4/6 Coriolis Perturbation, (Term 3)
if ((brastate==2 && ketstate==3) || (brastate==3 && ketstate==2)) && braK==ketK
    H_o(braindex,ketindex)=H_o(braindex,ketindex) ...
        +h3A64*J*(J+1)*ketK;
end
%h4A64 4/6 Coriolis Perturbation, (Term 4)
if brastate==3 && ketstate==2 && braK==ketK+2
    H_o(braindex,ketindex)=H_o(braindex,ketindex) ...
        +0.5*h4A64*(2*ketK+2) ...
        * ((J*(J+1)-ketK*(ketK+1))*(J*(J+1)-(ketK+1)*(ketK+2)))^0.5;
end
if brastate==2 && ketstate==3 && braK+2==ketK

```

## A. Appendix

```

    H_o(braindex,ketindex)=H_o(braindex,ketindex) ...
    +0.5*h4A64*(2*braK+2) ...
    *((J*(J+1)-braK*(braK+1))*(J*(J+1)-(braK+1)*(braK+2)))^0.5;
end
if brastate==3 && ketstate==2 && braK==ketK-2
    H_o(braindex,ketindex)=H_o(braindex,ketindex) ...
    +0.5*h4A64*(2*ketK-2) ...
    *((J*(J+1)-ketK*(ketK-1))*(J*(J+1)-(ketK-1)*(ketK-2)))^0.5;
end
if brastate==2 && ketstate==3 && braK-2==ketK
    H_o(braindex,ketindex)=H_o(braindex,ketindex) ...
    +0.5*h4A64*(2*braK-2) ...
    *((J*(J+1)-braK*(braK-1))*(J*(J+1)-(braK-1)*(braK-2)))^0.5;
end
%h5A64 4/6 Coriolis Perturbation, (Term 5)
if brastate==3 && ketstate==2 && braK==ketK+2
    H_o(braindex,ketindex)=H_o(braindex,ketindex) ...
    +0.5*h5A64*((ketK+2)^2+ketK^2) ...
    *((J*(J+1)-ketK*(ketK+1))*(J*(J+1)-(ketK+1)*(ketK+2)))^0.5;
end
if brastate==2 && ketstate==3 && braK+2==ketK
    H_o(braindex,ketindex)=H_o(braindex,ketindex) ...
    +0.5*h5A64*((braK+2)^2+braK^2) ...
    *((J*(J+1)-braK*(braK+1))*(J*(J+1)-(braK+1)*(braK+2)))^0.5;
end
if brastate==3 && ketstate==2 && braK==ketK-2
    H_o(braindex,ketindex)=H_o(braindex,ketindex) ...
    -0.5*h5A64*((ketK-2)^2+ketK^2) ...
    *((J*(J+1)-ketK*(ketK-1))*(J*(J+1)-(ketK-1)*(ketK-2)))^0.5;
end
if brastate==2 && ketstate==3 && braK-2==ketK
    H_o(braindex,ketindex)=H_o(braindex,ketindex) ...
    -0.5*h5A64*((braK-2)^2+braK^2) ...
    *((J*(J+1)-braK*(braK-1))*(J*(J+1)-(braK-1)*(braK-2)))^0.5;
end
%h1B34 3/4 Coriolis Perturbation, (Term 1)
if brastate==4 && ketstate==2 && braK==ketK+1
    H_o(braindex,ketindex)=H_o(braindex,ketindex) ...
    +0.5*h1B34*(J*(J+1)-ketK*(ketK+1))^0.5;
end
if brastate==2 && ketstate==4 && braK+1==ketK
    H_o(braindex,ketindex)=H_o(braindex,ketindex) ...
    +0.5*h1B34*(J*(J+1)-braK*(braK+1))^0.5;
end
if brastate==4 && ketstate==2 && braK==ketK-1
    H_o(braindex,ketindex)=H_o(braindex,ketindex) ...
    +0.5*h1B34*(J*(J+1)-ketK*(ketK-1))^0.5;
end
if brastate==2 && ketstate==4 && braK-1==ketK
    H_o(braindex,ketindex)=H_o(braindex,ketindex) ...
    +0.5*h1B34*(J*(J+1)-braK*(braK-1))^0.5;
end
end

```

## A.1. MATLAB code for simulating 1+1' REMPI spectra

```

%h3B34 3/4 Coriolis Perturbation, (Term 2)
if brastate==4 && ketstate==2 && braK==ketK+1
    H_o(braindex,ketindex)=H_o(braindex,ketindex) ...
        +0.5*h3B34*J*(J+1)*(J*(J+1)-ketK*(ketK+1))^0.5;
end
if brastate==2 && ketstate==4 && braK+1==ketK
    H_o(braindex,ketindex)=H_o(braindex,ketindex) ...
        +0.5*h3B34*J*(J+1)*(J*(J+1)-braK*(braK+1))^0.5;
end
if brastate==4 && ketstate==2 && braK==ketK-1
    H_o(braindex,ketindex)=H_o(braindex,ketindex) ...
        +0.5*h3B34*J*(J+1)*(J*(J+1)-ketK*(ketK-1))^0.5;
end
if brastate==2 && ketstate==4 && braK-1==ketK
    H_o(braindex,ketindex)=H_o(braindex,ketindex) ...
        +0.5*h3B34*J*(J+1)*(J*(J+1)-braK*(braK-1))^0.5;
end
%h1C36 3/6 Coriolis Perturbation, (Term 1)
if brastate==4 && ketstate==3 && braK==ketK+1
    H_o(braindex,ketindex)=H_o(braindex,ketindex) ...
        +0.5*h1C36*(J*(J+1)-ketK*(ketK+1))^0.5;
end
if brastate==3 && ketstate==4 && braK+1==ketK
    H_o(braindex,ketindex)=H_o(braindex,ketindex) ...
        +0.5*h1C36*(J*(J+1)-braK*(braK+1))^0.5;
end
if brastate==4 && ketstate==3 && braK==ketK-1
    H_o(braindex,ketindex)=H_o(braindex,ketindex) ...
        -0.5*h1C36*(J*(J+1)-ketK*(ketK-1))^0.5;
end
if brastate==3 && ketstate==4 && braK-1==ketK
    H_o(braindex,ketindex)=H_o(braindex,ketindex) ...
        -0.5*h1C36*(J*(J+1)-braK*(braK-1))^0.5;
end
%h2C36 3/6 Coriolis Perturbation (Term 2)
if brastate==4 && ketstate==3 && braK==ketK+1
    H_o(braindex,ketindex)=H_o(braindex,ketindex) ...
        +0.5*h2C36*(2*ketK+1)*(J*(J+1)-ketK*(ketK+1))^0.5;
end
if brastate==3 && ketstate==4 && braK+1==ketK
    H_o(braindex,ketindex)=H_o(braindex,ketindex) ...
        +0.5*h2C36*(2*braK+1)*(J*(J+1)-braK*(braK+1))^0.5;
end
if brastate==4 && ketstate==3 && braK==ketK-1
    H_o(braindex,ketindex)=H_o(braindex,ketindex) ...
        +0.5*h2C36*(2*ketK-1)*(J*(J+1)-ketK*(ketK-1))^0.5;
end
if brastate==3 && ketstate==4 && braK-1==ketK
    H_o(braindex,ketindex)=H_o(braindex,ketindex) ...
        +0.5*h2C36*(2*braK-1)*(J*(J+1)-braK*(braK-1))^0.5;
end
%h1Anh23 2/3 'Anharmonic' (?) Perturbation

```

## A. Appendix

```

        H_o(braindex,ketindex)=H_o(braindex,ketindex) ...
        +0.5*h1Anh23*((J*(J+1)-ketK*(ketK+1))*(J*(J+1)-(ketK+1)*(ketK+2)))^0.5;
    end
    if brastate==4 && ketstate==5 && braK+2==ketK
        H_o(braindex,ketindex)=H_o(braindex,ketindex) ...
        +0.5*h1Anh23*((J*(J+1)-braK*(braK+1))*(J*(J+1)-(braK+1)*(braK+2)))^0.5;
    end
    if brastate==5 && ketstate==4 && braK==ketK-2
        H_o(braindex,ketindex)=H_o(braindex,ketindex) ...
        +0.5*h1Anh23*((J*(J+1)-ketK*(ketK-1))*(J*(J+1)-(ketK-1)*(ketK-2)))^0.5;
    end
    if brastate==4 && ketstate==5 && braK-2==ketK
        H_o(braindex,ketindex)=H_o(braindex,ketindex) ...
        +0.5*h1Anh23*((J*(J+1)-braK*(braK-1))*(J*(J+1)-(braK-1)*(braK-2)))^0.5;
    end
end
end
end

%mp.Digits(50);
%[T E]=vpa(eig(H));
%old=digits;
%digits(100);
%[T E]=eig(sym(H));
%Energies=double(real(diag(E)));
%[Energies index]=sort(Energies);
%T=real(double(T));
%T=T(:,index);
%for n=1:length(index)
%    T(:,n)=T(:,n)/norm(T(:,n));
%end
%E=real(double(E));
%E=E(:,index);

% [T E]=eig(H);
% Energies=diag(E);

%digits(old)

%Wang version
W_e=zeros(length(qnos_e(:,1)));
for braindex=1:length(qnos_e(:,1))
    for ketindex=1:length(qnos_e(:,1))
        if qnos_e(braindex,2)==qnos_e(ketindex,2) && qnos_e(ketindex,3)>0 &&
            qnos_e(braindex,3)==-qnos_e(ketindex,3)
            W_e(braindex,ketindex)=-1/sqrt(2);
        elseif qnos_e(braindex,2)==qnos_e(ketindex,2) && qnos_e(braindex,3)==0 &&
            qnos_e(ketindex,3)==0
            W_e(braindex,ketindex)=1;
        elseif qnos_e(braindex,2)==qnos_e(ketindex,2) &&
            abs(qnos_e(braindex,3))==abs(qnos_e(ketindex,3))

```

### A.1. MATLAB code for simulating 1+1' REMPI spectra

```

        W_e(braindex,ketindex)=1/sqrt(2);
    end
end
end
if J~=0
    W_o=zeros(length(qnos_o(:,1)));
    for braindex=1:length(qnos_o(:,1))
        for ketindex=1:length(qnos_o(:,1))
            if qnos_o(braindex,2)==qnos_o(ketindex,2) && qnos_o(ketindex,3)>0 &&
                qnos_o(braindex,3)==-qnos_o(ketindex,3)
                W_o(braindex,ketindex)=-1/sqrt(2);
            elseif qnos_o(braindex,2)==qnos_o(ketindex,2) && qnos_o(braindex,3)==0 &&
                qnos_o(ketindex,3)==0
                W_o(braindex,ketindex)=1;
            elseif qnos_o(braindex,2)==qnos_o(ketindex,2) &&
                abs(qnos_o(braindex,3))==abs(qnos_o(ketindex,3))
                W_o(braindex,ketindex)=1/sqrt(2);
            end
        end
    end
end
end
W=zeros(length(qnos(:,1)));
for braindex=1:length(qnos(:,1))
    for ketindex=1:length(qnos(:,1))
        if qnos(braindex,2)==qnos(ketindex,2) && qnos(ketindex,3)>0 &&
            qnos(braindex,3)==-qnos(ketindex,3)
            W(braindex,ketindex)=-1/sqrt(2);
        elseif qnos(braindex,2)==qnos(ketindex,2) && qnos(braindex,3)==0 &&
            qnos(ketindex,3)==0
            W(braindex,ketindex)=1;
        elseif qnos(braindex,2)==qnos(ketindex,2) &&
            abs(qnos(braindex,3))==abs(qnos(ketindex,3))
            W(braindex,ketindex)=1/sqrt(2);
        end
    end
end
end
end

```

## A. Appendix

```

HWang_e=W_e'*H_e*W_e;
HWang_e=HWang_e.*(abs(HWang_e)>1E-10);

HWang_es=HWang_e(1:(length(HWang_e)+1)/2,1:(length(HWang_e)+1)/2);
%even Ka, symmetric wang fcn
HWang_ea=HWang_e((length(HWang_e)+1)/2+1:length(HWang_e),
(length(HWang_e)+1)/2+1:length(HWang_e));
%even Ka, antisymm wang fcn
[T_es, EWang_es]=eig(HWang_es);
Energies_es=diag(EWang_es);
[T_ea, EWang_ea]=eig(HWang_ea);
Energies_ea=diag(EWang_ea);

if J~=0
    HWang_o=W_o'*H_o*W_o;
    HWang_o=HWang_o.*(abs(HWang_o)>1E-10);

    HWang_os=HWang_o(1:length(HWang_o)/2,1:length(HWang_o)/2);
    %odd Ka, symm Wang fcn
    HWang_oa=HWang_o(length(HWang_o)/2+1:length(HWang_o),
length(HWang_o)/2+1:length(HWang_o)); %odd Ka, antisymm Wang fcn
    [T_os, EWang_os]=eig(HWang_os);
    Energies_os=diag(EWang_os);
    [T_oa, EWang_oa]=eig(HWang_oa);
    Energies_oa=diag(EWang_oa);
end

%The following code takes the symmetrized output and concatenates it into a
%single energy vector and basis state transformation matrix. The order of
%the symmetrized basis states is
%K=J/sym Wang, K=J-1/sym Wang, ..., K=0, ..., K=J-1/antisym Wang,K=J/antisym Wang
Tconcat=zeros(2*J+1);
Energiesconcat=zeros(2*J+1,1);

counter_es=1;
counter_ea=1;
counter_os=1;
counter_oa=1;
counter_tot=1;
for Ka=0:J
    if Ka==0
        for Tindex=1+mod(J,2):2:J+1
            Tconcat(Tindex,counter_tot)=T_es((Tindex+1-mod(J,2))/2,counter_es);
        end
        Energiesconcat(counter_tot)=Energies_es(counter_es);
        counter_tot=counter_tot+1;
        counter_es=counter_es+1;
    elseif K>0
        for Kc=[J-Ka+1,J-Ka]
            if Kc==J-Ka+1 %antisym Wang fcn (lower energy)
                if mod(Ka,2)==1 %Ka odd
                    for Tindex=J+2:2:2*J+1
                        Tconcat(Tindex,counter_tot)=T_oa((Tindex-J)/2,counter_oa);
                    end
                end
            end
        end
    end
end

```

### A.1. MATLAB code for simulating 1+1' REMPI spectra

```

end
Energiesconcat(counter_tot)=Energies_oa(counter_oa);
counter_tot=counter_tot+1;
counter_oa=counter_oa+1;
elseif mod(Ka,2)==0 %Ka even
for Tindex=J+3:2:2*J+1
Tconcat(Tindex,counter_tot)=T_ea((Tindex-(J+1))/2,counter_ea);
end
Energiesconcat(counter_tot)=Energies_ea(counter_ea);
counter_tot=counter_tot+1;
counter_ea=counter_ea+1;
end
elseif Kc==J-Ka %symm Wang fcn (higher energy)
if mod(Ka,2)==1 %Ka odd
for Tindex=2-mod(J,2):2:J
Tconcat(Tindex,counter_tot)=T_os((Tindex+mod(J,2))/2,counter_os);
end
Energiesconcat(counter_tot)=Energies_os(counter_os);
counter_tot=counter_tot+1;
counter_os=counter_os+1;
elseif mod(Ka,2)==0 %Ka even
for Tindex=1+mod(J,2):2:J+1
Tconcat(Tindex,counter_tot)=T_es((Tindex+1-mod(J,2))/2,counter_es);
end
Energiesconcat(counter_tot)=Energies_es(counter_es);
counter_tot=counter_tot+1;
counter_es=counter_es+1;
end
end
end
end
end
end

```

## A. Appendix

### Input section for the $\tilde{A}$ state

```
*****
% Diagonalization for the Hamilton Matrix in the A state
*****
function [qnos Tconcat Energiesconcat W]=PerrinWangL(Jin)
%Parameters
%Perrin, Keller, Flaud, 2003 JMS, Vol 221, pg 192

numstates = 1;
v0=zeros(1,numstates);
A=v0;
B=v0;
C=v0;
DK=v0;
DJK=v0;
DJ=v0;
deltaK=v0;
deltaJ=v0;
HK=v0;
HKJ=v0;
HJK=v0;
HJ=v0;
phiK=v0;
phiJK=v0;
phiJ=v0;

%v4' spectroscopic parameters relevant for the transition employed in this work
%These are from Ramsay review paper (Annu. Rev. Phys. Chem. 34, 31)
v0(1)=28312.561;
A(1)=8.75194;
B(1)=1.12501;
C(1)=1.01142;
DK(1)=0.0004995;
DJK(1)=0.0000656;
DJ(1)=2.59E-6;
deltaK(1)=0.0000207;
deltaJ(1)=2.05E-6;
HK(1)=0;
HKJ(1)=0;
HJK(1)=0;
HJ(1)=0;
phiK(1)=0;
phiJK(1)=0;
phiJ(1)=0;
LK(1)=0;
LKKJ(1)=0;
LJK(1)=0;
LJJK(1)=0;
LKJ(1)=0;
```



## Calculation of direction-cosine matrix elements

```

%*****
% Calculation of Direction-Cosine Matrix Elements
%*****
%According to Microwave Spectroscopy C.H. Townes and A. L. Schawlow
function [out]=Perrin(braJ,braK,ketJ,ketK,dir)
if braJ==ketJ+1
    phiJJ=(4*(ketJ+1)*((2*ketJ+1)*(2*ketJ+3))^0.5)^(-1);
elseif braJ==ketJ && braJ~=0
    phiJJ=(4*ketJ*(ketJ+1))^(-1);
elseif braJ==ketJ-1
    phiJJ=(4*ketJ*(4*ketJ^2-1)^0.5)^(-1);
else phiJJ=0;
end
%for the investigated b-type band dir='b' applies
if dir=='a' && braJ==ketJ+1 && braK==ketK
    phiJKJK=2*((ketJ+1)^2-ketK^2)^0.5;
elseif dir=='a' && braJ==ketJ && braK==ketK
    phiJKJK=2*ketK;
elseif dir=='a' && braJ==ketJ-1 && braK==ketK
    phiJKJK=2*(ketJ^2-ketK^2)^0.5;
elseif dir=='b' && braJ==ketJ+1 && braK==ketK+1
    phiJKJK=-((ketJ+ketK+1)*(ketJ+ketK+2))^0.5;
elseif dir=='b' && braJ==ketJ+1 && braK==ketK-1
    phiJKJK=+((ketJ-ketK+1)*(ketJ-ketK+2))^0.5;
elseif dir=='b' && braJ==ketJ && braK==ketK+1
    phiJKJK=((ketJ-ketK)*(ketJ+ketK+1))^0.5;
elseif dir=='b' && braJ==ketJ && braK==ketK-1
    phiJKJK=((ketJ+ketK)*(ketJ-ketK+1))^0.5;
elseif dir=='b' && braJ==ketJ-1 && braK==ketK+1
    phiJKJK=((ketJ-ketK)*(ketJ-ketK-1))^0.5;
elseif dir=='b' && braJ==ketJ-1 && braK==ketK-1
    phiJKJK=-((ketJ+ketK)*(ketJ+ketK-1))^0.5;
elseif dir=='c' && braJ==ketJ+1 && braK==ketK+1
    phiJKJK=-((ketJ+ketK+1)*(ketJ+ketK+2))^0.5;
elseif dir=='c' && braJ==ketJ+1 && braK==ketK-1
    phiJKJK=-((ketJ-ketK+1)*(ketJ-ketK+2))^0.5;
elseif dir=='c' && braJ==ketJ && braK==ketK+1
    phiJKJK=((ketJ-ketK)*(ketJ+ketK+1))^0.5;
elseif dir=='c' && braJ==ketJ && braK==ketK-1
    phiJKJK=-((ketJ+ketK)*(ketJ-ketK+1))^0.5;
elseif dir=='c' && braJ==ketJ-1 && braK==ketK+1
    phiJKJK=((ketJ-ketK)*(ketJ-ketK-1))^0.5;
elseif dir=='c' && braJ==ketJ-1 && braK==ketK-1
    phiJKJK=+((ketJ+ketK)*(ketJ+ketK-1))^0.5;
else phiJKJK=0;
end

if abs(ketK)>ketJ || abs(braK)>braJ
    phiJKJK=0;
end

out=phiJJ*phiJKJK;

```

## A.2. Best fit parameters for rotationally resolved 1+1' REMPI spectra of directly scattered formaldehyde from Au(111)

**Table A.1.:** Best fit parameters obtained from a fit of a simulation to the experimental observed spectra as shown in Figure 7.17. The simulation uses the population model given in Equation 7.6 with the constraints  $T_{\text{fit}} = T_a = T_{bc}$  and  $\sigma_a = 850 \text{ cm}^{-1}$ . The fit parameters  $T_{\text{fit}}$ ,  $S$ ,  $E_0$  are listed for each incidence translational energy  $E_i$ .

$E_i / \text{eV}$	$T_{\text{fit}} / \text{K}$	$S / 1$	$E_0 / \text{cm}^{-1}$
1.21	$820 \pm 120$	$0.58 \pm 0.26$	$970 \pm 80$
0.88	$910 \pm 290$	$0.47 \pm 0.05$	$870 \pm 80$
0.48	$690 \pm 140$	$0.27 \pm 0.10$	$720 \pm 60$
0.47	$790 \pm 150$	$0.32 \pm 0.17$	$880 \pm 70$
0.39	$770 \pm 150$	$0.26 \pm 0.09$	$480 \pm 80$
0.33	$570 \pm 90$	$0.14 \pm 0.18$	$460 \pm 50$

## A.3. MATHEMATICA program for classical trajectory calculations

The MATHEMATICA notebook written by Dr. Sascha Kandratsenka and Dr. Kai Golibruch used for classical trajectory calculations on molecule-surface collision is shown below. The program has been recently extended by Dr. Sascha Kandratsenka, Dr. G. Barratt Park and Bastian C. Krüger in order to describe 3D rigid body rotation enabling the simulation of rotational excitation in formaldehyde surface collision. The program solves the classical equations of motions according to reference [145] numerically using a rigid geometry of formaldehyde according to reference [140].

# Molecular Collisions with a Wall in 3D

Written by Kai Golibrzuch and Sascha Kandratsenka, IPC, Georg-Augusta, 37077 Göttingen, DE (2013).

Upgrade by Sascha Kandratsenka, G. Barrat Park, Bastian C. Krüger  
2016, July: 3D rigid body rotation with quaternions (the original 2D case deleted)

## Molecules:

rigid: NO, CO, CO<sub>2</sub>, acetylene, benzene, formaldehyde;

## Surfaces:

Cu, Ag, Au

## Potentials :

exponentially repulsive wall;  
Lennard - Jones (12 - 6, \*9-3, \*10-5);  
\* NO/Ag from Tully (used by Kimman et al)  
\* not adjusted for the new 3D eqns input

## Surface Models:

structureless wall;  
harmonic oscillator surface model with Debye frequency

---

## Useful Options, Unit Conversions, and LJ parameters

```
SetDirectory[NotebookDirectory[]]
|Jege Verzeichnis- |Notebook-Verzeichnis
C:\Users\Administrator\Desktop\Mathematica Notebooks und Programme\Formaldehyde Theory
Set some default options for plot functions
SetOptions[#, Axes -> False, Frame -> True,
|setze Optionen |Axen |falsch |Rahmen |wahr
PlotStyle -> {Black, Blue, Red, Green, Gray, Black} & /@
|schwarz|blau |rot |grün |grau |schwarz
{Plot, ListPlot, ListLinePlot, ParametricPlot};
|stell... |listenbezo... |listenbezogene L... |parametrische Darstellung
```

Working units are amu, Angstrom and fs. To convert the energy from eV to working units the factor eV2w is used.

## A. Appendix

```
eV2w = QuantityMagnitude[  
  [Wert einer Größe  
  UnitConvert["Electronvolts",  $\frac{\text{"AtomicMassUnitChemical" "Angstroms"}^2}{\text{"Femtoseconds"}^2}$ ]]]  
  
eV2kJ = QuantityMagnitude[UnitConvert[  
  [Wert einer Größe [konvertiere in Einheit  
  "Electronvolts" "AvogadroConstant", "Kilojoules" / "Moles"]]  
eV2kcal = QuantityMagnitude[UnitConvert["Electronvolts" "AvogadroConstant",  
  [Wert einer Größe [konvertiere in Einheit  
  "KilocaloriesThermochemical" / "Moles"]]  
T2w = QuantityMagnitude[UnitConvert[Quantity[1, "Kelvins"]  
  [Wert einer Größe [konvertiere in ...] Größe  
   $\frac{\text{Quantity}[1, \text{"BoltzmannConstant"}]}{\text{Quantity}[1, \text{"PlanckConstant"}]}, \frac{1}{\text{"Femtoseconds"}}$ ]]]  
0.00964895  
96.48533  
23.060548  
0.0000208366  
  
Lennard-Jones potential parameters from the Universal Force Field (UFF), see Rappe et al, JACS  
114 (1992) 10024  
{eH, eC, eN, eO, eCu, eAg, eAu} =  
  {0.044, 0.105, 0.069, 0.060, 0.005, 0.036, 1800 * 0.039}  $\frac{\text{eV2w}}{\text{eV2kcal}}$ ;  
{rmH, rmC, rmN, rmO, rmCu, rmAg, rmAu} = {2.886, 3.851, 3.660, 3.500, 3.495, 3.148, 3.293};
```

---

## Surfaces

Select a surface by executing corresponding cells.

The surface is defined by a set of parameters (effective mass, lattice constant, speed of sound, potential parameters etc)

Cu

Ag

### A.3. MATHEMATICA program for classical trajectory calculations

#### Au

```
 $\mu = 197;$   
 $eS = eAu;$   
 $rms = rmAu;$   
 $e1fc = 2 \pi 170 T2\omega;$   
 $LatticeConst = 4.0782;$   
 $speedofsound = 1740 * \frac{10^{10}}{10^{15}};$ 
```

---

## Molecules

Select a molecule by executing corresponding cells together with the c.of-m. system cell.

The molecule is defined by a set of parameters (atomic masses, geometry, van-der-Waals radii, LJ potential parameters, colours etc)

NO

CO

CO<sub>2</sub>

Acetylene (C<sub>2</sub> H<sub>2</sub>)

Benzene (C<sub>6</sub> H<sub>6</sub>)

---

## Formaldehyde (H<sub>2</sub> CO)

See: Burleigh et al. *JCP* **104**(1996)480

## A. Appendix

```

names = {"H", "H", "C", "O"}
      [Ko... [Ordnung von
colors = {LightGray, LightGray, Gray, Red}
      [hellgrau [hellgrau [grau [rot
masses = {1., 1., 12., 16.}
natoms = Length[masses];
      [Länge

reqCO = 1.2096;
reqCH = 1.1033;
φeqHCH = 116.19 Degree;
      [Grad

positions = {{0, -reqCH Sin[φeqHCH/2], -reqCH Cos[φeqHCH/2]},
            {0, reqCH Sin[φeqHCH/2], -reqCH Cos[φeqHCH/2]}, {0, 0, 0}, {0, 0, reqCO}};

rvdw = {1.2, 1.2, 1.7, 1.52};

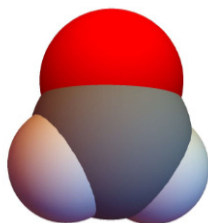
εlj = √{εH, εH, εC, εO} εs ;
rmlj = (rmH, rmH, rmC, rmO) + rms
      2
{H, H, C, O}
{█, █, █, █}
{1., 1., 12., 16.}

```

### A.3. MATHEMATICA program for classical trajectory calculations

#### C.-of-m. system: positions, Inertia tensor, etc.

```
mtot = Total[masses]
      |Gesamtsumme
δr = (positionsT - masses . positions / mtot)T;
Itensor = Sum[
      |summiere
      masses[[i]] (δr[[i]] . δr[[i]] IdentityMatrix[3] - Outer[Times, δr[[i]], δr[[i]]]),
      |Einheitsmatrix |äuße... |multipliziere
      {i, Length[masses]};
      |Länge
Itensor // TableForm
      |Tabellendarstellung
Graphics3D[Table[{colors[[i]], Sphere[δr[[i]], rvdw[[i]]}], {i, Length[masses]}],
|3D-Graphik |Tabelle |Kugel |Länge
Boxed → False, ImageSize → Small]
      |falsch |Bildgröße |klein
30.
```



---

## Potentials

Constructing a potential energy table **pot**[( $x_i, y_i, z_i$ )] of **natoms** length

### Exponential repulsion $A e^{-\alpha(z-z_0)}$

Parameters:

amplitude **a** (eV) defines at which energy an atom “touches” the surface

steepness  $\alpha$  ( $\text{\AA}^{-1}$ )

atomic “radius” **s** ( $\text{\AA}$ )

```
pexp[z_, α_, a_, s_] := a Exp[-α (z - s)]
      |Exponentialfunktion
```

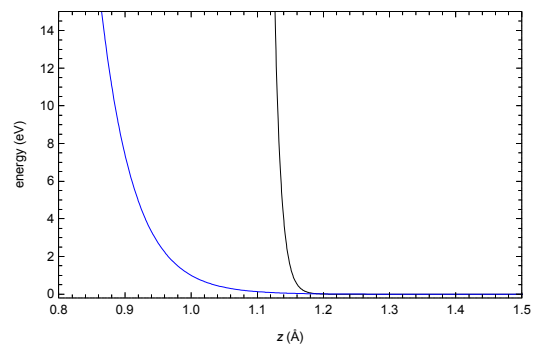
```
pot[{x_, y_, z_}] := pexp[z, α, a, s] /. {α → 20, a → 1 eV2w, s → rvdw}
```

**rvdw**

```
{1.2, 1.2, 1.7, 1.52}
```

## A. Appendix

```
Plot[{pexp[z, 100, 1 eV2w, rvdw[[1]]], pexp[z, 20, 1, 1]}, {z, 0, 2},
|stelle Funktion graphisch dar
FrameLabel -> {"z (Å)", "energy (eV)"}, PlotRange -> {{0.8, 1.5}, {- .2, 15}}
|Rahmenbeschriftung |Koordinatenbereich der Graphik
```



**Lennard - Jones (lj 12-6)**  $\epsilon \left[ \left( \frac{r_m}{r} \right)^{12} - 2 \left( \frac{r_m}{r} \right)^6 \right]$

Parameters:

depth of the potential well  $\epsilon$  (eV)

minimum position  $r_m$  (Å)

$\text{plj}[r\_ , \epsilon\_ , r\_m\_ ] := \epsilon \left( \left( \frac{r\_m}{r} \right)^{12} - 2 \left( \frac{r\_m}{r} \right)^6 \right);$

$\text{pot}[\{x\_ , y\_ , z\_ \}] := \text{plj}[z, \epsilon\text{lj}, r\text{mlj}];$



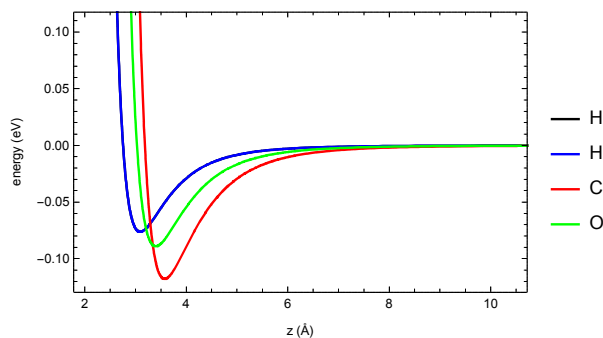
### A.3. MATHEMATICA program for classical trajectory calculations

```

{ε, rm} = {Max[ $\frac{\epsilon_{lj}}{eV2w}$ ], Max[rm1j]};
Plot[MapThread[p1j[z, #1, #2] &, { $\frac{\epsilon_{lj}}{eV2w}$ , rm1j}] // Evaluate,
{z, 0, 3 rm}, FrameLabel → {"z (Å)", "energy (eV)"},
PlotRange → {{ $\frac{rm}{2}$ , 3 rm}, {-1.1 ε, ε}}, PlotLegends → names]

```

{ε, rm} = .;



\* Lennard - Jones (**lj 9-3**) force

\* Lennard - Jones (**lj 10-5**) force (reasonable agreement with Tully's empirical potential from J. Chem Phys 1985, 83, 2594)

\* Potentials for NO/Ag (Tully, J.Chem Phys 1985, 83, 2594, modified parameters from Kimman et al, PRL 1986, 57, 2053)

Surface interaction potential (chemical interaction)

Surface interaction potential with van-der-Waals interaction

Morse potential for N - O interaction

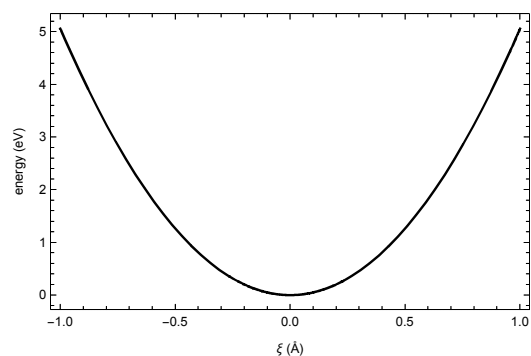
Elastic (**elf**) force

```

pels[r_, r0_, k_] :=  $\frac{k}{2} (r - r0)^2$ ;
potsurf[ξ_] := pels[ξ, 0, μ (elfc)2]

```

Plot [pe1s[ $\xi$ ,  $\theta$ , (e1fc)<sup>2</sup>  $\mu$ ] / eV2w, { $\xi$ , -1, 1}, FrameLabel -> {" $\xi$  (Å)", "energy (eV)"}]  
[stelle Funktion graphisch dar] [Rahmenbeschriftung]



## Simulations

### Fixed Surface

### Moving surface (harmonic oscillator with Debye Frequency)

#### Initialization

Simulation conditions:

number of trajectories **ntrajs**  
 integration time **tf** (fs)

Translations:

incidence energy **Einc** (eV)  
 incidence angle **θinc**  
 initial position of molecular c.-of-m. **rcm0** (Å) (axes origin is at the surface)

Rotations:

incidence energy of rotation around principal axes **ERinc** (eV) (negative sign means clockwise rotation)  
 initial molecular orientation is defined by sampling random quaternions uniformly  
 (S.M. LaValle *Planning Algorithms* (2006), <http://planning.cs.uiuc.edu/web.html>)

Surface motion:

initial surface kinetic energy **EWi** (eV), negative value means motion against z-axis  
 initial surface coordinate **ξ0** (Å)

### A.3. MATHEMATICA program for classical trajectory calculations

```

ntrajs = 10000;
tf = 2400;

(* translations *)
Einc = 0.2 eV2w;
einc = 0;

z0 = RandomReal[{10, 12}];
      [reelle Zufallszahl]

{vx0, vy0, vz0} =  $\sqrt{\frac{2 Einc}{mtot}}$  {Sin[einc], 0, -Cos[einc]};
      [Sinus] [Kosinus]

(* rotations *)
ERinc = {0.0, 0., 0.} eV2w;

qsubs = Thread[{q00, q10, q20, q30} ->
      [fädle auf]
      { $\sqrt{1 - \#[[1]]}$  Sin[2  $\pi$   $\#[[2]]$ ],
      [Sinus]
       $\sqrt{1 - \#[[1]]}$  Cos[2  $\pi$   $\#[[2]]$ ],
      [Kosinus]
       $\sqrt{\#[[1]]}$  Sin[2  $\pi$   $\#[[3]]$ ],
      [Sinus]
       $\sqrt{\#[[1]]}$  Cos[2  $\pi$   $\#[[3]]$ ]}] & /@ Table[RandomReal[1, 3], {ntrajs}];
      [Kosinus] [Tabelle [reelle Zufallszahl]

{ $\omega_{px0}$ ,  $\omega_{py0}$ ,  $\omega_{pz0}$ } = Sign[ERinc]  $\sqrt{\frac{2 Abs[ERinc]}{Diagonal[Itensor]}}$ ;
      [Vorzeichen]

(* surface motion *)
Ewi = 1.38 * 10^(-23) / (1.602 * 10^(-19)) * 300 * 0.5 eV2w;

xi0 = 0;

vxi0 = Sign[Ewi]  $\sqrt{\frac{2 Abs[Ewi]}{\mu}}$ ;
      [Vorzeichen]

```

#### Equations of Motion

DoFs:

- molecular c.-of-m. position vector  $(x, y, z)$
- quaternion  $\mathbf{q} = (q_0, q_1, q_2, q_3)$  with constraint  $\mathbf{q} \cdot \tilde{\mathbf{q}} = 1$
- surface shift  $\xi = (0, 0, \xi)$  along the normal (z-axis direction)

## A. Appendix

Its motion is governed by (Allen & Tildesley *Computer Simulation of Liquids*, 1987)

$$\text{c.-of.m. equation of motion } M \ddot{\mathbf{r}}_{\text{cm}} = \mathbf{F}$$

$$\text{Euler-Newton equation in the body-fixed frame: } \dot{\mathbf{L}} + \boldsymbol{\omega} \times \mathbf{L} = \mathbf{T} \quad (\mathbf{L} = \mathbf{I} \cdot \boldsymbol{\omega})$$

$$\text{equation for rotation of body-fixed frame: } 2 \dot{\mathbf{q}} = \mathbf{q} \tilde{\boldsymbol{\omega}} \cdot (0, \boldsymbol{\omega})$$

$$\text{equation of motion for the surface } \mu \ddot{\boldsymbol{\xi}} = \Xi - F_z$$

where

$$\mathbf{F} = \sum \mathbf{F}_i = -\sum \nabla U_j(\mathbf{r}_{\text{cm}} + \mathbf{R}^T \cdot \delta \mathbf{r}_b - \boldsymbol{\xi}) \text{ is the total force and}$$

$$\mathbf{T} = \sum (\mathbf{r}_i - \mathbf{r}_{\text{cm}}) \times \mathbf{F}_i = \sum (\mathbf{R}^T \cdot \delta \mathbf{r}_b) \times \mathbf{F} \text{ is the torque relative c.-of.m. exerted on a molecule;}$$

$$\Xi(\boldsymbol{\xi}) \text{ is the surface internal force}$$

Rotation matrix **rotm** handles the conversion from space-fixed frame to body-fixed frame.

**qi** $[\boldsymbol{\theta}, \boldsymbol{\phi}, \boldsymbol{\psi}]$  relates Euler angles to quaternion components

**anmom** is the angular momentum in the body-fixed frame

$$q_{0i}[\theta_-, \phi_-, \psi_-] := \text{Cos}\left[\frac{\theta_-}{2}\right] \text{Cos}\left[\frac{\phi_- + \psi_-}{2}\right];$$

$$q_{1i}[\theta_-, \phi_-, \psi_-] := \text{Sin}\left[\frac{\theta_-}{2}\right] \text{Cos}\left[\frac{\phi_- - \psi_-}{2}\right];$$

$$q_{2i}[\theta_-, \phi_-, \psi_-] := \text{Sin}\left[\frac{\theta_-}{2}\right] \text{Sin}\left[\frac{\phi_- - \psi_-}{2}\right];$$

$$q_{3i}[\theta_-, \phi_-, \psi_-] := \text{Cos}\left[\frac{\theta_-}{2}\right] \text{Sin}\left[\frac{\phi_- + \psi_-}{2}\right];$$

### A.3. MATHEMATICA program for classical trajectory calculations

```

rotm = {{q0[t]^2 + q1[t]^2 - q2[t]^2 - q3[t]^2,
        2 (q1[t] q2[t] + q0[t] q3[t]), 2 (q1[t] q3[t] - q0[t] q2[t])},
        {2 (q1[t] q2[t] - q0[t] q3[t]), q0[t]^2 - q1[t]^2 + q2[t]^2 - q3[t]^2,
        2 (q2[t] q3[t] + q0[t] q1[t])}, {2 (q1[t] q3[t] + q0[t] q2[t]),
        2 (q2[t] q3[t] - q0[t] q1[t]), q0[t]^2 - q1[t]^2 - q2[t]^2 + q3[t]^2}};
anmom = Itensor.{wpX[t], wpy[t], wpz[t]};

force = Simplify[-Table[D[pot[{x, y, z}][[i]], {{x, y, z}}] /. Thread[
    {x, y, z} -> {x[t], y[t], z[t]} + rotm.T.Dr[[i]] - {0, 0, xi[t]}], {i, natoms}]];
torque = Sum[(rotm.T.Dr[[i]]) * force[[i]], {i, natoms}];
fsurf = -D[potsurf[xi[t]], xi[t]];

eqtr = Thread[mtot {x''[t], y''[t], z''[t]} == Total[force]];
eqrot =
    MapThread[Equal, {D[anmom, t], (-{wpX[t], wpy[t], wpz[t]} * anmom + rotm.torque)}];
equat = MapThread[Equal,
    {D[{q0[t], q1[t], q2[t], q3[t]}, t], .5 {{q0[t], -q1[t], -q2[t], -q3[t]},
    {q1[t], q0[t], -q3[t], q2[t]}, {q2[t], q3[t], q0[t], -q1[t]},
    {q3[t], -q2[t], q1[t], q0[t]}}.{0, wpX[t], wpy[t], wpz[t]}}];
quatconstr = {{q0[t], q1[t], q2[t], q3[t]}.{q0[t], q1[t], q2[t], q3[t]} == 1};

eqsurf = {mu xi''[t] == fsurf - Total[force][[3]]};

icond = {x[0] == 0, y[0] == 0, z[0] == z0, x'[0] == vx0, y'[0] == vy0,
        z'[0] == vz0, q0[0] == q00, q1[0] == q10, q2[0] == q20, q3[0] == q30,
        wpX[0] == wpX0, wpy[0] == wpy0, wpz[0] == wpz0, xi[0] == xi0, xi'[0] == vxxi0};

Timing[sol = Table[NDSolve[Join[eqtr, eqrot, equat, eqsurf, icond /. qsubs[[i]]],
    {x, y, z, q0, q1, q2, q3, wpX, wpy, wpz, xi}, {t, 0, tf}], {i, ntrajs}]];

```

## Analysis

### Binning

```

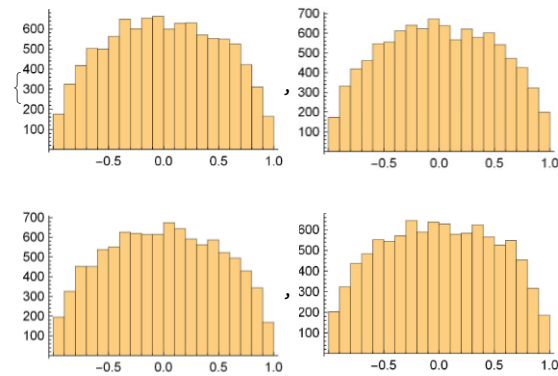
liste = Select[Evaluate[z[tf] /. sol[[All, 1]]], # > 4 / 5 z0 &];
nliste = Select[Evaluate[z[tf] /. sol[[All, 1]]], # < 4 / 5 z0 &];
hlist = Flatten[Table[
  Position[Evaluate[z[tf] /. sol[[All, 1]]], liste[[i]], {i, 1, Length[liste]}]];
nlisten = Flatten[Table[Position[Evaluate[z[tf] /. sol[[All, 1]]], nliste[[i]],
  {i, 1, Length[nliste]}]];
atrap = (ntrajs - Length[hlist]) / ntrajs / 1.0

```

```

Histogram[Flatten[# /. sol]] & /@ {q0[0], q1[0], q2[0], q3[0]}

```



$$Etrnf = \frac{mtot}{2} \text{Flatten}[D[z[t] /. \#, t] /. t \rightarrow tf \& /@ \text{sol}[[hlist]]]^2 / eV2w;$$

$$Etr1f = \frac{mtot}{2} (\text{Flatten}[D[x[t] /. \#, t] /. t \rightarrow tf \& /@ \text{sol}[[hlist]]]^2 + \text{Flatten}[D[y[t] /. \#, t] /. t \rightarrow tf \& /@ \text{sol}[[hlist]]]^2) / eV2w;$$

{Erotx, Eroty, Erotz} =

$$\text{Transpose} \left[ \frac{1}{2} \text{Flatten}[\{\omega px[t], \omega py[t], \omega pz[t]\} /. \# /. t \rightarrow tf \& /@ \text{sol}[[hlist]], 1]^2, \right]$$

Itensor] / eV2w;

### A.3. MATHEMATICA program for classical trajectory calculations

```

vf = {x'[tf], z'[tf]} /. sol[[hlist, 1]];
wf = phi'[tf] /. sol[[hlist, 1]];
vw = xi'[tf] /. sol[[hlist, 1]];
efinal = xi[tf] /. sol[[hlist, 1]];
Epotsurffinal = potsurf[efinal] / eV2w;
{Etrxf, Etrzf} =  $\frac{m}{2} vf^2 / eV2w$ ;
Erotf =  $\frac{Iy}{2} wf^2 / eV2w$ ;
Ewf = 1 / 2 mu vw^2 / eV2w;

```

#### Analysis of the rotation

```

Jliste = Select[Erotz, # > 0.2 &];
      [wähle aus]
Jliste2 = Flatten[Table[Position[Erotz, Jliste[[i]]], {i, 1, Length[Jliste]}]];
      [Lebne ein] [Tabelle] [Position] [Länge]

q0i[theta_, phi_, psi_] := Cos[ $\frac{\theta}{2}$ ] Cos[ $\frac{\phi + \psi}{2}$ ];
      [Kosinus] [Kosinus]
q1i[theta_, phi_, psi_] := Sin[ $\frac{\theta}{2}$ ] Cos[ $\frac{\phi - \psi}{2}$ ];
      [Sinus] [Kosinus]
q2i[theta_, phi_, psi_] := Sin[ $\frac{\theta}{2}$ ] Sin[ $\frac{\phi - \psi}{2}$ ];
      [Sinus] [Sinus]
q3i[theta_, phi_, psi_] := Cos[ $\frac{\theta}{2}$ ] Sin[ $\frac{\phi + \psi}{2}$ ];
      [Kosinus] [Sinus]

eulertoqrotm[theta_, phi_, psi_] := rotm /. Thread[{q0[t], q1[t], q2[t], q3[t]} ->
      [fädle auf]
      {q0i[theta, phi, psi], q1i[theta, phi, psi], q2i[theta, phi, psi], q3i[theta, phi, psi]}]
(*These relations can be derived from the rotation matrix written in *)
eulerthetaq[ntraj_] := 1. ArcCos[(rotm /. t -> theta)[[3, 3]] /. sol[[ntraj]]]
      [Arkuskosinus]
eulerPhiq[ntraj_] := ArcTan[-(rotm /. t -> theta)[[3, 2]] /. sol[[ntraj]],
      [Arkustangens]
      (rotm /. t -> theta)[[3, 1]] /. sol[[ntraj]]]
eulerPsiq[ntraj_] := ArcTan[(rotm /. t -> theta)[[2, 3]] /. sol[[ntraj]],
      [Arkustangens]
      (rotm /. t -> theta)[[1, 3]] /. sol[[ntraj]]]

```

## A. Appendix

```

Theta0 = Flatten[Table[eulerthetaq[i], {i, hlist}]];
      |ebne ein |Tabelle
Phi0 = Flatten[Table[eulerPhiq[i], {i, hlist}], 1];
      |ebne ein |Tabelle
Psi0 = Flatten[Table[eulerPsiq[i], {i, hlist}], 1];
      |ebne ein |Tabelle
rotliste = Prepend[Transpose[{Theta0, Phi0, Psi0, Erotx, Eroty, Erotz}],
      |stelle vo...|transponiere
      {"Theta", "Phi", "Psi", "Erotx", "Eroty", "Erotz"}];

Export[StringJoin["LJ1800_Ei", ToString[Einc / eV2w], ".dat"], rotliste]
|exporti...|vereinige Zeichenketten |als Zeichenkette
LJ1800_Ei0.2.dat

{Histogram[Theta0], Histogram[Phi0], Histogram[Psi0]}
|Histogramm |Histogramm |Histogramm

thetadependenz = {Round[#[[1, 1]], 0.04], Mean[#[[All, 2]]]} & /@
      |runde |arithmeti...|alle
      Gather[Transpose[{Theta0, Erotz}], Round[#1[[1]], 0.04] == Round[#2[[1]], 0.04] &];
      |sammler|transponiere |runde |runde
thetadependenz = {Round[#[[1, 1]], 0.04], Mean[#[[All, 2]]]} & /@
      |runde |arithmeti...|alle
      Gather[Transpose[{Theta0, Erotx}], Round[#1[[1]], 0.04] == Round[#2[[1]], 0.04] &];
      |sammler|transponiere |runde |runde
thetadependenz = {Round[#[[1, 1]], 0.04], Mean[#[[All, 2]]]} & /@
      |runde |arithmeti...|alle
      Gather[Transpose[{Theta0, Eroty}], Round[#1[[1]], 0.04] == Round[#2[[1]], 0.04] &];
      |sammler|transponiere |runde |runde
Phidependenz = {Round[#[[1, 1]], 0.04], Mean[#[[All, 2]]]} & /@
      |runde |arithmeti...|alle
      Gather[Transpose[{Phi0, Erotz + Erotx + Eroty}],
      |transponiere
      Round[#1[[1]], 0.04] == Round[#2[[1]], 0.04] &];
      |runde |runde
Psidependenz = {Round[#[[1, 1]], 0.04], Mean[#[[All, 2]]]} & /@
      |runde |arithmeti...|alle
      Gather[Transpose[{Psi0, Erotz + Erotx + Eroty}],
      |transponiere
      Round[#1[[1]], 0.04] == Round[#2[[1]], 0.04] &];
      |runde |runde

ListPlot3D[Transpose[{Phi0, Psi0, Erotz}],
|listenbezoge...|transponiere
PlotRange -> {All, All, All}, AxesLabel -> {"Phi", "Psi", "Erot"}]
|Koordinatenber...|alle |alle |alle |Achsenbeschriftung

ListPlot3D[Transpose[{Theta0, Psi0, Eroty}],
|listenbezoge...|transponiere
PlotRange -> {All, All, All}, AxesLabel -> {"Theta", "Psi", "Erot"}]
|Koordinatenber...|alle |alle |alle |Achsenbeschriftung

```



### A.3. MATHEMATICA program for classical trajectory calculations

```

ListPlot3D[Transpose[{Theta0, Psi0, Erotx}],
|listenbezoge...|transponiere
PlotRange -> {All, All, All}, AxesLabel -> {"Theta", "Psi", "Erot"}]
|Koordinatenber...|alle |alle |alle |Achsenbeschriftung

ListPlot3D[Transpose[{Theta0, Psi0, Erotz}], PlotRange -> {All, {0, Pi}, All},
|listenbezoge...|transponiere |Koordinatenber...|alle |Kre...|alle
AxesLabel -> {" $\theta / ^\circ$ ", " $\phi / ^\circ$ ", ""}, LabelStyle -> FontSize -> 50]
|Achsenbeschriftung |Beschriftungsstil |Schriftgröße

ListPlot[Transpose[{Theta0, Erotz}], PlotRange -> All];
|listenbez...|transponiere |Koordinatenb...|alle

ListPlot[Transpose[{Psi0, Erotz}], PlotRange -> All];
|listenbez...|transponiere |Koordinatenb...|alle

ListPlot[{thetadependenz, thetadependenzx, thetadependenzey},
|listenbezogene Graphik
PlotRange -> {All, All}, PlotStyle -> PointSize[0.03]];
|Koordinatenber...|alle |alle |Darstellungsstil |Punktgröße

ListPlot[Phidependence, PlotRange -> {{-Pi / 2, Pi / 2}, All}];
|listenbezogene Graphik |Koordinatenbereich...|Kreis... |Kreiszahl |alle

ListPlot[Psidependence, PlotRange -> {{-Pi / 2, Pi / 2}, All}];
|listenbezogene Graphik |Koordinatenbereich...|Kreis... |Kreiszahl |alle

Manipulate[Graphics3D[Table[{colors[[i]],
|manipuliere |3D-Graphik |Tabelle
Sphere[({x[t], y[t], z[t]} +  $\delta r[[i]] \cdot \text{rotm}$ ) /. sol[[n, 1]] /. t -> k, rvdw[[i]]}],
|Kugel
{i, natoms}], Boxed -> True, PlotRange -> {{-5, 7}, {-5, 5}, {0, 15}}],
|einger... |wahr |Koordinatenbereich der Graphik
{{k, 0, "Time (fs)", 0, tf}, {{n, 1, "Trajectory"}, Jliste2}];

Histogram[Flatten[# /. sol[Jliste2]]] & /@ {q0[0], q1[0], q2[0], q3[0]};
|Histogramm |ebne ein

Histogram[Table[rotmtoeulertheta[Jliste2[[i]], {i, 1, Length[Jliste2]}]];
|Histogramm |Tabelle |Länge

Histogram[Table[rotmtoeulerphi[Jliste2[[i]], {i, 1, Length[Jliste2]}]];
|Histogramm |Tabelle |Länge

Histogram[Table[rotmtoeulerPsi[Jliste2[[i]], {i, 1, Length[Jliste2]}]];
|Histogramm |Tabelle |Länge

```

## General Analysis

```
Jliste = Select[Erotz, # < 0.003 &];  
      |wähle aus  
Jliste2 = Flatten[Table[Position[Erotz, Jliste[[i]]], {i, 1, Length[Jliste]}]];  
      |Ebne ein |Tabelle |Position |Länge  
  
(Erotz + Erotx + Eroty + Epotsurffinal + Etrnf + Ewf - Ewi / eV2w) [[1 ;; 20]]  
{0.199545, 0.200107, 0.200008, 0.199524, 0.199414, 0.201668,  
 0.201737, 0.19933, 0.199482, 0.199605, 0.200016, 0.199333, 0.199359,  
 0.199339, 0.199377, 0.199911, 0.199662, 0.199403, 0.199464, 0.20126}  
  
Histogram[Etrnf, {.025}]  
|Histogramm  
  
Histogram[Etrnf[[Jliste2]], {.025}]  
|Histogramm  
  
Histogram[Etrnf, {0.025}]  
|Histogramm  
  
ast = HistogramList[Etrnf, {0.025}]  
      |Histogramm-Liste  
Efinalz =  
  MovingAverage[ast[[1]], 2][[Flatten[Position[ast[[2]], Max[ast[[2]]]]][[1]]] * 1.0  
      |gleitender Durchschnitt |Ebne ein |Position |größtes Element  
astlowz = HistogramList[Etrnf[[Jliste2]], {0.025}];  
      |Histogramm-Liste  
Efinalzlowz = MovingAverage[astlowz[[1]], 2][[  
      |gleitender Durchschnitt  
      Flatten[Position[astlowz[[2]], Max[astlowz[[2]]]]][[1]]] * 1.0  
      |Ebne ein |Position |größtes Element
```

### A.3. MATHEMATICA program for classical trajectory calculations

```
rotbin = 0.025;
{Histogram[{(Eroty + Erotx) / 2}, {rotbin}], Histogram[{Erotz}, {rotbin}],
  Histogram[{Erotx + Eroty + Erotz}, {rotbin}]} // TableForm
erotxuyd2 = HistogramList[(Eroty + Erotx) / 2, {rotbin}][[2]];
binlistxuy2 = Table[(2 i - 1) / 2 * rotbin, {i, 1, Length[erotxuyd2]}];
erotxylst = Transpose[{binlistxuy2, erotxuyd2}];
erotz = HistogramList[(Erotz) / 2, {rotbin}][[2]];
binlistz = Table[(2 i - 1) / 2 * rotbin, {i, 1, Length[erotz]}];
erotzlst = Transpose[{binlistz, erotz}];
erotg = HistogramList[(Erotx + Eroty + Erotz) / 2, {rotbin}][[2]];
binlistg = Table[(2 i - 1) / 2 * rotbin, {i, 1, Length[erotg]}];
erotglist = Transpose[{binlistg, erotg}];

ListPlot[{erotxylst, erotzlst, erotglist}, PlotRange -> All]
Clear[resmovsurf]
resmovsurf[Einc / eV2w] =
  {Einc / eV2w, Mean[Erotx + Eroty + Erotz], Mean[(Erotx + Eroty) / 2], Mean[Erotz],
  Efinalz, Efinalzlowz, Mean[Epotsurffinal + Ewf - Ewi / eV2w], atrap}
{0.2, 0.0513905, 0.0125396, 0.0263113, 0.0375, 0.0375, 0.0806653, 0.5433}

Save["movsurfLJAUF1800selectJz.dat", resmovsurf]
```

Visualization

Add



## B. List of abbreviations

<b>Abbreviation</b>	<b>Meaning</b>
BBO	beta-barium borate
DFT	density functional theory
ECDL	external cavity diode laser
FWHM	full width at half maximum
IESH	independent electron surface hopping
IR	infrared
KTP	potassium titanyl phosphate
LIF	laser induced fluorescence
MCP	micro-channel plate
“ML”	monolayer (unit)
Nd:YAG	neodymium-doped yttrium aluminum garnet
Nd:YLF	neodymium-doped yttrium lithium fluoride
OPA	optical parametric amplifier
OPO	optical parametric oscillator
PZT	piezoelectric transducer
REMPI	resonance-enhanced multiphoton ionization
TPD	temperature programmed desorption
UHV	ultra-high vacuum
UV	ultraviolet
VUV	vacuum ultraviolet



## C. References

- [1] J. H. Sinfelt, Role of surface science in catalysis, *Surf. Sci.* **2002**, *500*(1), 923–946, doi: 10.1016/S0039-6028(01)01532-1.
- [2] G. a. Somorjai, Y. Li, Impact of surface chemistry, *Proc. Natl. Acad. Sci.* **2011**, *108*(3), 917–924, doi: 10.1073/pnas.1006669107.
- [3] G. Ertl, Primary steps in catalytic synthesis of ammonia, *J. Vac. Sci. Technol. A* **1983**, *1*(2), 1247–1253, doi: 10.1116/1.572299.
- [4] J. W. Erisman, M. A. Sutton, J. Galloway, Z. Klimont, W. Winiwarter, How a century of ammonia synthesis changed the world, *Nat. Geosci.* **2008**, *1*, 636–639, doi: 10.1038/ngeo325.
- [5] A. von Zastrow, J. Onvlee, S. N. Vogels, G. C. Groenenboom, A. van der Avoird, S. Y. T. van de Meerakker, State-resolved diffraction oscillations imaged for inelastic collisions of NO radicals with He, Ne and Ar, *Nat. Chem.* **2014**, *6*, 216–221, doi: 10.1038/nchem.1860.
- [6] N. Bartels, B. C. Krüger, D. J. Auerbach, A. M. Wodtke, T. Schäfer, Controlling an electron-transfer reaction at a metal surface by manipulating reactant motion and orientation, *Angew. Chem. Int. Ed.* **2014**, *53*(50), 13690–13694, doi: 10.1002/anie.201407051.
- [7] B. C. Krüger, N. Bartels, C. Bartels, A. Kandratsenka, J. C. Tully, A. M. Wodtke, T. Schäfer, NO Vibrational Energy Transfer on a Metal Surface: Still a Challenge to First-Principles Theory, *J. Phys. Chem. C* **2015**, *119*(6), 3268–3272, doi: 10.1021/acs.jpcc.5b00388.
- [8] N. Shenvi, S. Roy, J. C. Tully, Dynamical steering and electronic excitation in NO scattering from a gold surface, *Science* **2009**, *326*(5954), 829–832, doi: 10.1126/science.1179240.

### C. References

- [9] K. Golibrzuch, N. Bartels, D. J. Auerbach, A. M. Wodtke, The Dynamics of Molecular Interactions and Chemical Reactions at Metal Surfaces: Testing the Foundations of Theory, *Annu. Rev. Phys. Chem.* **2015**, *66*(1), 399–425, doi: 10.1146/annurev-physchem-040214-121958.
- [10] J. C. Tully, Perspective on "Zur Quantentheorie der Molekeln", *Theor. Chem. Acc.* **2000**, 173–176, doi: 10.1007/s002149900049.
- [11] Y. Huang, C. T. Rettner, D. J. Auerbach, A. M. Wodtke, Vibrational Promotion of Electron Transfer, *Science* **2000**, *290*(5489), 111–114, doi: 10.1126/science.290.5489.111.
- [12] R. Cooper, Z. Li, K. Golibrzuch, C. Bartels, I. Rahinov, D. J. Auerbach, A. M. Wodtke, On the determination of absolute vibrational excitation probabilities in molecule-surface scattering: case study of NO on Au(111), *J. Chem. Phys.* **2012**, *137*(6), 064705, doi: 10.1063/1.4738596.
- [13] J. D. White, J. Chen, D. Matsiev, D. J. Auerbach, A. M. Wodtke, Vibrationally promoted electron emission from low work-function metal surfaces., *J. Chem. Phys.* **2006**, *124*(6), 64702, doi: 10.1063/1.2166360.
- [14] A. M. Wodtke, D. Matsiev, D. J. Auerbach, Energy transfer and chemical dynamics at solid surfaces: The special role of charge transfer, *Prog. Surf. Sci.* **2008**, *83*(3), 167–214, doi: 10.1016/j.progsurf.2008.02.001.
- [15] S. Monturet, P. Saalfrank, Role of electronic friction during the scattering of vibrationally excited nitric oxide molecules from Au(111), *Phys. Rev. B.* **2010**, *82*(7), 075404, doi: 10.1103/PhysRevB.82.075404.
- [16] K. Golibrzuch, P. R. Shirhatti, I. Rahinov, A. Kandratsenka, D. J. Auerbach, A. M. Wodtke, C. Bartels, The importance of accurate adiabatic interaction potentials for the correct description of electronically nonadiabatic vibrational energy transfer: A combined experimental and theoretical study of NO( $v = 3$ ) collisions with a Au(111) surface, *J. Chem. Phys.* **2014**, *140*(4), 044701, doi: 10.1063/1.4861660.
- [17] K. Golibrzuch, P. R. Shirhatti, J. Altschäffel, I. Rahinov, D. J. Auerbach, A. M. Wodtke, C. Bartels, State-to-state time-of-flight measurements of NO scattering from Au(111): direct observation of translation-to-vibration coupling in electronically nonadiabatic energy transfer., *J. Phys. Chem. A* **2013**, *117*(36), 8750–8760, doi: 10.1021/jp403382b.



- [18] C. Rettner, F. Fabre, J. Kimman, D. Auerbach, Observation of Direct Vibrational Excitation in Gas-Surface Collisions: NO on Ag(111), *Phys. Rev. Lett.* **1985**, 55(18), 1904–1907, doi: 10.1103/PhysRevLett.55.1904.
- [19] C. Steinsiek, Molecular Beam Scattering from Ultrathin Metallic Films, PhD thesis, Georg-August-Universität Göttingen, **2017**.
- [20] I. Rahinov, R. Cooper, C. Yuan, X. Yang, D. J. Auerbach, A. M. Wodtke, Efficient vibrational and translational excitations of a solid metal surface: State-to-state time-of-flight measurements of HCl( $v = 2, J = 1$ ) scattering from Au(111), *J. Chem. Phys.* **2008**, 129(21), 214708, doi: 10.1063/1.3028542.
- [21] T. Schäfer, N. Bartels, K. Golibrzuch, C. Bartels, H. Köckert, D. J. Auerbach, T. N. Kitsopoulos, A. M. Wodtke, Observation of direct vibrational excitation in gas-surface collisions of CO with Au(111): a new model system for surface dynamics., *Phys. Chem. Chem. Phys.* **2013**, 15(6), 1863–1867, doi: 10.1039/c2cp43351f.
- [22] P. Burrow, J. Michejda, Electron transmission study of the formaldehyde electron affinity, *Chem. Phys. Lett.* **1976**, 42(2), 223–226, doi: 10.1016/0009-2614(76)80351-X.
- [23] G. J. Schulz, Resonances in Electron Impact on Diatomic Molecules, *Rev. Mod. Phys.* **1973**, 45, 423–486, doi: 10.1103/RevModPhys.45.423.
- [24] I. Rahinov, R. Cooper, D. Matsiev, C. Bartels, D. J. Auerbach, A. M. Wodtke, Quantifying the breakdown of the Born-Oppenheimer approximation in surface chemistry, *Phys. Chem. Chem. Phys.* **2011**, 13(28), 12680–12692, doi: 10.1039/c1cp20356h.
- [25] J. Liu, H. T. Kim, S. L. Anderson, Multiphoton ionization and photoelectron spectroscopy of formaldehyde via its 3p Rydberg states, *J. Chem. Phys.* **2001**, 114(22), 9797–9806, doi: 10.1063/1.1370943.
- [26] F. R. Gilmore, Potential energy curves for N<sub>2</sub>, NO, O<sub>2</sub> and corresponding ions, *J. Quant. Spectrosc. Radiat. Transfer* **1965**, 5(2), 369–IN3, doi: 10.1016/0022-4073(65)90072-5.
- [27] D. C. Jacobs, R. J. Madix, R. N. Zare, Reduction of 1+1 resonance enhanced MPI spectra to population distributions: Application to the NO X<sup>2</sup>Π-A<sup>2</sup>Σ<sup>+</sup> system, *J. Chem. Phys.* **1986**, 85(10), 5469–5479, doi: 10.1063/1.451557.

### C. References

- [28] C. Amiot, R. Bacis, G. Guelachvili, Infrared study of the  $X^2\Pi$   $v = 0, 1, 2$  levels of  $^{14}\text{N}^{16}\text{O}$ . Preliminary results on the  $v = 0, 1$  levels of  $^{14}\text{N}^{17}\text{O}$ ,  $^{14}\text{N}^{18}\text{O}$  and  $^{15}\text{N}^{16}\text{O}$ , *Can. J. Phys.* **1978**, *56*, 251–265, doi: 10.1139/p78-032.
- [29] C. Amiot, J.-P. Maillard, J. Chauville, Fourier spectroscopy of the OD infrared spectrum. Merge of electronic, vibration-rotation, and microwave spectroscopic data, *J. Mol. Spectrosc.* **1981**, *87*(1), 196–218, doi: 10.1016/0022-2852(81)90089-8.
- [30] C. Amiot, The infrared emission spectrum of NO: Analysis of the  $\Delta v = 3$  sequence up to  $v = 22$ , *J. Mol. Spectrosc.* **1982**, *94*(1), 150–172, doi: /10.1016/0022-2852(82)90301-0.
- [31] J. Brown, E. Colbourn, J. Watson, F. Wayne, An effective Hamiltonian for diatomic molecules: Ab initio calculations of parameters of  $\text{HCl}^+$ , *J. Mol. Spectrosc.* **1979**, *74*(2), 294–318, doi: 10.1016/0022-2852(79)90059-6.
- [32] J. Danielak, U. Domin, R. Ke, M. Rytel, M. Zachwieja, Reinvestigation of the Emission  $\gamma$  Band System ( $A^2\Sigma^+-X^2\Pi$ ) of the NO Molecule, *J. Mol. Spectrosc.* **1997**, *181*(2), 394–402, doi: 10.1006/jmsp.1996.7181.
- [33] M. de Lange, J. van Leuken, M. Drabbels, J. Bulthuis, J. Snijders, S. Stolte, Direct spectroscopic determination of the degree of orientation of parity-selected NO, *Chem. Phys. Lett.* **1998**, *294*(4-5), 332–338, doi: 10.1016/S0009-2614(98)00865-3.
- [34] D. J. Clouthier, D. A. Ramsay, The spectroscopy of formaldehyde and thioformaldehyde, *Annu. Rev. Phys. Chem.* **1983**, *34*, 31–58, doi: 10.1146/annurev.pc.34.100183.000335.
- [35] P. R. Bunker, P. Jensen, *Molecular Symmetry and Spectroscopy*, NRC Research Press, Ottawa, **1998**.
- [36] D. Papoušek, *Molecular Vibrational-Rotational Spectra*, Elsevier, Amsterdam, **1982**.
- [37] P. F. Bernath, *Spectra of Atoms and Molecules*, Oxford University Press, New York, **1995**.

- [38] J. K. G. Watson, in *Vibrational Spectra and Structure*, volume 6, (edited by J. Durning), Elsevier, Amsterdam, **1976**, p. 1.
- [39] K. Yamanouchi, *Quantum Mechanics of Molecular Structures*, Springer, Heidelberg, New York, Dordrecht, London, **2012**.
- [40] H. S. P. Müller, G. Winnewisser, J. Demaison, A. Perrin, A. Valentin, The ground state spectroscopic constants of formaldehyde, *J. Mol. Spectrosc.* **2000**, 200(1), 143–144, doi: 10.1006/jmsp.1999.8027.
- [41] P. Jensen, P. Bunker, The geometry and the inversion potential function of formaldehyde in the  $\tilde{A}^1A_2$  and  $\tilde{a}^3A_2$  electronic states, *J. Mol. Spectrosc.* **1982**, 94(1), 114–125, doi: /10.1016/0022-2852(82)90298-3.
- [42] D. C. Moule, A. D. Walsh, Ultraviolet spectra and excited states of formaldehyde, *Chem. Rev.* **1975**, 75(1), 67–84, doi: 10.1021/cr60293a003.
- [43] R. N. Zare, *Angular Momentum*, Wiley, New York, **1988**.
- [44] N. Bartels, Orientation-dependent energy transfer in gas-surface collisions: Scattering of vibrationally excited nitric oxide from Au(111), PhD thesis, Georg-August-Universität Göttingen, **2015**.
- [45] J. C. Tully, *Nonadiabatic Processes in Molecular Collisions*, in *Dynamics of Molecular Collisions, Part B: Modern Theoretical Chemistry 2*, (edited by W. H. Miller), Plenum Press, New York, **1976**.
- [46] M. Born, R. Oppenheimer, Zur Quantentheorie der Molekeln, *Annalen der Physik* **1927**, 84, 457–484, doi: 10.1002/andp.19273892002.
- [47] H. S. W. Massey, Collisions between atoms and molecules at ordinary temperatures, *Rep. Prog. Phys.* **1949**, 12, 248–269.
- [48] L. Landau, Zur Theorie der Energieübertragung, *Phys. Z. Sowjetunion* **1932**, 2, 46–51.
- [49] C. Zener, Non-adiabatic crossing of energy levels, *Proc. R. Soc. London Ser. A* **1932**, 137, 696–702, doi: 10.1098/rspa.1932.0165.
- [50] E. C. G. Stueckelberg, Theorie der unelastischen Stösse zwischen Atomen, *Helv. Phys. Acta* **1932**, 5, 369–422.

### C. References

- [51] J. V. Barth, H. Brune, G. Ertl, R. J. Behm, Scanning tunneling microscopy observations on the reconstructed Au(111) surface: atomic structure, long-range superstructure, rotational domains, and surface defects, *Phys. Rev. B.* **1990**, *42*(15), 9307–9318, doi: 10.1103/PhysRevB.42.9307.
- [52] S. Roy, N. A. Shenvi, J. C. Tully, Model Hamiltonian for the interaction of NO with the Au(111) surface, *J. Chem. Phys.* **2009**, *130*(17), 174716, doi: 10.1063/1.3122989.
- [53] I. Razado-Colambo, J. He, H. M. Zhang, G. V. Hansson, R. I. G. Uhrberg, Electronic structure of Ge (111)c(2x8): STM, angle-resolved photoemission, and theory, *Phys. Rev. B.* **2009**, *79*(20), 205410, doi: 10.1103/PhysRevB.79.205410.
- [54] W. Mönch, *Semiconductor Surfaces and Interfaces, Third Edition*, in *Springer Series in Surface Sciences*, (edited by G. Ertl, G. R., H. Lüth, D. L. Mills), Springer, Berlin, Heidelberg, New York, **2001**.
- [55] K. Hermann, F. Rammer, (FHI Berlin), Surface Explorer visualization software based on Balsac, (C), <http://surfexp.fhi-berlin.mpg.de/> **2016**.
- [56] W. M. Haynes, *CRC Handbook of Chemistry and Physics 77th Edition*, CRC press, Boca Raton, New York, London, Tokyo, **1996**.
- [57] G. Gobeli, F. Allen, Photoelectric properties and work function of cleaved germanium surfaces, *Surf. Sci.* **1964**, *2*, 402–408, doi: /10.1016/0039-6028(64)90081-0.
- [58] F. Reinert, G. Nicolay, S. Schmidt, D. Ehm, S. Hüfner, Direct measurements of the *L*-gap surface states on the (111) face of noble metals by photoelectron spectroscopy, *Phys. Rev. B.* **2001**, *63*(11), 115415, doi: 10.1103/PhysRevB.63.115415.
- [59] Y. Varshni, Temperature dependence of the energy gap in semiconductors, *Physica* **1967**, *34*(1), 149–154, doi: 10.1016/0031-8914(67)90062-6.
- [60] P. Heimann, H. Neddermeyer, H. F. Roloff, Ultraviolet photoemission for intrinsic surface states of the noble metals, *J. Phys. C* **1977**, *10*(1), L17–L21, doi: 10.1088/0022-3719/10/1/004.
- [61] W. D. Grobman, D. E. Eastman, J. L. Freeouf, Photoemission spectroscopy using synchrotron radiation. II. The electronic structure of germanium, *Phys. Rev. B* **1975**, *12*, 4405–4433, doi: 10.1103/PhysRevB.12.4405.

- [62] J. E. Hurst, C. A. Becker, J. P. Cowin, K. C. Janda, L. Wharton, D. J. Auerbach, Observation of Direct Inelastic Scattering in the Presence of Trapping-Desorption Scattering: Xe on Pt(111), *Phys. Rev. Lett.* **1979**, *43*, 1175–1177, doi: 10.1103/PhysRevLett.43.1175.
- [63] C. T. Rettner, The search for direct vibrational excitation in gas-surface collisions of CO with Au(111), *J. Chem. Phys.* **1993**, *99*(7), 5481–5489, doi: 10.1063/1.465965.
- [64] A. M. Wodtke, H. Yuhui, D. J. Auerbach, Insensitivity of trapping at surfaces to molecular vibration, *Chem. Phys. Lett.* **2005**, *413*(4-6), 326–330, doi: 10.1016/j.cplett.2005.06.031.
- [65] A. Tomsic, N. Marković, J. B. C. Pettersson, Direct scattering and trapping-desorption of large water clusters from graphite, *Chem. Phys. Lett.* **2000**, *329*(4), 200–206, doi: 10.1016/S0009-2614(00)01002-2.
- [66] C. T. Rettner, E. K. Schweizer, C. B. Mullins, Desorption and trapping of argon at a 2H-W(100) surface and a test of the applicability of detailed balance to a nonequilibrium system, *J. Chem. Phys.* **1989**, *90*(7), 3800, doi: 10.1063/1.455838.
- [67] M. Korolik, M. M. Suchan, M. J. Johnson, D. W. Arnold, H. Reisler, C. Wittig, Survival of HCl( $v = 2$ ) in trapping-desorption from MgO(100), *Chem. Phys. Lett.* **2000**, *326*(1-2), 11–21, doi: 10.1016/S0009-2614(00)00690-4.
- [68] C. T. Rettner, J. Kimman, D. J. Auerbach, Inelastic scattering of NO from Ag(111): Internal state, angle, and velocity resolved measurements, *J. Chem. Phys.* **1991**, *94*(1), 734–750, doi: 10.1063/1.460342.
- [69] E. K. Grimmelmann, J. C. Tully, M. J. Cardillo, Hard-cube model analysis of gas-surface energy accommodation, *J. Chem. Phys.* **1980**, *72*(2), 1039–1043, doi: 10.1063/1.439271.
- [70] E. Kuipers, M. Tenner, M. Spruit, A. Kleyn, Differential trapping probabilities and desorption of physisorbed molecules: Application to NO/Ag(111), *Surf. Sci.* **1988**, *205*(1), 241–268, doi: 10.1016/0039-6028(88)90175-6.
- [71] C. R. Arumainayagam, G. R. Schoofs, M. C. McMaster, R. J. Madix, Dynamics of molecular adsorption of ethane with platinum(111): a supersonic molecular beam study, *J. Phys. Chem.* **1991**, *95*(3), 1041–1047, doi: 10.1021/j100156a005.

### C. References

- [72] C. T. Rettner, Molecular beam studies of trapping dynamics, *J. Vac. Sci. Technol. A* **1990**, 8(3), 2699–2704, doi: 10.1116/1.576653.
- [73] M. G. Tenner, E. W. Kuipers, A. W. Kleyn, S. Stolte, Steric effects in molecular adsorption, *J. Chem. Phys.* **1988**, 89(10), 6552–6553, doi: 10.1063/1.455376.
- [74] M. A. Hines, R. N. Zare, The interaction of CO with Ni(111): Rainbows and rotational trapping, *J. Chem. Phys.* **1993**, 98(11), 9134–9147, doi: 10.1063/1.464421.
- [75] A. W. Kleyn, A. C. Luntz, D. J. Auerbach, Rotational Energy Transfer in Direct Inelastic Surface Scattering: NO on Ag(111), *Phys. Rev. Lett.* **1981**, 47, 1169–1172, doi: 10.1103/PhysRevLett.47.1169.
- [76] M. G. Tenner, F. H. Geuzebroek, E. W. Kuipers, A. E. Wiskerke, A. W. Kleyn, S. Stolte, A. Namiki, Orientation dependence of rotational excitation in NO scattering from Ag(111), *Chem. Phys. Lett.* **1990**, 168(1), 45–50, doi: 10.1016/0009-2614(90)85100-Q.
- [77] M. Tenner, E. Kuipers, A. Kleyn, S. Stolte, Classical trajectory study of the interaction of oriented NO and Ag (111), *Surf. Sci.* **1991**, 242, 376–385, doi: 10.1016/0039-6028(91)90295-4.
- [78] H. Voges, R. Schinke, A double rainbow interpretation of rotational energy transfer in energetic NO/Ag(111) collisions, *Chem. Phys. Lett.* **1983**, 100(3), 245–250, doi: /10.1016/0009-2614(83)87285-6.
- [79] J. Barker, A. Kleyn, D. Auerbach, Rotational energy distributions in molecule surface scattering: Model calculations for NO/Ag(111), *Chem. Phys. Lett.* **1983**, 97(1), 9–13, doi: /10.1016/0009-2614(83)87173-5.
- [80] A. E. Wiskerke, C. A. Taatjes, A. Kleyn, R. J. W. E. Lahaye, S. Stolte, D. K. Bronnikov, B. E. Hayden, Survival mechanism for rotational rainbows in highly attractive molecule-surface systems: NO scattering from Pt(111), *Chem. Phys. Lett.* **1993**, 216(1-2), 93–99, doi: 10.1016/0009-2614(93)E1258-I.
- [81] B. D. Kay, T. D. Raymond, M. E. Coltrin, Observation of a dynamical propensity rule in rotationally inelastic gas-surface scattering: NH<sub>3</sub> on Au(111), *Phys. Rev. B.* **1987**, 36(12), 6695–6697, doi: 10.1103/PhysRevB.36.6695.

- [82] M. E. Coltrin, B. D. Kay, Quasiclassical trajectory study of rotational energy transfer in the scattering of NH<sub>3</sub> from a flat, rigid gold surface, *J. Chem. Phys.* **1988**, 89(1), 551–561, doi: 10.1063/1.455444.
- [83] O. Bünermann, H. Jiang, Y. Dorenkamp, A. Kandratsenka, S. M. Janke, D. J. Auerbach, A. M. Wodtke, Electron-hole pair excitation determines the mechanism of hydrogen atom adsorption, *Science* **2015**, 350(6266), 1346–1349, doi: 10.1126/science.aad4972.
- [84] G. R. Stewart, Measurement of low-temperature specific heat, *Rev. Sci. Instrum.* **1983**, 54(1), 1–11, doi: 10.1063/1.1137207.
- [85] J. Thewlis, Unit-cell dimensions of lithium fluoride made from Li<sup>6</sup> and Li<sup>7</sup>, *Acta Cryst.* **1955**, 8, 36–38, doi: 10.1107/S0365110X55000091.
- [86] C. T. Rettner, F. Fabre, J. Kimman, D. J. Auerbach, Observation of direct vibrational excitation in gas-surface collisions: NO on Ag(111), *Phys. Rev. Lett.* **1985**, 55(18), 1904–1907, doi: 10.1103/PhysRevLett.55.1904.
- [87] S. Li, H. Guo, Monte Carlo wave packet study of negative ion mediated vibrationally inelastic scattering of NO from the metal surface, *J. Chem. Phys.* **2002**, 117(9), 4499–4508, doi: 10.1063/1.1498479.
- [88] R. Cooper, C. Bartels, A. Kandratsenka, I. Rahinov, N. Shenvi, K. Golibrzuch, Z. Li, D. J. Auerbach, J. C. Tully, A. M. Wodtke, Multiquantum vibrational excitation of NO scattered from Au(111): quantitative comparison of benchmark data to ab initio theories of nonadiabatic molecule-surface interactions, *Angew. Chem. Int. Ed.* **2012**, 51(20), 4954–4958, doi: 10.1002/anie.201201168.
- [89] K. Golibrzuch, P. R. Shirhatti, I. Rahinov, D. J. Auerbach, A. M. Wodtke, C. Bartels, Incidence energy dependent state-to-state time-of-flight measurements of NO( $v = 3$ ) collisions with Au(111): the fate of incidence vibrational and translational energy, *Phys. Chem. Chem. Phys.* **2014**, 16(16), 7602–7610, doi: 10.1039/c3cp55224a.
- [90] N. Bartels, K. Golibrzuch, C. Bartels, L. Chen, D. J. Auerbach, A. M. Wodtke, T. Schäfer, Observation of orientation-dependent electron transfer in molecule-surface collisions, *Proc. Natl. Acad. Sci.* **2013**, 110(44), 17738–17743, doi: 10.1073/pnas.1312200110.

### C. References

- [91] N. Bartels, K. Golibrzuch, C. Bartels, L. Chen, D. J. Auerbach, A. M. Wodtke, T. Schäfer, Dynamical steering in an electron transfer surface reaction: Oriented NO( $v = 3$ ,  $0.08 < E_i < 0.89$  eV) relaxation in collisions with a Au(111) surface, *J. Chem. Phys.* **2014**, *140*(5), 054710, doi: 10.1063/1.4863862.
- [92] P. M. Hundt, B. Jiang, M. E. van Reijzen, H. Guo, R. D. Beck, Vibrationally Promoted Dissociation of Water on Ni(111), *Science* **2014**, *344*(6183), 504–507, doi: 10.1126/science.1251277.
- [93] R. D. Beck, P. Maroni, D. C. Papageorgopoulos, T. T. Dang, M. P. Schmid, T. R. Rizzo, Vibrational Mode-Specific Reaction of Methane on a Nickel Surface, *Science* **2003**, *302*(5642), 98–100, doi: 10.1126/science.1088996.
- [94] K. Golibrzuch, J. H. Baraban, P. R. Shirhatti, J. Werdecker, C. Bartels, A. M. Wodtke, Observation of Translation-to-Vibration Excitation in Acetylene Scattering from Au(111): A REMPI Based Approach, *Z. Phys. Chem.* **2015**, *229*, 1929–1949, doi: 10.1515/zpch-2015-0606.
- [95] M. Herman, A. Campargue, M. I. E. Idrissi, J. V. Auwera, Vibrational Spectroscopic Database on Acetylene,  $\tilde{X}^1\Sigma_g^+$  ( $^{12}\text{C}_2\text{H}_2$ ,  $^{12}\text{C}_2\text{D}_2$ , and  $^{13}\text{C}_2\text{H}_2$ ), *J. Phys. Chem. Ref. Data* **2003**, *32*(3), 921–1361, doi: 10.1063/1.1531651.
- [96] B. D. Kay, T. D. Raymond, M. E. Coltrin, Observation of Direct Multiquantum Vibrational Excitation in Gas-Surface Scattering:  $\text{NH}_3$  on Au(111), *Phys. Rev. Lett.* **1987**, *59*, 2792–2794, doi: 10.1103/PhysRevLett.59.2792.
- [97] A. C. Wight, R. E. Miller, Rainbow scattering of methane from LiF(100): Probing the corrugation and anisotropy of the gas-surface potential, *J. Chem. Phys.* **1998**, *109*(5), 1976–1982, doi: 10.1063/1.476773.
- [98] A. C. Terentis, S. E. Waugh, G. F. Metha, S. H. Kable, HCO ( $N, K_a, K_c, J$ ) distributions from near-threshold photolysis of  $\text{H}_2\text{CO}$  ( $J, K_a, K_c$ ), *J. Chem. Phys.* **1998**, *108*(1998), 3187–3198, doi: 10.1063/1.475736.
- [99] U. Even, J. Jortner, D. Noy, N. Lavie, C. Cossart-Magos, Cooling of large molecules below 1 K and He clusters formation, *J. Chem. Phys.* **2000**, *112*(18), 8068–8071, doi: 10.1063/1.481405.
- [100] L. Velarde, D. P. Engelhart, D. Matsiev, J. LaRue, D. J. Auerbach, A. M. Wodtke, Generation of tunable narrow bandwidth nanosecond pulses in the deep ultraviolet



- for efficient optical pumping and high resolution spectroscopy., *Rev. Sci. Instrum.* **2010**, *81*(6), 063106, doi: 10.1063/1.3436973.
- [101] K. Golibrzuch, Quantum-state specific scattering of molecules from surfaces, PhD thesis, Georg-August-Universität Göttingen, **2014**.
- [102] N. Bartels, B. C. Krüger, S. Meyer, A. M. Wodtke, T. Schäfer, Suppression of Spontaneous Emission in the Optical Pumping of Molecules: Pump-Dump-Sweep-Probe, *J. Phys. Chem. Lett.* **2013**, *4*, 2367–2370, doi: 10.1021/jz401266m.
- [103] X. Yang, a. M. Wodtke, Efficient state-specific preparation of highly vibrationally excited NO( $X^2\Pi$ ), *J. Chem. Phys.* **1990**, *92*(1), 116–120, doi: 10.1063/1.458480.
- [104] G. B. Park, B. C. Krüger, S. Meyer, A. M. Wodtke, T. Schäfer, A  $1 + 1'$  resonance-enhanced multiphoton ionization scheme for rotationally state-selective detection of formaldehyde via the  $\tilde{A}^1A_2 \leftarrow \tilde{X}^1A_1$  transition, *Phys. Chem. Chem. Phys.* **2016**, *18*, 22355–22363, doi: 10.1039/C6CP03833F.
- [105] M. Meisinger, A. M. Schulenburg, F. Merkt, P. P. Radi, Rotationally resolved spectroscopy and dynamics of the  $3p_x^1A_2$  Rydberg state of formaldehyde., *Phys. Chem. Chem. Phys.* **2010**, *12*(48), 15592–15599, doi: 10.1039/c0cp00191k.
- [106] D. P. Engelhart, Electron Emission from Metastable Carbon Monoxide Molecules at Adsorbate Covered Au(111) Surfaces, PhD thesis, Georg-August-Universität Göttingen, **2015**.
- [107] Spence, R. and Wild, W., The preparation of liquid monomeric formaldehyde, *Journal of the Chemical Society* **1935**, 338–340, doi: 10.1039/jr9350000338.
- [108] G. Herzberg, *Molecular Spectra and Molecular Structure: I. Spectra Of Diatomic Molecules*, Van Nostrand Reinhold Company, New York, **1950**.
- [109] C. H. Townes, A. L. Schawlow, *Microwave Spectroscopy*, Dover Publications, Inc., New York, **1975**.
- [110] D. J. Auerbach, *Velocity Measurements by Time-of-flight Methods*, in *Atomic and Molecular Beam Methods: Volume 1*, (edited by G. Scoles), Oxford University Press, New York, Oxford, **1988**.

### C. References

- [111] B. C. Krüger, N. Bartels, A. M. Wodtke, T. Schäfer, Final rotational state distributions from NO( $v_1 = 11$ ) in collisions with Au(111): the magnitude of vibrational energy transfer depends on orientation in molecule-surface collisions, *Phys. Chem. Chem. Phys.* **2016**, *18*, 14976–14979, doi: 10.1039/C6CP02100J.
- [112] R. Schinke, Rotational rainbows in diatom(solid) surface scattering, *J. Chem. Phys.* **1982**, *76*(5), 2352–2359, doi: 10.1063/1.443263.
- [113] D. P. Engelhart, R. J. Wagner, A. Meling, A. M. Wodtke, T. Schäfer, Temperature programmed desorption of weakly bound adsorbates on Au(111), *Surf. Sci.* **2015**, *650*, 11–16, doi: 10.1016/j.susc.2015.06.010.
- [114] J. Kimman, C. T. Rettner, D. J. Auerbach, J. A. Barker, J. C. Tully, Correlation Between Kinetic-Energy Transfer to Rotation and to Phonons in Gas-Surface Collisions of NO with Ag(111), *Phys. Rev. Lett.* **1986**, *57*, 2053–2056, doi: 10.1103/PhysRevLett.57.2053.
- [115] B. C. Krüger, S. Meyer, A. Kandratsenka, A. M. Wodtke, T. Schäfer, Vibrational Inelasticity of Highly Vibrationally Excited NO on Ag(111), *J. Phys. Chem. Lett.* **2016**, *7*(3), 441–446, doi: 10.1021/acs.jpcllett.5b02448.
- [116] C. T. Rettner, D. J. Auerbach, H. A. Michelsen, Observation of direct vibrational excitation in collisions of H<sub>2</sub> and D<sub>2</sub> with a Cu(111) surface, *Phys. Rev. Lett.* **1992**, *68*, 2547–2550, doi: 10.1103/PhysRevLett.68.2547.
- [117] F. Budde, a. Mödl, a.V. Hamza, P. Ferm, G. Ertl, State-resolved investigation of the dynamics of scattering and formation of NO at Ge surfaces, *Surf. Sci.* **1987**, *192*(2-3), 507–528, doi: 10.1016/S0039-6028(87)81143-3.
- [118] I. Razado-Colambo, H. M. Zhang, R. I. G. Uhrberg, Electronic structure of H/Ge(111)1 x 1 studied by angle-resolved photoelectron spectroscopy, *Phys. Rev. B.* **2009**, *80*(19), 193403, doi: 10.1103/PhysRevB.80.193403.
- [119] S. Hunklinger, *Festkörperphysik*, Oldenbourg Verlag, München, **2009**.
- [120] D. J. Griffiths, *Introduction to Electrodynamics*, Prentice Hall, Upper Saddle River, **1999**.
- [121] M. Golze, M. Grunze, W. Hirschwald, The effect of attractive lateral interactions on flash-desorption spectra, *Vacuum* **1981**, *31*(10), 697–703, doi: 10.1016/0042-207X(81)90098-1.

- [122] D. A. Outka, R. Madix, Acid-base and nucleophilic chemistry of atomic oxygen on the Au(110) surface: Reactions with formic acid and formaldehyde, *Surf. Sci.* **1987**, *179*(2), 361–376, doi: 10.1016/0039-6028(87)90063-X.
- [123] R. Gorte, L. Schmidt, J. L. Gland, Binding states and decomposition of NO on single crystal planes of Pt, *Surf. Sci.* **1981**, *109*(2), 367–380, doi: 10.1016/0039-6028(81)90494-5.
- [124] L. E. Fleck, Z. C. Ying, M. Feehery, H. L. Dai, The adsorption geometry and energetics of formaldehyde physisorbed on Ag(111): An EELS and TPD study, *Surf. Sci.* **1993**, *296*(3), 400–409, doi: 10.1016/0039-6028(93)90034-H.
- [125] W. K. Chen, S. H. Liu, M. J. Cao, Q. G. Yan, C. H. Lu, Adsorption and dissociation of methanol on Au(111) surface: A first-principles periodic density functional study, *J. Mol. Struct.: THEOCHEM* **2006**, *770*(1-3), 87–91, doi: 10.1016/j.theochem.2006.05.040.
- [126] B. C. Krüger, G. B. Park, S. Meyer, R. J. V. Wagner, A. M. Wodtke, T. Schäfer, Trapping-desorption and direct-scattering of formaldehyde at Au(111), *Phys. Chem. Chem. Phys.* **2017**, *19*, 19896–19903, doi: 10.1039/C7CP03907G.
- [127] S. Andreyev, V. Antonov, I. Knyazev, V. Letokhov, Two-step photoionization of H<sub>2</sub>CO by radiation of N<sub>2</sub>- and H<sub>2</sub>- lasers and measurement of the lifetime of its <sup>1</sup>A<sub>2</sub> state, *Chem. Phys. Lett.* **1977**, *45*(1), 166–168, doi: 10.1016/0009-2614(77)85235-4.
- [128] J. E. Mentall, E. P. Gentieu, M. Krauss, D. Neumann, Photoionization and Absorption Spectrum of Formaldehyde in the Vacuum Ultraviolet, *J. Chem. Phys.* **1971**, *55*(12), 5471–5479, doi: 10.1063/1.1675711.
- [129] D. T. Co, T. F. Hanisco, J. G. Anderson, F. N. Keutsch, Rotationally Resolved Absorption Cross Sections of Formaldehyde in the 28100-28500 cm<sup>-1</sup> (351-356 nm) Spectral Region: Implications for in Situ LIF Measurements, *J. Phys. Chem. A* **2005**, *109*(47), 10675–10682, PMID: 16863116, doi: 10.1021/jp053466i.
- [130] H. Zacharias, R. Schmiedl, K. H. Welge, State selective step-wise photoionization of NO with mass spectroscopic ion detection, *Appl. Phys.* **1980**, *21*(2), 127–133, doi: 10.1007/BF00900674.

### C. References

- [131] G. B. Park, B. C. Krüger, S. Meyer, D. Schwarzer, T. Schäfer, The  $\nu_6$  fundamental frequency of the  $\tilde{A}$  state of formaldehyde and Coriolis perturbations in the  $3\nu_4$  level, *J. Chem. Phys.* **2016**, *144*(19), 194308, doi: 10.1063/1.4948635.
- [132] W. E. Henke, H. L. Selzle, T. R. Hays, E. W. Schlag, S. H. Lin, Single rotational lifetimes of formaldehyde in a hypersonic jet, *J. Chem. Phys.* **1982**, *76*(3), 1327–1334, doi: 10.1063/1.443126.
- [133] J. C. Weisshaar, C. B. Moore, Collisionless nonradiative decay rates of single rotational levels of S1 formaldehyde, *J. Chem. Phys.* **1979**, *70*(11), 5135–5146, doi: 10.1063/1.437354.
- [134] C. Bechtel, E. Elias, B. F. Schramm, Nuclear spin symmetry state relaxation in formaldehyde, *J. Mol. Struct.* **2005**, *741*(1), 97–106, doi: 10.1016/j.molstruc.2005.01.056.
- [135] K. Shibuya, E. K. C. Lee, Rotational dependence of the fluorescence quantum yields of H<sub>2</sub>CO and D<sub>2</sub>CO ( $\tilde{A}^1A_2$ ): single rovibronic level values and their average values for the  $4^1$  level, *J. Chem. Phys.* **1978**, *69*(12), 5558–5560, doi: 10.1063/1.436552.
- [136] L. G. Dodson, L. Shen, J. D. Savee, N. C. Eddingsaas, O. Welz, C. A. Taatjes, D. L. Osborn, S. P. Sander, M. Okumura, VUV photoionization cross sections of HO<sub>2</sub>, H<sub>2</sub>O<sub>2</sub>, and H<sub>2</sub>CO, *J. Phys. Chem. A* **2015**, *119*(8), 1279–1291, doi: 10.1021/jp508942a.
- [137] L. Rothman, I. Gordon, Y. Babikov, A. Barbe, D. C. Benner, P. Bernath, M. Birk, L. Bizzocchi, V. Boudon, L. Brown, A. Campargue, K. Chance, E. Cohen, L. Coudert, V. Devi, B. Drouin, A. Fayt, J.-M. Flaud, R. Gamache, J. Harrison, J.-M. Hartmann, C. Hill, J. Hodges, D. Jacquemart, A. Jolly, J. Lamouroux, R. L. Roy, G. Li, D. Long, O. Lyulin, C. Mackie, S. Massie, S. Mikhailenko, H. Müller, O. Naumenko, A. Nikitin, J. Orphal, V. Perevalov, A. Perrin, E. Polovtseva, C. Richard, M. Smith, E. Starikova, K. Sung, S. Tashkun, J. Tennyson, G. Toon, V. Tyuterev, G. Wagner, The HITRAN2012 molecular spectroscopic database, *J. Quant. Spectrosc. Radiat. Transfer* **2013**, *130*, 4–50, doi: /10.1016/j.jqsrt.2013.07.002.
- [138] E. Kuipers, M. Tenner, A. Kleyn, S. Stolte, Dependence of the NO/Ag(111) trapping probability on molecular orientation, *J. Chem. Phys.* **1989**, *138*(2), 451–460, doi: 10.1016/0301-0104(89)87151-4.

- [139] G. B. Park, B. C. Krüger, S. Meyer, A. Kandratsenka, A. M. Wodtke, T. Schäfer, An axis-specific rotational rainbow in the direct scatter of formaldehyde from Au(111) and its influence on trapping probability, *Phys. Chem. Chem. Phys.* **2017**, *19*, 19904–19915, doi: 10.1039/C7CP03922K.
- [140] D. C. Burleigh, A. B. McCoy, E. L. Sibert, An accurate quartic force field for formaldehyde, *J. Chem. Phys.* **1996**, *104*(2), 480–487, doi: 10.1063/1.471531.
- [141] A. K. Rappe, C. J. Casewit, K. S. Colwell, W. A. Goddard, W. M. Skiff, UFF, a full periodic table force field for molecular mechanics and molecular dynamics simulations, *JACS* **1992**, *114*(25), 10024–10035, doi: 10.1021/ja00051a040.
- [142] H. Goldstein, C. P. Poole, J. L. Safko, *Classical Mechanics Third Edition*, Pearson, Essex, **2014**.
- [143] R. J. V. Wagner, N. Henning, B. C. Krüger, G. B. Park, A. M. Wodtke, Vibrational relaxation of highly vibrationally excited CO scattered from Au(111): Evidence for formation of transient CO<sup>-</sup>, *submitted to J. Phys. Chem. Lett.* **2017**.
- [144] C. Benoit, R. Abouaf, Low-energy electron collisions with formaldehyde: interference phenomena in the differential vibrational excitation cross section, *Chem. Phys. Lett.* **1986**, *123*(1-2), 134–138, doi: 10.1016/0009-2614(86)87028-2.
- [145] M. Allen, D. J. Tildesley, *Computer Simulation of Liquids*, Oxford University Press, Oxford, New York, **1987**.



# Acknowledgements

First, I would like to thank Prof. Dr. Alec M. Wodtke for enabling the work presented in this thesis. His merits are not only the creation of a workgroup with a gigantic expertise in surface science including the available scientific infrastructure but also the excellent supervision of this work leaving me enough freedom in the research, however at the same time being there for fruitful discussions and stepping in when his help was needed. Especially, I appreciated the opportunity to learn from scientists from all over the world that frequently visited the group, for instance in the context of the annual group meetings in Ringberg. Special thanks go to Prof. Dr. Dirk Schwarzer who is the second referee of this thesis. His impact on this work is very large. In particular, the design of the heatable nozzle by him which is crucial for all scattering experiments on formaldehyde presented here has to be highlighted.

Many and special thanks go to Dr. Tim Schäfer. He is not only an excellent scientist but also an ideal mentor. His skills cover the whole range from plumbing to mastering the field of quantum mechanics. At the same time, he is to a great extent responsible for the encouraging team spirit in the work group and does many things that certainly go beyond the obligations determined in his contract. I have learned a lot of things from him not only about science.

Dr. Nils Bartels has been my predecessor on the “orientation machine” and did a great job in introducing me to the laboratory and important analysis techniques. Moreover, he is an excellent scientist and has an exceptional skill for teaching. This also applies to Dr. G. Barratt Park who joined me for the formaldehyde project. His knowledge about spectroscopy and related topics seems to be endless. In some years, I hope and I would not be surprised to notice that he became a “Big Professor”.

It is very important to thank six people who taught me a lot about surface science. Dr. Alexander Kandratsenka’s valuable guidance concerning theoretical chemistry as well as computer problems was crucial to the development of this work. Dr. Christof Bartels, Dr. Pranav R. Shirhatti, Dr. Kai Golibrzuch, Dr. Dan Harding, and Dr. Hongyan Jiang were always there for long and fruitful discussions.

Many thanks go to my colleagues Roman Wagner, Sven Meyer, and Niklas Henning. Roman Wagner is my “desk neighbor” and gave me valuable advices concerning a lot of different topics. Sven Meyer worked together with me on the “orientation machine” and is very talented in finding practical solutions to the everyday challenges in the lab. Niklas Henning is an excellent coworker —both highly motivated and talented.

Special thanks go to Birgit Freyberg who introduced me to “her” homebuilt optical parametric oscillators and was always there when her technical expertise was needed. In addition, I would like to thank Reinhard Bürsing and the workshop team of the Institute for Physical Chemistry for their technical support.

Many thanks for proofreading this thesis go to Dr. Marie Bergner, Barbara Hubrich, Dr. G. Barratt Park and Dr. Tim Schäfer.

Last but not least I would like to thank my family Nils, Christa and Manfred Krüger as well as Barbara Hubrich for continuous support and motivation. Without you this work would not have been possible.



# Curriculum Vitae

Bastian Christopher Krüger

Born March 9, 1988 in Wilhelmshaven

Nationality: German

## Education

- 2014-2017      **PhD thesis** under the supervision of Prof. Dr. A. M. Wodtke, University of Göttingen: “From diatomic to polyatomic quantum-state-resolved molecule-surface scattering”
- 2013-2015      **Distance learning: Laser techniques**, University of Jena, Certificate in Laser techniques, overall grade: very good (1)
- 2011-2013      **M. Sc. Chemistry**, University of Göttingen  
overall grade: very good (1.1) with distinction  
Master thesis (04-10/2013): “Orientation dependent multiquantum vibrational relaxation of highly vibrationally excited nitric oxide scattered from a Au(111) surface” under the supervision of Prof. Dr. A. M. Wodtke
- 2008-2011      **B. Sc. Chemistry**, University of Göttingen  
overall grade: very good (1.1) with distinction  
Bachelor thesis (06-08/2011): “Untersuchung zur Druckabhängigkeit der Partikel- und Produktbildung bei der Alkenozonolyse” under the supervision of PD Dr. T. Zeuch
- 2007-2008      Alternative civilian service
- 2007              High-school diploma “Abitur”, Lothar-Meyer-Gymnasium Varel  
overall grade: very good (1.4)

## Awards

2015	Hot Topic Prize at Bunsentagung 2015
2014	Bunsen-book prize for an excellent master thesis
2007	DPG Award for the best high-school graduate in physics
2007	GDCh Award for the best high-school graduate in chemistry

## Publications

P. T. M. Carlsson, J. E. Dege, C. Keunecke, B. C. Krüger, J. L. Wolf, T. Zeuch, Pressure dependent aerosol formation from the cyclohexene gas-phase ozonolysis in the presence and absence of sulfur dioxide: a new perspective on the stabilisation of the initial clusters, *Phys. Chem. Chem. Phys.* **2012**, *14*, 11695-11705.

P. T. M. Carlsson, C. Keunecke, B. C. Krüger, M.-C. Maaß, T. Zeuch, Sulfur dioxide oxidation induced mechanistic branching and particle formation during the ozonolysis of  $\beta$ -pinene and 2-butene, *Phys. Chem. Chem. Phys.* **2012**, *14*, 15637-15640.

N. Bartels, B. C. Krüger, D. J. Auerbach, A. M. Wodtke, T. Schäfer, Suppression of Spontaneous Emission in the Optical Pumping of Molecules: Pump-Dump-Sweep-Probe, *J. Phys. Chem. Lett.* **2013**, *4*, 2367-2370.

N. Bartels, B. C. Krüger, D. J. Auerbach, A. M. Wodtke, T. Schäfer, Controlling an electron-transfer reaction at a metal surface by manipulating reactant motion and orientation, *Angew. Chem. Int. Ed.* **2014**, *53*(50), 13690-13694.

B. C. Krüger, N. Bartels, C. Bartels, A. Kandratsenka, J. C. Tully, A. M. Wodtke, T. Schäfer, NO Vibrational Energy Transfer on a Metal Surface: Still a Challenge to First-Principles Theory, *J. Phys. Chem. C* **2015**, *119*(6), 3268-3272.

B. C. Krüger, N. Bartels, J. Altschäffel, A. M. Wodtke, T. Schäfer, Controlling collisions of highly vibrationally excited NO with a Au(111) surface, *Bunsenmagazin* **2015**, *5*, 185.

G. B. Park, B. C. Krüger, S. Meyer, A. M. Wodtke, T. Schäfer, A 1+1' resonance-enhanced multiphoton ionization scheme for rotationally state-selective detection of formaldehyde via the  $\tilde{A}^1A_2 \leftarrow \tilde{X}^1A_1$  transition, *Phys. Chem. Chem. Phys.* **2016**, *18*, 22355-22363.

G. B. Park, B. C. Krüger, S. Meyer, D. Schwarzer, T. Schäfer, The  $\nu_6$  fundamental frequency of the  $\tilde{A}$  state of formaldehyde and Coriolis perturbations in the  $3\nu_4$  level, *J. Chem. Phys.* **2016**, *144*(19), 194308.

B. C. Krüger, N. Bartels, A. M. Wodtke, T. Schäfer, Final rotational state distributions from  $\text{NO}(v_i = 11)$  in collisions with Au(111): the magnitude of vibrational energy transfer depends on orientation in molecule-surface collisions, *Phys. Chem. Chem. Phys.* **2016**, *18*, 14976-14979.

B. C. Krüger, S. Meyer, A. Kandratsenka, A. M. Wodtke, T. Schäfer, Vibrational Inelasticity of Highly Vibrationally Excited NO on Ag(111), *J. Phys. Chem. Lett.* **2016**, *7*(3), 441-446.

A. Kastner, T. Ring, B. C. Krüger, G. B. Park, T. Schäfer, A. Senftleben, T. Baumert, Intermediate state dependence of the photoelectron circular dichroism of fenchone observed via femtosecond resonance-enhanced multi-photon ionization, *J. Chem. Phys.* **2017**, *147*, 013926.

B. C. Krüger, G. B. Park, S. Meyer, R. J. V. Wagner, A. M. Wodtke, T. Schäfer, Trapping-desorption and direct-scattering of formaldehyde at Au(111), *Phys. Chem. Chem. Phys.* **2017**, *19*, 19896-19903.

G. B. Park, B. C. Krüger, S. Meyer, A. Kandratsenka, A. M. Wodtke, T. Schäfer, An axis-specific rotational rainbow in the direct scatter of formaldehyde from Au(111) and its influence on trapping probability, *Phys. Chem. Chem. Phys.* **2017**, *19*, 19904-19915.